PROGRESS IN RESEARCH

April 1, 2022 - March 31, 2023

CYCLOTRON INSTITUTE

Texas A&M University

College Station, Texas

PROGRESS IN RESEARCH

APRIL 1, 2022 - MARCH 31, 2023

Prepared By

The Cyclotron Institute Staff

Texas A&M University

College Station, TX 77843-3366

Phone: (979) 845-1411
Fax: (979) 845-1899

Web: http://cyclotron.tamu.edu

July 2023

TABLE OF CONTENTS

SECTION II: HEAVY ION REACTIONS

SECTION III: NUCLEAR THEORY

SECTION IV: SUPERCONDUCTING CYCLOTRON, INSTRUMENTATION AND RIB UPGRADE

Introduction
April 1, 2022 – March 31, 2023

Progress in research and operations at the Texas A&M Cyclotron Institute is summarized in this report for the period April 1, 2022 through March 31, 2023. The CI has had a remarkably productive year and I am indebted to the dedicated operations staff that keeps the facility running. The discovery science program continues to produce exciting results as outlined in the chapters that follow. At-211 has successfully been shipped overnight to collaborators at the University of Alabama – Birmingham.

Cyclotron physicist Dr. Ralf Rapp is the PI for a new Topical Theory Collaboration Heavy-Flavor Theory (HEFTY) for QCD Matter. The collaboration will develop a theoretical framework for describing the behavior of some of the heaviest particles within a unique form of matter that characterized our universe in its earliest stages.

Funding for the DOE – NP Center of Excellence that supports the Cyclotron Based Nuclear Science program has been renewed for an additional 3 years. Additionally, the DOE/NNSA Center of Excellence CENTAUR has also been selected for a 5-year renewal. With funding from the radiation effects community we have initiated a project to enhance the range of beams from the K150 and reliability of K500.

During this period the K500 provided 5292 hours and the K150 provided 3912 hours of beam for both science and radiation-effects testing. For the first time, both the new ECR4 ion source and the repaired ECR1 ion source were used to supply injected beam for the K500. Development has continued with the K150, most notably the testing of the effect of the internal helium cryopanel on extracted beam. The intensity of a 3 MeV/u gold beam increased by over a factor of thirty when the cryopanel was cooled down. Also, the MIVOC (Metal Ions from VOlatile Compounds) method was tried for introducing metallocene compounds into ECR2 for the production of metallic ions to be accelerated by the K150. Metallocenes are organometallic compounds with high vapor pressures, so they require higher conductances and sometimes heating elements to gain enough flow of vapor into the ion source. They should enable much longer periods of uninterrupted beam production than the micro-ovens usably used to vaporize metals inside the ion source.

Institute scientists remain active in a number of collaborative research efforts around the world. Major programs include: measurements of beta decays with the TRINAT collaboration at TRIUMF; nuclear structure measurements with TexAT at TRIUMF; continued work with the STAR collaboration at RHIC; and participation in the SAMURAI collaboration at RIBF in Tokyo, Japan.

The format of this report follows that of previous years. Sections I through III contain reports from individual research projects. Operation and technical developments are given in Section IV. Section V lists the publications with Cyclotron Institute authors and outside users and the Appendix gives additional information including talks presented by members of the Institute during the past year. Once again, the full volume of this year's Progress in Research is available only on our web site (http://cyclotron.tamu.edu).

Since most of the contributions presented here are truly reports on progress in research, results and conclusions should not be quoted from the report without the consent of the authors.

I am indebted to Dr. Y.-W. Lui for assembling this report.

S.J. Yennello
Sept 13, 2023

SECTION I

NUCLEAR STRUCTURE, FUNDAMENTAL INTERACTIONS AND ASTROPHYSICS

Improved decay data for the long-lived fission product ^{111}Ag

V.E. Iacob,[1] J.C. Hardy,[1] D. Melconian,[1] K. Kolos,[2] D.E.M. Hoff,[2] N.D. Scielzo,[2] M. Brodeur,[4] N. Callahan,[3] J.A. Clark,[3] M. Gott,[3] B. Liu,[3,4] W-J. Ong,[2] R. Orford,[4] D. Ray,[3,5] A. Richard,[2] D. Santiago-Gonzalez,[3] G. Savard,[3,7] K.S. Sharma,[5] M.A. Stoyer,[2] A.A. Valverde,[3,6] and L. Varriano[7]

[1]*Cyclotron Institute*, *Texas A&M University, College Station, Texas, 77843*

[2]*Lawrence Livermore National Laboratory,*

[3]*Argonne National Laboratory,*

[4]*University of Notre Dame,*

[5]*Lawrence Berkeley National Laboratory,*

[6]*University of Manitoba,*

[7]*University of Chicago*

Continuing our collaborative effort TAMU-LLNL-ANL [1,2,3] to improve the experimental data for long lived fission products, we performed a branching ratio measurement on ^{111}Ag ($t_{1/2}$ = 7.5d). We combined measurements of g singles, b-g coincidences, and scaled b singles in a manner similar to the one described in Ref. [1].

Two high purity ^{111}Ag sources implanted in a thin (40 μg/cm^2) carbon foil were collected at the CARIBU facility at ANL. Immediately after harvesting, each source was shipped to the Cyclotron Institute (CI) at TAMU. The source activities at the time of their arrival at the CI were 1140 Bq and 1830 Bq.

The experimental setup involved a 4π proportional counter with continuous methane flow, our high-precision absolute efficiency calibrated HPGe detector [4,5] and the acquisitions system described in Refs. [1,6].

We inserted the first source in the gas counter and carefully adjusted the source to HPGe distance to 151 mm, the distance used in the absolute efficiency calibration. We could then start a g-singles measurement. The start of the b-g coincidences had to be postponed for ~6 hr, time needed to flush the gas counter after the source insertion. We stopped the measurements of the first source at the arrival of the second, more intense one.

Repeating the steps followed for the previous source, we measured g singles, b-g coincidences and scaled b singles for the canonical distance source to HPGe cap of 151 mm. The top panel in Fig. 1 presents the g ray spectrum observed in prompt coincidence with b^- particles. The main peak at 342 keV (a 6.7% intense transition) contains ~2.2×10^5 events, enough to guarantee the aimed branching ratio accuracy of 0.5%. Along with g peaks from the ^{111}Ag decay, we identified peaks from ^{95}Zr ($t_{1/2}$=64d) and its daughter ^{95}Nb ($t_{1/2}$=35d). These radioactive impurities originate in oxides of ^{95}Zr and ^{95}Nb or their A=95 precursors in the b decay chain ($t_{1/2}$<11min): These oxides have the mass needed to pass the isobar separator at ANL that was set for A=111 nuclei. Notice the high background for the energy region above the dominant peak at 342 keV. This significantly increases the uncertainty in the areas of peaks in this region, up to the point of making some of them undetectable.

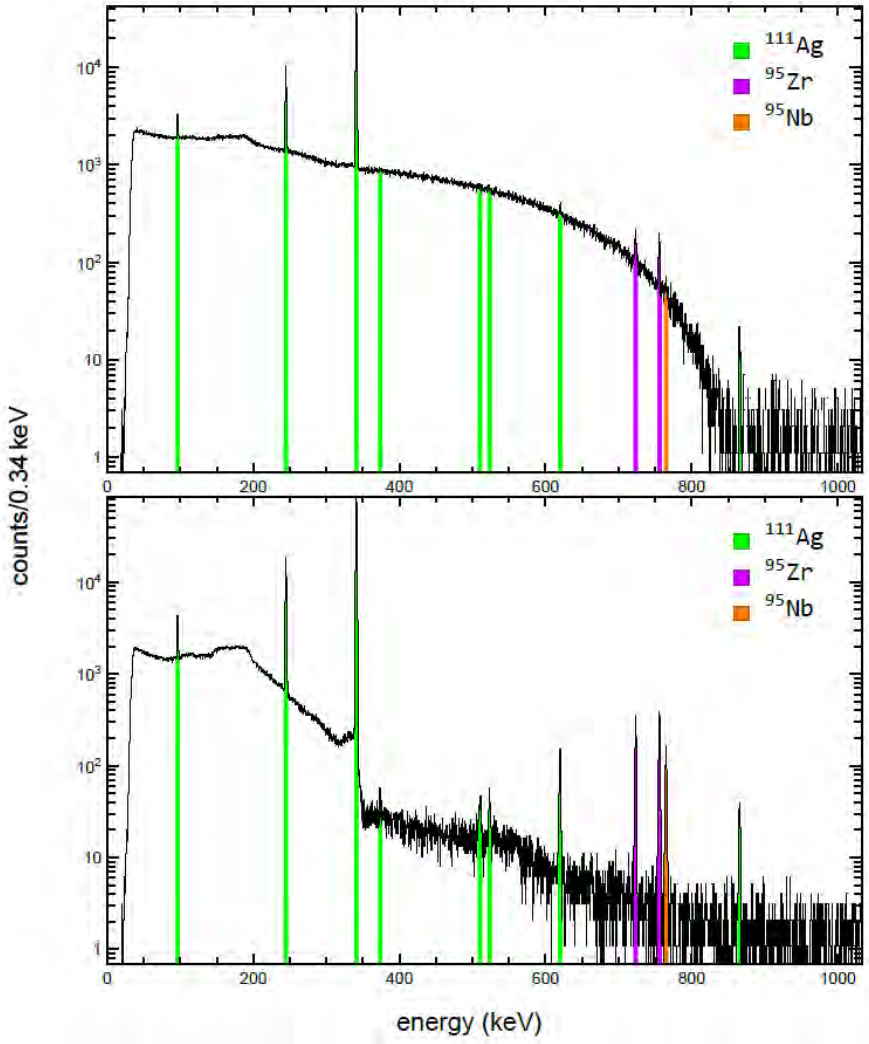

Fig. 1. γ ray spectra observed in prompt coincidence with electrons from the decay of the second ^{111}Ag source. The spectrum in the upper panel was measured with the source at the canonical distance of 151 mm to the HPGe detector cap. The spectrum in the lower panel was measured with the source at 51 mm to the HPGe cap, and a 4.7 mm thick Plexiglass plate in-between serving as a β^- screen.

A second measurement of this source began a week after its arrival at the CI. We made two important changes: (i) to compensate for the activity drop, we positioned the source at 51 mm to the HPGe cap, and (ii) to reduce the above-mentioned background, we introduced between the source and HPGe a 4.7 mm thick Plexiglass plate acting as a β^- screen. The observed γ ray spectrum coincident with β^- particles is presented in the bottom panel of Fig. 1. Notice the significant improvement in the data quality for the weak g rays. Data extracted from this measurement require however absolute efficiencies for the close geometry (with the Plexiglass screen); these can be obtained from pairs of source measurements in close canonical geometries.

Data analysis is in progress.

[1] K. Kolos *et al*, Nucl. Instrum. Methods Phys. Res. **A1000**, 165240 (2021).
[2] K. Kolos *et al*., *Progress in Research*, Cyclotron Institute, Texas A&M University (2018-2019), p. I-37.
[3] M. Bencomo *et al*., *Progress in Research*, Cyclotron Institute, Texas A&M University (2020-2021), p. I-21.
[4] R.G. Helmer *et al.*, Nucl. Instrum. Methods Phys. Res. **A511**, 360 (2003).
[5] R.G. Helmer *et al.*, Appl. Radiat. Isot. **60**, 173 (2004).
[6] V.E. Iacob *et al.*, Phys. Rev. C **101**, 045501 (2020).

Precise half-life measurement for ^{29}P

D.G. Melconian, V.E. Iacob, N. Nica, D. McClain, M. Nasser, G. Chubarian, V. Kolhinen, B Roeder, and A. Saastamoinen

The most precise value for the up-down quark mixing element V_{ud} in the Cabbibo-Kobayashi-Maskawa (CKM) matrix, comes from superallowed $0^+ \rightarrow 0^+$ beta decays [1]. An independent test of its value can be obtained from ft-values measured on T=1/2 nuclear mirror transitions [2], particularly from 5 cases: ^{19}Ne, ^{21}Na, ^{29}P, ^{35}Ar and ^{37}K. When compared to the superallowed decays, there is an added difficulty in extracting V_{ud} from these transitions: being mixed Fermi and Gamow-Teller decays, they require an additional measurement of the relative contribution of the vector and axial vector components.

In this context we report here a precise measurement of the half-life of ^{29}P. The radioactive beam was produced in the ^{30}Si(H,^{29}P) reaction. Using the Magnetic Achromat Recoil Spectrometer (MARS), a better than 99% beam purity was achieved in spectrograph's focal plane (see Fig. 1). The radioactive beam at 22 *A* MeV was extracted in air, passed through a 0.3mm thick BC404 plastic scintillator, a series of Al degraders, eventually being implanted in a 76 mm-thick Mylar tape of our fast tape transport system. The scintillator-degrader combination further refined the beam purity. When compared to MARS's focal plane, the tape-retained activity contained only traces of ^{30}P and ^{26}Si, at levels of 10^{-4} relative to ^{29}P. Fig. 2 details the status of the impurities retained in the Mylar tape. Note that we have set the centroid of the ^{29}P implantation closer to the back side of the Mylar tape (beam's perspective); this ensures that the dominant impurity at MARS's focal plane ^{27}Si punches through the Mylar tape, leading to its complete elimination in the tape-retained activity. To ensure a high data quality, a mandatory requirement in high precision experiments, the beam purity was checked daily over the duration of the experiment.

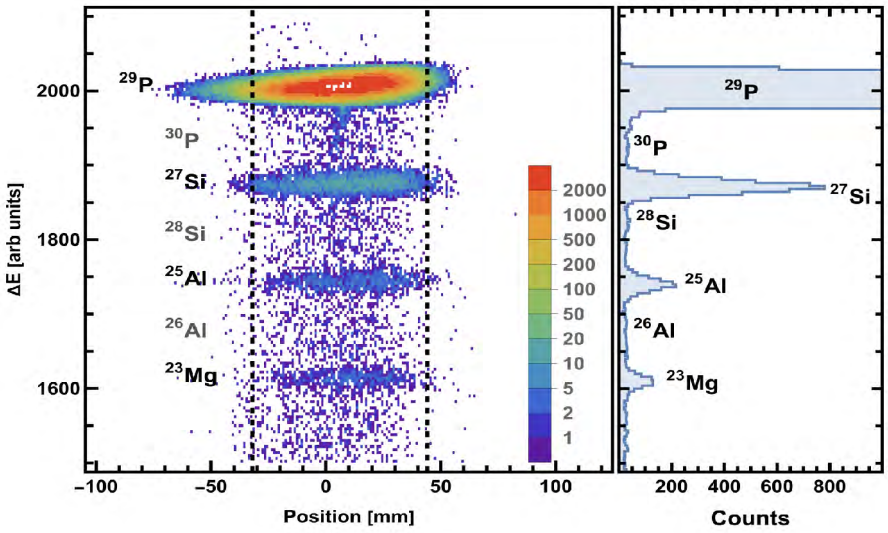

Fig. 1. Radioactive beam purity as observed in MARS's focal plane.

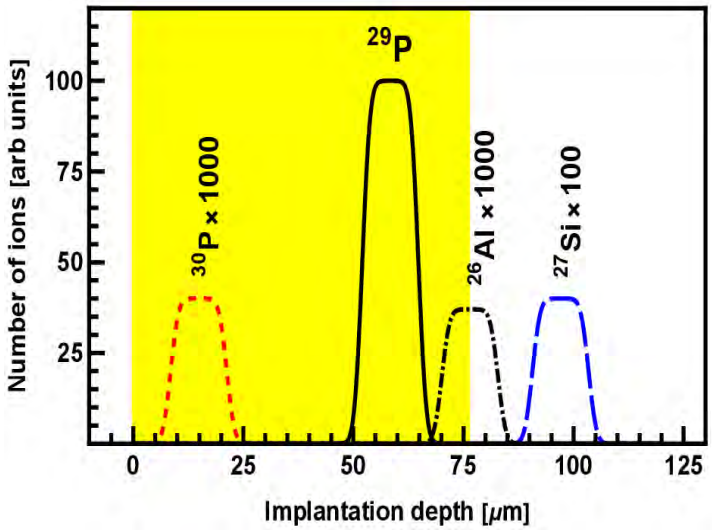

Fig. 2. Depth distribution of implanted ions. The yellow region indicates the 76mm-thick tape. The implanted beam enters the left side.

The data was acquired in cycles. Each cycle started with activity collection: ^{29}P nuclei were implanted for up to two half-lives in the Mylar tape. Then, with the beam turned off, the activity was moved in the center of our 4p proportional counter, where the decays were measured for 20 half-lives. Cycles were repeated until the desired statistics was achieved. In a seven day experiment we collected more than 100 million ^{29}P decays.

The signal processing began with a high-gain amplification aiming at preserving the time information. The amplified signals were then sent to a leading-edge discriminator, whose output was then passed to two non-retriggering gate generators, that inserted two independent major non-extending dead-times. These two parallel event streams were then multiscaled and recorded for each cycle.

The experiment was split in sub-runs, differing from one another by critical acquisition parameters: detector bias (from 2350 to 2650 V, in steps of 50 V), discrimination threshold (150-, 200-, and 250-mV), and dominant dead-times (4-, 6-, and 8-ms). More experimental details can be found in the report [3].

We performed half-life fits on pre-sorted dead-time corrected data: We carefully analyzed each cycle, and accepted it in the fit only if:

(1) the implantation beam provided more than 5000 ^{29}P nuclei,
(2) the ratio of detected betas to implanted nuclei was at least 90% of the expected value, and
(3) the cycle c^2 was below an upper limit set such that the probability for higher values is less than 10^{-4}.

Each sub-run was subject to a maximum likelihood fit as described in [4]. To test for possible abnormalities in the reduced half-life, we grouped the sub-runs based on detector bias and discriminating

threshold. The results (see Fig. 3) show no inconsistencies between the bias and discriminator sub-groups. Similarly, we see no dead-time effects in the extracted half-life: Almost no difference is observed between corresponding results from the two parallel streams differing only in the inserted dominant dead-time.

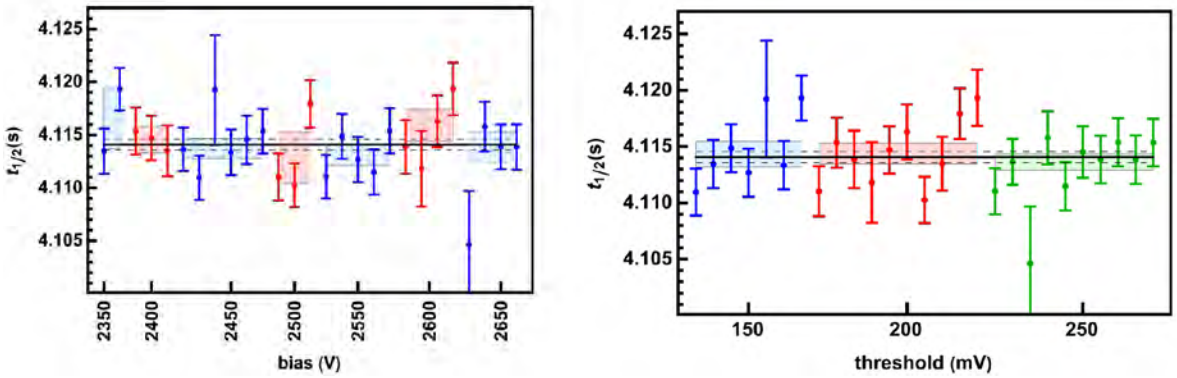

Fig. 3. Test for ^{29}P half-life dependencies on major acquisition parameters. Left panel: extracted half-life from runs with common detector bias. Right panel: extracted half-life from runs with common discrimination threshold.

We couldn't identify abnormalities neither in the data, nor in the extracted half-life. Our preliminary result is 4.1140(8) s. This value is more precise but above the recent result of J.Long *et al.* [5], the only published measurement with a precision close to 0.1%. Their result is 4.1055(44) s; however, they estimate the radioactive impurities from the fit, which we believe is the cause of the discrepancy with our result.

[1] J.C. Hardy and I.S. Towner, Phys. Rev C **102**, 045501(2020).

[2] O. Naviliat-Cuncic and N. Severijns, Phys. Rev. Lett. **102**, 142302 (2009).

[3] V.E. Iacob *et al., Progress in Research*, Cyclotron Institute, Texas A&M University (2021-2022), p. I-3.

[4] V.T. Koslowsky *et al*, Nucl. Instrum. Methods Phys. Res. **A401**, 289 (1997).

[5] J. Long *et al*., Phys Rev C **101**, 015501 (2020).

Constraints on key $^{17}O(\alpha,\gamma)^{21}Ne$ resonances and impact on the weak s process

M. Williams,[1,2,] A.M. Laird,[2] A. Choplin,[3] P. Adsley,[4,5] B. Davids,[1,6] U. Greife,[7] K. Hudson,[1,6] D. Hutcheon,[1] A. Lennarz,[1,8] and C. Ruiz[1]

[1]*TRIUMF, 4004 Wesbrook Mall, Vancouver, British Columbia V6T 2A3, Canada*

[2]*Department of Physics, University of York, Heslington, York YO10 5DD, United Kingdom*

[3]*Institut d'Astronomie et d'Astrophysique, Université Libre de Bruxelles, CP 226, B-1050 Brussels, Belgium*

[4]*Cyclotron Institute, Texas A&M University, College Station, Texas 77843, USA*

[5]*Department of Physics & Astronomy, Texas A&M University, College Station, Texas 77843, USA*

[6]*Department of Physics, Simon Fraser University, 8888 University Drive, Burnaby, British Columbia V5A 1S6, Canada*

[7]*Department of Physics, Colorado School of Mines, Golden, Colorado 80401, USA*

[8]*Department of Physics and Astronomy, McMaster University, Hamilton, Ontario L8S 4L8, Canada*

This work has been published, M. Williams *et al.*, Phys. Rev. C **105**, 065805 (2022).

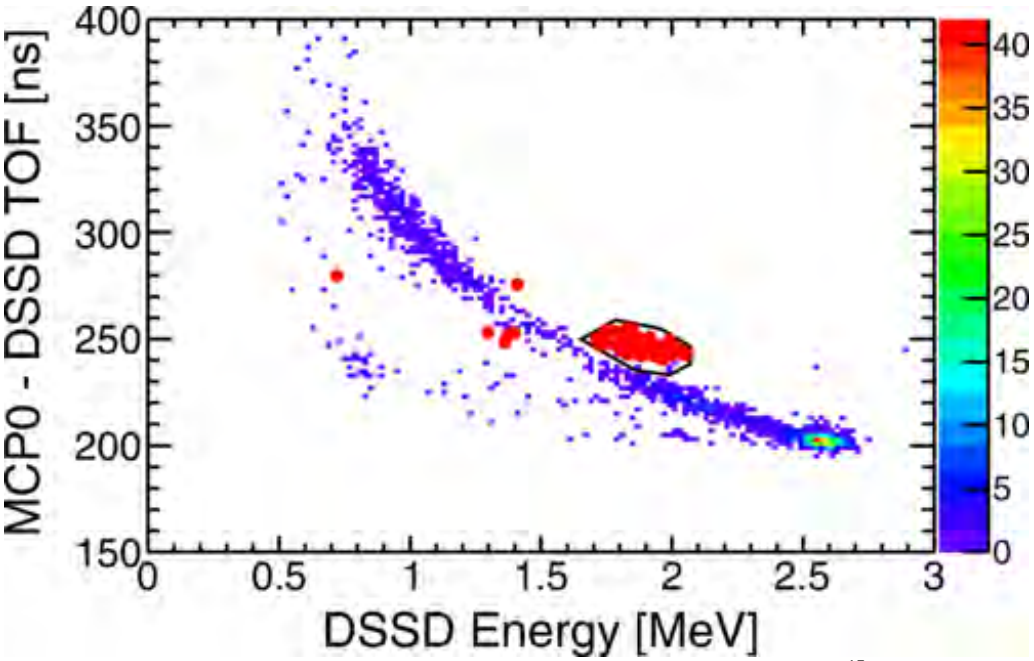

Fig. 1. MCP-DSSD time-of-flight against DSSD energy for one resonance in $^{17}O(a,g)$. The red circles show coincidence events within the separator time-of-flight window. The black line is the graphical cut around the ^{21}Ne recoils. The colour plot are all of the events.

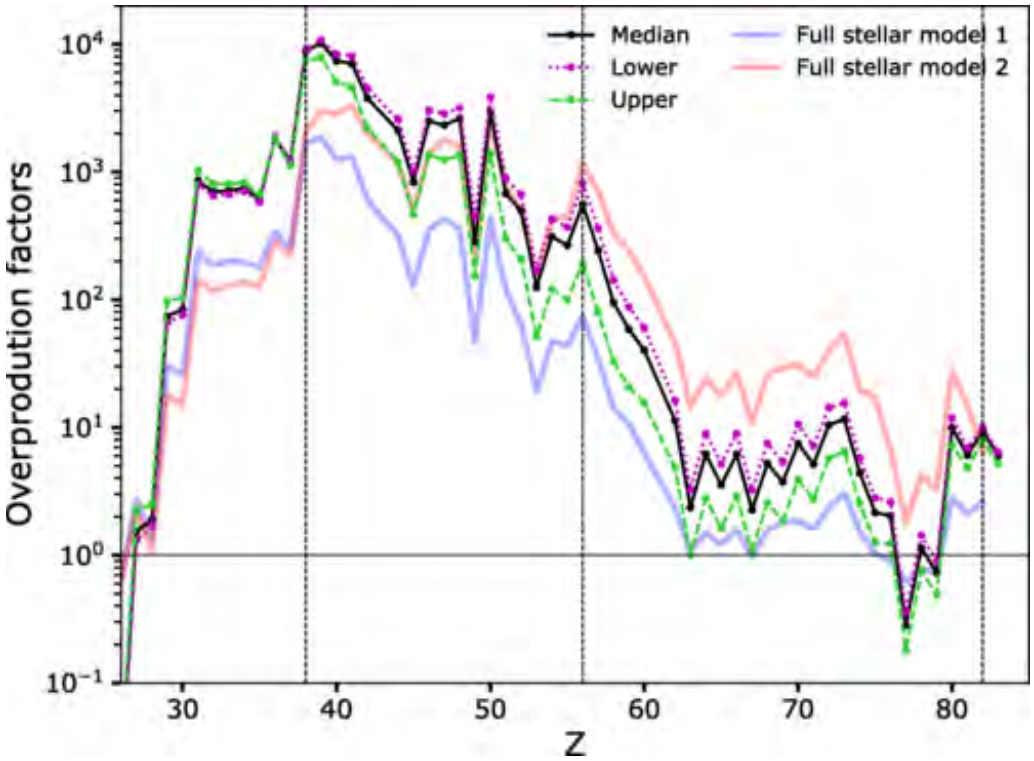

Fig. 2. s-process yields with various 17O(a,g) and 17O(a,n) reaction rates. The median, lower and upper curves show the s-process yields from the 17O(a,g) reaction rates from the present works. The Full Stellar Model curves show the reaction rate using the 17O(a,g) rate from Best *et al*.[1] or the Best rate divided by a factor of ten.

Elemental abundance anomalies in globular clusters - I

D.P. Carrasco-Rojas,[1] M. Williams,[2, 3] P. Adsley,[4, 5, 6, 7] L. Lamia,[8, 9, 10] B. Bastin,[11] T. Faestermann,[12] C. Fougeres,[11] F. Hammache,[13] D.S. Harrouz,[13] R. Hertenberger,[14] M. La Cognata,[8] A. Meyer,[13] F. de Oliveira Santos,[11] S. Palmerini,[15, 16] R.G. Pizzone,[8] S. Romano,[8] N. de Sereville,[13] A. Tumino,[8, 17] and H.-F. Wirth[14]

[1]*Department of Physics, The University of Texas at El Paso, El Paso, TX 79968-0515, USA*

[2]*TRIUMF, Vancouver, BC V6T 2A3, Canada*

[3]*Department of Physics, University of York, Heslington, York, YO10 5DD, United Kingdom*

[4]*Department of Physics and Astronomy, Texas A&M University, College Station, Texas 77843-4242, USA*

[5]*Cyclotron Institute, Texas A&M University, College Station, Texas 77843-3636, USA*

[6]*iThemba Laboratory for Accelerator Based Sciences, Somerset West 7129, South Africa*

[7]*School of Physics, University of the Witwatersrand, Johannesburg 2050, South Africa*

[8]*Laboratori Nazionali del Sud - Istituto Nazionale di Fisica Nucleare, Via Santa Sofia 62, 95123 Catania, Italy*

[9]*Dipartimento di Fisica e Astronomia "E.Majorana", Universit`a di Catania, Italy*

[10]*Centro Siciliano di Fisica Nucleare e Struttura della Materia (CSFNSM), Catania, Italy*

[11]*GANIL, CEA/DRF-CNRS/IN2P3, Bvd Henri Becquerel, 14076 Caen, France*

[12]*Physik Department E12, Technische Universit¨at M¨unchen, D-85748 Garching, Germany*

[13]*Universit´e Paris-Saclay, CNRS/IN2P3, IJCLab, 91405 Orsay, France*

[14]*Fakult¨at f¨ur Physik, Ludwig-Maximilians-Universit¨at M¨unchen, D-85748 Garching, Germany*

[15]*Dipartimento di Fisica e Geologia, Universit`a degli Studi di Perugia, via A. Pascoli s/n, 06125 Perugia, Italy*

[16]*Istituto Nazionale di Fisica Nucleare - Sezione di Perugia, via A. Pascoli s/n, 06125 Perugia, Italy*

[17]*Facolt`a di Ingegneria e Architettura, Universit`a degli Studi di Enna "Kore", Cittadella Universitaria, 94100 Enna, Italy*

Most globular clusters show anticorrelations between some elemental abundances such as the common sodium-oxygen (NaO) anticorrelation, as well as more unusual cases such as magnesium-potassium (MgK) anticorrelations. These abundance anomalies cannot have been caused by the current generation of stars within globular clusters, but must have resulted from some previous stars. The nature of these stars is unclear due to uncertainties in the nuclear reaction rates controlling the creation and destruction of the elements seen in the abundance anomalies.

There are a number of important reactions which are being investigated at various laboratories around the world. The ^{22}Ne(p,γ)^{23}Na reaction produces sodium, relevant to the NaO anticorrelation. There are some large uncertainties in this reaction due to unclear spectroscopic information on the compound nucleus, ^{23}Na. There may be additional low-energy resonances which could enhance the reaction rate by a factor of ten. The direct ^{22}Ne(p,γ)^{23}Na measurement is highly challenging due to the low cross section; detailed studies at the Laboratory for Underground Nuclear Astrophysics (LUNA at INFN-Gran Sasso have pushed the limits for these low-lying resonance strengths down to very low levels but the factor ten uncertainty persists. We have used the ^{23}Na(p,p') reaction, which has weak to no selectivity to the

structure of the excited states, at the Munich Q3D spectrometer to search for possible resonance states and have concluded that they do not exist, reducing the uncertainty in the reaction rate at temperatures relevant to hot-bottom burning from a factor of ten to around 40%.

These data were analysed by a TREND student, Diana Carrasco-Rojas, and are under review in Phys. Rev. C.

Fig. 1 shows the excitation-energy spectrum of ^{23}Na following the ^{23}Na(p,p') reaction. The green vertical lines show the expected location of the tentative resonance states which have not been observed in the present measurement.

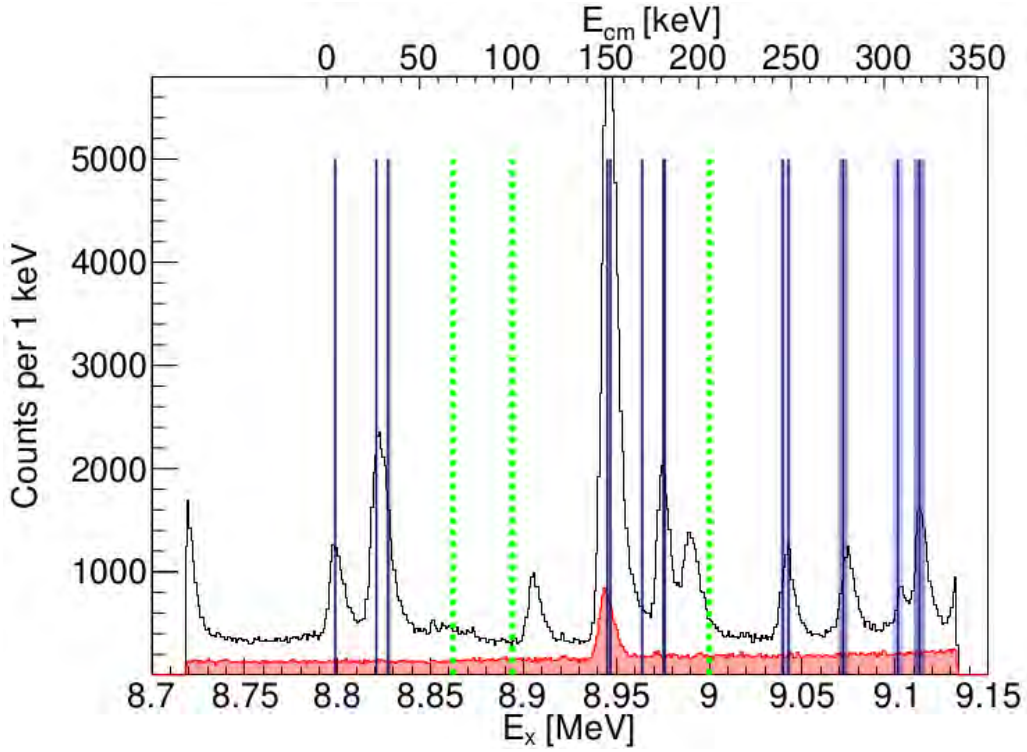

Fig. 1. The excitation-energy spectrum in ^{23}Na following the ^{23}Na(p,p') reaction. The excitation energy is given on the bottom axis and the centre-of-mass energy of the ^{22}Ne+p system on the top axis. The green dashed lines show the positions of the tentative states in ^{23}Na which may enhance the reaction rate. The black lines show the energies of known ^{23}Na levels and the grey/blue boxes show the uncertainties from (grey) literature and (blue) the present experiment.

Elemental abundance anomalies in globular clusters - II

Philip Adsley,[1, 2, 3, 4,] Matthew Williams,[5, 6] Nicolas de Sereville,[7] Richard Longland,[8, 9] Barry Davids,[6] Uwe Greife,[10] Fairouz Hammache,[7] Djamila Sarah Harrouz,[7] David Hutcheon,[6] Annika Lennarz,[6] Alison M. Laird,[5] Francois d'Oliveira Santos,[11] Athanasios Psaltis,[12] and Christopher Ruiz[6, 13]

[1]*Cyclotron Institute, Texas A&M University, College Station, Texas 77843, USA*

[2]*Department of Physics and Astronomy, Texas A&M University, College Station, Texas 77843, USA*

[3]*iThemba Laboratory for Accelerator Based Sciences, Somerset West 7129, South Africa*

[4]*School of Physics, University of the Witwatersrand, Johannesburg 2050, South Africa*

[5]*Department of Physics, University of York, Heslington, York, YO10 5DD, United Kingdom*

[6]*TRIUMF, Vancouver, BC V6T 2A3, Canada*

[7]*Institut de Physique Nucl´eaire d'Orsay, UMR8608, IN2P3-CNRS, Universit´e Paris Sud 11, 91406 Orsay, France*

[8]*North Carolina State University, Raleigh, North Carolina 27695, USA*

[9]*Triangle Universities Nuclear Laboratory, Durham, North Carolina 27708, USA*

[10]*Department of Physics, Colorado School of Mines, Golden, Colorado 80401, USA*

[11]*GANIL, CEA/DRF-CNRS/IN2P3, Bvd Henri Becquerel, 14076 Caen, France*

[12]*Institut f¨ur Kernphysik, Technische Universit¨at Darmstadt, Schlossgartenstr. 2, Darmstadt 64289, Germany*

[13]*Department of Physics and Astronomy, University of Victoria, Victoria, BC V8W 2Y2, Canada*

Another reaction important to globular cluster nucleosynthesis is ^{39}K(p,γ)^{40}Ca. This reaction destroys potassium, changing the MgK anticorrelation. The reaction has been directly measured with the DRAGON recoil separator at TRIUMF in 2019. A beam of around 10^{11} ^{39}K ions per second was incident on a windowless hydrogen gas target. Recoiling ^{40}Ca ions were transported through the DRAGON magnetic-electric-magnetic-electric dipole separator sequence to a focal plane consisting of a silicon detector placed within an ionisation chamber. An array of Bismuth Germanate detectors (BGOs) around the target position were used to detect resulting gamma rays. Recoils of interest were identified through their time of flight through the DRAGON.

The analysis of the data is substantially complete but two outstanding tasks remain. The first is the simulation of the efficiency of the detection of γ rays at the DRAGON target and the transmission of heavy recoils through the DRAGON recoil separator and the second is the measurement of the charge-state distributions of the ^{40}Ca ions leaving the windowless gas target. The simulations are currently in progress and should be complete during the summer of 2023. The ongoing analysis has shown that the literature γ-ray decays of ^{40}Ca do not describe the present data well, suggesting that the literature branching ratios are incorrect. The charge-state distributions will be measured using a ^{44}Ca beam at the end of July 2023. A publication will be submitted before the end of the year.

Fig. 1 shows the separator time-of-flight spectrum for the E_r=606-keV resonance in the ^{39}K(p,γ)^{40}Ca reaction.

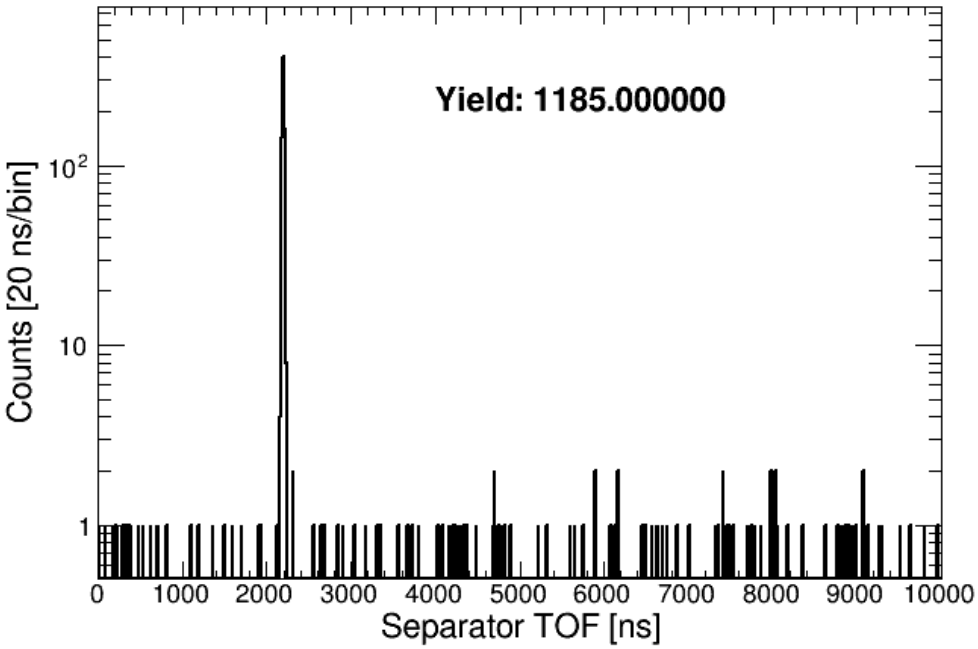

Fig. 1. The separator time-of-flight spectrum for the E_r = 606-keV resonance. This time-of-flight is between a hit in the BGO detectors around the DRAGON target and the heavy recoil hitting the focal plane. The large peak corresponds to ^{40}Ca recoils and the rest of the spectrum corresponds to "leaky" ^{39}K beam.

Elemental abundance anomalies in globular clusters - III

P. Adsley,[1,2] P. Jones,[3] L. Donaldson,[3] S. Jongile,[3] S. Binda,[3] A. Bahani,[3] A. Netshiya,[3] S. Mthembu,[3] J. W. Brummer,[3] E. Lawrie,[3] K. Malatji,[3] and R. Neveling[3]

[1]*Cyclotron Institute, Texas A&M University, College Station, Texas 77843, USA*

[2]*Department of Physics and Astronomy, Texas A&M University, College Station, Texas 77843, USA*

[3]*iThemba Laboratory for Accelerator Based Sciences, Somerset West 7129, South Africa*

The MgK anticorrelation does not only depend on the destruction of ^{39}K but also on its production. We have previously constrained one of the most important reactions along this path, ^{30}Si(p,γ)^{31}P, using the ^{30}Si(^{3}He,d)^{31}P reaction at Munich with the Q3D spectrograph[1]. However, a lack of spectroscopic information on the compound nuclei of other important reactions. Notably, the ^{37}Ar(p,γ)^{38}K and ^{38}Ar(p,γ)^{39}K reactions, which proceed through excited states in ^{38}K and ^{39}K are poorly constrained. The lack of spectroscopic information on these nuclei is so profound that it is not even clear which resonances must be measured to properly constrain the rate.

In an attempt to identify potential astrophysically important resonance, an experiment was performed at iThemba LABS in South Africa in October 2022 using a proton beam on a natural calcium target. Gamma rays resulting from the interaction of the beam with the target were observed in the AFRODITE array of high-purity germanium detectors. These gamma rays will be used to deduce spectroscopic information relevant to the ^{37}Ar(p,γ)^{38}K and ^{38}Ar(p,γ)^{39}K reactions and provide guidance for future direct experimental studies at facilities such as DRAGON.

The analysis is currently underway with a number of low-energy gamma rays in ^{36,37,38}Ar, ^{38,39}K and ^{39,40}Ca currently identified. Some example online spectra, using only two clovers from 2% of the total data are shown in Fig. 1.

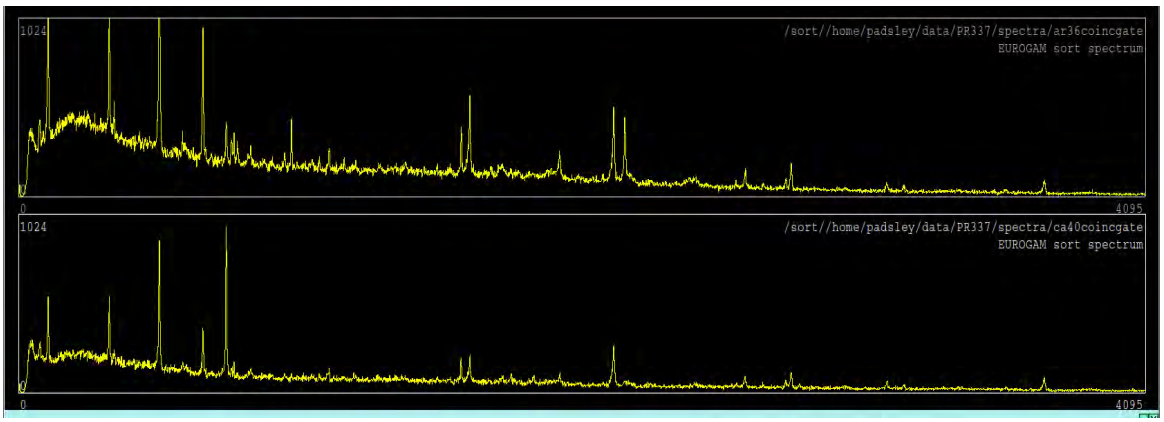

Fig. 1. γ-ray spectra gated on ^{36}Ar and ^{40}Ca transitions.

[1] D. S Harrouz *et al.* Phys. Rev. C **105** 015805 (2022).

Recycling neutrons in the s-process: determining the $^{17}O+\alpha$ reaction rates

F. Hammache,[1] P. Adsley,[2, 3] L. Lamia,[4, 5, 6] D.S. Harrouz,[1] N. de Sereville,[1] B. Bastin,[7] T. Faestermann,[8] C. Fougeres,[7] R. Hertenberger,[9] M. La Cognata,[4] A. Meyer,[1] S. Palmerini,[10, 11] R.G. Pizzone,[4] F.de Oliveira,[7] S. Romano,[4, 5, 6] A. Tumino,[4, 12] and H.-F. Wirth[9]

[1]Universite Paris-Saclay, CNRS/IN2P3, IJCLab, 91405 Orsay, France

[2]School of Physics, University of the Witwatersrand, Johannesburg 2050, South Africa

[3]iThemba Laboratory for Accelerator Based Sciences, Somerset West 7129, South Africa

[4]Laboratori Nazionali del Sud - Istituto Nazionale di Fisica Nucleare, Via Santa Sofia 62, 95123 Catania, Italy

[5]Dipartimento di Fisica e Astronomia E. Majorana, Univ. di Catania, Catania, Italy

[6]Centro Siciliano di Fisica Nucleare e Struttura della Materia-CSFNSM, Catania, Italy

[7]Grand Acc´el´erateur National d'Ions Lourds (GANIL),
CEA/DRF-CNRS/IN2P3, Bd. Henri Becquerel, 14076 Caen, France

[8]Physik Department E12, Technische Universit¨at M¨unchen, D-85748 Garching, Germany

[9]Fakult¨at f¨ur Physik, Ludwig-Maximilians-Universit¨at M¨unchen, D-85748 Garching, Germany

[10]Dipartimento di Fisica e Geologia, Universit`a degli Studi di Perugia, Perugia, Italy

[11]Istituto Nazionale di Fisica Nucleare, Sezione di Perugia, Perugia, Italy

[12]Facolt`a di Ingegneria e Architettura, Universit`a degli Studi di Enna, Italy

The $^{20}Ne(d,p)^{21}Ne$ reaction is capable of providing information on excitation energies, spins and parities, and neutron widths but one major important piece of information needed for the $^{17}O+\alpha$ reaction

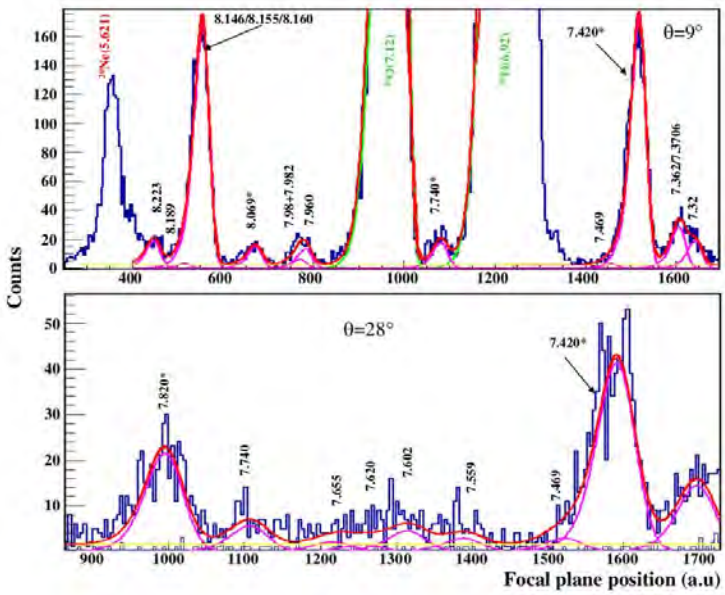

Fig. 1. Two focal-plane spectra taken at (top) 9 and (bottom) 28 degrees. The red line shows the total fit, the pink, yellow and green show individual contributions from ^{21}Ne, ^{20}Ne and ^{16}O states, respectively. The ^{21}Ne state excitation energies (in MeV) are labelled in black, the ^{20}Ne in red and the ^{16}O in green.

rates, the α-particle partial widths of the excited levels in ^{21}Ne, are unknown. α-particle transfer reactions such as ^{17}O(^{7}Li,t)^{21}Ne can be used to deduce these partial widths from the magnitude of the transfer cross sections. In order to do this, we performed a measurement of this reaction using the Munich Q3D spectrograph. The targets were enriched tungsten oxide deposited on a carbon backing. The beam energy, $E_{^{7}Li}$ = 42 MeV, was low enough that the reactions between the lithium and the tungsten were suppressed due to the Coulomb barrier and so only reactions on the oxygen and carbon (and other contaminants in the targets) took place. Example focal-plane spectra are shown in Fig. 1.

From the spectroscopic information obtained in this reaction, the ^{17}O+α reactions were again recalculated. This supports the previous calculations which favoured a stronger neutron recycling from the ^{17}O+α reactions and a stronger s-process in rotating metal-poor stars. Fig. 2 shows the ratios of the reaction rates obtained in this work compared to previous rate evaluations, and additionally the ^{17}O(α,n)/^{17}O(α,γ) reaction-rate ratio. This work has been submitted and is under review.

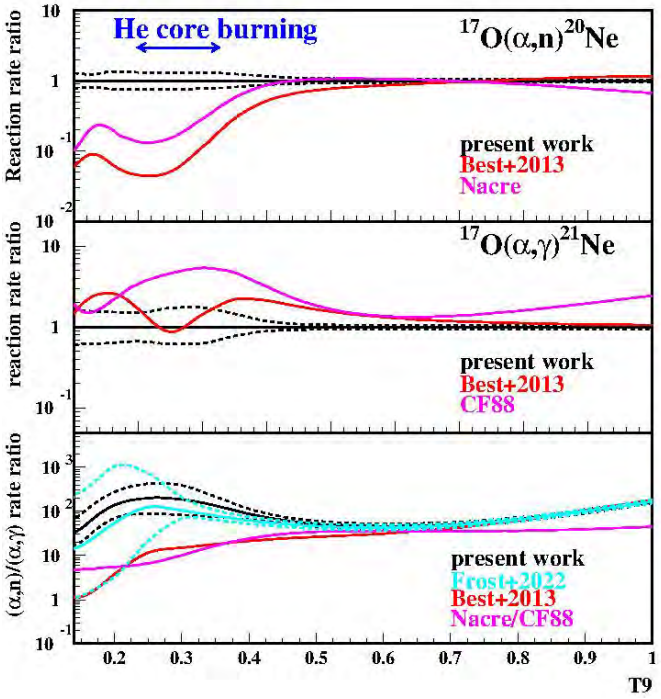

Fig. 2. The top two panels show the ratio of the reaction rates described in this work compared to those from previous evaluations. The bottom panel shows the ratio of the ^{17}O(α,n)/^{17}O(α,γ) reaction rates, a measure of the efficiency of the neutron recycling. Ratios above 1 mean that most of the neutrons are recycled.

The impact of ^{17}O+α reaction rate uncertainties on the s-process in rotating massive stars

J. Frost-Schenk,[1] P. Adsley,[2,3,4,5] A.M. Laird,[1] R. Longland,[6,7] C. Angus,[1,8] C. Barton,[1] A. Choplin,[9] C. Aa. Diget,[1] R. Hirschi,[10,11] C. Marshall,[6,7] F. Portillo Chaves [6,7] and K. Setoodehnia[6,7]

[1]*Department of Physics, University of York, York YO10 5DD, UK*

[2]*School of Physics, University of the Witwatersrand, Johannesburg 2050, South Africa*

[3]*iThemba LABS, National Research Foundation, PO Box 722, Somerset West 7129, South Africa*

[4]*Cyclotron Institute, Texas A&M University, College Station, Texas, TX 77843, USA*

[5]*Department of Physics and Astronomy, Texas A&M University, College Station, Texas, TX 77843, USA*

[6]*Department of Physics North Carolina State University, Raleigh, North Carolina, NC 27695-8202, USA*

[7]*Triangle Universities Nuclear Laboratory, Durham, North Carolina, NC 27708-0308, USA*

[8]*TRIUMF, 4004 Wesbrook Mall, Vancouver, BC V6T 2A3, Canada*

[9]*Institut d'Astronomie et d'Astrophysique, Universite´ Libre de Bruxelles, CP 226, B-1050 Brussels, Belgium*

[10]*Astrophysics Group, Lennard-Jones Laboratories, Keele University, Keele ST5 5BG, UK*

[11]*Kavli IPMU (WPI), The University of Tokyo, Kashiwa, Chiba 277-8583, Japan*

Half of the elements heavier than iron were produced in the s-process. Neutrons are produced from source reactions, more importantly ^{13}C(α,n) and ^{22}Ne(α,n) and captured on seed nuclei. The neutron-capture rate is rather slower than the beta-decay rate and thus the nuclei produced during this process are close to the line of stability. In reality, "the" s-process is something of a misnomer since various different slow neutron-capture processes take place in different astrophysical locations caused by different reactions and with different characters.

A number of factors influence the elemental abundances of the elements created in the s-process. These include the amount of s-process neutron seed material (^{13}C and ^{22}Ne) available, the metallicity of the star, and the rates of various nuclear reactions both in producing the neutrons for the s-process and the capture rate for those neutrons. One important set of reactions are neutron sinks: ^{16}O captures neutrons to make ^{17}O. The ^{17}O(α,γ) reaction locks the captured neutron away, preventing additional nucleosynthesis. The ^{17}O(α,n) reaction recycles the neutrons causing additional neutron-capture reactions to take place. The ^{17}O+α reactions depend on the properties of excited states in the compound nucleus, ^{21}Ne. To investigate the spectroscopic properties of these states, we used the ^{20}Ne(d,p)^{21}Ne reaction with the TUNL Split-Pole (Enge) spectrograph. A focal-plane spectrum showing excited states in ^{21}Ne is shown in Fig. 1. Using this reaction, we measured excitation energies and assigned spins and parities, and neutron widths to excited states in ^{21}Ne and recomputed the ^{17}O+α reaction rates. We found that the neutron recycling of the ^{17}O+α reactions is stronger than predicted by previous rate estimates, and that the s-process in rotating metal-poor stars can potentially make elements up to at least barium (Z=56). This work has been published in Monthly Notices of the Royal Astronomical Society[1]. Another paper is in preparation reporting on states in ^{21}Ne below the α-particle threshold which may be interesting for nuclear structure.

[1] J. Frost-Schenk *et al.* MNRAS 514 2650 (2022)

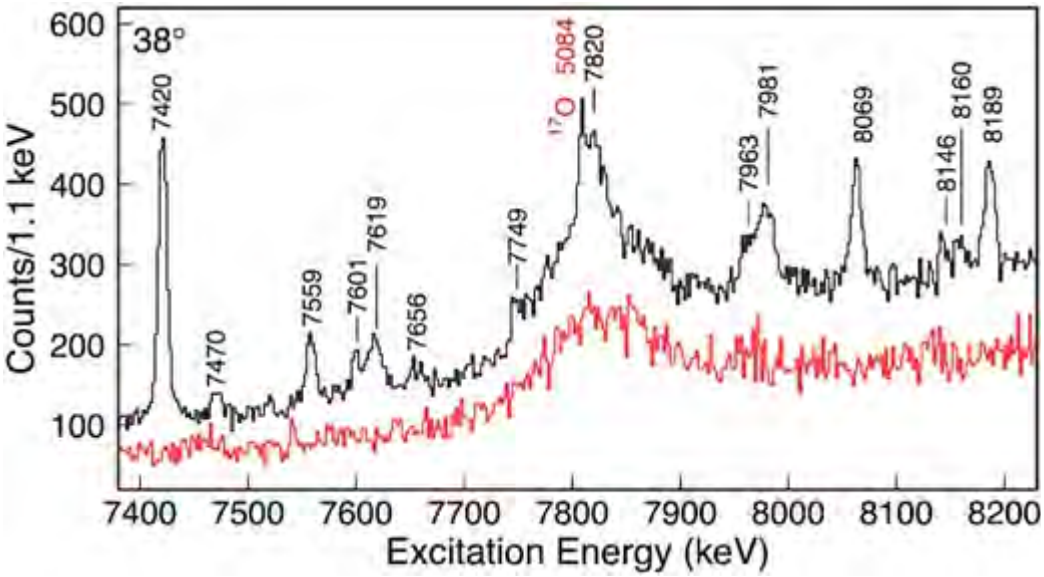

Fig. 1. The focal-plane excitation-energy spectrum for the ^{20}Ne(d,p)^{21}Ne reaction. The black spectrum shows the results from the neon-implanted carbon target and the red spectrum is that for only the carbon backing.

An additional experiment studying the ^{20}Ne(d,p) reaction using the HELIOS spectrometer at Argonne National Laboratory was performed in inverse kinematics. The resulting data will be published in another forthcoming paper.

Elastic scattering measurements for the ^{12}N + ^{197}Au system at Elab = 70 MeV

P.L.D. Magro,[1] R. Linares,[2] V. Guimarães,[1] J. Rangel,[3] G. Rogachev,[4] E. Koshchiy,[4] B.T. Roeder,[4] M. Barbui,[4] J. Bishop,[4] C.E. Parke,[4] E. Harris,[4] and A. Saastamoinen[4]

[1]*Institute of Physics, Universidade de São Paulo, Brazil.*

[2]*Institute of Physics, Universidade Federal Fluminense, Brazil.*

[3]*Universidade Estadual do Rio de Janeiro, Brazil.*

[4]*Cyclotron Institute, Texas A&M University*

Some light nuclei away from the valley of stability are characterized by low binding energies and long tail matter distributions, leading to the formation of a halo, an extended special distribution of the valence nucleon wave function [1]. This exotic nuclear structure manifests in the cross sections of elastic, fusion, transfer, and breakup reactions, mostly at energies around the Coulomb barrier [2]. The interplay between these unusual structures and reaction channels is paramount to describe experimental data obtained for reactions carried out for "halo" nuclei, such as ^{6}He, ^{8}B, ^{11}Li, and ^{11}Be [3]. For these nuclei, the angular distribution for the elastic cross sections, measured at energies around the Coulomb barrier, exhibits a damping of the Fresnel peak (interference between Coulomb and nuclear components) [4]. In this work, we present new experimental data of the elastic scattering for the ^{12}N+^{197}Au system at E_{lab} = 70 MeV. The experiment was performed at the Cyclotron Institute of Texas A&M University. The radioactive ^{12}N beam was produced by the recoil separator MARS [5] using the ^{3}He(^{10}B,^{12}N) reaction. The radioactive ^{12}N beam had an intensity of 1×10^{3} p/s and was impinged into the 4.7 mg/cm^2 thick ^{197}Au target at the scattering chamber. The schematic view of the detection system is shown in Fig. 1. The detection setup consisted of three double sided silicon strip detectors (DSSSD) with 128 vertical and 128 horizontal fixed strips producing a highly segmented detection system. The detector pixels were mapped by a simulation of the experimental setup and used to determine the scattering angles.

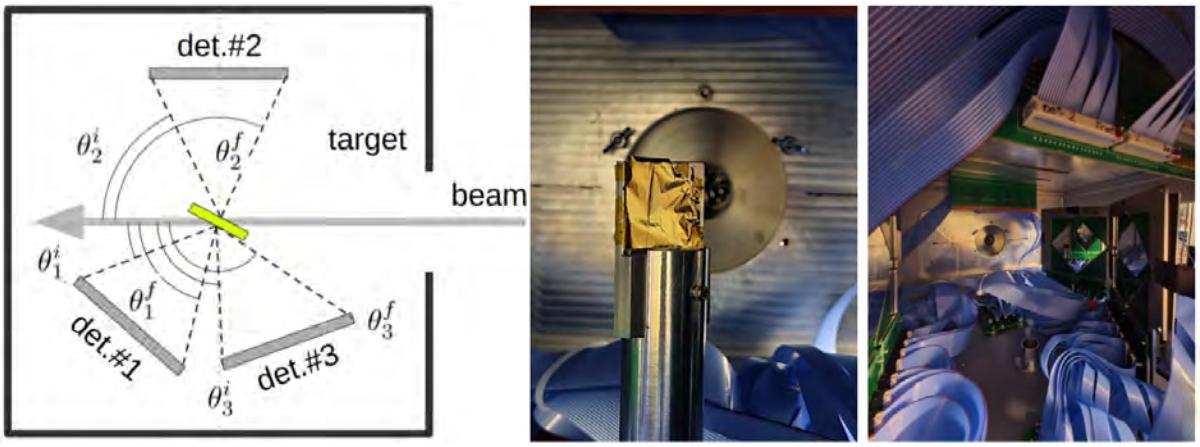

Fig. 1. Schematic view of the experimental setup. On the right is an inside picture of the scattering chamber.

The measured angular distribution was obtained from 40° to 140° in the center of the mass frame, as shown in Fig. 2. The error bars in the experimental cross sections correspond to the statistics and the systematic uncertainties due to the normalization method used. In the first approach for the analysis of experimental angular distribution, we considered the optical model (OM) calculations, with the phenomenological Woods-Saxon (WS) and double folding São Paulo potentials for real and imaginary parts. The parameters for the WS-1 potential were obtained from another proton-rich projectile 10C+208Pb data at Elab = 66 MeV [6]. In contrast, the WS-2 parameters correspond to a fitting procedure with initial parameters from the previous calculation. These parameters are shown in Table I. Also, São Paulo Potential (SPP) [7], with standard (NR=1.0 and NI=0.78) and adjusted normalizations (NR=0.1 and NI=25) for the real and imaginary parts, were applied. The results of these calculations are also shown in Fig. 2. As can be observed in the figure, a strong absorption damps the Fresnel peak, which can be attributed to the possible halo formation of the valence proton in 12N. Although the adjusted potentials could reproduce the data quite well, the normalization parameters for the SPP are unrealistic. A large imaginary potential for the Woods-Saxon is also obtained to describe the strong absorption. As the results, the obtained total reaction cross section is quite large.

Table I. Parameters of the optical potentials obtained by fitting the elastic scattering.

projectile	V	r_V	a_V	W	r_W	a_W	σ_R (mb)
^{10}C	82.2	1.19	0.12	17.6	1.60	0.14	753
^{12}N	28.6	1.28	0.39	79.9	1.85	0.11	1297

Since the binding energy of ^{12}N for the breakup to ^{11}C+p is relatively small (S_P=0.60 MeV), the breakup might be an important channel for decay. To investigate the effect of this channel on the elastic scattering, we performed continuum discretized coupled-channels calculations (CDCC). For this, some potentials of the three-body system ^{12}N (^{11}C+p)+^{197}Au must be considered. For the ^{11}C+^{197}Au sub-system, the Arkyus-Winther and SPP potential, while for p+^{197}Au, the Koning-Delaroche Potential and for p+^{11}C, a standard WS potential (r=1.25 and a=0.65 fm). By using these potentials, without any couplings (one-channel calculation), the data's description is reasonable, again indicating the importance of the model structure of ^{12}N as formed by ^{11}C+p. The couplings to the continuum (CDCC) calculations have also been performed, and preliminary results are shown in Fig. 2. The Next step is to perform the reaction channel calculation (CRC) to describe the rising of the cross sections for the backward angles.

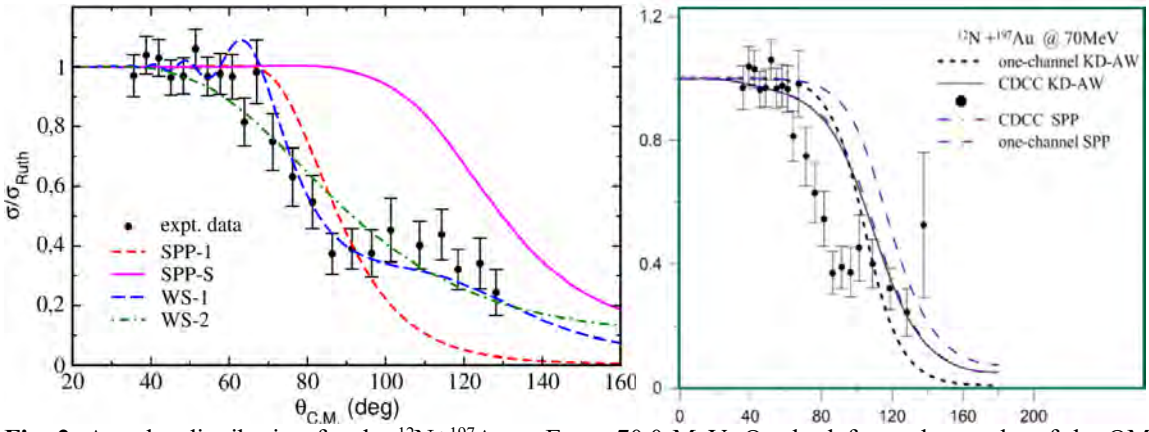

Fig. 2. Angular distribution for the $^{12}N+^{197}Au$ at E_{lab} = 70.0 MeV. On the left are the results of the OM analysis, and on the right are the results of one-channel and CDCC calculations with Arkyus-Winther and SPP potentials.

[1] I. Tanihata, H. Savajols, and R. Kanungo, Prog in Part. Nucl. Phys. **68**, 215 (2013).

[2] F. Canto *et al.*, Phys. Rep. **596**, 1 (2015).

[3] J.J. Kolata, V. Guimaraes, and E.F. Aguilera, Eur. Phys. J. A **52**, 123 (2016).

[4] N. Keeley, N. Alamanos, K.W. Kemper, and K. Rusek, Phys. Rev. C **82**, 034606 (2010).

[5] R.E. Tribble *et al*., Nucl. Phys. **A701**, 278 (2002).

[6] R. Linares *et al.,* Phys. Rev. C **103**, 044613 (2021).

[7] L.C. Chamon *et al*., Phys. Rev. C **66**, 014610 (2002).

Measurement of ^{14}O(α,p) at MARS/RIKEN with TexAT

S. Ahn,[1] C. Park,[1] M. Barbui,[2] J. Bishop,[2] E. Koshchiy,[2] C.E. Parker,[2] B. Roeder,[2] G. Rogachev,[2,3,4]
M. Roosa,[3,4] A. Saastamoinen,[2] and CENS[1]/CNS[5] collaborators

[1]*Center for Exotic Nuclear Studies, Institute for Basic Science, 34126 Daejeon, Republic of Korea*

[2]*Cyclotron Institute, Texas A&M University, College Station, TX 77843, USA*

[3]*Department of Physics & Astronomy, Texas A&M University, College Station, TX 77843, USA*

4*Nuclear Solutions Institute, Texas A&M University, College Station, TX 77843, USA*

[5]*Center for Nuclear Study (CNS), University of Tokyo, Wako, Japan*

Sensitivity studies have shown that ^{14}O(α,p)^{17}F is one of the most important reactions affecting the light curve in multi-zone X-ray burst models [1]. Increases or decreases in the reaction rate can affect the peak brightness and time variation. In addition, the breakout path from the hot CNO cycle to the rp-process at T>0.5 GK is also determined by this reaction rate – mainly through a single resonance at E_x = 6.15 MeV. The previously measured cross sections for this reaction are shown in Fig. 1 where a large disagreement across the energy regime of interest is clearly observed.

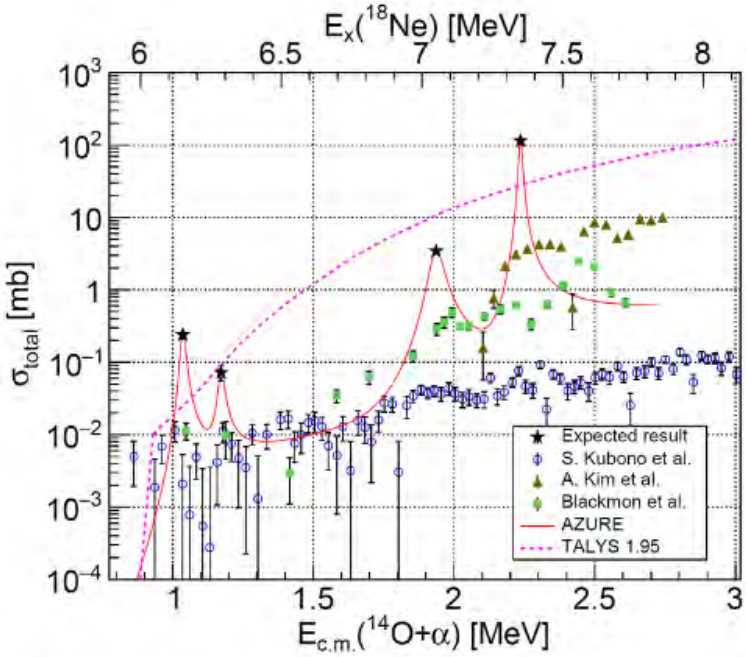

Fig. 1. Previously-measured data and the predicted AZURE cross section using the known resonances.

In order to better understand the importance of this reaction, a measurement was performed with the TexAT TPC [2] to measure the ^{14}O(α,p) reaction cross section across a range of energies using a ^{14}O beam impinging onto a He:CO2 gas mixture. Following a provisional measurement at the Cyclotron Institute where a high-purity MARS beam was delivered at around a peak intensity of 10^5 pps, the

experiment was performed at the CRIB beamline in RIKEN, Japan in collaboration with the Center for Exotic Nuclear Studies, Republic of Korea who acted as the spokesperson.

The preliminary run at MARS yielded a multitude of insights into how to best measure this extremely challenging reaction. In particular, it was observed that at high beam intensities – the Micromegas of TexAT were approaching the Raether limit and this was causing an unintended consequence of triggers in the data acquisition that did not correspond to real events – so called "dark triggers". In addition, to increase the solid-angle coverage and therefore statistics, CENS modified TexAT to have a much larger number of silicon detectors (X6 type) of thickness 1 mm and also modified the field cage to be smaller so the detectors could be placed closer. These X6 detectors were then backed by a set of CsI crystals readout with a Si MPPC. Due to the higher thickness, the beta-decay of the stopped ^{14}O beam lead to a high real trigger rate in the Si detectors. In order to address this, a more complicated L0L1 trigger scheme was implemented where the first trigger comes from the MARS upstream scintillator and the L1 trigger is then validated by the Si detectors. This then ensured that the beta trigger rate was greatly suppressed and only random coincidences made it into this time window.

To address the issue of the high rate on the Micromegas, CENS produced a gating grid for the central beam region where the biases between parallel wires could be modified to restrict the transparency of electrons from the drift region to the avalanche region as shown in Fig. 2. This was first tested at CRIB and was shown to be highly-effective and was able to suppress the amplitude in the beam region by a factor of ~6.

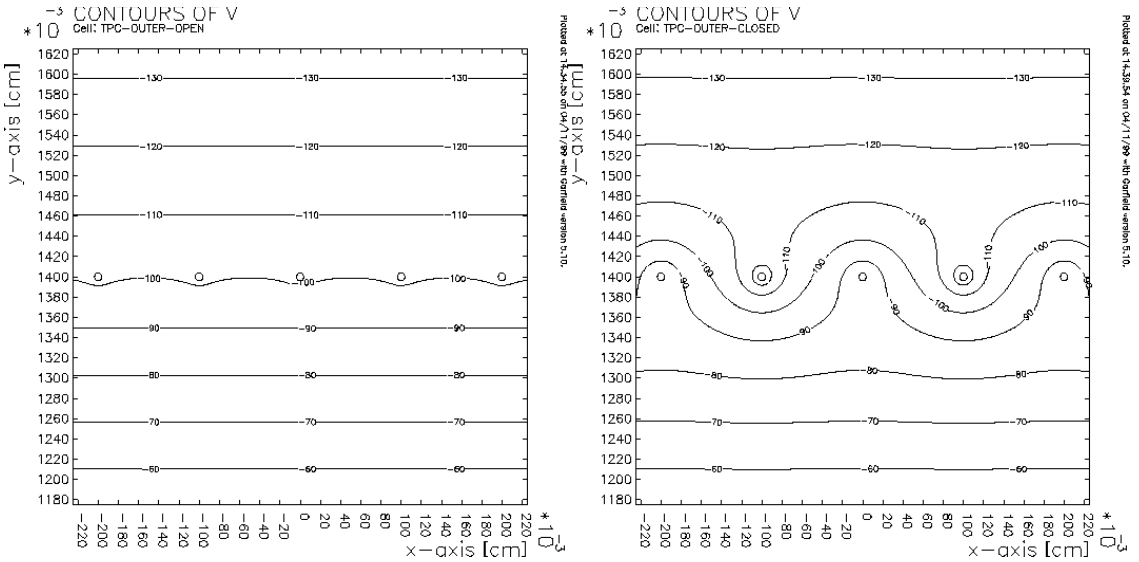

Fig. 2. Left: Electric field contours of a gating grid when set to be transparent (from [3]). Right: Electric field contours when adjacent wires are set to have a different voltage and the transparency of the gating grid to electrons is reduced (from [3]).

Following the successes of adapting to the challenges encountered at MARS – the production experiment at CRIB occurred in March 2023 with the implementation of the gating grid, additional field wires being added to the field cage to increase field uniformity, a further increase in X6 detector number

to 30, and the MARS scintillator being replaced by a scintillator placed internally to the TexAT chamber which was readout by two MPPCs that then become the new L0 trigger. The gas pressure of the He:CO_2 used to stop the beam at the end of the Micromegas was 300 Torr. A schematic and photograph of the experimental setup with the new silicon detectors can be seen in Fig. 3.

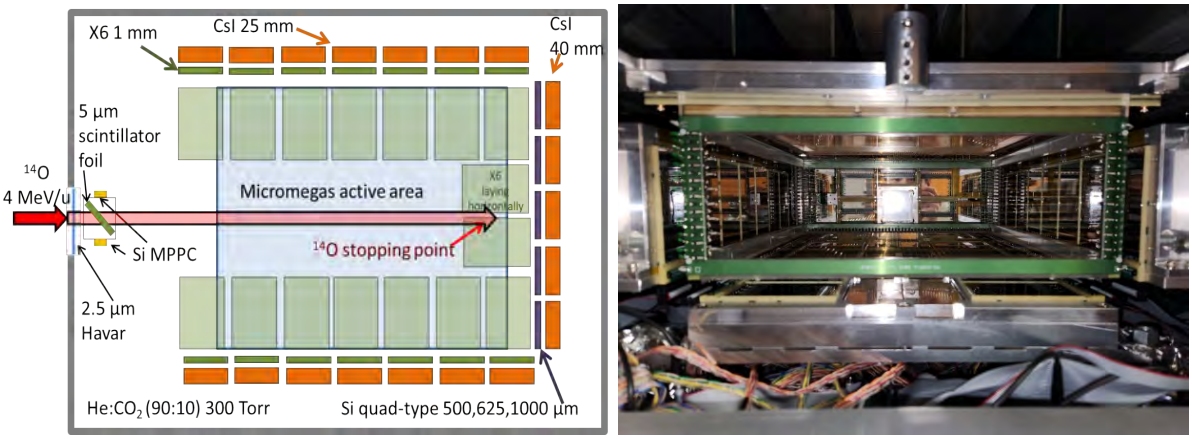

Fig. 3. (Left) Schematic of the experimental setup at CRIB-RIKEN. (Right) Photo of the inside of the chamber showing the arrangement of silicon detectors when looking down the beamline.

The purity of the CRIB beam was around 90% with 10% admixture of the primary ^{14}N beam which was differentiated by the amplitude of the signal measured in the scintillator. Additionally, an independent data acquisition system used multiple PPACs along the beamline to measure the purity of the beam run-by-run.

Given the short time since the run, data analysis is currently ongoing but there were hints of promising (α,p) events seen via the online event viewer that signify the gain in the Micromegas was sufficient to see protons above the threshold while maintaining a high beam rate. The effort as part of this work has also proved extremely useful to be able to understand how to better measure reactions with high beam rates with TexAT more generally.

[1] R.H. Cyburt *et al.*, Astrophys. J. **830**, 55 (2016).
[2] E. Koshchiy *et al.*, Nucl. Instrum. Methods. Phys. Res. **A957**, 163398 (2020).
[3] https://www.star.bnl.gov/public/tpc/hard/tpcrings/page11.html

Radiative decay branching ratio of the Hoyle

Z. Luo,[1,2] G. Rogachev,[1,2] M. Barbui,[2] J. Bishop,[2] G. Chubaryan,[2] V. Goldberg,[2] E. Harris,[1,2] H. Jayatissa,[1,2,*] E. Koshchiy,[2] M. Roosa,[1,2] A. Saastamoinen,[2] and D. Scriven[1,2]
[1]*Department of Physics and Astronomy, TAMU, College Station, TX 77843*
[2]*Cyclotron Institute, TAMU, College Station, TX 77840*

Introduction

The triple-alpha process is a crucial reaction in nuclear astrophysics. It consists of two consecutive steps: a) $\alpha + \alpha \rightarrow {}^{8}\mathrm{Be}$(g.s.), and b) ${}^{8}\mathrm{Be} + \alpha \rightarrow \gamma + {}^{12}\mathrm{C}$, ultimately leading to the formation of carbon. The second reaction occurs via a 0^+ state in ${}^{12}\mathrm{C}$ at an excitation energy of 7.65 MeV (Hoyle state) – just above the α-decay threshold. The rate of the triple-alpha process is determined by the product of the α-decay width (Γ_α) and the radiative width (Γ_{rad}) divided by their sum ($\Gamma_\alpha + \Gamma_{rad}$), which reduces to Γ_{rad} due to the significantly larger value of Γ_α compared to Γ_{rad}. A method of determining the value of Γ_{rad} involves measuring the branching ratio for electromagnetic decay (Γ_{rad}/Γ) and utilizing the established partial width Γ_π(E0) for electron-positron pair production, i.e., $\Gamma_{\mathrm{rad}} = \frac{\Gamma_{\mathrm{rad}}}{\Gamma} \times \frac{\Gamma}{\Gamma_\pi(\mathrm{E0})} \times \Gamma_\pi(\mathrm{E0})$.

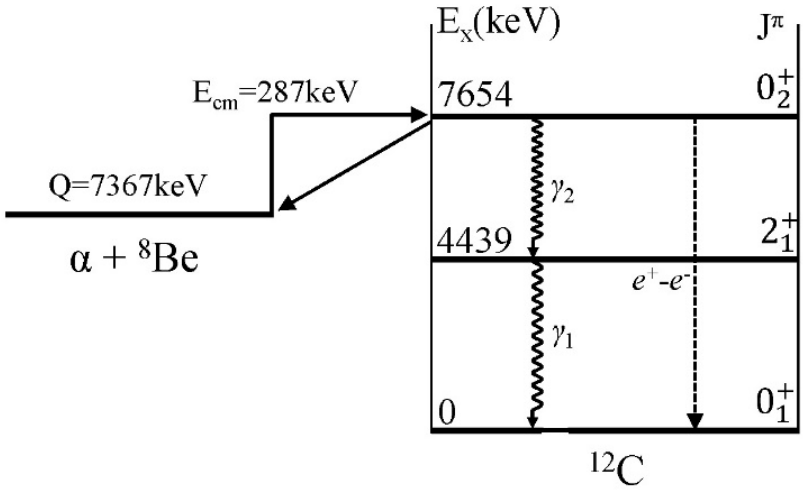

Fig. 1. Decay modes of Hoyle state.

A recent study by Kibedi *et al.* [1] reports a deviation of more than 3σ from the currently adopted value for Γ_{rad}/Γ, as reported in the reference by Freer *et al.* [2]. The values are summarized in Table I. *The goal of this project is to make an independent measurement of the Γ_{rad}/Γ branching ratio to resolve the discrepancy.*

Table 1. Summary of measurements of radiative branching ratio, pair-production branching ratio, and pair-production width of the Hoyle state.

Parameter	Adopted [1]	Recent
Γ_{rad}/Γ	$4.03(10) \times 10^{-4}$	$6.2(6) \times 10^{-4}$ [2]
$\Gamma_{\pi}(E0)/\Gamma$	$6.7(6) \times 10^{-6}$	$7.6(4) \times 10^{-6}$ [3]
$\Gamma_{\pi}(E0)$	$62.3(2)\mu eV$	-
Γ_{rad}	3.8×10^{-3} eV	$5.1(6) \times 10^{-3}$ eV [2]

Experiment

The experiment was conducted at the Cyclotron Institute using the K150 cyclotron in September 2021. Fig. 2 illustrates the experimental setup, while Fig. 3 depicts the DAQ system. We utilized the charged-particle coincidence method for this measurement. The Hoyle state was populated through the reaction $^{12}C(\alpha, \alpha')^{12}C^{*}$. The α' particles, which were elastically scattered, were detected by a ΔE-E silicon telescope positioned at an angle of 81° relative to the beam axis. The ^{12}C(g.s.) ions, produced as a result of the electromagnetic decay of the Hoyle state, were detected by the MDM-TexPPAC system at an angle of 35.3°. The spectrometer covers an angle of 4° in both the vertical and horizontal directions. The idea of these measurements is simple as the radiative decay branching ratio is given by the ratio of the number of ^{12}C ions produced in the decay of the Hoyle state and measured in the TexPPAC system to the total number of the Hoyle states populated. The challenge is to obtain the desired accuracy in view of the small branching ratio of less than 0.1%.

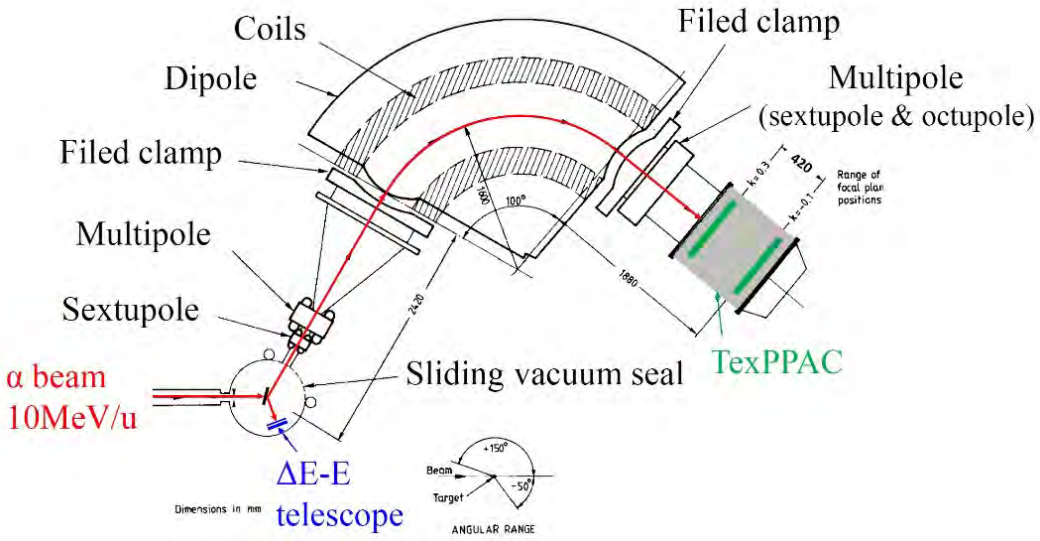

Fig. 2. Schematic of experimental setup.

The identification of the ^{12}C ions is performed in MDM spectrometer using magnetic rigidity $B\rho = \frac{mv}{q} = \frac{m}{q}\sqrt{2\frac{E_k}{m}}$. However, both $^{4}He^{2+}$ and $^{12}C^{6+}$ share the same m/q ratio. Consequently, fully stripped helium and ^{12}C ions have the same rigidity if they have the same energy per nucleon. Figure 3 displays the Geant4 simulation depicting the energies of the ^{4}He from the alpha-decay of the Hoyle state (dominant decay mode) and ^{12}C ions as they enter the slit box (MDM spectrometer entrance). To reduce the transmission of unwanted ^{4}He, the spectrometer was configured for $^{12}C^{5+}$ ions, thereby allowing only a small number of $^{4}He^{2+}$ ions, which travel 1.2 times faster than $^{12}C^{5+}$ ions, to pass through. By measuring the time of flight (ToF), we can further distinguish the transmitted $^{4}He^{2+}$ ions from the $^{12}C^{5+}$ ions, eliminating any chance for misidentification of ^{12}C.

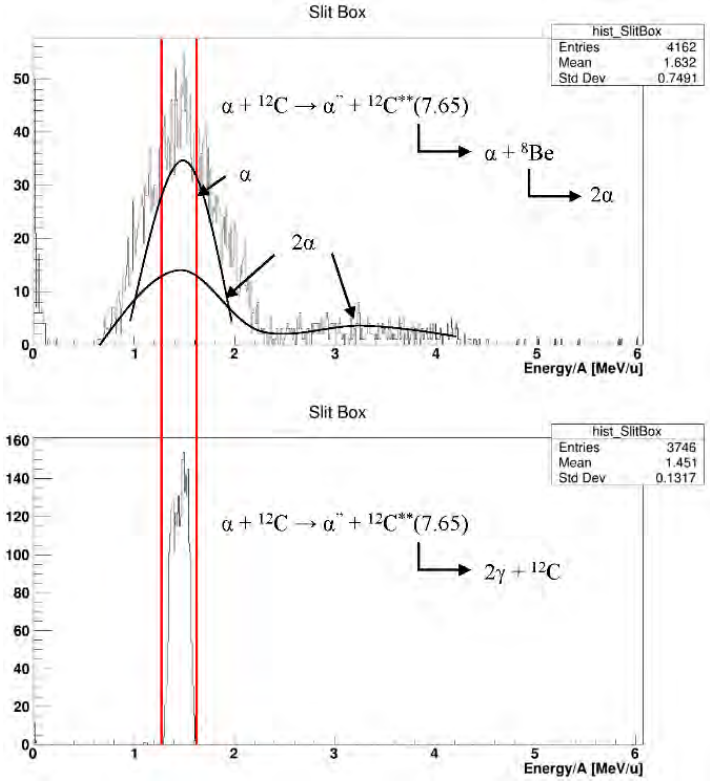

Fig. 3. Energy distribution of $^{12}C(\mathbf{0_2^+})$ decay products that enter MDM spectrometer.

Analysis of the experimental results

The first step in the analysis is to determine the charge state fractions for the ^{12}C ions. The ^{12}C ions emitted from the target exhibit charge states ranging from 1^+ to 6^+. In order to ascertain the distribution of charge states, we performed elastic scattering measurements by tuning the MDM spectrometer to detect ^{12}C

in each charge state individually. The outcome is presented in Figure 4 for the ^{12}C energy after the target at 1.5 MeV/u. Notably, it can be observed that $^{12}C^{5+}$ holds the highest fraction, with $F_{5+} = 0.495 \pm 0.026$.

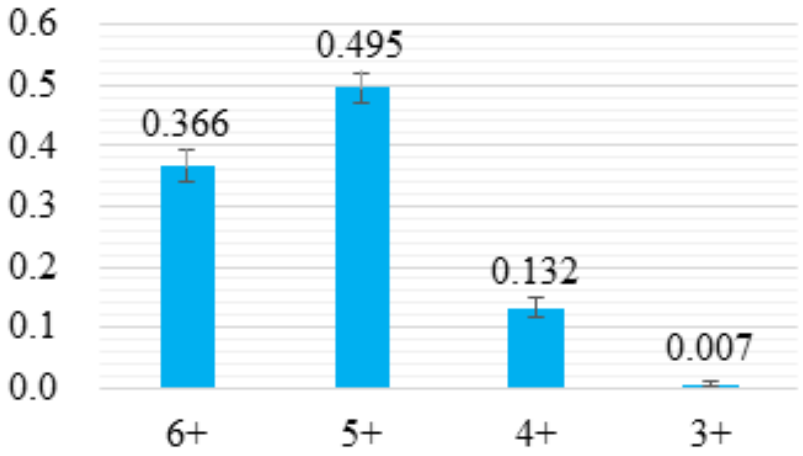

Fig. 4. Charge state distribution of ^{12}C out of 200 μm/cm^2 ^{12}C target at energy 1.5 MeV/u.

Particles detected by the TexPPACs travel a distance of more than 7 meters, whereas the particles detected by the silicon detectors only covered a distance of 17 cm. The ToF for the first type of particles (T_1) is on the order of 300 ns, while the ToF for the second type (T_{Si}) is approximately 10 ns. Fig. 5 exhibits

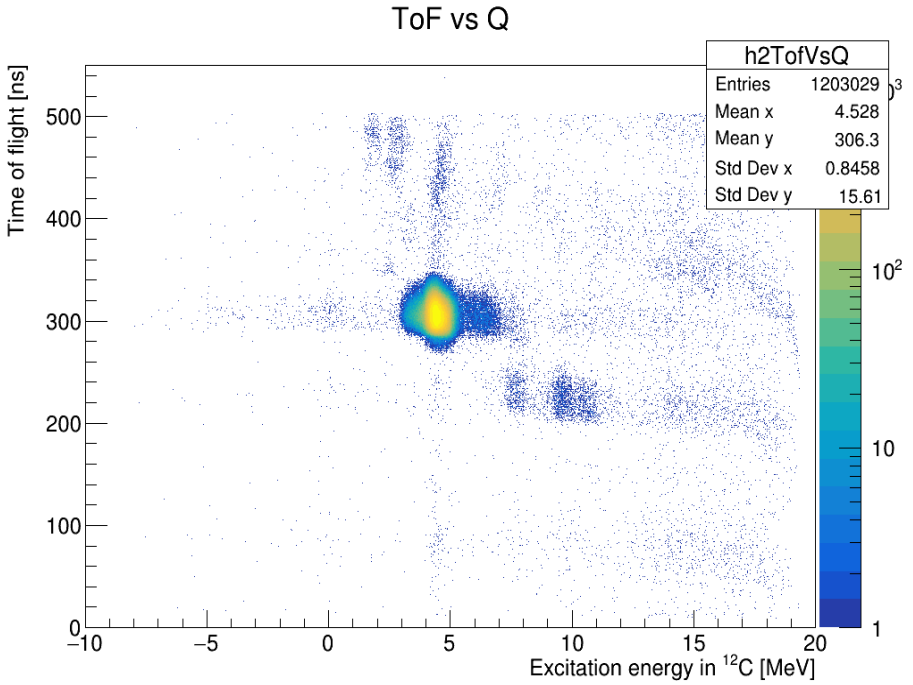

Fig. 5. ToF difference between TexPPAC1 and E detector. The boxes show the clusters of $^{12}C^{5+}$ ions and $^{4}He^{2+}$ respectively.

the plot of T_1-T_{Si} against the excitation energy in ^{12}C. The clusters observed in the upper and lower regions correspond to events involving $^{12}C^{5+}$ and $^{4}He^{2+}$ respectively. As previously discussed, the α-particles are faster compared to the ^{12}C ions due to their 1.2 times higher velocity. This characteristic enables effective discrimination between α particles and ^{12}C.

Figs 6(a) and 6(b) display the excitation-energy spectra of both singles and coincidence events centered around the Hoyle state measured by DSSD detector telescope. In the coincidence spectrum, a small peak associated with the Hoyle state was observed on the higher energy side of a larger peak, which is most likely due to the $^{16}O(\alpha,\alpha')^{16}O^*\rightarrow^{12}C+\alpha$ reaction originating on the oxygen impurities of the isotopically enriched ^{12}C target used for this experiment.

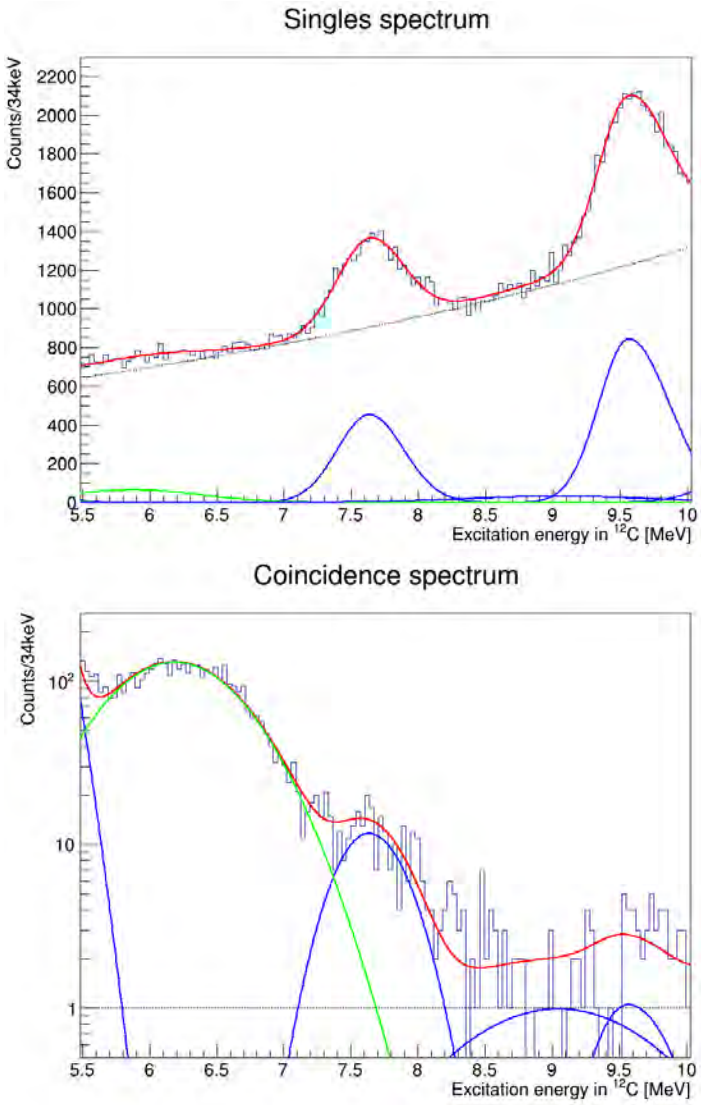

Fig. 6. Excitation-energy spectrum of ^{12}C around the Hoyle state for (a) the singles events and (b) the coincidence events in the inelastic α-scattering.

To determine the yields of singles and coincidence events, both spectra were fitted using Gaussian functions for the 0_2^+ and 3_1^- states, as well as other peaks, while a smooth function was employed for the continuum. The centroids and widths of the Gaussian functions were adjusted to reproduce the singles spectrum, and the same parameters were utilized for the coincidence spectrum. Two different functions were tested to fit the continuum: an exponential function and a semi-phenomenological function obtained from [5] with an added constant offset. The measured spectra were then subtracted by the fit functions for the continuum, and the remaining spectra were integrated to obtain the yields of the Hoyle state. This approach was employed to mitigate errors resulting from discrepancies between the Gaussian fit function and the actual measured peak shape.

The reduced χ^2 values for the fits using the semi-phenomenological function and the exponential function were found to be 1.93 and 1.23, respectively. Given that the exponential function yielded a better reduced χ^2 value, the yield obtained from this fit was adopted as the most probable value. The difference between the two yields was considered as the systematic uncertainty arising from the ambiguity of the continuum function. Consequently, the present $\frac{\Gamma_{\mathrm{rad}}}{\Gamma}$ of the Hoyle state in ^{12}C was determined to be $\frac{\Gamma_{\mathrm{rad}}}{\Gamma} \times 10^4 = 5.5 \pm 0.6\,(stat.) \pm 0.2\,(syst.)$.

Conclusion

The Hoyle state radiative branching ratio established in this work is consistent with the most recent results by Kibedi *et al.*, [1] within the experimental uncertainties and is 2.5σ above the previous recommended values. Statistical uncertainty dominates our measurements, and it would be desirable to repeat this or a similar experiment with better statistics (by at least a factor of four) before the final verdict can be made.

[1] T. Kibedi, B. Alshahrani, A.E. Stuchbery *et al.,* Phys. Rev. Lett. **125**, 182701 (2020).
[2] M. Freer and H. Fynbo, Prog. Part. Nucl. Phys. **78**, 1 (2014).
[3] T.K. Eriksen, T. Kibedi, M.W. Reed *et al*., Phys. Rev. C **102**, 024320 (2020).
[4] W.R. Zimmerman, M.W. Ahmed, B. Bromberger, *et al*., Phys. Rev. Lett. **110**, 152502 (2013).
[5] A. Erell, J. Alster, J. Lichtenstadt, *et* al., Phys. Rev. C **34**, 1822 (1986).

R matrix analysis of ^{22}Ne states populated in the ^{18}O(α,α) resonant elastic scattering

V.Z. Goldberg,[1] G.V. Rogachev,[1,2] A. Volya,[1,3] A.K. Nurmukhanbetova,[4] G.E. Serikbayeva,[4] and D.K. Nauruzbayev[5]

[1]*Cyclotron Institute, Texas A&M University, MS3366 College Station, Texas, 77843, USA*

[2]*Department of Physics and Astronomy, Texas A&M University, College Station, Texas 77843, USA*

[3]*Department of Physics, Florida State University, Tallahassee, Florida 32306-4350, USA*

[4]*Energetic Cosmos Laboratory, Nazarbayev University, Nur-Sultan, 010000, Kazakhstan*

[5]*Nazarbayev University Research and Innovation System, Nur-Sultan, 010000, Kazakhstan*

It is well known [1] that low energy ^{18}O+ α interaction may play an important role in astrophysical processes. The ^{18}O(α,γ) reaction synthesizes ^{22}Ne, the main neutron source for the weak s process, and the reaction ^{18}O(α,n)^{21} Ne has been proposed as a weak neutron source in a reaction chain to produce ^{19}F in TP-AGB stars. A few years ago detailed measurements of the excitation functions for the ^{18}O(α,n_0) and ^{18}O(α,n_1) reactions were performed in the astrophysically important region of 10.6 -11.5 MeV ^{22}Ne excitation energy [1].

Simultaneously properties of ^{22}Ne states populated in the ^{18}O(α,α) resonant interaction are of interest for cluster development in neon region and, specifically, to better understand extra neutron influence on alpha cluster structure [2]. It is also important from the perspective of a comparison of alpha cluster properties in mirror resonant reactions ^{18}O+α and ^{18}Ne+α. The measurements for the α+^{18}O elastic scattering were made in a broad energy interval and high energy resolution in two old works [3,4] and in a inverse kinematics publication [5]. None of these data were analyzed in the framework of R matrix theory.

We performed new measurements of the α+^{18}O elastic scattering in the inverse kinematics setup at lower energy than in the reference [5] to observe the states at a lower excitation energy at better conditions, and we made the first R matrix analysis of the available data on the α+^{18}O resonant elastic scattering in the energy region 11-15 MeV excitation energy in ^{22}Ne. Here we report on R matrix analysis of the oldest data [3] for the 11.5-12.5 MeV excitation region in ^{22}Ne, a part of a broader investigation of the α+^{18}O resonant interaction.

In future publications, together with an analysis of a higher excitation region in ^{22}Ne, we consider new requirements for enhanced theoretical predictions important for high excitation region of high density of states and several decay modes. We also intend to outline the merits and restrictions of different experimental approaches in resonant studies of nuclear structure at these conditions.

The data [3] were obtained at the ^{4}He beam of the ORNL 5.5-MV Van de Graaff well over half a century ago. The elastic scattering of alpha particles from α+^{18}O interaction was observed at θcm. = 90.0°, 125.3°, 140.7°, 152.3°, and 164.4°. The angles 90.0°, 125.3°, and 140.7° correspond, respectively, to the zeros of Legendre polynomials of odd order, order two, and order three. The authors [3] normalized data at the lowest energy of alpha particles of 2.40 MeV to the Rutherford-plus-hard-sphere scattering cross sections and claimed 6% counting statistics. The experimental data were analyzed in Ref. [3] using the single level [5] and two-level [6] approximations.

We used multilevel, multichannel R matrix code, AZURE [7], to fit the experimental data [3]. The resonances in the investigated excitation region in ^{22}Ne decay by alpha particles back to the ground state in ^{18}O and by neutrons to the ground $5/2^+$ state and to the $½^+$ first excited state in ^{17}O. Data [1,4] showed that both states in ^{17}O might be populated with comparable probability by these decays. We have included in the analysis only n decay to the ground state in ^{17}O to restrict the number of free parameters of the fit. However, we checked the influence of an inclusion of the second n channel to the fit of several strong resonances. We did not observe any important changes in the fit of the elastic scattering of alpha particles due to distribution of the reduced widths between two neutron decay channels. A stronger influence to neutron yield was observed. However, there are available data only on the total neutron yield for this excitation region in ^{22}Ne [8], and these data evidently less detailed and less precise than the excitation functions for alpha particle scattering. Therefore, we used data on the neutron yield [8] only as a final test of the analysis and did not include these data in the fit.

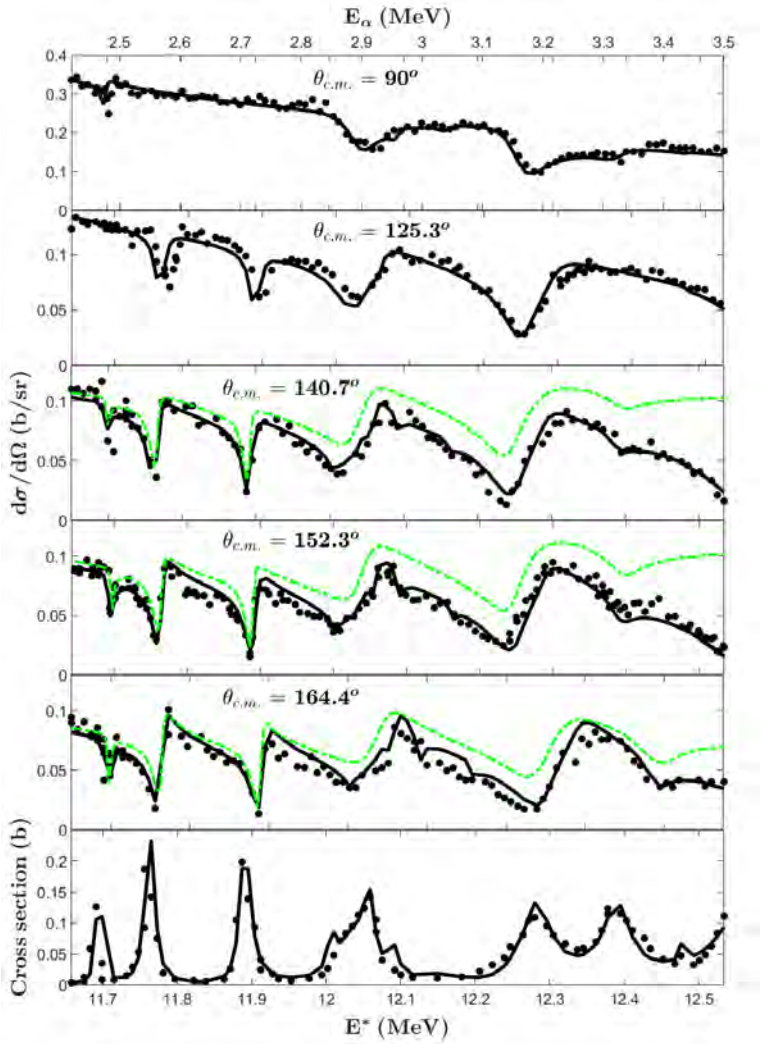

Fig. 1. R matrix fit of the excitation functions for the α+^{18}O elastic scattering [3] and the total 18O(α,n) reaction [8] (the lowest panel). The dash line shows a previous fit [3].

Fig.1 presents fit of the present work to the data [3]. Though the authors [3] claimed the data normalization at the lowest energies, we found that an additional scaling by 7% of the experimental data at 125.3° and 152.3° improves overall fit including the lowest energies.

An analysis of development of alpha cluster structure from ^{19}F and ^{20}Ne [9-11] to ^{21,22}Ne shows that the changes depend upon the nuclear parity of the state. We are looking for explanations in the frameworks of cluster or shell models, however, no reliable answer has been found yet.

[1] A. Best, S. Falahat, J. Görres, M. Couder, R. deBoer, R.T. G¨uray, A. Kontos, K.-L. Kratz, P.J. LeBlanc,Q. Li, S. O'Brien,N. Ökan, K. Sonnabend, R. Talwar, E. Uberseder, and M. Wiescher, Phys. Rev. C **87**, 045806 (2013).

[2] A.K. Nurmukhanbetova ,V.Z. Goldberg, D.K. Nauruzbayev, M.S. Golovkov, and A. Volya, Phys. Rev. **C** 100, 602802 (2019).

[3] D. Powers, J.K. Bair, J.L.C. Ford Jr., and H.B. Willard; Phys.Rev. **134**, B1237 (1964).

[4] S. Gorodezky, M. Port, G. Graff, J.M. Thirion, et G.Chouraqui; J. de Phys. **29**, 271 (1968).

[5] J.M. Blatt and L.C. Biedenharn; Rev. Mod. Phys. **24**, 258 (1952).

[6] A.M. Lane and R.G. Thomas; Rev. Mod. Phys. **30**, 257 (1958).

[7] R. Azuma, E. Uberseder, E. Simpson, C. Brune, H. Costantini, R. de Boer, J.G¨orres, M. Heil, P. LeBlanc, C. Ugalde , and M. Wiescher; Phys. Rev. C **81**, 045805 (2010).

[8] J.K. Bair and H.B. Willard; Phys. Rev. **128**, 299 (1962).

[9] D.K. Nauruzbayev, V.Z. Goldberg, A.K. Nurmukhanbetova, M.S. Golovkov, A. Volya, G.V. Rogachev, and R.E. Tribble; Phys. Rev. C **96**, 014322 (2017).

[10] A. Volya, V.Z. Goldberg, A.K. Nurmukhanbetova, D.K. Nauruzbayev, G.E. Serikbayeva, and G.V. Rogachev, Phys. Rev. C **105**, 014614 (2022).

[11] A. Best, M. Beard, J. Gorres, M. Couder, R. deBoer, S. Falahat, R.T. Guray, A. Kontos, K.-L.Kratz, P.J. LeBlanc, Q.Li, S. ÓBrien, N. Ozkan, M. Pignatari, K. Sonnabend, R. Talwar, W. Tan, E. Uberseder, M. Wiescher, Phys. Rev. C **87**, 045805 (2013).

Cyclotron institute evaluation center report: US nuclear structure data program

N. Nica and J.C. Hardy

Nuclear data evaluation is the main activity designed to capitalize the results of nuclear science research. From its beginnings more than a century ago, it became evident that nuclear science evolves over the years in such a way that establishing the "best" parameters at any given time is an important and challenging task. Thus, very early in its development the scientific community became aware, as Marie Curie wrote [1], that "*the need has arisen for the publication of special Tables of the Radioactive Constants*", which she, together with a prestigious group of contemporary scientists, co-authored the first major international nuclear data evaluation paper, titled "*The Radioactive Constants as of 1930*". Moreover, as she continues, "*This responsibility has been assumed by the International Radium Standards Commission chosen in Brussels in 1910 (...)*", which means that, due to its practical importance, this type of activity got institutionalized from its beginnings. Therefore, the origins of what today is known as *nuclear data evaluation* dates to the dawn of nuclear science itself.

In more recent times, it was recognized that the diversity of published data, not to mention their occasional inconsistencies, demanded that all published results should be assembled and reconciled by a specialized group of experienced scientists. Even collecting the relevant information from all the world's publications, was a nontrivial task, but documented databases were gradually established. This culminated with today's *Nuclear Science Reference* (NSR) database, which is maintained at the National Nuclear Data Center (https://www.nndc.bnl.gov/nsr/). Gradually after several cycles of systematic data analyses the community arrived at "practical standards" of data, which are then revisited periodically to include the continuous updates of newly published data. In this way, nuclear data evaluation has become a new research domain with its own specificity.

A new turning point emerged after the Second World War when the United States got the leading position in the nuclear research field, and consequently the transatlantic nuclear data evaluation changed shores, with the US becoming its main contributor. The United States Nuclear Structure Data Program (USNDP) was started (with its two main subcomponents, one for nuclear reactions and one for nuclear structure), being designed to maintain the so-called Evaluated Nuclear Structure Data File (ENSDF) database, the most extensive nuclear structure data repository in the world. This effort was shared initially among several national institutes and was extended to gradually include a few universities, of which Texas A&M Cyclotron Institute has been one since 2005. It was first funded by a contract with Brookhaven National Laboratory, but in 2017 we started to receive direct funding through the DOE Grant DE-FG02-93ER40773, "Cyclotron-based Nuclear Science". At that time, we became the Texas A&M Cyclotron Institute independent ENSDF Data Evaluation Center, one of the important contributors to the USNDP, as well as to the Nuclear Structure and Decay Data international network hosted by the IAEA Vienna.

Between 2005 and 2020, we completed and published the following full mass-chain evaluations: the superheavy A=252 mass chain [2]; the very data-rich mid-mass chains, A=140 [3], A=141 [4], A=147 [5] and A=148 [6]; and the relatively lighter chains, A=97 [7] and A=84 [8], the latter in a large international collaboration. In collaboration with B. Singh and a group of authors from McMaster

University, Canada, we also published the A=77 [9], A=37 [10], A=36 [11], and A=34 [12] mass chains. At the beginning of 2016, we published another large mass chain, A=157, in Nuclear Data Sheets [13], followed by A=158 in 2017 [14], the renewed full evaluation of A=140 in 2018 [15], A=155 in 2019 [16], A=153 in 2020 [17] and A=160 in 2021 [18].

As mentioned in our previous reports, our community has been passing through two crises: a critical shortage of evaluators, followed by a similar shortage of reviewers, due mainly to the retirement of several experienced evaluators. Moreover, the publication pipeline became more demanding, with a prereview process, followed by the main technical review with a couple of iterations, and finally by an editorial review, which together propagated substantial delays of 2-3 years to the currency of the ENSDF database.

In the interval of this report, Apr 1, 2022 – March 31, 2023, between April-September we continued the full evaluation work on the A=154 mass chain, covering a period of more than 14 years since the publication of its last evaluation. This mass chain was successfully submitted to NNDC before Oct 1, 2022, when it was due.

In parallel with the mainstream work, we also completed a technical review of the A=200 mass chain as assigned by NNDC. Although it was 300 pages long, we succeeded in returning the reviewed manuscript at the end of Feb 2023, less than five months after receiving it. The review itself had taken two months of dedicated effort.

After addressing the most substantial part of the after-review and editorial work on the A=147 mass chain during the Fall of 2021 (our second full evaluation of A=147 after that in 2009), this mass chain finally was published in the March-April 2022 issue of Nuclear Data Sheets [19]. This mass chain was published in collaboration with B. Singh who evaluated ^{147}Pm (including the half-life of its β^- decay parent, ^{147}Nd).

During about two months in the Summer of 2022, we also completed the after-review work for the A=141 mass chain, followed by the editorial review and preparations for publication during the Fall of that year. We finally published the A=141 mass chain in Nuclear Data Sheets in early 2023 [20].

Together with our previously published full evaluation of the A=147 mass chain (available on-line on Apr. 12, 2022), we succeeded to publish the two A=147 and A=141 mass chains in the 12 months interval now under review, Apr.1, 2022 – Mar 31, 2023. This is notable since we customarily manage to publish only one mass chain per 12 months interval.

In April 2023 we also started the post-review work on the large A=162 mass chain. The manuscript is more than 500 pages long.

After Oct 2022 we did a substantial part of the work on this fiscal year's principal commitment, the A=148 full mass-chain evaluation, which we evaluated previously in 2014 [6]. This mass chain involves more than 1200 experimental publications, of which more than 116 have been added since our last evaluation. This work is currently in progress and is to be submitted to NNDC by Sept 30, 2023.

[1] M. Curie, A. Debierne, A.S. Eve, H. Geiger, O. Hahn, S.C. Lind, S. Meyer, E. Rutherford, E. Schweidler, Rev. Mod. Phys. **3**, 427 (1931).

[2] N. Nica, Nucl. Data Sheets **106**, 813 (2005).

[3] N. Nica, Nucl. Data Sheets **108**, 1287 (2007).

[4] N. Nica, Nucl.Data Sheets **122**, 1 (2014).
[5] N. Nica, Nucl. Data Sheets **110**, 749 (2009).
[6] N. Nica, Nucl. Data Sheets **117**, 1 (2014).
[7] N. Nica, Nucl. Data Sheets **111**, 525 (2010).
[8] D. Abriola *et al.*, Nucl. Data Sheets **110**, 2815 (2009).
[9] B. Singh and N. Nica, Nucl. Data Sheets **113**, 1115 (2012).
[11] N. Nica, J. Cameron, and B. Singh, Nucl. Data Sheets **113**, 1 (2012).
[12] N. Nica and B. Singh, Nucl. Data Sheets **113**, 1563 (2012).
[13] N. Nica, Nucl.Data Sheets **132**, 1 (2016).
[14] N. Nica, Nucl.Data Sheets **142**, 1 (2017).
[15] N. Nica, Nucl.Data Sheets **154**, 1 (2018).
[16] N. Nica, Nucl.Data Sheets **160**, 1 (2019).
[17] N. Nica, Nucl.Data Sheets **170**, 1 (2020).
[18] N. Nica, Nucl.Data Sheets **176**, 1 (2021).
[19] N. Nica, B. Singh, Nucl.Data Sheets **181**, 1 (2022).
[20] N. Nica, Nucl.Data Sheets **187**, 1 (2023).

Cold QCD physics with STAR at RHIC

B.E. Aboona, C.A. Gagliardi, and R.E. Tribble and the STAR Collaboration

Our group continues to play a major role in the STAR spin physics program. Over the past year, our analysis efforts have focused on two measurements: the Collins effect in 200 GeV *p*+Au collisions and an investigation of the contribution from diffractive processes to the large transverse single-spin asymmetry, A_N, that is seen for forward rapidity electromagnetic jets (EM-jets) in 200 GeV *pp* collisions. In addition, the paper describing the STAR measurements of the Collins effect in 200 GeV *pp* collisions, based on data that STAR recorded during 2012 and 2015, was published [1]. Dr. Gagliardi and his former post-doc, T. Lin, carried the full responsibility for the 2015 data analysis as well as the process of merging the 2012 and '15 results together. Notably, the latter required calculation of several corrections and systematic uncertainties for the 2012 data to account for differences in the basic analysis procedures between the two years. Drs. Gagliardi and Lin were two of the five principal authors. Dr. Gagliardi also played a significant role in the preparation of the RHIC Cold QCD White Paper for input to the upcoming NSAC Long-Range Plan [2]. In addition, group members have continued to carry a wide range of administrative responsibilities for STAR.

Our graduate student B. Aboona is analyzing data that STAR recorded during 2015 to determine the size of the Collins effect in $\sqrt{s_{NN}}$ = 200 GeV *p*+Au collisions. This will provide unique insight into the possible factorization breaking that has been predicted for transverse-momentum-dependent phenomena in hadronic collisions, in addition to a spin-dependent probe of the hadronization mechanism in cold nuclear matter.

Last year's report discussed the completion of incorporating B. Aboona's improvement to start-less TOF into the data structure at STAR. The first level of data structure at STAR is called StEvent, which is then further processed into MuDst files. MuDst's can be further processed into PicoDst's or jet trees. B. Aboona's improvements were incorporated in the MuDst, PicoDst, and jet tree data structures. For the purpose of the Collins analysis, jet trees will be used as the input data structure. He also reported the completion and documentation of the quality assurance analysis of the 2015 $\sqrt{s_{NN}}$ = 200 GeV *p*+Au data set.

A very important step in the *p*+Au Collins effect analysis is to be able to perform high quality particle identification (PID). STAR primarily relies on *dE/dx* information from the Time Projection Chamber (TPC) for PID. Previous reports have discussed details of B. Aboona's improvements to the "start-less" Time of Flight (TOF) algorithm. This algorithm makes use of measurements obtained from the Barrel Time of Flight (BTOF) detector to provide complementary PID to the *dE/dx* information from the TPC. Developing a robust and high quality PID scheme requires a detailed understanding of the response of the PID quantities commonly used in STAR analyses. PID from the TPC is obtained by using a quantity known as n_σ. This quantity returns the difference between the measured and the calculated *dE/dx* of a track in units of resolution, σ. For example, a reconstructed track whose $n_\sigma(\pi)\sim 0$ is very likely to be a pion. Similarly, PID from TOF is obtained by using $n_{\sigma,TOF}$. Here, the quantity returns the difference between the measured and the calculated time of flight of a given track divided by the TOF resolution.

B. Aboona conducted a study of $n_\sigma(e)$ and $n_{\sigma,TOF}(e)$ obtained from the progeny particles of conversion photons. The results are plotted in 8 psuedorapidity (η) bins in the range $-1.33 \leq \eta < 1.33$ and 7 variable momentum bins in the range $1 \leq p < 10$ GeV/c. The left side of Fig. 1 shows the $n_\sigma(e)$ distribution for both the raw unlike-sign (US) and like-sign (LS) lepton pairs in the η and momentum bins $0.33 \leq \eta < 0.67$ and $2 \leq p < 2.5$ GeV/c, respectively. On the right, Fig. 1 shows the corrected US $n_\sigma(e)$, which is obtained by subtracting the LS $n_\sigma(e)$ distribution from the raw US $n_\sigma(e)$. The corrected US $n_\sigma(e)$

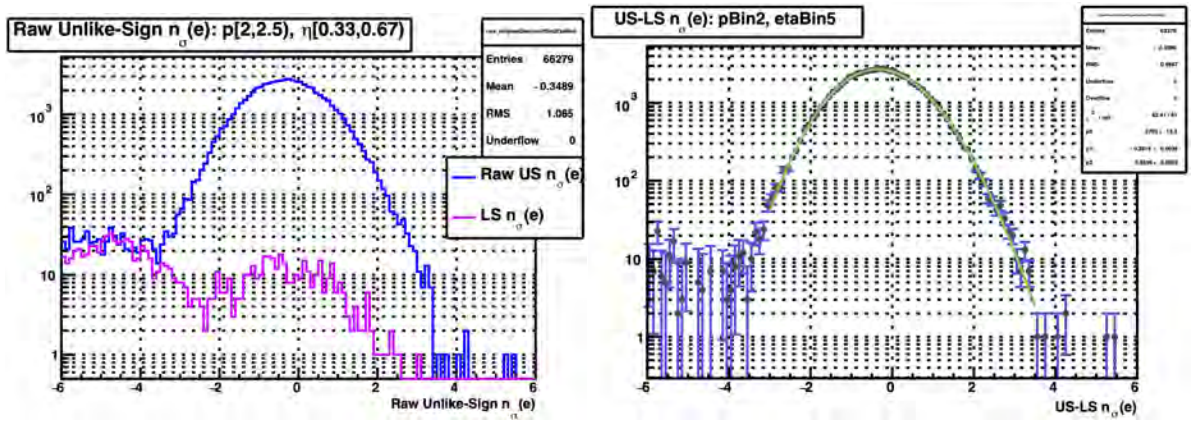

Fig. 1. The plot on the left shows the $\boldsymbol{n_\sigma(e)}$ distributions for raw unlike-sign (US) lepton pairs in blue and the like-sign (LS) lepton pairs in magenta for the momentum bin $\boldsymbol{2 \leq p < 2.5}$ GeV/c and $\boldsymbol{\eta}$ bin $\boldsymbol{0.33 \leq \eta < 0.67}$. The plot on the right shows the background-subtracted US $\boldsymbol{n_\sigma(e)}$ distribution fitted with a skewed Gaussian function over the range $\boldsymbol{-3 < n_\sigma(e) < 3.5}$.

is fitted with a skewed Gaussian function over the range $-3 < n_\sigma(e) < 3.5$. Equation 1 gives the functional form adopted for the skewed Gaussian. A constant value for the skew parameter, b, is found to work very well over the full momentum and pseudorapidity range. Also, the value of b that is found for electrons also works well for pions, kaons, and protons. Fig. 2 shows the same procedure for $n_{\sigma,TOF}(e)$. However, a correlated double Gaussian function of the form described in Eq. 2, where α, μ_2, and σ_2 are constants, is used to fit the corrected US $n_{\sigma,TOF}(e)$ distribution shown on the right in Fig. 2. The fit performs very well over the range $-4 < n_{\sigma,TOF}(e) < 4$.

$$f(x) = Ae^{-\frac{1}{2}\left[\frac{x-\mu}{\sigma+b(x-\mu)}\right]^2} \qquad (1)$$

$$f(x) = A_1\left[e^{-\frac{1}{2}\left(\frac{x-(\langle x\rangle-0.085)}{\sigma_1}\right)^2} + \alpha e^{-\frac{1}{2}\left(\frac{x-(\langle x\rangle-0.085+\mu_2)}{(\sigma_1+\sigma_2)}\right)^2}\right] \qquad (2)$$

B. Aboona has also made significant progress in understanding the n_σ and $n_{\sigma,TOF}$ response of pions, kaons, and protons. For this study, he utilizes two-dimensional log-likelihood fits. Since, to first order, the TPC and TOF measurements are independent, the functional form of the two-dimensional fit is then given by the product of the skewed Gaussian, Eq. 1, and the correlated double Gaussian, Eq. 2, found

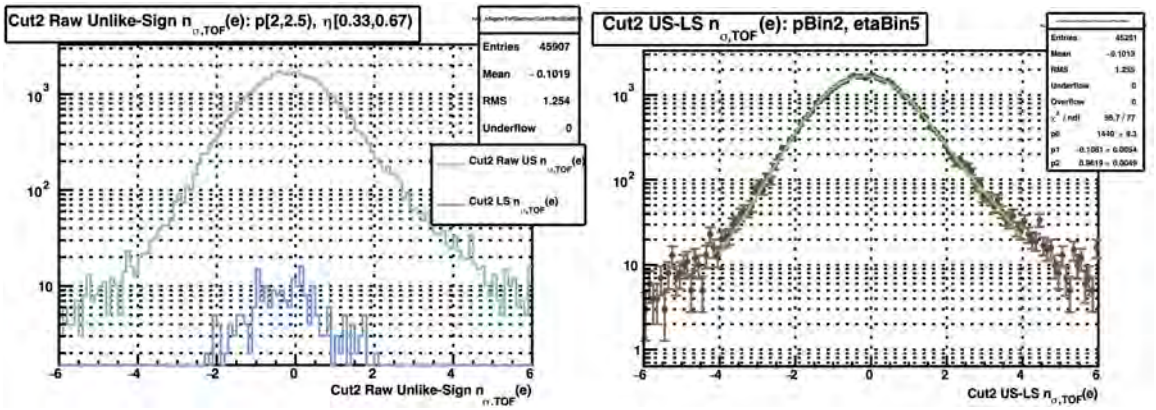

Fig. 2. The plot on the left shows the $\boldsymbol{n_{\sigma,TOF}(e)}$ distributions for raw unlike-sign (US) lepton pairs in green and the like-sign (LS) lepton pairs in blue for the momentum bin $\mathbf{2 \leq p < 2.5}$ GeV/c and $\boldsymbol{\eta}$ bin $\mathbf{0.33 \leq \eta < 0.67}$. The plot on the right shows the background-subtracted US $\boldsymbol{n_{\sigma,TOF}(e)}$ distribution fitted with a correlated double Gaussian function over the range $\mathbf{-4 < n_{\sigma,TOF}(e) < 4}$.

from his conversion photon studies. Fig. 3 shows an example of a two-dimensional fit for $n_\sigma(\pi)$ vs. $n_{\sigma,TOF}(\pi)$ in the momentum and η bins $2.8 \leq p < 2.9$ GeV/c and $-0.67 \leq \eta < -0.33$, respectively. Here, the pions are centered around zero on both axes, the background electrons are clustered above the pions,

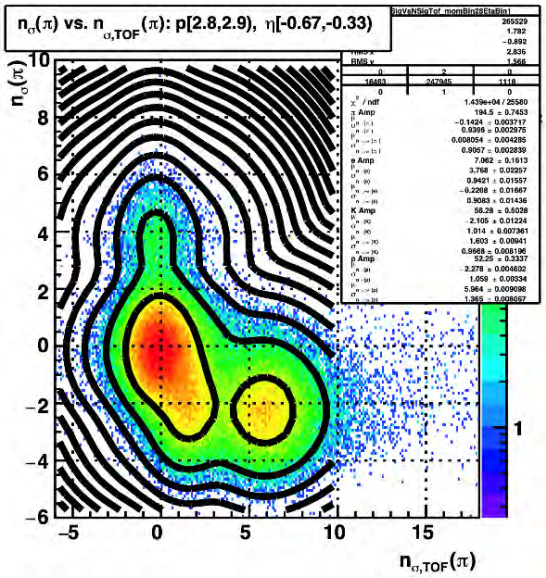

Fig. 3. An example of a two-dimensional fit for $\boldsymbol{n_\sigma(\pi)}$ vs. $\boldsymbol{n_{\sigma,TOF}(\pi)}$ in the $\boldsymbol{\eta}$ and momentum bins $\mathbf{-0.67 \leq \eta < -0.33}$ and $\mathbf{2.8 \leq p < 2.9}$ GeV/c, respectively.

the background kaons are below and slightly to the right of the pions, and the background protons are well separated on right with respect to the pions. These two-dimensional fits were done in multiple momentum bins ranging from $1 \leq p < 3.8$ GeV/c. A similar study is done for $n_\sigma(K)$ vs. $n_{\sigma,TOF}(K)$ and $n_\sigma(p)$ vs. $n_{\sigma,TOF}(p)$. A summary of the means of $n_{\sigma,TOF}(\pi, K, p)$ vs. p/m (or $\beta\gamma$) from all the momentum bins and

the η bin $-1 \leq \eta < -0.67$ is shown in Fig. 4. This study has been well received by various groups in STAR and has broad impact beyond B. Aboona's analysis. The next step is to explore charge dependence in the $n_\sigma(\pi, K, p)$ and $n_{\sigma,TOF}(\pi, K, p)$ distributions.

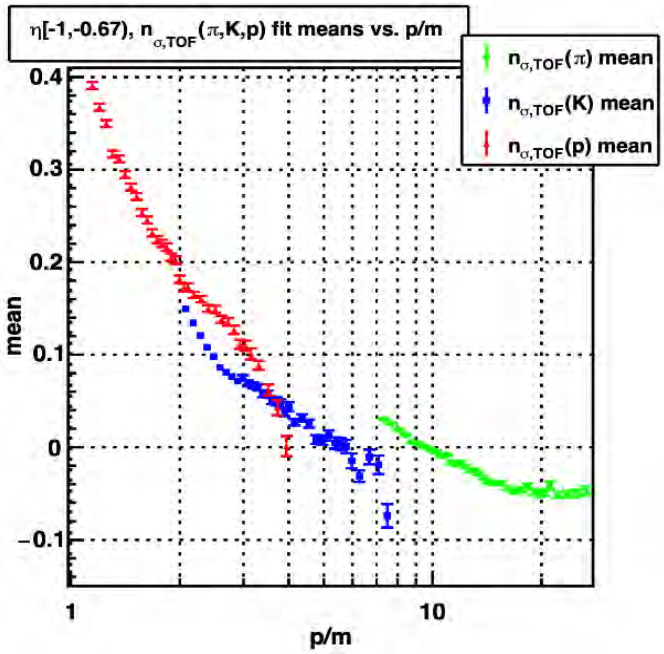

Fig. 4. Means of $\boldsymbol{n_{\sigma,TOF}(\pi, K, p)}$ vs. *p/m* (or $\boldsymbol{\beta\gamma}$) for the $\boldsymbol{\eta}$ bin $\boldsymbol{-1 \leq \eta < -0.67}$.

Recently, STAR published measurements of forward π^0 and EM-jet A_N [3] that indicate the large transverse single-spin asymmetries that have been seen for inclusive hadron production at forward rapidities are unlikely to arise from either the Collins or Sivers effects. This led to the question whether the large asymmetries might arise from diffractive processes. The UC-Riverside group began a study of EM-jets observed in *pp* data at $\sqrt{s}$ = 200 GeV that STAR recorded during 2015 to explore this question, and asked Dr. Gagliardi to join the effort. Two different diffractive processes have been investigated. In one case, A_N has been measured for the case where a moderate to high-p_T EM-jet and a low-p_T proton are both observed at forward rapidity, with the summed energy of the EM-jet and proton consistent with initial beam energy. The observed asymmetry appears to be negative, which is opposite in sign to the inclusive EM-jet asymmetry. In the other case, EM-jets that arise from single diffraction are being studied by measuring the probability that beam-like protons are seen in the opposite hemisphere. Random coincident protons make a spin asymmetry measurement difficult in this case. But it is straightforward to estimate and subtract the randoms to determine the fraction of EM-jets with a single-diffractive origin. Raw coincidence rates are now in hand. However, no physics conclusion can be drawn until detailed simulations are completed that are needed to correct the raw data for acceptance effects.

Finally, we continue to carry various administrative responsibilities for STAR. Dr. Gagliardi is a member of the STAR Trigger Board for RHIC Run 23. He also served on god parent committees for five STAR heavy ion papers. One of the five was published in EPJC [4], one is under review at JHEP [5], two

are currently under Collaboration review, and one is approaching Collaboration review. In parallel, Mr. Aboona has served on the god parent committee for a STAR spin paper that was recently submitted to PRL [6].

[1] M.S. Abdallah *et al*. (STAR Collaboration), Phys. Rev. D **106**, 072010 (2022).
[2] E.C. Aschenauer *et al*., arXiv:2302.00605.
[3] J. Adam *et al*. (STAR Collaboration), Phys. Rev. D **103**, 092009 (2021).
[4] M.S. Abdallah *et al*. (STAR Collaboration), Eur. Phys. J. C **82**, 1150 (2022).
[5] STAR Collaboration, arXiv:2303.06590.
[6] STAR Collaboration, arXiv:2305.10359.

SECTION II

HEAVY ION REACTIONS

Capability of studying N-Z equilibration using FAUST

T. Hankins, B.M. Harvey, A. Hannaman, A.B. McIntosh, K. Hagel, Z. Tobin, and S.J. Yennello

In heavy-ion collisions (HICs) near the Fermi energy, the formation of atypical nuclear matter affords methods of probing the nuclear equation of state (nEOS), an outstanding question in the field of nuclear science that legislates the nature of both intrinsic and extrinsic properties of nuclear matter. The nEOS, comprised of several interrelated components, suffers from associated uncertainties, of which the density dependence of the asymmetry energy remains the least constrained.

Observation of nucleon exchange between reaction participants led to the development of a method that uses the preferential migration of nucleons within a system to constrain the asymmetry energy dependence, a process known as neutron-proton (N-Z) equilibration. Studying angular and isospin correlations between the fragments produced in HICs can provide insight into the length and strength of the interaction; observing this across systems of varying isospin content can then provide information about the nature of the asymmetry energy of the nEOS. A more comprehensive discussion regarding the phenomenon is provided by [1] and references therein.

N-Z equilibration was previously studied at Texas A&M University (TAMU) using the near-4π Neutron Ion Multidetector for Reaction Oriented Dynamics (NIMROD) for all beam and target permutations of ^{70}Zn and ^{64}Ni at 35 MeV/u [2-5] in which equilibration was characterized for subsystems of varying Z compositions [5]. Equilibration is characterized by observing the relationship between the N-Z composition of the heaviest and second-heaviest fragments originating from the projectile-like fragment (PLF) in an event and their corresponding alignment angle, α, defined as

$$\alpha \equiv \operatorname{acos}\left(\frac{\vec{v}_{CM} \cdot \vec{v}_{rel}}{\|\vec{v}_{CM}\| \cdot \|\vec{v}_{rel}\|}\right) \quad ; \quad \vec{v}_{rel} = \vec{v}_{HF} - \vec{v}_{LF}. \tag{1}$$

In these equations, v_{CM}, v_{rel}, v_{HF}, and v_{LF} refer to the velocity of the center-of-mass of the (reconstructed) PLF, the relative velocity between the heavy fragment (HF) and light fragment (LF), the laboratory velocity of the HF, and the laboratory velocity of the LF, respectively. The full results for each aforementioned study are summarized in the respective references; the purpose of this report is to investigate whether N-Z equilibration can be studied with the Forward Array Using Silicon Technology (FAUST) at TAMU. FAUST is a position-sensitive charged particle array that covers most of 1.6-45.5° of forward angles via 68 ΔE-E telescopes. FAUST, despite significantly less overall angular coverage in comparison to NIMROD, possesses excellent position and angular resolution unachievable by NIMROD (in its current state) consequent of the dual-axis duo lateral (DADL) position-sensitive silicon detectors serving as the ΔE of the telescopes.

To understand the capacity of N-Z equilibration in FAUST, simulations of Heavy-Ion Phase Space Exploration (HIPSE) coupled with statistical de-excitation afterburner were produced for systems of ^{70}Zn + ^{70}Zn, ^{40}Ca + ^{40}Ca, and ^{48}Ca + ^{40}Ca at 35 MeV/nucleon and filtered using simulated filters for both FAUST and NIMROD. The zinc system was simulated as a “standard” for N-Z studies; the calcium

systems were simulated because a) the relative isospin magnitude for ^{48}Ca is greater than any participant in a zinc or nickel-based system, and b) the lesser total Z of the system takes advantage of FAUST's lighter-particle isotopic resolution. The near mass symmetry of all systems considered means that the products are less forward focused on average, and thus concerns for FAUST geometry become significant (Fig. 1a). However, as the HF and LF originate from the PLF which is moving forward of mid-velocity, these components will be forward focused enough that FAUST geometry is sufficient (Fig. 1b). The diagrams provided as example are the smallest Z LF and HF that are traditionally gated on in these analyses [5]. Higher Z components are increasingly forward focused; by LF Z = 6, nearly 100% of the distribution is forward of $\theta_{lab} = 45°$.

In the interest of furthering this study, analyses similar to those conducted in experiment (see, for

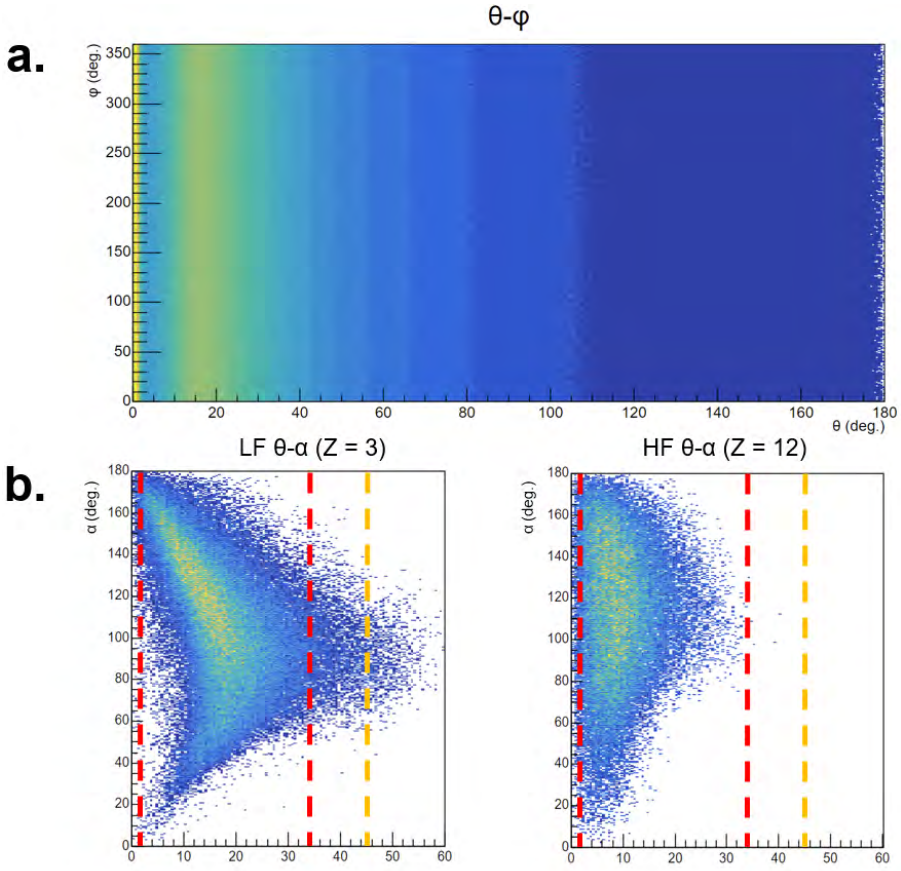

Fig. 1. (a) Laboratory θ-φ distribution of particles from simulated ^{70}Zn + ^{70}Zn @ 35 MeV/nucleon. This distribution illustrates that while most particles are forward of $\theta_{lab} = 90°$, a significant amount are present backward. (b) Laboratory θ-α distribution of particles identified as the LF and HF in an event based on particle Z and velocity conditions. For each diagram, the red dashed lines enclose the region of θ_{lab} that is effectively covered by FAUST geometry, while the orange dashed line designates the maximum θ_{lab} in FAUST. Coverage in this intermediate region reduces approximately exponentially. See discussion in text.

example, [5]) were replicated for the unfiltered and filtered HIPSE data. Fig. 2 summarizes results for distributions of α (therein provided as cos(α)) and Fig. 3 summarizes results for Δ vs. α (therein provided

as α) for all permutations of systems and filters. These distributions were produced using an overall velocity cut on the LF of 0.2c; this imposed velocity gate accounts for differing isotopes have differing velocity thresholds for detection. Particle velocities are highly correlated to the measured α; neutron-rich fragments, possessing lower velocity thresholds than their corresponding neutron-poor isotopes, would contribute disproportionately and lead to a more neutron-rich LF on average for small α without a velocity cut. Ideally, cuts would be made on a Z basis to best utilize the available statistics, but a generalized cut was used here in the interest of efficiently probing the potential for further studies.

In Fig. 2, the excess in the cos(α) distributions leading to asymmetry about zero would indicate the presence of a non-statistical decay contribution, but comparing these to an experimental equivalent [5] shows that the distributions are inverted about zero. This suggests that the present trend is instead an

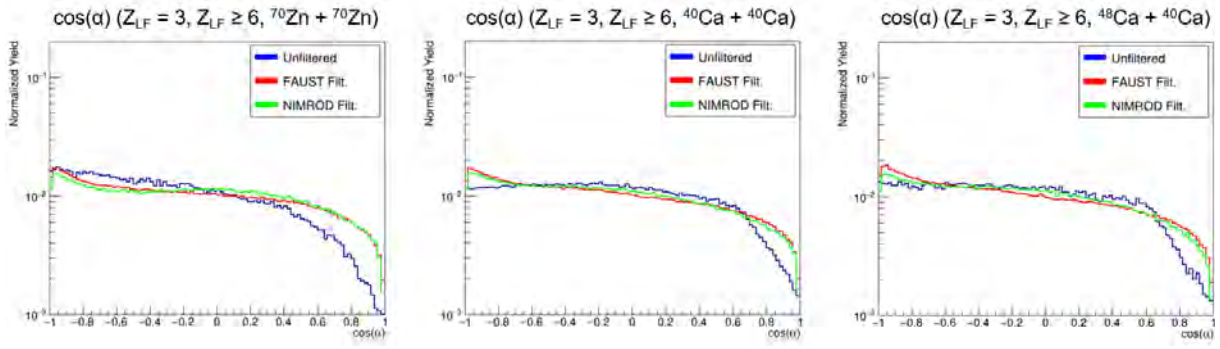

Fig. 2. cos(α) distributions for systems of ^{70}Zn + ^{70}Zn (left), ^{40}Ca + ^{40}Ca (middle), and ^{48}Ca + ^{40}Ca (right). These distributions compare normalized yield between unfiltered (blue), FAUST filtered (red), and NIMROD filtered (green) HIPSE.

analytic artifact. However, in Fig. 3, the evolution of Δ as a function of increasing α for the ^{70}Zn and ^{48}Ca systems also suggests that dynamical contribution may be present in the simulation data, albeit suppressed as a consequence of statistics. This is further reinforced by the comparative *lack* of evolution in the ^{40}Ca system; this system, possessing N = Z overall, is not affected by a driving force for nucleon migration

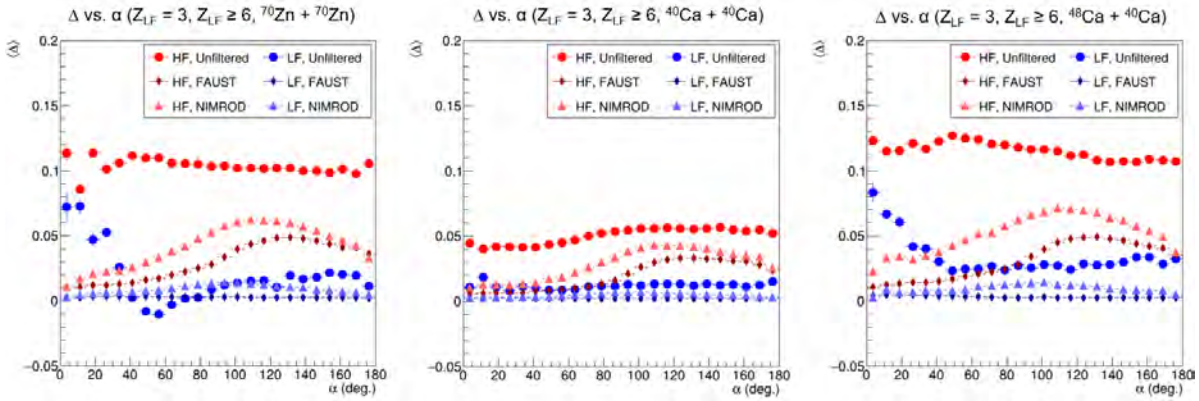

Fig. 3. Δ vs. α distributions for systems of ^{70}Zn + ^{70}Zn (left), ^{40}Ca + ^{40}Ca (middle), and ^{48}Ca + ^{40}Ca (right). Both the ^{70}Zn and ^{48}Ca show distinguishable features with the evolution of α, while the ^{40}Ca does not. In consideration of the nature of ^{40}Ca + ^{40}Ca, this may suggest that some of the dynamical nature of N-Z equilibration is captured by HIPSE simulations. It is important to note that the abnormal behavior of these plots is due to a combination of limited statistics and the nature of HIPSE simulation.

during the initial collision (as there is no asymmetry penalty to mitigate) and thus no potential for equilibration afterward (beyond native fluctuation). Because the ^{40}Ca + ^{40}Ca Δ versus α is essentially featureless in comparison to the other two systems, further analysis to understand the discrepancy in the cos(α) is needed as well as review of the HIPSE framework to determine if observing N-Z trends in simulation is reasonable. Comparison between the filters for each system reveals that FAUST performance in relation to NIMROD in the context of N-Z studies is plausible – the result of filtering raw HIPSE leads to the same general conclusion in terms of evolution of the trend. While a more comprehensive study is desired to support these conclusions, preliminary results suggest that conducting an N-Z experiment with FAUST would be doable from a geometric acceptance and resolution standpoint and should be considered further in the future of the FAUST research campaign. Finally, concerning the plausibility of N-Z studies for a smaller system such as ^{40}Ca + ^{40}Ca, a recent experiment conducted with the INDRA-VAMOS charged particle array-spectrometer and the beam/target combinations discussed herein was able to demonstrate equilibration [6]. With this in mind, further investigation into these reaction systems with differing experimental conditions may be of interest to comprehensively understand the dynamics at play.

[1] A.B. McIntosh and S.J. Yennello. Prog. in Part. and Nuc. Phys. **108**, 103707 (2019).
[2] A. Rodriguez Manso *et. al.* Il Nuovo Cimento C **5**, 188 (2018).
[3] A. Rodriguez Manso *et. al.* Phys. Rev. C **100**, 044612 (2019).
[4] A. Hannaman *et. al.* Phys. Rev. C **101**, 034605 (2020).
[5] A. Jedele, Ph. D. Thesis, Texas A&M University, 2020.
[6] Q. Fable, *et. al.* Phys. Rev. C, **106** 024605 (2022).

DAPPER: PSF forward analysis on ^{58}Fe

M. Sorensen, A. Abbott, A.B McIntosh, A. Alvarez, K. Hagel, J. Gauthier, G. Potel, and S.J. Yennello

The purpose of DAPPER (Detector Array for Photons, Protons, and Exotic Resides) is to measure the photon strength function (PSF) of nuclei. The PSF describes the average quantum mechanical component of photon emission probabilities and thus it is important in describing the de-excitation process of neutron capture reactions. Of particular interest are the PSFs of nuclei away from the line of stability. Direct neutron capture reactions on radioactive nuclei are typically not feasible due to both the beam and the target being unstable, thus these measurements typically require radioactive beams. To get around this problem indirect (d,pγ) reactions will be used. In order to first test the methodology and setup of the proposed radioactive beam experiment a stable inverse kinematic experiment was done with ^{57}Fe(d,pγ)^{58}Fe. The analysis methodology that I am using to constrain the photon strength function is known as the forward method [1].

The DAPPER array consists of 128 BaF_2 detectors and an S3 Annular Silicon detector. The primary benefit of BaF_2 detectors is that they provide high gamma ray efficiency which will be important for any future radioactive beam experiments. The proton produced in the reaction can then be detected by the S3 annular silicon detector in order to calculate the excitation energy of the residue. On August 2nd 2021 the first run with DAPPER was conducted. ^{57}Fe at 7.5 MeV/u was on a CD_2 target at the end of the MARS (Momentum Achromat Recoil Spectrometer) line to produce ^{58}Fe and a free proton. Carbon targets were also used in order to subtract out the gamma rays associated with reaction on carbon.

The forward method works by simulating the gamma ray cascade assuming a certain PSF and nuclear level density (NLD), and then comparing the simulation to the experimental results. In order to compare the simulated data to the experimental ones the simulated cascades must be subject to the same experimental constraints as the experimental data. To do this we have chosen to use GEANT4 to simulate DAPPER's response. To test the GEANT4 simulation of the DAPPER array multiple gamma ray sources where used. Shown in Fig. 1 is the simulated efficiency compared to its experimental counterpart as a function of gamma ray energy (γE). Efficiency was evaluated for both simulation and experiment by taking the ratio between the yield within 300keV*sqrt(γE) of the known γE of the peak and the number of gamma rays of that energy. This gate formalism was chosen to account for the absolute resolution of the BaF_2 detectors broadening for higher energy gamma rays. The simulated efficiencies are systematically too high by roughly 10%. However, the general trend of efficiencies as a function of gamma ray energy and multiplicity appears to be reproduced by the GEANT4 simulation. Specifically, due to the large effective Z of the BaF_2 crystals the efficiency as a function of energy appears roughly flat. Further work with lab testing is currently planned to better understand the source of the difference.

In addition to the GEANT4 simulation the initial spin of the ^{58}Fe nucleus must also be accounted for. For each PSF and NLD multiple initial spins states must also be sampled, and their contributions then

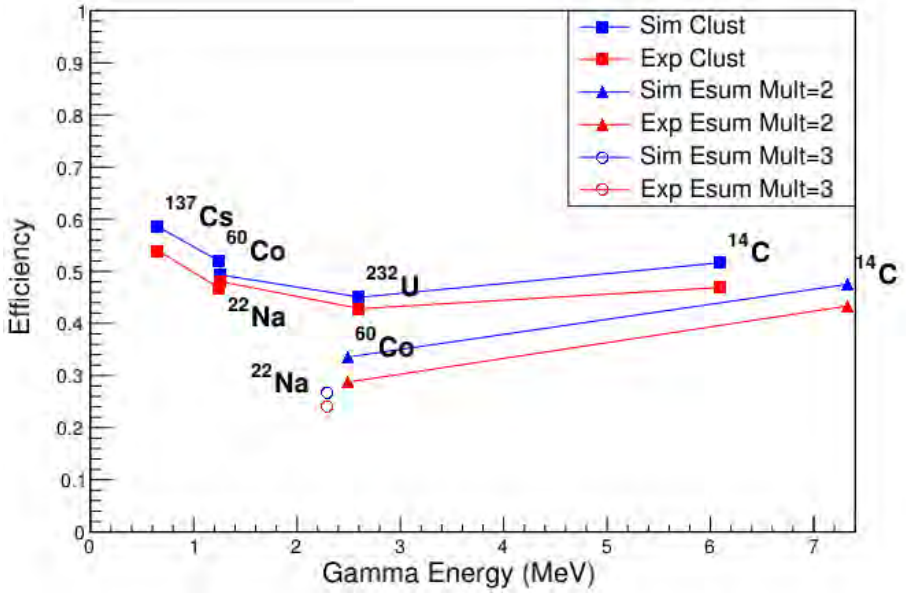

Fig. 1. : Efficiency of simulated (blue) and experiment (red). Efficiency is defined as ratio of the integral within 300KeV*sqrt(γE) symmetric gate of the gamma ray energy and the number of decays. Square points are for the cluster efficiency, triangles are for true multiplicity 2 BaF_2 Esum, and open circles are for true multiplicity 3 BaF_2 Esum. No error bars calculated.

must be weighed by a predicted spin distribution as a function of excitation energy. Dr. Potel provided some theoretical predictions of how much each l-wave contribution to the (d,p) reaction, allowing us to predict the yield as a function of excitation energy for each of the different J states (Fig. 2) [2]. Due to a strong d-wave contribution the spin population of 1^-, 2^-, and 3^- are the major contributors. Yield is

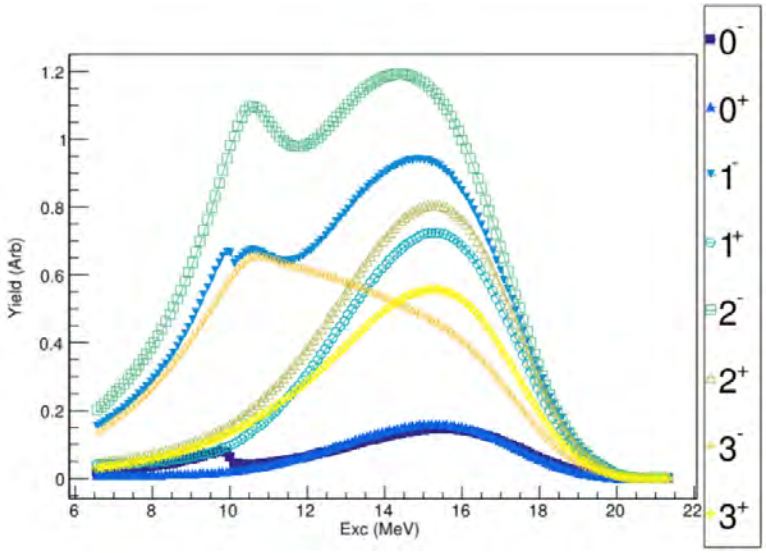

Fig. 2. Predicted spin distribution of the initial state populated in ^{58}Fe for both positive and negative parities up to spin 3.

integrated over the angular range of the S3 detector. With those distributions the same gating conditions can be applied to both experiment and simulation to determine which models are consistent with the data. Currently the only major remaining hindrance to a final result lies in the GEANT4 simulation not agreeing perfectly with the experimental standards used.

[1] F. Becvar, Nucl. Instrum. Methods Phys. Res. **A417**, 434 (1998).
[2] G. Potel, F.M. Nunes, and I.J. Thompson, Phys. Rev. C **92**, 034611 (2015).

Investigating resonant state modification with a Coulomb trajectory model

T. Hankins, B.M. Harvey, A. Hannaman, A.B. McIntosh, K. Hagel, Z. Tobin, and S.J. Yennello

Heavy-ion collisions in the proper kinematic regime can produce excited projectile-like fragments (PLF*) that will subsequently de-excite via accessible pathways. Heavier and more excited nuclei favor the emission of light charged particles (LCP) and intermediate mass fragments (IMF) [1]; if the emitted component is an excited state IMF (IMF*), it will also de-excite, often by decaying into several LCPs. This de-excitation mechanism is well-understood for isolated decays, i.e., decays occurring without a spectator nucleus, but is otherwise less clear.

Unstable nuclei in isolation decay with well-defined energy distributions parameterized by their intrinsic energy and lifetime; however, when ejected from a de-exciting parent nucleus, these distributions can be modified following interactions with the parent's Coulomb field. The capacity for modification is directly related to the mean lifetime of the unstable ejectile; long-lived states decay unperturbed while shorter-lived states decay in the vicinity of the parent. This alteration is also dependent on the final *Z* compositions of the LCPs, ejection energy from the de-exciting parent, decay orientation, and decay energy of the ejectile. This class of dynamical interactions is known as resonant state modification.

Modification for two-body decays is quantified by the relative energy of decay of the state with respect to the breakup orientation angle, β, defined as the angle between the center-of-mass velocity vector of the children particles in the remnant frame and the relative velocity vector of the children particles (Fig. 1). Previous work investigating resonant state modification demonstrated that it was reproducible through simulation [2], although not beyond first order. It was hypothesized that the discrepancies present between simulation and experiment were consequent of influences from PLF* deformation, thermal fluctuations, and IMF*-PLF nuclear surface stabilization, but iterative incorporation of these failed to mitigate the differences [2].

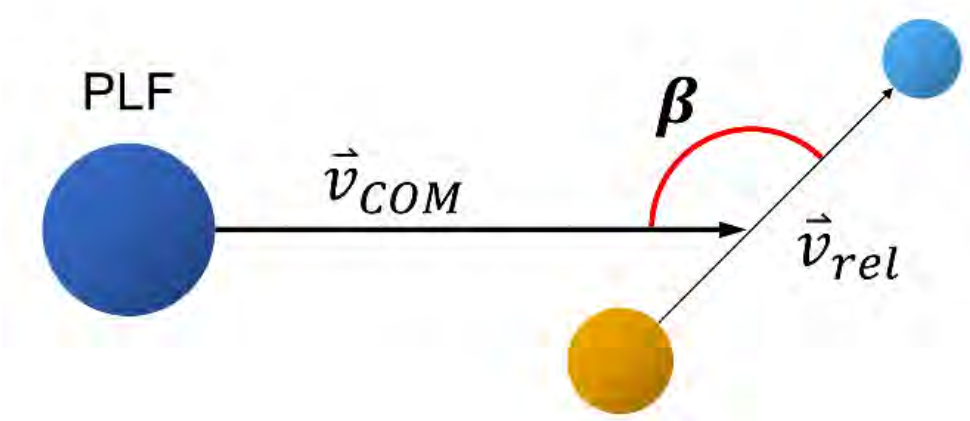

Fig. 1. Depiction of a two-body IMF* decay into two LCPs. For mass-asymmetric decays, β is defined as the angle between the COM velocity vector and the lighter child.

Experimental 35 MeV/nucleon ^{28}Si + ^{12}C collision data were taken with the position-sensitive Forward Array Using Silicon Technology (FAUST) at Texas A&M University; the excellent angular information provided by the array has permitted a more in-depth study of resonant state modification. The analysis method used is detailed in [3] but can be summarized as follows: events are selected based on if desired particles are present and those selected are used in the calculation of relative energy distributions of the children particles gated on regions of β. The means of these distributions are then isolated by uncorrelated background subtraction (mixed event analysis) and Gaussian peak fitting (Fig. 2).

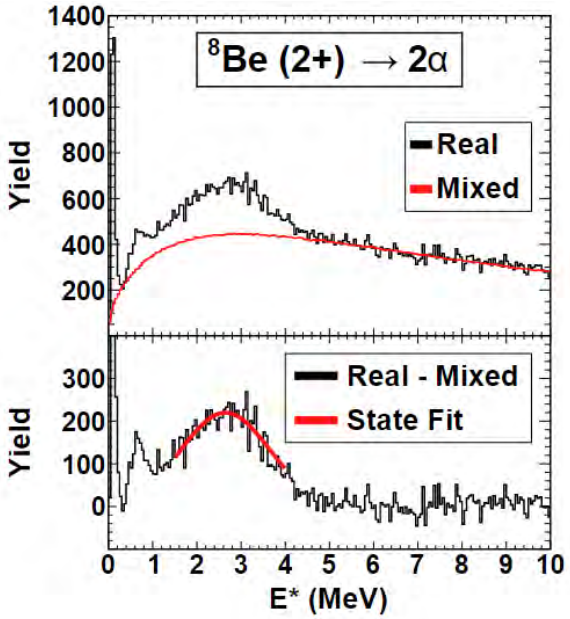

Fig. 2. Method for determining the relative energy mean value, performed here for ^{8}Be (2+) for 20° ≤ β < 25° [3]. (Top) Real (black) and mixed (red) event distributions in MeV. (Bottom) Real - mixed distribution overlaid with Gaussian fit of ^{8}Be (2+) peak (red).

To holistically investigate the phenomenon, a novel C++/ROOT Coulomb trajectory model is being developed to better understand the contribution and interplay of all relevant factors. Like its predecessors, the model simulates nuclei present in an event, performs the IMF* decay, then propagates all particles as legislated by the many-body Coulomb interaction. Properties of the simulation are sampled from corresponding distributions; simulations sample emission velocity from an experimental distribution of a stable isotope of the IMF*, breakup orientation from a sine distribution (assumed to be isotropic), decay time as exponential with parameter $\tau = 1/\Gamma(E)$, and decay energy in accordance with a one-level *R*-matrix description of the resonant state [4]. It is important to note that the decay time is not described by a standard singularly parameterized exponential ((i.e., $P(t) \propto \exp(t \cdot \tau_{literature}^{-1})$);i.e., rather, it is parameterized on an event-by-event basis using the width dependent on the sampled energy, $1/\Gamma(E)$ (Fig. 3).

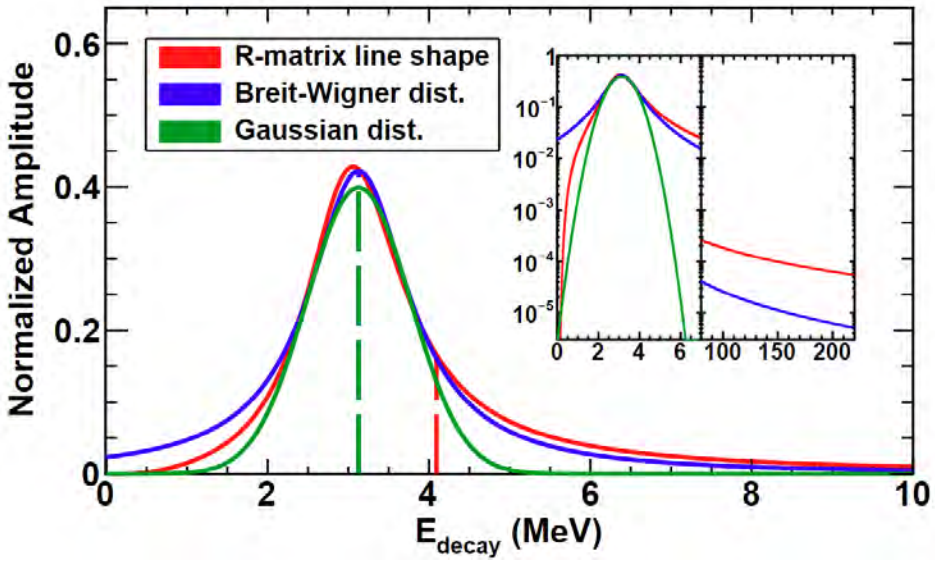

Fig. 3. *R*-matrix line shape for ^{8}Be (2^{+}) → α + α from which the decay energy is sampled compared to a one-level Breit-Wigner and Gaussian description. The inset depicts the low- and high-energy tails of the distributions and how they compare. Decay energy samples are used to parameterize unique exponential curves from which lifetimes of events are sampled.

Preliminary results from the model for ^{8}Be (2^{+}) are promising; further than simply replicating the experimentally observed trend of increasing relative energy with increasingly transverse breakup, the agreement between model and simulation within standard error is comprehensive across β (Fig. 4). In addition to changing various sampling distributions to investigate dependence, the starting position configuration of the remnant and unstable ejectile and that of the children particles were also varied. Initial simulations probing position dependence began with surface-surface configurations in which the nuclei, modeled as point particles, were separated by a distance $d = r_1 + r_2$ where each r is one nuclear radius (calculated as $r = r_0 A^{1/3}$ where $r_0 = 1.25$ *fm*). Introducing additional offsets acted to move the particles away from each other. Regarding ^{8}Be (2^{+}), the inclusion of offsets for both the ejection and breakup configurations appeared to improve experiment and simulation agreement (Fig. 4).

While these results are promising, ^{8}Be (2^{+}) is both mass- and charge-symmetric and decomposes into children particles that have a high detection efficiency in FAUST. To further characterize resonant state modification, investigating behavior of mass- and charge-asymmetric resonant states and states that decay into harder-to-detect products is necessary. An ideal candidate for such investigation is the ^{5}Li (3/2-) → $p + \alpha$ channel; this system, aside from being a resonant state modification candidate, satisfies *both* requirements by being both mass- and charge-asymmetric and by decaying into alphas and protons, the latter being harder to detect in FAUST.

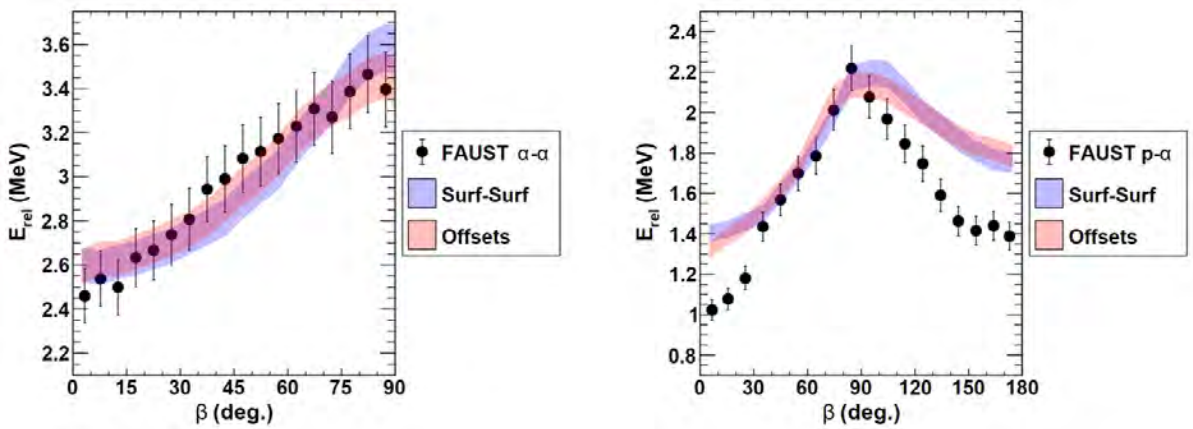

Fig. 4. Relative energy of decay versus breakup angle β for ^{8}Be (left) and ^{5}Li (right); experimental and simulated data use a remnant of Z = 10 and 8 ≤ Z ≤ 11, respectively. Touching spheres configuration is given as the blue curve and position offsets of 4 fm and 2 fm for ejectile-remnant and children, respectively, is given as the red curve. The inclusion of offsets has a non-negligible impact on the results.

Preliminary results from the model for ^{5}Li (3/2^{-}) are also promising, but they do expose shortcomings with the current formulation of the model. As with ^{8}Be (2^{+}), simulations reproduce the experimentally observed relationship between the relative energy and breakup orientation; however, orientations nearer parallel emissions systematically over predict the mean relative energy (Fig. 4). This effect is more pronounced for breakups near 180°, in which the proton emitted in the decay is more forward in the center of mass, versus near 0°, in which it is more backward; it was first believed that this was due to protons in the former orientation having a higher lab frame energy on average than protons in other orientations resulting in comparably less detection efficiency with the filter, but it was later surmised that this effect alone would act to *decrease* the mean relative energy. Subsequent hypotheses focus instead on "double filtering"; converting to the lab frame after simulating in the system center of mass relies on experimental data which implicitly incorporates geometric and particle acceptance. Regarding changes to initial position configurations, the inclusion of offsets in a similar fashion to ^{8}Be (2^{+}) had an effect of similar magnitude, although the change was neither wholly favorable or unfavorable.

In the interest of comparing the results for this work with those of previous, simulations using various sampling methods for the emission and breakup energies of ^{8}Be (2^{+}) were performed to determine where the largest discrepancies arise; this information is consolidated in Fig. 5. It can be seen that simple changes in the sampling methods have significant impacts on the simulated relative energy versus β distributions.

Future work investigating resonant state modification intends to continue exploring the "double-filtering" effect associated with ^{5}Li (3/2-) and to develop handling methods. Additionally, as used to justify the study of ^{5}Li, the continued exploration of resonant candidates with varying mass- and charge-asymmetries and intrinsic lifetimes is needed to fully characterize RSM. Current states of interest beyond what is shown here include ^{7}Li (1+) → t + α (Γ = 0.093 MeV) and ^{7}Be (7/2-) → h + α (Γ = 0.175 MeV) which aid specifically in the exploration of longer-lived states and sensitivities to modification. Although not shown, results for these are also very good and indicate that the bulk dynamical behavior for these systems is captured by the model.

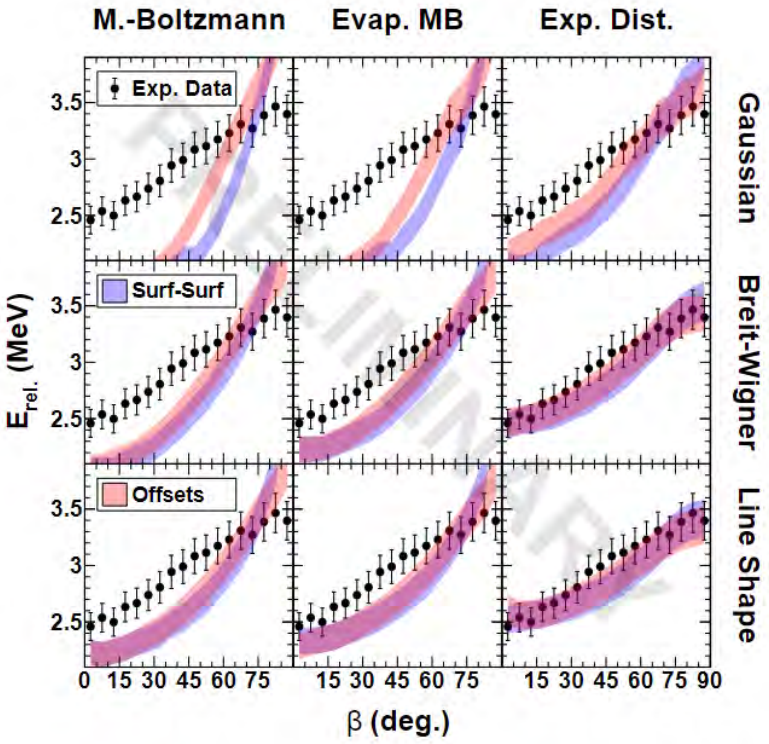

Fig. 5. Results for ^{8}Be (2+) simulations based on the sampling method for emission and decay energies. Emission energies are organized based on column and decay energies based on row. As can be seen, both the emission and decay energy distributions have a discernible effect on the accuracy of the simulation in comparison to experiment.

[1] R. Ghetti, *et. al.*, Nucl. Phys. **A765**, 307 (2006).

[2] A.B. McIntosh *et. al.*, Phys. Rev. Lett., **99**, 132701 (2007).

[3] A. Hannaman, *Progress in Research*, Cyclotron Institute, Texas A&M University (2021-2022) p. II-8.

[4] A.M. Lane and R.G. Thomas, Rev. Mod. Phys. **30**, 257 (1958).

Measuring transfer reaction particle correlations with FAUST to improve stellar models

T. Hankins, P. Adsley, A.B. McIntosh, A. Hannaman, B.M. Harvey, and S.J. Yennello

The $^{12}C(\alpha, \gamma)^{16}O$ reaction in stellar nucleosynthesis is considered to be the most significant aside from the triple-α process as it directly influences the $^{12}C/^{16}O$ elemental ratio and the properties of stars beyond helium burning [1]. Despite this importance, the relative uncertainty associated with the reaction cross section at stellar energies is large as direct measurements are Coulomb-inhibited and two dominant multipolar contributions exist rather than one. Estimating the cross section is only possible through extrapolation of models which are parameterized and constrained by resonance properties of ^{16}O and thus a comprehensive understanding of $^{16}O^*$ as a function of energy is needed to perform accurate extrapolations.

One of the most significant uncertainties associated with the extrapolation is the measurement of relative contribution between the E1 and E2 transitions at energies approaching the stellar regime. As with the production of ^{16}O, absolute measurements result in contributions from all available transition multipolarities; this alone does not aid in the constraint of models as independent contributions must be known. Conventional measurements rely on extraction of contributions via angular correlations, i.e., taking advantage of the angular distribution of emitted radiations of given multipolarity to preferentially isolate yield. An example of this is shown in Fig. 1; as shown, the isolation of E1 contribution from superposed E1-E2 can be performed by measuring the amplitude of radiations emitted at 90° then using this information in conjunction with an extended angular fit to extract E2 contributions. However, this E2 measurement is a single indirect extrapolation. With the proper detector apparatus and reaction, a more comprehensive determination of the E2 magnitude can be made.

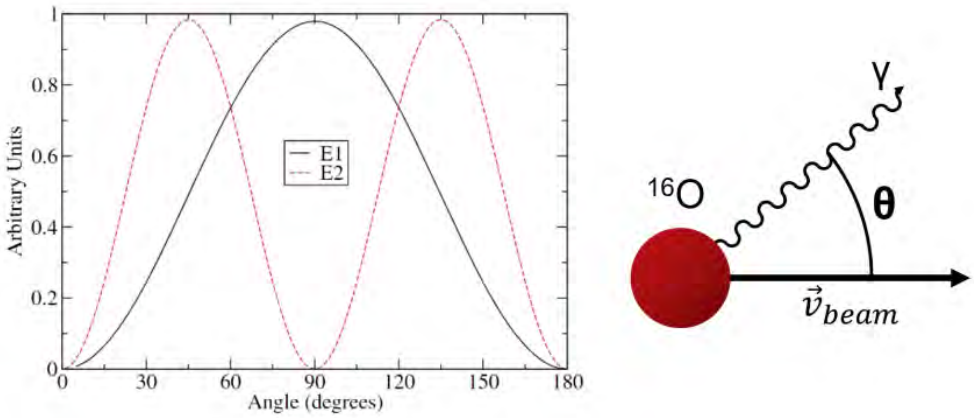

Fig. 1. (Left) Comparison of E1 and E2 angular distributions in the system center of mass for transitions of $^{12}C(\alpha, \gamma)^{16}O$ [2]. (Right) A simplified figure showing the described angle for this process.

Due to the difficulty associated with direct reaction measurements, indirect methods are often used in the study of astrophysical reactions to supplement the extraction of residual nucleus or reaction properties; in the case of $^{12}C(\alpha, \gamma)^{16}O$, α-transfer reactions are most frequently used. The reaction relevant in this context is $^{7}Li(^{12}C, t)^{16}O^*(\alpha)^{12}C$ with coincidence measurements made between the triton, α, and

^{12}C. A triple-coincidence measurement permits the measurement of emitted α particles with respect to the reaction plane, thus allowing the type of measurement discussed in the previous paragraph.

The Forward Array Using Silicon Technology (FAUST) at TAMU is a position-sensitive charged particle array that covers most of 1.6-45.5° of forward angles via 68 ΔE-E telescopes (Fig. 2). Capable of providing sub-mm continuous position information (depending on particle ID and energy) in addition to ~1-2% energy resolution, this array is currently being investigated for studying particle correlations of an α-transfer reaction to obtain information about the properties of ^{16}O relevant for (α, γ). As a large-area silicon array, FAUST is capable of performing high-count measurements with the intent of further clarifying E1-E2 contributions as a function of E* for energies relevant to the (α, γ) process via an indirect probe.

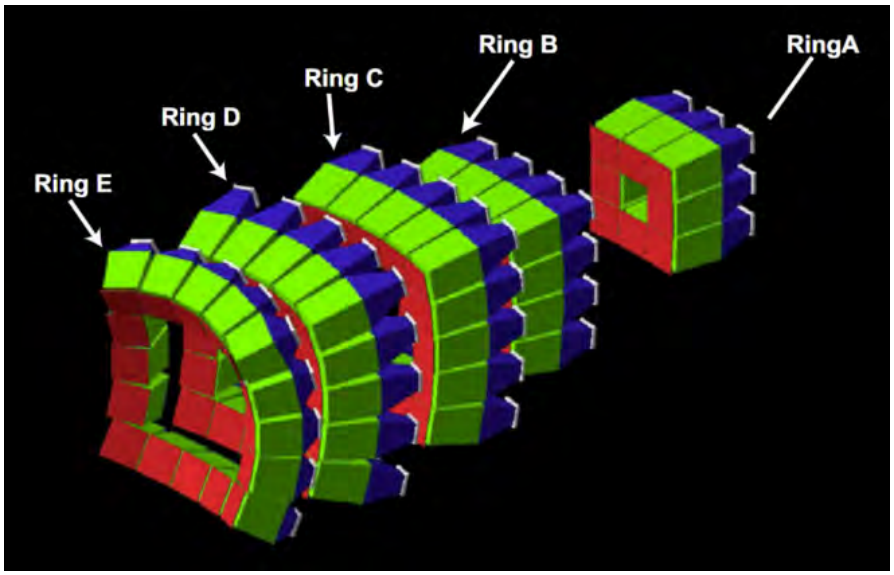

Fig. 2. Isometric projection render of FAUST [3]. The target position is located upstream such that the detector faces are oriented perpendicular.

The current plan involves augmenting FAUST with an upstream position-sensitive annular S3 silicon detector [4] for capturing particle yield behind the target position and performing a measurement of ^{7}Li(^{12}C, t)^{16}O*(α)^{12}C with incident energy of 15 MeV/nucleon. Using FAUST for this measurement provides access to the φ degree of freedom for angular correlations which is typically not possible due to detector constraints. Several simulations have been performed judging the viability of this measurement, primarily focusing on the imposed particle multiplicity and energy-momentum discretization methods that are employed in place of universal particle identification. As an illustration, Fig. 3 demonstrates that reactions of (^{6}Li, d) and (^{7}Li, t) can be separated using these requirements (given proper placement of the S3) despite not possessing comprehensive PID; the left figure depicts the centroids and 3σ widths of the Gaussian momentum distributions for a given S3 distance and that comprehensive separation is attainable with proper placement while the right reconsolidates that information in the form of peak separation (absolute difference between centroids) in addition to solid angle subtended by the S3 at a given distance. Regarding preliminary simulations, considerations of variable beamspot location, alternate reaction

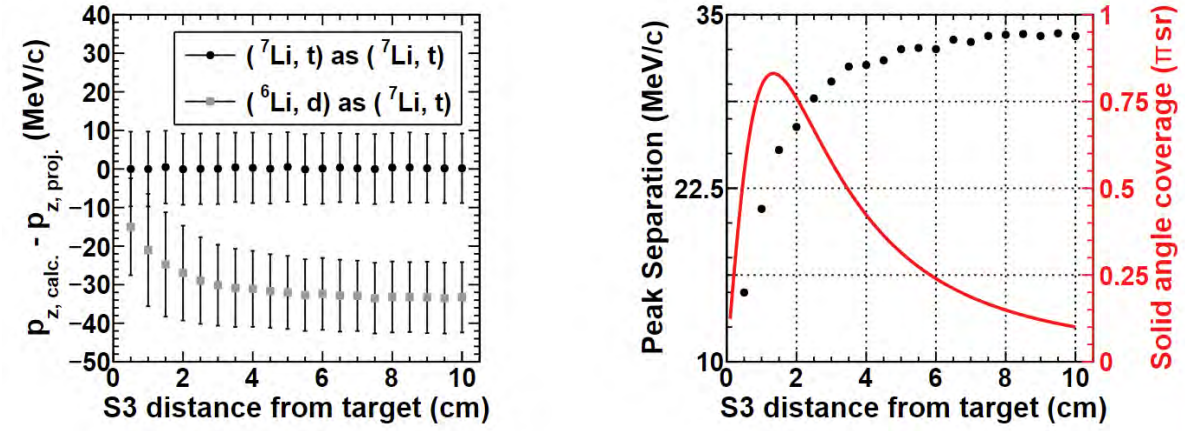

Fig. 3. (Left) Difference between the calculated beam axis momentum for exit channel particles and the initial projectile momentum between phase-space simulated (^{6}Li, d) and (^{7}Li, t) reactions analyzed as (^{7}Li, t) versus S3 distance from the target; error bars are 3σ of the corresponding distribution. (Right) Comparison between solid angle coverage (red) and separation of the distribution peaks (black) as a function of the S3 distance.

channels, and yield/coincidence estimates have also been performed; for the former two, the analysis method proposed satisfied all necessary requirements, and for the latter, an estimated 10% triple-coincidence yield was predicted (Fig. 4). Additional auxiliary detectors upstream could be used to improve efficiency.

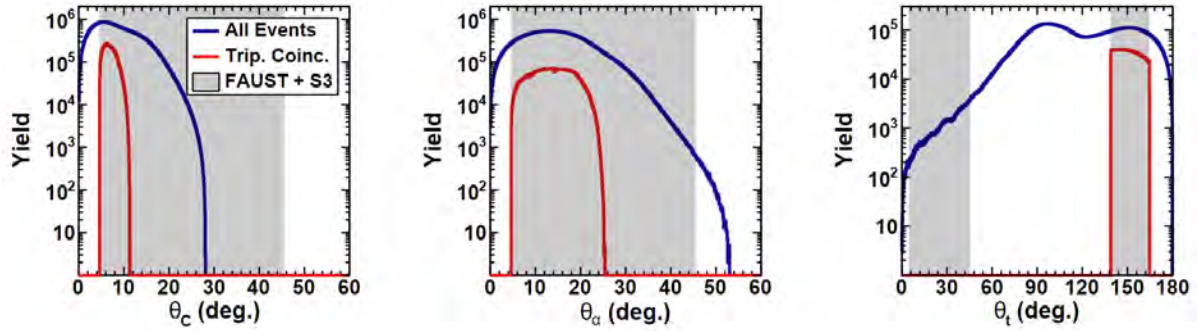

Fig. 4. Yield plots for all (blue) and triple coincidence (red) events for the three particles to be detected in experiment as a function of incident laboratory θ. The triton angular distribution was generated from a preliminary distorted-wave Born approximation (DWBA) calculation [5] for the reaction and energy of interest.

Given success with preliminary simulations, a series of test runs in various running configurations and a full-length experiment in the finalized configuration are being planned for the next calendar year of beam.

[1] M. Fey, *et. al.* Nucl. Phys. **A718**, 131 (2003).
[2] R.J. deBoer *et. al.,* Rev. Mod. Phys. **89**, 3 (2017).
[3] P. Cammarata, *et. al.* Nucl. Instrum. Methods Phys. Rev. **A792**, 61 (2015).
[4] Micron Semiconductor Ltd. S3. http://www.micronsemiconductor.co.uk/product/s3/, (2023).
[5] I.J. Thompson, Comput. Phys. Rep. C **7**, 167 (1988), http://www.fresco.org.uk.

Progress in photon strength function of ^{58}Fe using Oslo and shape methods

A. Abbott,[1,2] M. Sorensen,[1,2] A. Alvarez,[2,3] A. B. McIntosh,[2] K. Hagel,[2] J. Gauthier[2]
A. Richard,[4] and S.J. Yennello[1,2,3]
[1]*Department of Chemistry, Texas A&M University, College Station, TX 77840*
[2]*Cyclotron Institute, Texas A&M University, College Station, TX 77840*
[3]*Department of Physics and Astronomy, Texas A&M University, College Station, TX 77840*
[4]*Lawrence Livermore National Laboratory, Livermore, CA 94550*

In August 2021, an experiment was performed using the Detector Array for Photons, Protons and Exotic Residues (DAPPER) to measure the photon strength function (PSF) of ^{58}Fe. An important quantity in neutron capture cross-section calculations for s/r-process nucleosynthesis, the PSF describes the energy-dependent strength of gamma-ray emission from nuclei. The ^{58}Fe nucleus was excited using an indirect method of the (d,pγ) transfer reaction in inverse kinematics. The resulting coincidence between protons and gamma-rays is used to extract the PSF using the well-documented Oslo method [1] and an offshoot of the original method called the Shape method [2] which reduces the dependence on external data. The current progress in extracting the PSF using these methods will be discussed.

DAPPER utilizes an S3 annular silicon and 128 BaF_2 scintillators to detect the coincidence between charged particles and gamma-rays respectively. The charged particle of interest in this experiment is the proton from the (d,p) which is utilized to calculate the initial excited state of the ^{58}Fe nucleus. Fig. 1 shows the raw coincidence data from the August experiment. From this point, a simulation of the array is required to generate a response function that describes how the experimental setup treats the true gamma-ray energies. This is done by simulating many initial gamma-rays in GEANT4 and recording the intensities of the photopeak, annihilation and escape peaks where applicable.

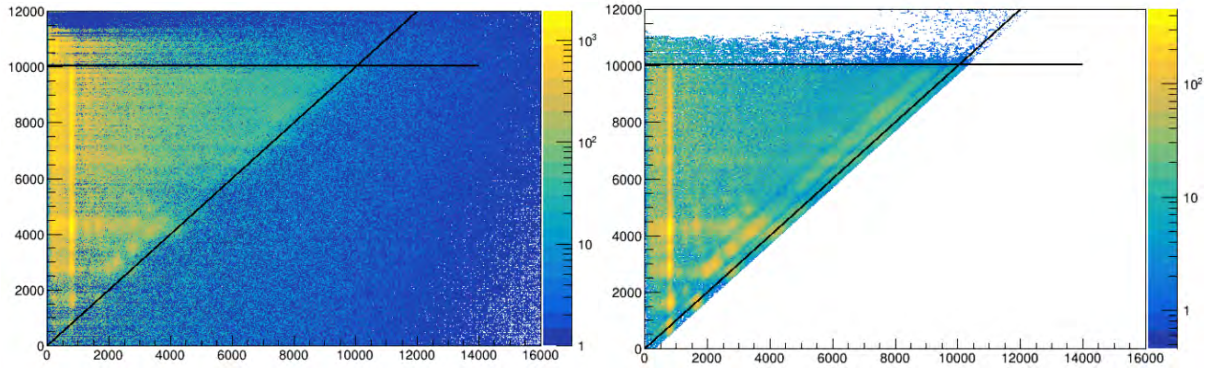

Fig. 1. Raw coincidence data with calculated excitation energy and the total gamma-ray energy. Panel A shows the ungated data while panel B shows the data gated on the total gamma-ray energy peak. The horizontal line indicates the neutron separation energy of ^{58}Fe and the diagonal is the y=x line.

To model the Compton background, these peaks of interest are removed from the spectra and the characteristic shape is retained. These values are then interpolated for all gamma energies. The resulting response matrix is folded into the raw matrix using an iterative procedure [3]. This unfolded matrix is then used to pull out the primary gamma-rays from each state. It is assumed that the primary gamma-rays for the decay from a specific state can be obtained by subtracting a weighted sum of all lower lying states gamma spectra. This is done for each excitation bin and the resulting primary matrices are shown in Fig. 2.

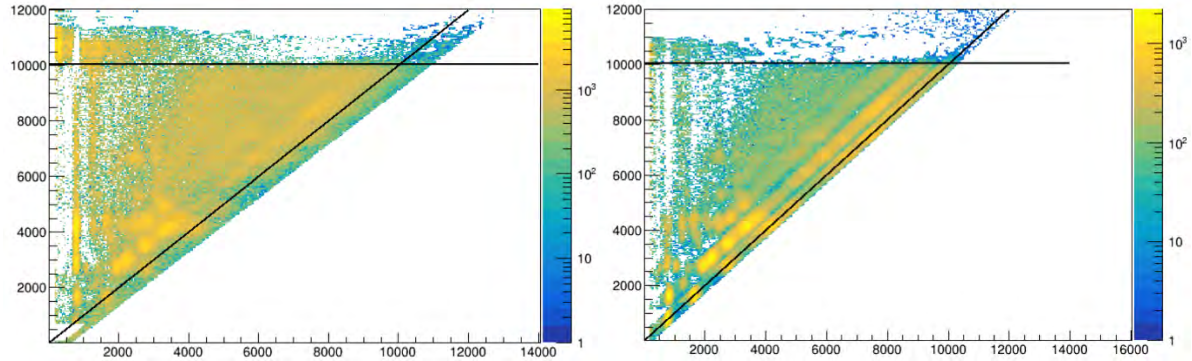

Fig. 2. Primary matrices of data using current GEANT4 simulated DAPPER response. Clear states and transitions can be observed.

From this point, the Oslo method and Shape method begin to differ. To proceed with the original Oslo method, an absolute normalization is performed using external data like gamma partial widths, and s-wave spacing at the neutron separation energy to constrain the infinite possible solutions to Equation 1, which relates the primary matrix ($P(E_x, E_\gamma)$) to the nuclear level density (NLD) at the final state ($\rho(E_x - E_\gamma)$) and the transmission coefficient ($T(E_\gamma)$). A simultaneous extraction is performed and the NLD and PSF are determined. The preliminary results are shown in Fig. 3.

$$P(E_x, E_\gamma) \propto \rho(E_x - E_\gamma) T(E_\gamma) \tag{1}$$

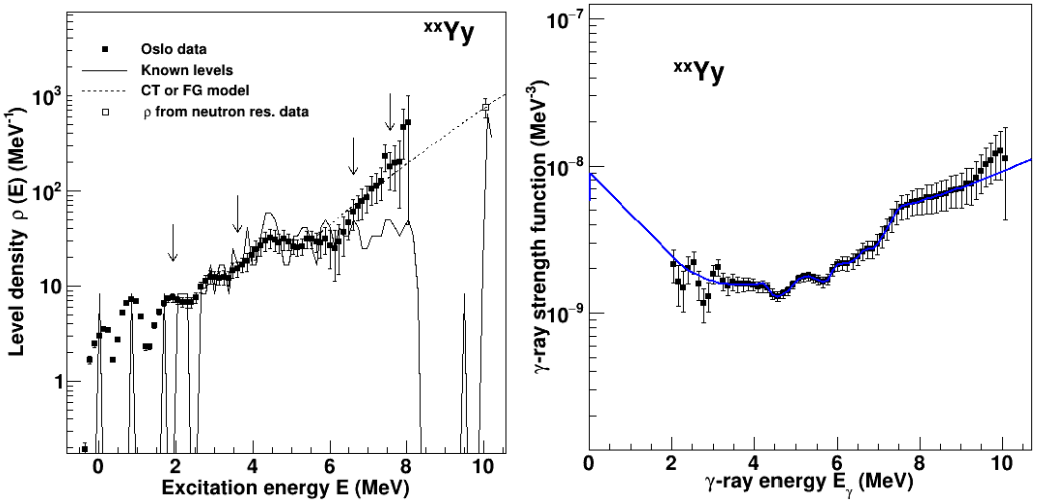

Fig. 3. Extracted NLD and PSF from the Oslo method.

The Shape method utilizes the entries (N) in strong gamma transitions to final states (D) to obtain a ratio of the strength which is estimated from Eq. 2. A sewing method is then used to obtain the characteristic shape of the PSF which is overlayed with the Oslo method PSF in Fig. 4. See reference [2] for a detailed description of the sewing procedure.

$$f(E_\gamma) \propto \frac{N_D}{E_{\gamma D}^3} \tag{2}$$

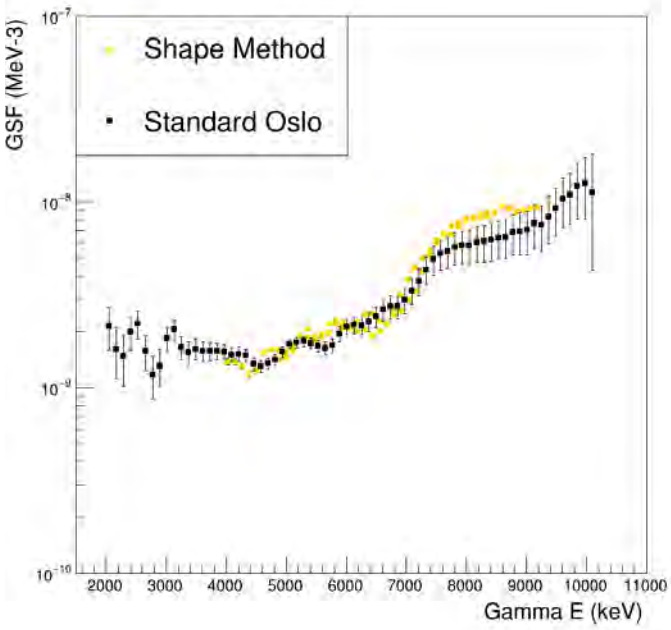

Fig. 4. Comparison of scaled Shape method PSF to Oslo method PSF. There is self-consistency in the slopes indicating proper use of methods however, the simulated DAPPER response is still in progress.

The self-consistency between the two methods validates the use of the Shape method to acquire the characteristic features of the PSF without requiring normalization to external data. Due to the current state of the GEANT4 simulation of DAPPER, the response matrix is not well representing the experimental data and so the extracted PSFs here are preliminary. Current work is ongoing to improve the simulated response which will reproduce a more accurate primary matrix.

[1] A. Schiller *et al.,* Nucl. Instrum. Methods Phys. Res. **A447**, 498 (2000).
[2] M. Wiedeking *et al*., Phys. Rev. C **104**, 014311 (2021).
[3] M. Guttormsen *et al*., Nucl. Instrum. Methods Phys. Res. **A374**, 371 (1996).

The study of alpha conjugate reactions in FAUST

B.M. Harvey, A. Hannaman, K. Hagel, A.B. McIntosh, and S.J. Yennello

Theoretical research from the past 60 years has provided extensive backing behind the potential of exotic nuclear configurations like toroidal [1], linear chains, and bubble under high angular momentum and energy conditions. The existence (or nonexistence) of these kinds of exotic nuclear structure would push our understanding of the limits of nuclear stability and our understanding of the theory that predicts them. Further, investigations of decay pathways of alpha-conjugate nuclear states, especially near threshold states have astrophysical implications [2].

To study these topics, a series of experiments were conducted at the Texas A&M Cyclotron Institute with the Forward Array Using Silicon Technology (FAUST). FAUST is a multi-detector array comprised of 68 Si and CsI telescopes. Measuring the energy deposited in the Si and CsI detectors gives particle energy and identification information. The Si detectors are Dual Axis Duo Lateral detectors, which have resistive surfaces granting them position sensitivity, and signals are read off of both the fronts and the backs, allowing for the position sensitivity to extend in both directions. The angular resolution of alpha particles is ~1-2 degrees.

The data collected for the studies of alpha-conjugate nuclei and their breakup are summarized in Table I. All experiments were <alpha-conjugate-beam> + natural carbon at 35 MeV/nucleon. The calibrations (including particle identification) are still underway, but a preliminary event count with at least one alpha particle identified is listed.

Table I. Alpha-conjugate reactions studied at the indicated dates and statistics acquired.

System	Date	# Events w/ alpha
^{16}O + C @ 35 MeV/u	Oct 2022	82 M
^{20}Ne + C @ 35 MeV/u	Jun 2022	276 M
^{24}Mg + C @ 35 MeV/u	Aug 2022	126 M
^{28}Si + C @ 35 MeV/u	Jun 2021	275 M
^{32}S + C @ 35 MeV/u	Aug 2022	266 M
^{36}Ar + C @ 35 MeV/u	Oct 2022	721 M

While most of the data is still being finely calibrated, the preliminary calibrations show promise for high resolution measurements of multiparticle excitation energy reconstruction with alpha particle reconstructions. Fig. 1 shows the quality of the particle identification achievable across FAUST, which also highlights the energy resolution that can be achieved with FAUST. One can see isotopic resolution through Z=14.

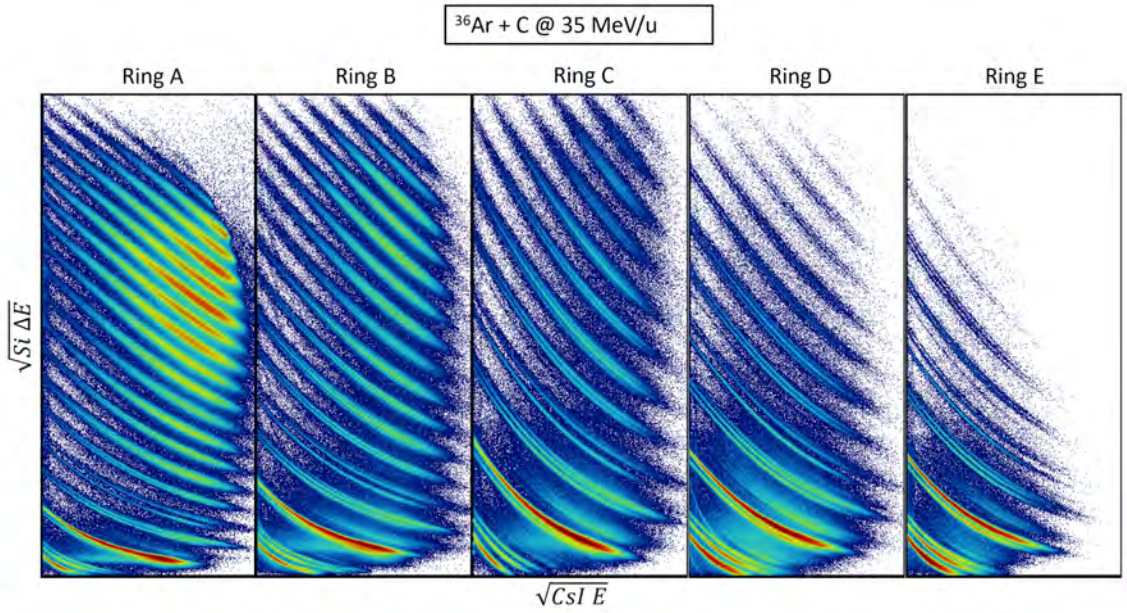

Fig. 1. ΔE vs E maps indicating particle id for the various FAUST rings

Many-particle measurements can be used to reconstruct excitation energy by assuming the particles are from the same source. Fig.2 shows 2 and 3 alpha E* distributions which give high resolution measurements of many carbon and beryllium states. The resolution of FAUST allows for a measured 55 keV FWHM of the Be-8 ground state, even with crude first order calibrations. The shown resolution is an upper limit of the resolutions achievable by FAUST.

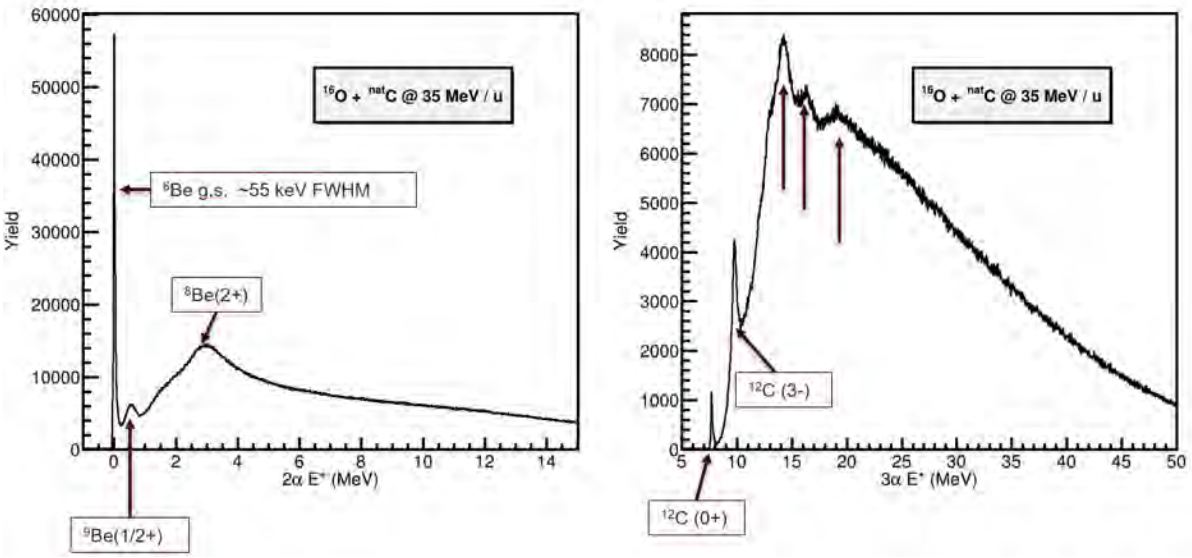

Fig. 2. Two-alpha (left) and 3α excitation energy distributions showing the various observed states.

[1] X.G. Cao, E.J. Kim, K. Schmidt, K. Hagel, M. Barbui, J. Gauthier, S. Wuenschel, G. Giuliani, M.R.D. Rodriguez, S. Kowalski, H. Zheng, M. Huang, A. Bonasera, R. Wada, N. Blando, G.Q. Zhang, C.Y. Wong, A. Staszczak, Z.X. Ren, Y.K. Wang, S.Q. Zhang, J. Meng, and J.B. Natowitz, Phys. Rev. C **99**, 014606 (2019). https://doi.org/10.1103/PhysRevC.99.014606

[2] https://www.sciencedirect.com/science/article/pii/S2095927323002852?via%3Dihub#f0015(accessed 5.12.23).

Dissolution of a ^{224}Ra mock sample for future nuclear forensic analyses of a ^{226}Ra pigment sample

J.R. Garcia,[1,2] E.M. Bond,[2] and C.M. Folden III[1,2]
[1]*Department of Chemistry*, *Texas A&M University, College Station Texas 77840*
[2]*Nuclear and Radiochemistry (C-NR) group*, *Los Alamos National Laboratory, Los Alamos NM 87544*

Radium pigments and paints were popularized in the early 1900s due to their attractive, self-luminescent properties with applications in the watch dial industry, the military, and households [1-3]. Many biological and environmental hazards have been identified with the use of these products [1,3,4]. Consequently, the IAEA has identified ^{226}Ra, the major radioactive component of radium pigments and paints, as a potential threat in nuclear terrorism events in the form of radiological dispersive devices [4,5]. To combat such events, the field of nuclear forensics was created as a method of determining source attribution of materials of unknown origins and intentions [5]. Many nuclear forensic techniques used to analyze nuclear materials are well documented in the literature [3]; however, literature pertaining to ^{226}Ra pigments and paints regarding nuclear forensics is nonexistent. This work aims to develop a methodology for the nuclear forensic analysis of ^{226}Ra pigment and paint samples. This report will detail necessary procedures for recreating the radium pigment sample in addition to procedures for the dissolution of said sample. Preliminary results are reported here.

For this project, the main nuclear forensic signature will be derived from a radiochronometric analysis of a historical ^{226}Ra pigment sample. The chosen radiochronometric parent/daughter pairs are ^{210}Pb/^{226}Ra and ^{210}Po/^{226}Ra due to the daughters' long half-lives (22 y and 138 d, respectively) and favorable decay characteristics (easily detected γ line and α particle, respectively). Although the historical ^{226}Ra pigment sample has already been received, the sample is very limited in quantity; thus, it is necessary to attempt to recreate the sample based on a literature description of these samples in the early 1900s for initial tests. The predicted composition of the sample is ~ 99% ZnS and ~1% $^{226}RaX_2$ (X=Cl or Br) [1]. To replicate this mixture, ^{224}Ra/^{133}Ba (Ba is the homolog of Ra chemically) will be substituted for ^{226}Ra as they are more available commercially. The procedure for creating the mock radium pigment sample is as follows: First, ^{224}Ra is eluted via a ^{228}Th generator. ^{228}Th is loaded in conc. HCl solution to a DGA-branched resin column with 1 mL of resin. The column is then rinsed with 5 mL of conc. HCl. The eluate then contains the ^{224}Ra. The eluate is evaporated to dryness and then reconstituted with 2 mL of Millipore Omnitrace 18.2 MΩ H_2O. this solution is evaporated to dryness once more. Next, it is reconstituted with 1 mL of Millipore 18.2 MΩ Omnitrace H_2O. To this solution, ~40 mg of ZnS is added and the slurry is evaporated to leave a radioactive material containing ZnS powdered sample. The ^{224}Ra in this sample has a half-life of 3.66 d, so the sample will usually last a maximum of 30 days.

Before any radiochronometric analysis can be performed, it is necessary to convert the sample into a form that can easily be manipulated via dissolution. Surprisingly, dissolving this sample was not straightforward. Due to very dissimilar chemical properties between ZnS and RaX_2 (in addition to all its daughters), mineral acids which are commonly used to dissolve many radiological samples are ineffective in this case [6,7]. Various chelators such as EDTA have been explored as well with no success. In recent literature, phosphonium salts have tested for their effectiveness on FeS scales in oil fields with promising results [8]. The dissolution of FeS scales using a mixture of tetrakis(hydroxymethyl)phosphonium sulfate

(THPS) and ammonium chloride (NH_4Cl) at temperatures of approximately 85 °C resulted in ≥90% efficiency [6]. In hopes of achieving similar results, these methods were tested on the mock ^{224}Ra pigment sample in addition to a mock ^{133}Ba pigment sample. A 1 M solution of tetrakis(hydroxymethyl)phosphonium chloride (THPC) was mixed with NH_4Cl in a ratio of 10:1 by mass followed by the mock pigment sample (0.08% by mass of the total solution) and stirred at ~85 °C for 2-4 h. Overall, the dissolution efficiencies for $^{133}BaCl_2$, $^{224}RaCl_2$, and $^{212}PbCl_2$ (^{212}Pb is a daughter in ^{224}Ra's decay chain) were 103 ± 8%, 100 ± 3%, and 103 ± 3% respectively. As for ZnS, the solid qualitatively appears to dissolve completely, but the dissolution efficiency has yet to be measured. This will involve tracing ZnS with ^{65}Zn which will be part of future studies. Overall, this mixture of THPC and NH_4Cl will be used for future studies with the mock pigment sample.

Once the sample could be dissolved, it was necessary to determine a separation pathway of elements within the pigment to appropriately isolate the radiochronometers of interest ($^{210}Pb/^{226}Ra$ and $^{210}Po/^{226}Ra$). Generally, column chromatography is the most commonly used technique for separation of elements and there is significant literature on various elements and their behaviors with various resins and acid systems [9, 10]. However, THPC and NH_4Cl are less common reagents to work with and literature is very sparse [11] so converting the THPC/NH_4Cl solution to a more commonly studied medium (such as HCl or HNO_3) is not plausible. Additional research is necessary to study the behavior of the elements in this system (Ra, Ba, Pb, Po, Bi, and Zn) in solutions of THPC and NH_4Cl on various resins to best separate them. Weight distribution ratios, D_w, are used to quantify an element's affinity to a particular resin under certain conditions (such as acid concentration). These values can be experimentally measured using batch studies given a specific acid media, resin, and element of interest. In Fig. 1, the D_w values for ^{133}Ba were measured in solutions of THPC on Chelex-100 ion exchange resin. The results of this

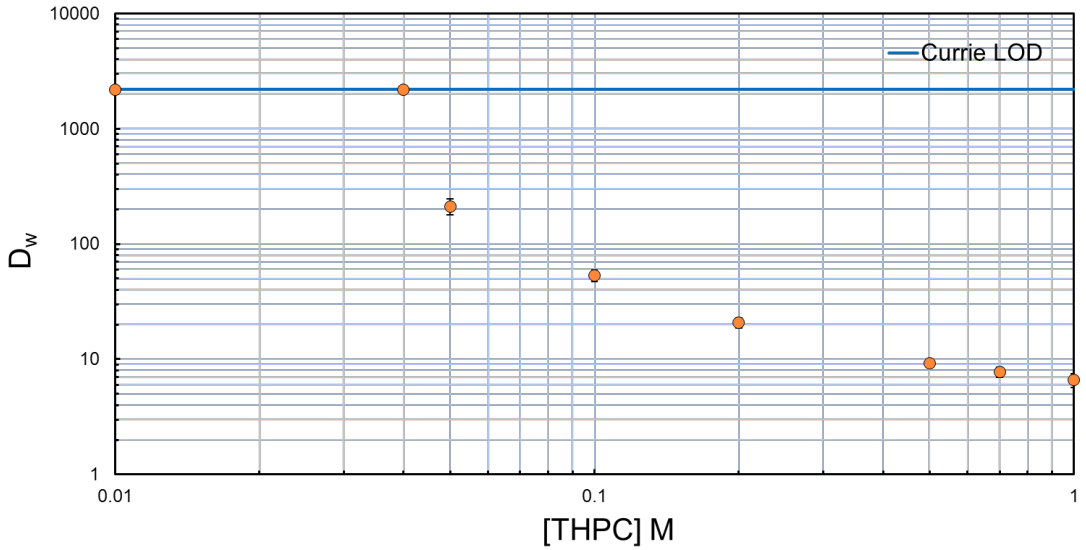

Fig. 1. Measured D_w values for ^{133}Ba on Chelex-100 in solutions of THPC. High D_w values indicate a strong affinity to the resin while low values indicate low uptake of ^{133}Ba. The Currie LOD illustrates the limits of detection. [12].

experiment showed that Ba does not have a strong affinity for Chelex-100 at higher concentrations of THPC.

Currently, the information on an effective pathway for separation of elements of interest is incomplete. Future work will be focused around performing more batch studies including ^{65}Zn in solutions of THPC and NH_4Cl with various resins because Zn is 99% of the sample matrix. Its elimination is important so that it does not affect the chemistry of elements in much lesser quantities (such as Ra, Pb, Po, and Bi). If further batch studies show no promise in separating these elements given the current THPC/NH_4Cl solution they are dissolved in, it may be necessary to find a way to digest the THPC and convert the solution to more commonly studied media.

In all, this work aims to perform a nuclear forensic analysis of a historical ^{226}Ra pigment sample. Presently, this work has discussed efforts made toward performing a radiochronometric analysis including the dissolution and separation of a mock, ^{224}Ra pigment sample. After successfully producing a procedure for making a mock pigment sample, the dissolution of the sample has shown ~100% dissolution efficiency. Investigation of the separation capabilities of various resins and THPC/NH_4Cl solutions are still ongoing and a full radiochronometric analysis on the mock sample is to be accomplished in the near future. In conclusion, this work aims to aid in overall national security by pioneering the field of ^{226}Ra nuclear forensics.

[1] D. I. Harvie, Endeav **23**, 100 (1999). doi:10.1016/S0160-9327(99)01201-6

[2] H.A. Taylor, Sci. Am. **137**, 430 (1927).

[3] R.G.M. Crockett and G.K. Gillmore, Geol. Soc. Spec. Publ. 451, **49** (2018). doi:10.1144/sp451.4

[4] D.G. Kelly and T. Mumby, Health Phys. **117**, 278 (2019). doi:10.1097/hp.0000000000001099

[5] S. Friedrich, R. Stan, and Z. Lyudmila, AIP Conf. Proc. 1034, 3 (2008). doi:10.1063/1.2991254

[6] P. Butkalyuk, I. Butkalyuk, R. Kuznetsov, A. Kupriyanov, and R. Abdullov, Radiochemistry **61**, 12 (2019). doi:10.1134/S106636221901003X

[7] M. Salutsky and H. Kirby, *The radiochemistry of radium* (1964).

[8] A. Hussein and H. Mohamed, Int. J. Corros. Scale Inhib. **6**, 349 (2017). doi:10.17675/2305-6894-2017-6-3-9

[9] E.R. Bertelsen, J.A. Jackson, and J.C. Shafer, Solvent Extr. Ion Exch. **38**, 3 (2020). doi:10.1080/07366299.2020.1720958

[10] E.P. Horwitz, R. Chiarizia, M.L. Dietz, and H. Diamond, Analytica Chimica Acta **281**, 2 (1993). doi:10.1016/0003-2670(93)85194-O

[11] N. Mirzayev, A.P. Marinova, G.M. Marinov, K. Mammadov, V. Karandashev, A. Rakhimov, A. Baimukhanova, D.V. Karaivanov, and D.V. Filosofov, Solvent Extr. Ion Exch. **37**, 6 (2019). doi:10.1080/07366299.2019.1679458

[12] L.A. Currie, Anal. Chem. **40**, 3 (1968). doi:10.1021/ac60259a007

Measuring the survival of Rn compound nuclei in the fusion of Ti and Gd

J.A. Mildon,[1,2] A.S. Kirkland,[1,2] E.E. Tereshatov,[1] V. Zakusilova,[1] J.R. Garcia,[1,2] I.W. Haynes,[1,2] and C.M. Folden III[1,2]

[1]*Cyclotron Institute, Texas A&M University, College Station, Texas 77843*

[2]*Department of Chemistry, Texas A&M University, College Station, Texas 77843*

From 1981 to 2004, 11 new elements were synthesized: element 107 (bohrium) to element 116 (livermorium), and element 118 (oganesson). Since then, however, only one new SHE has been synthesized: element 117 (tennessine) in 2009, despite numerous attempts to do so. Attempts have been made to synthesize both elements 119 and 120 without success [1]. A lack of understanding of the factors that affect the survival of the compound nucleus is one of the reasons that previous attempts have been unsuccessful at producing elements heavier than 118 [1]. SHEs span a large range of quadrupole (β_2) deformations, with some SHEs, especially those away from the region of beta-stability, being predicted to have substantial deformations [2,3]. The consequence of a higher quadrupole deformation is an increase in the level density for the neutron decay mode, which increases the probability of the compound nucleus deexciting through neutron emission rather than fission. Deexcitation by fission, rather than neutron emission, results in a lower-than-expected cross section for fusion-fission reactions to form heavy spherical nuclei [4].

Previous work in the Heavy Elements Group focused on the effects of neutron binding energy on the survival probability of the compound nucleus, and the effects of deformation in the compound nucleus during fission (of otherwise near-spherical nuclei) [4-6]. The current work seeks to expand upon that previous analysis by examining how the highly deformed compound nucleus changes affects measured excitation functions. The long-term goal is to create an isotopic series by bombarding targets of Gd and Dy with ^{48}Ti, and to elucidate properties which can lead to successful synthesis of heavy compound nuclei. Recent research into production of elements 119 and 120 have focused heavily on the use of ^{50}Ti [7]. The current reactions being studied with ^{48}Ti projectiles provide an opportunity to learn more about the use of this projectile while being able to benefit from a much higher event rate. These reactions were chosen carefully, as they serve as both analogs for super-heavy element production, and the targets allow a variation in neutron number so that the effects of deformation can be observed. The more neutron deficient compound nuclei are more deformed. Further, these particular reactions are at the very limit of this type of experiment, as no systems exist beyond Ra whereby multiple compound nuclei of the same element can be viably produced with different neutron numbers by variation in the neutron number of the target in order to explore the effects of deformation on the compound nucleus.

In April 2022, an experiment was performed to measure the excitation function for the reactions of ^{48}Ti + Gd. These experiments were carried out using the K150 cyclotron at the Texas A&M University Cyclotron Institute. $^{48}Ti^{13+}$ with an energy of 6.6 MeV/u passed through a 15 μm Al window and a variable Al degrader, and a 2 μm Ti target backing. The targets were 446 μg/cm^2 ^{160}Gd and 334 μg/cm^2 ^{158}Gd, leading to compound nucleus excitation energies of 54.8-67.2 MeV for the ^{160}Gd target and 51.0-67.9 MeV for the ^{158}Gd target [8]. The products were separated using the AGGIE separator (Al Ghiorso's Gas-filled

Ion Equipment), which was set for magnetic rigidities of 1.62 T m and 1.61 T m (for ^{160}Gd and ^{158}Gd, respectively). The products were then focused to two double sided silicon detectors (DSSDs).

Preliminary results are shown in Figs. 1 and 2. The excitation functions appear to be surprisingly wide because the individual contributions have not been separated yet. We will also investigate the possibility of pxn exit channels, ^{48}Ti(^{158}Gd, pxn)$^{206-x}$At, which should be detectable as At isotopes with A< 204 have considerable alpha decay branches.

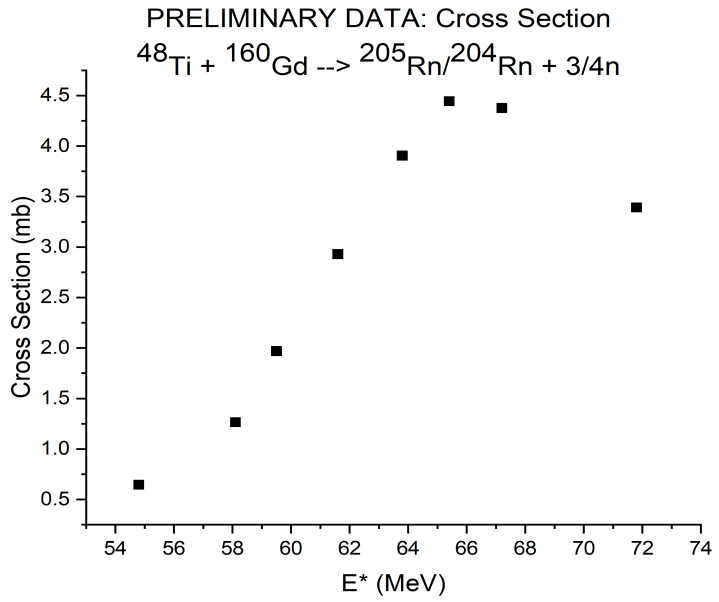

Fig. 1. Preliminary results on the ^{48}Ti + ^{160}Gd excitation function.

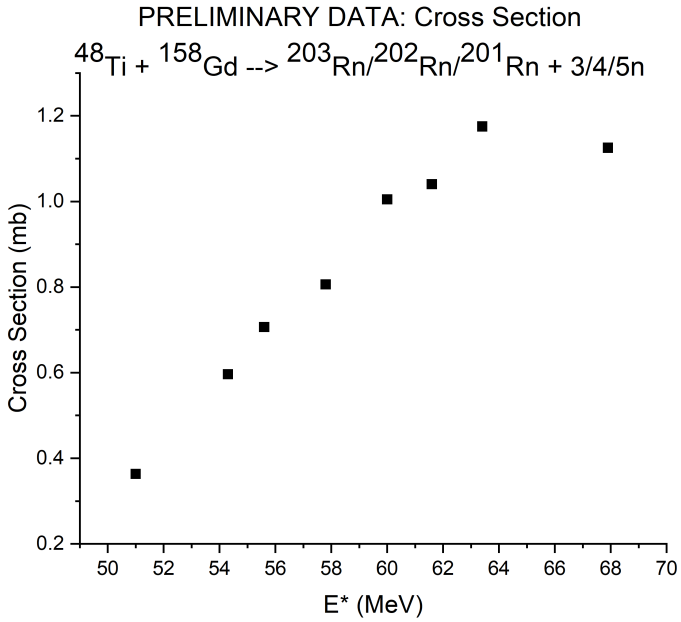

Fig. 2. Preliminary results on the ^{48}Ti + ^{158}Gd excitation function.

During an upcoming experiment, the excitation functions for the ^{160}Gd and ^{158}Gd targets will be finalized, in addition to completing the ^{157}Gd excitation function. Future work will consist of finishing the excitation functions for the Gd series and then performing a similar series of measurements for the reactions of ^{48}Ti with $^{164\text{-}160}$Dy. These data will then be compared to theoretical predictions to determine the effects of deformation on the survival of the compound nuclei of Rn and Ra.

[1] J. Khuyagbaatar *et al.*, Phys. Rev. C **102**, 064602 (2020). doi:10.1103/PhysRevC.102.064602

[2] P. Moller, J.R. Nix, W.D. Myers, and W.J. Swiatecki, At. Data Nucl. Data Tables **59**, 185 (1995). doi:10.1006/adnd.1995.1002

[3] P. Moller, A.J. Sierk, T. Ichikawa, and H. Sagawa, At. Data Nucl. Data Tables **109**, 1 (2016). doi:10.1016/j.adt.2015.10.002

[4] T.A. Werke, D.A. Mayorov, M.C. Alfonso, M.E. Bennett, M.J. DeVanzo, M.M. Frey, E.E. Tereshatov, and C.M. Folden III, Phys. Rev. C **92**, 034613 (2015). doi:10.1103/PhysRevC.92.034613

[5] T.A. Werke, D.A. Mayorov, M.C. Alfonso, E.E. Tereshatov, and C.M. Folden III, Phys. Rev. C **92** (2015). doi:10.1103/PhysRevC.92.054617

[6] D.A. Mayorov, T.A. Werke, M.C. Alfonso, M.E. Bennett, and C.M. Folden III, Phys. Rev. C **90** (2014). doi:10.1103/PhysRevC.90.024602

[7] G.G. Adamian, N.V. Antonenko, H. Lenske, and L.A. Malov, Phys. Rev. C **101**, 034301 (2020). doi:10.1103/PhysRevC.101.034301

[8] D.A. Mayorov, E.E. Tereshatov, T.A. Werke, M.M. Frey, and C.M. Folden III, Nucl. Instrum. Methods Phys. Res. **B407**, 256 (2017). doi:10.1016/j.nimb.2017.07.012

Nuclear forensic methodologies for americium

I.W. Haynes,[1,2] and C.M. Folden III[1,2]
[1]*Department of Chemistry, Texas A&M University, College Station, Texas 77843*
[2]*Cyclotron Institute, Texas A&M University, College Station, Texas 77843*

Pre-detonation nuclear forensics has historically focused on analyses of plutonium and of uranium from every step in the nuclear fuel cycle, from natural ore to reactor fuel. Other nuclear materials are underrepresented, including americium, a minor actinide of some proliferation attractiveness [1, 2]. While americium is a widely-proliferated nuclear material with relatively easy acquisition routes, little research is available on nuclear forensics of americium [3, 4]. This project aims to adapt existing nuclear forensic techniques to americium-based samples to establish their readiness ahead of a potential time-sensitive real-world investigation.

In the fall of 2022, an aged teaching source of ^{241}Am labeled in 1967 as 10^4 decays per minute (dpm) was acquired with no supporting documentation, and was used as a representative sample approximating a smoke detector source; 10^4 dpm is approximately 4 nCi, and is well below the legal limit on a commercial smoke detector's activity. At this small activity level, the primary nuclear forensic question is whether any daughter species can be measured so that radiochronometry can be performed, and if not, what minimum starting activity is needed before such an investigation is viable. Table I shows the results of γ- and α-spectrometry for the characterization of the americium source.

Table I. Activity of ^{241}Am Button Source.

	Activity (nCi)	***Activity (Bq)***
Labeled Activity (decay corrected to 6/6/23)	4[b]	150[b]
α-Spectrometry	4.71 ± 0.17	174.3 ± 6.2
γ-Spectrometry	4.76 ± 0.35	176 ± 13
Average Activity	**4.74 ± 0.39**	**175 ± 14**
Corrected Initial Activity (04/1967)	5.18 ± 0.43	192 ± 16

[a]Uncertainty quoted at 3σ. [b]Labeled activity does not include uncertainties.

The labeled activity of the source has an error of at least 25%, as confirmed by good agreement across γ- and α-measurements. However, these γ- and α-measurements were unable to detect any daughter nuclides in the ^{241}Am decay chain, which prevents any chronometric analysis. Table II shows the estimated minimum starting activity of ^{241}Am needed to detect daughter species in a source from 1967, given the rate of background in the spectra taken.

Table II. Lower Limits of Detection Estimates for ^{241}Am Daughters.

Measurement Type	Nuclide	2x Background[a]
γ	^{237}Np	2.2 μCi
γ	^{233}Pa	3.4 μCi
α	^{237}Np	70. nCi

[a]Value equal to the activity needed to produce a measured signal that is twice the background in the spectra recorded

Preliminary results from these measurements indicate that small americium sources such as smoke detector sources are difficult to age-date unless they have activities close to the upper limit of activity allowable in commercial smoke detectors, which are unlikely in any modern smoke detector sources.

We are working to acquire larger samples of americium. Planned analyses include the measurement of daughter radionuclides for chronometry, trace metal analysis, and trace fission product analysis for reactor-type discrimination.

[1] C.G. Bathke *et al.*, Nucl. Technol. **179**, 5 (2012). doi:10.13182/NT10-203

[2] O. o. S. a. S. P. Assurance (U.S. Department of Energy, 2005).

[3] J. Sommers, M. Jimenez, M. Adamic, J. Giglio, and K. Carney, J. Radioanal. Nucl. Chem. **282**, 929 (2009). doi:10.1007/s10967-009-0189-1

[4] K.J. Spencer, L. Tandon, D. Gallimore, X. Ning, K. Kuhn, L. Walker, and L. Townsend, J.Radioanal. Nucl. Chem. **282**, 549 (2009). doi:10.1007/s10967-009-0287-0

Recoil transfer chamber for polonium production, a lighter homolog of livermorium (Z=116)

A.S. Kirkland[1,2] and C.M. Folden III[1,2]
[1]*Cyclotron Institute, Texas A&M University, College Station, Texas 77843*
[2]*Department of Chemistry, Texas A&M University, College Station, Texas 77843*

The chemistry of superheavy elements is largely unknown. Due to low production rates, chemistry must be performed on a single atom at a time. A method for beginning to study the chemistry of superheavy elements is to use lighter homologs, including polonium (Po, Z=84), the expected lighter homolog of livermorium (Lv, Z=116). Typical superheavy element experiments are performed in the gas phase, so to utilize Po as a lighter homolog, a steady stream of gas phase Po must be produced. In the present work, a recoil transfer chamber (RTC) has been modified to act as a source of gas-phase Po. RTCs are gas stoppers that are used after a physical pre-separator during cyclotron-based experiments to thermalize evaporation residues for the study of the chemistry of superheavy elements and their homologs [1]. Preliminary results on the use of an RTC as a source of Po are presented here.

At Texas A&M University, two RTCs have been fabricated, the "big" RTC and the simple RTC (sRTC). The big RTC was designed to stop product beams from the Momentum Achromat Recoil Spectrometer (MARS), and has been described in previous work [2]. The big RTC consists of two chambers. The first is the main chamber (MC) and consists of a set of ring electrodes and a set of flower petal electrodes, as well as an extraction nozzle. A decreasing electric field can be placed on the electrodes. The second chamber is called the aerosol (AC chamber). Two Canberra large-area (~2000 mm^2), bakeable Si detectors capable of operating at high pressures are in place, one in the MC chamber and one in the AC chamber. A 0.67 μCi ^{228}Th source ($t_{1/2}$ = 1.91 y, ~100% α) is mounted to the front window. The source emanates ^{220}Rn ($t_{1/2}$ = 55.6 s, 100% α), which decays to positively charged ^{216}Po ($t_{1/2}$ = 145 ms, 100% α). The ^{216}Po is extracted by the decreasing electric field created by the electrodes to the extraction nozzle. A helium gas jet carries the activity through the nozzle to the AC chamber, where it can be measured with the AC detector.

The data show that when the electric field is turned on and the pressure is set to the proper values (MC chamber: 228 torr, AC chamber: 218 torr), extraction of ^{216}Po can be observed. A typical ^{228}Th α-spectrum can be seen in Fig. 1a. The ^{212}Po peak has a tail from a summed β^- decay from ^{212}Bi. ^{228}Th and ^{224}Ra are trapped within the source, and while 220Rn is immediately neutralized, it can emanate into the MC. It then decays to charged ^{216}Po, and the latter is extracted because it has a half-life that is short compared to the neutralization time. When the RTC is fully operational, where there is a difference in pressure of 10 Torr between the two chambers, there is a decreasing electric field applied to the electrodes, and the flow rate of He from the system is 2 L/min, ^{216}Po is extracted, as seen in Fig. 1b. The ^{216}Po alpha-peak is broadened and significantly more intense than the rest of the peaks in the spectrum. There are small amounts of the other isotopes in the source present in the spectra (visible at 6200 keV), that are coming directly from the source. This indicates that the primary species being extracted is ^{216}Po, and the other isotopes present in the source are not being extracted in any appreciable quantities. During a typical extraction experiment, the ^{216}Po count rate is >90 s^{-1}. Future work will utilize this source for

chemical experiments on the adsorption of Po onto Si detectors functionalized with a self-assembled monolayer.

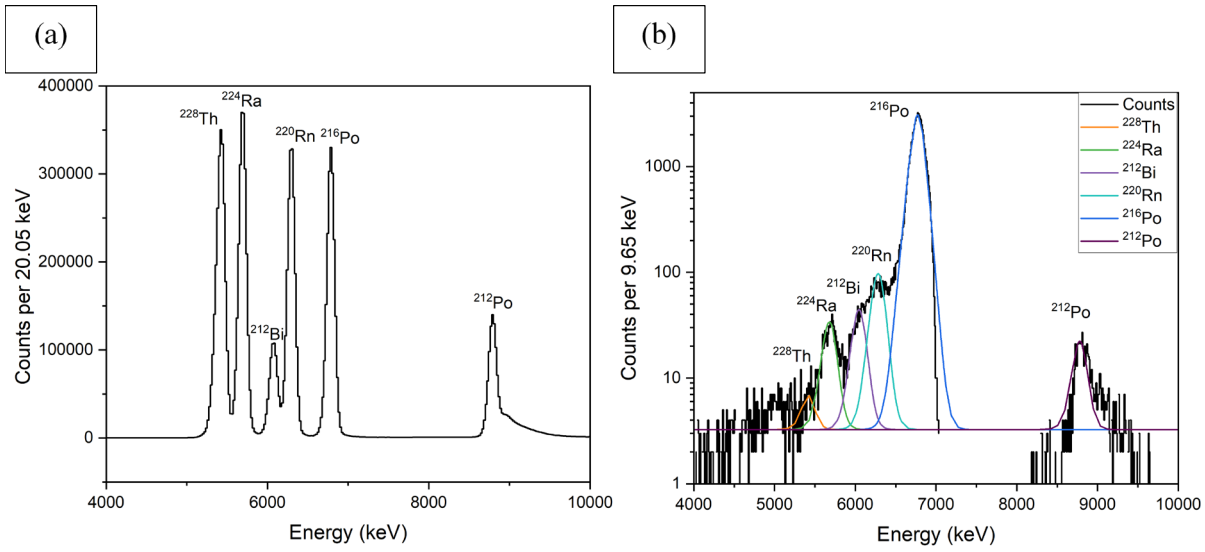

Fig. 2. (a) Typical ^{228}Th spectrum. (b) Spectrum of ^{228}Th where the big RTC was fully operational, meaning the gas flow and electric field were turned on. The primary peak is ^{216}Po, with limited amounts of the other nuclides present. The count time was 10 min.

[1] J. Even *et al.*, Nucl. Instrum. Methods Phys. Res. **A638**, 157 (2011). doi:10.1016/j.nima.2011.02.053

[2] M.C. Alfonso, E.E. Tereshatov, M.J. DeVanzo, J.A. Sefcik, M.E. Bennett, D.A. Mayorov, T.A. Werke, and C.M. Folden III, Nucl. Instrum. Methods Phys. Res. **A798**, 52 (2015). doi:10.1016/j.nima.2015.07.004

Resolving discrepancies in predicted excitation functions for the production of element 120

A. Rubio Reyes[1,2] and C.M. Folden III[1,2]
[1]*Cyclotron Institute, Texas A&M University, College Station, Texas 77843*
[2]*Department of Chemistry, Texas A&M University, College Station, Texas 77843*

There is significant disagreement among predictions of excitation functions for the production of element 120. This may be caused by differences in the mass model being used to predict excitation functions of element 120. The goal of this current work is to resolve differences among predicted excitation energies by correcting them to a standardized mass model. For this purpose, the mass table of P. Möller *et al*. [1] was used as a standard, and preliminary results are reported here.

Published excitation functions for the production of element 120 were collected from a literature search and digitized using the Graph Grabber application [2]. The sum of projectile energy in the center of mass frame E_{cm} [3] and the Q-value for compound nucleus formation Q_{CN} gives the compound nucleus excitation energy E_{CN}^* [4]. Q_{CN} is equal to the sum of the mass excesses of the reactants minus the sum of the mass excesses of the products, and therefore varies based on the mass model that was used. Q_{CN} was calculated using each individual paper's reference mass model and replaced with a new value calculated according to our standard mass model. This causes an energy shift in most cases, although any corresponding change in cross section was outside the scope of the current study. Figs. 1-6 show the "before and after" excitation functions for the 3n-5n exit channels.

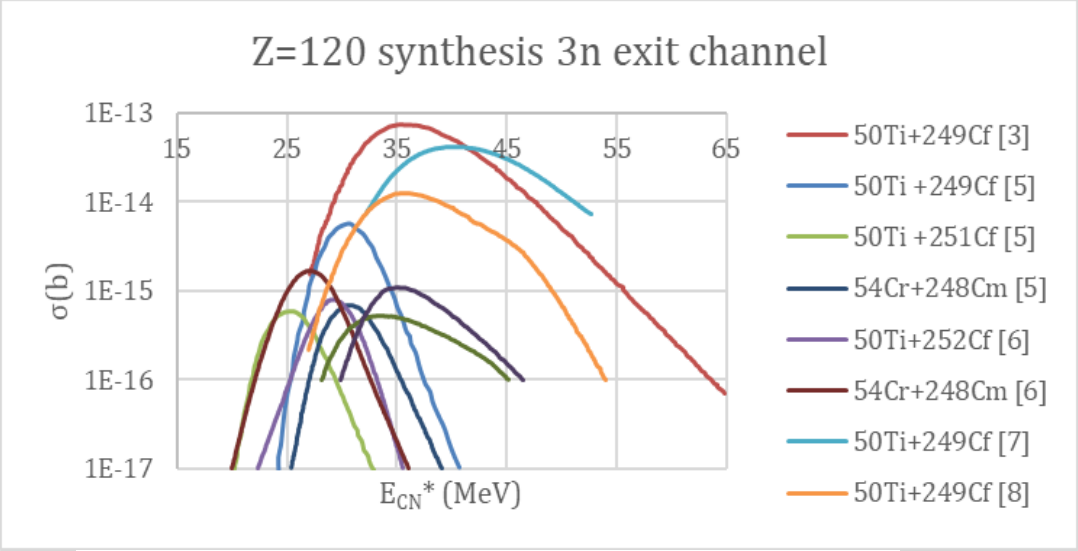

Fig. 1. Compiled raw excitation functions from Refs. [3,5-8] for the 3n exit channel.

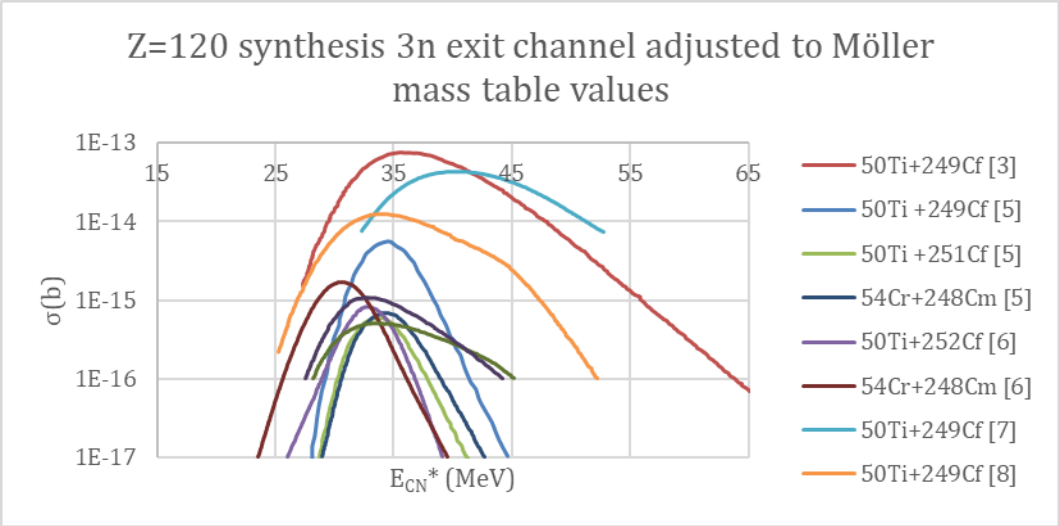

Fig. 2. Compiled excitation functions from Refs. [3,5-8] for the 3n exit channel adjusted using P. Möller *et al.* [1].

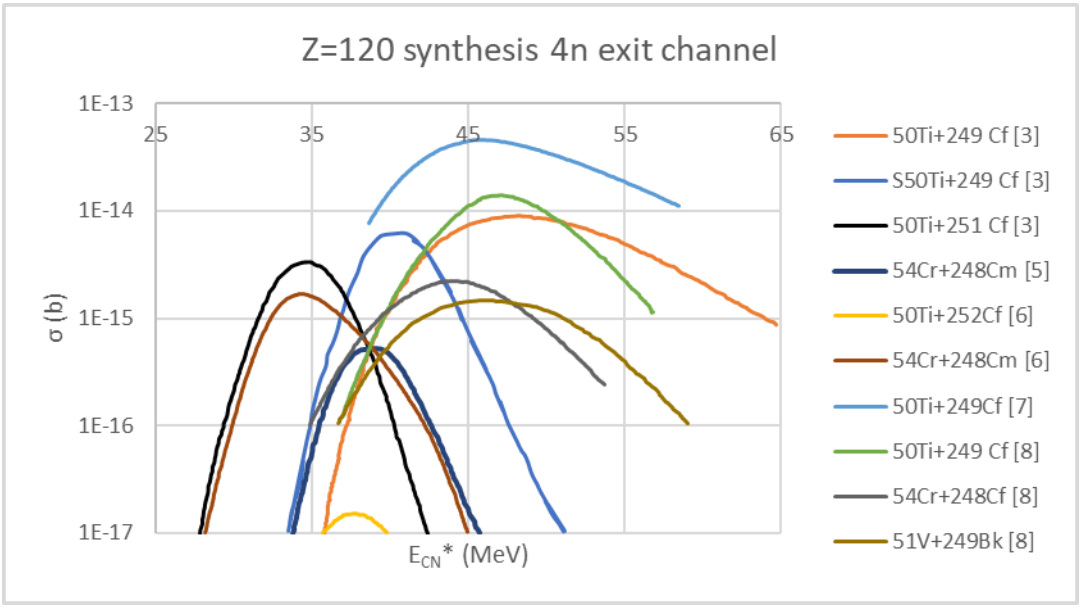

Fig. 3. Compiled raw excitation functions from Refs. [3,5-8] for the 4n exit channel.

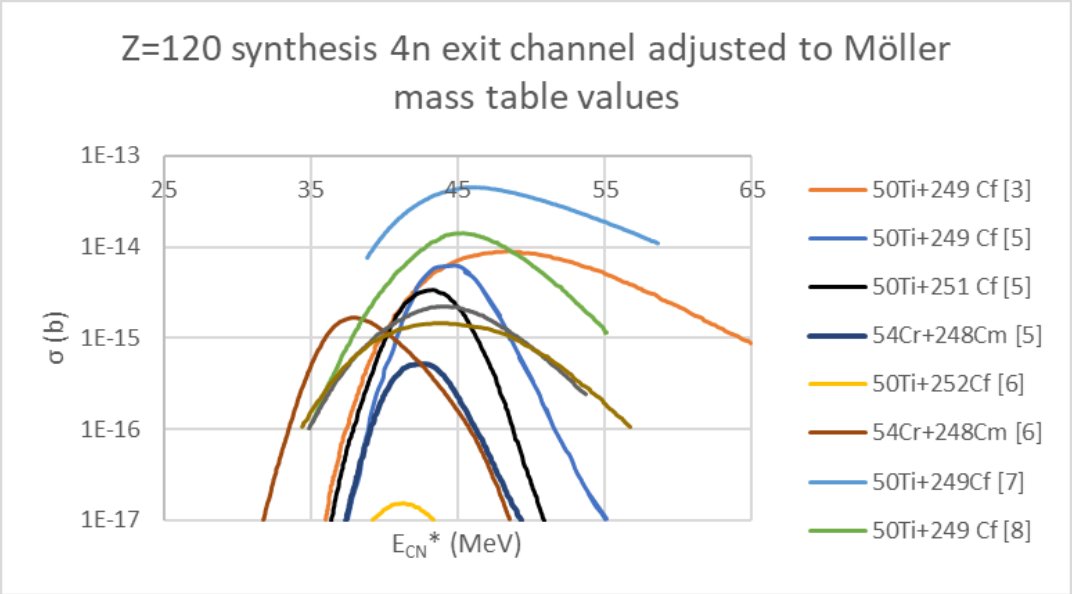

Fig. 4. Compiled excitation functions from Refs. [3,5-8] for the 4n exit channel adjusted using P. Möller *et al.* [1].

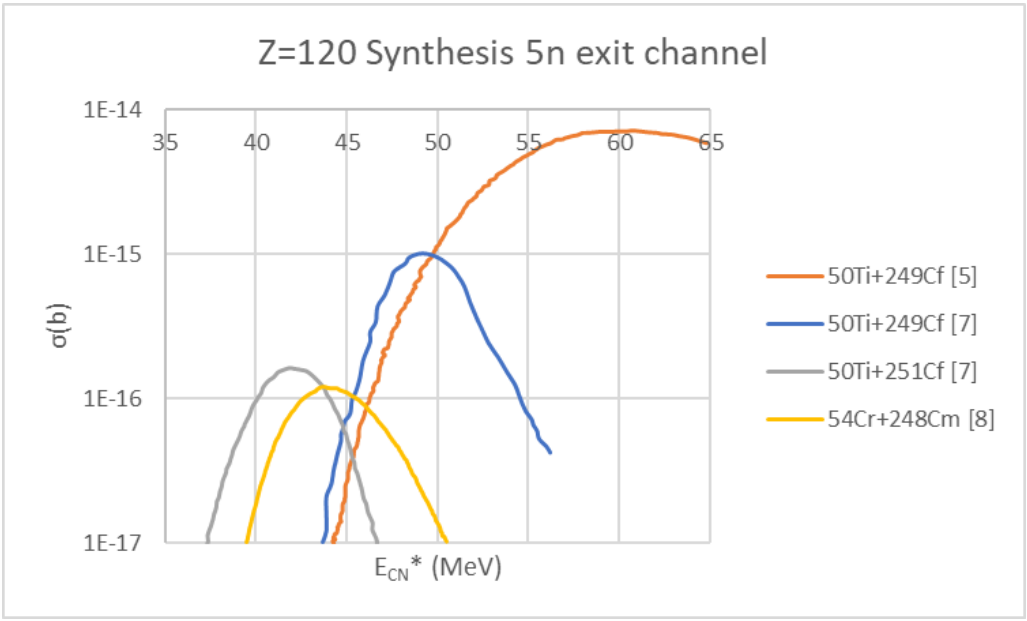

Fig. 5. Compiled raw excitation functions from Refs. [3,5-6] for the 5n exit channel.

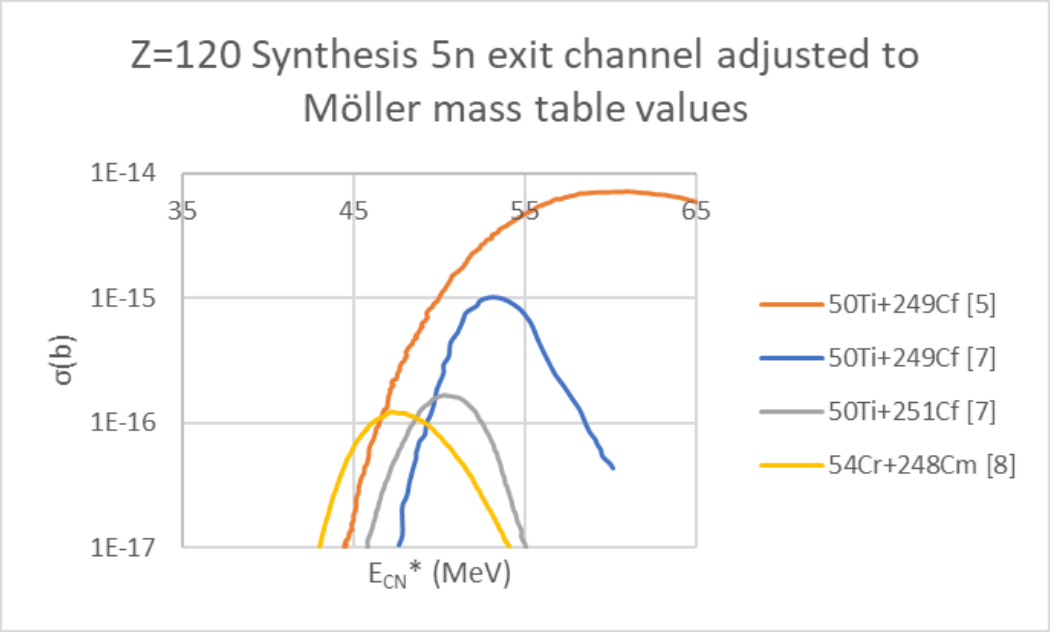

Fig. 6. Compiled excitation functions from Refs. [5,7-8] for the 5n exit channel adjusted using P. Möller *et al.* [1].

Even though the range of predicted optimal excitation energies is wide, the range is narrower after adjusting the Q-value, which suggests that much of the variation is due to differences in mass models. The adjusted data appear to give a higher degree of confidence for selecting the excitation energy that would be optimal for forming the compound nucleus that would lead to the discovery of element 120. This procedure could also be applied to the production of element 119, which has also yet to be discovered.

[1] P. Möller *et al.*, Nuclear Ground-State Masses and Deformations: FRDM (2012). At. Data Nucl. Data Tables **109**, 1 (2016); DOI: 10.1016/j.adt.2015.10.002
[2] S. Benbow, Graph Grabber 2.0.2 Quintessa Labs. (Accessed February 2023); https://www.quintessa.org/software/downloads-and-demos/graph-grabber-2.0.2
[3] J. Jiang *et al.*, Nucl. Phys. Rev. **30**, 4, 391 (2013); DOI: 10.11804/NuclPhysRev.30.04.391.
[4] C. Iliadis, Phys. Rev. C **99**, 065809, 1 (2019); DOI: 10.1103/PhysRevC.99.065809.
[5] K. Siwek-Wilczyńska *et al.*, Phys. Rev. C **84**, 1 (2012); DOI: 10.1103/PhysRevC.86.014611
[6] A. Nasirov *et al.*, Phys. Rev. C **84**, 044612 (2011); DOI:10.1103/PhysRevC.84.044612
[7] V. Zagrebaev and W. Greiner, Phys. Rev. C. **78**, 1 (2008);DOI:10.1103/PhysRevC.78.034610
[8] L. Zhou *et al.*, Phys. Rev. C **89**, 1 (2014); DOI: 10.1103/PhysRevC.89.024615

β- and γ-counting for pre-detonation nuclear forensics on Eu-155

I.W. Haynes,[1,2,3] I. May,[3] and C.M. Folden III[1,2]
[1]*Department of Chemistry, Texas A&M University, College Station, Texas 77843*
[2]*Cyclotron Institute, Texas A&M University, College Station, Texas 77843*
[3]*Chemistry Division, Los Alamos National Laboratory, Los Alamos, New Mexico 87545*

Post-detonation nuclear forensics was performed at Los Alamos National Laboratory (LANL) on ^{155}Eu, a fission product on the wing of the fission product production curve whose yield is sensitive to fission fuel and neutron energy. With a half-life of 4.753 years, ^{155}Eu provides a longer-lived option for these measurements than other fission products with similar mass numbers. The Chemistry Division Group - Nuclear and Radiochemistry, at LANL routinely measures a suite of fission products from ^{235}U fissions in thermal neutron flux experiments known as thermal calibration exercises, using a mixture of gas proportional β-decay counting and γ-spectrometry on HPGe detectors. The fission products of interest are reported relative to a high-yield reference fission product from the same sample to create a running-average ratio specific to neutron energy and fuel type; Equation 1 below shows the ratio-of-ratios R-value measured fission products are reported in:

$$R_{^{i}X} = \frac{\left[A(^{i}X)/A(^{99}Mo)\right]_{unknown}}{\left[A(^{i}X)/A(^{99}Mo)\right]_{^{235}U_{n,th}}} \quad (1)$$

where A denotes activity, ^{i}X is the nuclide of interest, and $^{235}U_{n,th}$ denotes irradiations of ^{235}U with thermal neutrons [1]. Measurements of unknown fission spectra are ratioed to a running-average of thermal calibration results, and the resulting R-value can be referenced against a library of irradiation conditions. This work adapted the existing methodology to ^{155}Eu and preliminary results are shown here. These results are in preparation for publication.

Both β-counting and γ-spectrometry were assessed for their viability in measurements of ^{155}Eu. β-decay counts ranged from 0.1 to 20 counts per minute when detectable, owing to several factors: low specific activity, low fission product yield, potential trace contaminants and a low β-decay energy, all of which hampered β-counting. The method is extremely sensitive to background fluctuations, with multiple available samples not distinguishable above background, and thus β-counting was determined to be unreliable for ^{155}Eu without considerable extra R&D. A method using only γ-spectrometry was developed, which can use running-averages of count rates on the same detector or can be converted to activity for comparison across detectors.

After thermal calibration samples were analyzed to create a running-average value for the denominator in Eq. 1, preliminary results using only γ-spectrometry to characterize non-standard irradiations were compiled, as shown in Figs. 1 and 2. Twelve separate samples representing six unique irradiation conditions were analyzed, using ^{235}U, ^{238}U, and ^{239}Pu fuels with three different neutron fields: thermal, fission and 14 MeV fusion; additionally, one experiment induced fission with a proton beam on natural uranium. Fig. 1 shows the greater precision this method provides over calculating expected values

based on published fission product yields from the JEFF-3.1.1 database, where literature on the irradiation conditions even exists [2]. Literature values shown are cumulative fission yields for different irradiation conditions reported as R-values for direct comparison. Due to large uncertainties on the fission yields of ^{155}Eu, the literature data show significantly worse precision than the measured values.

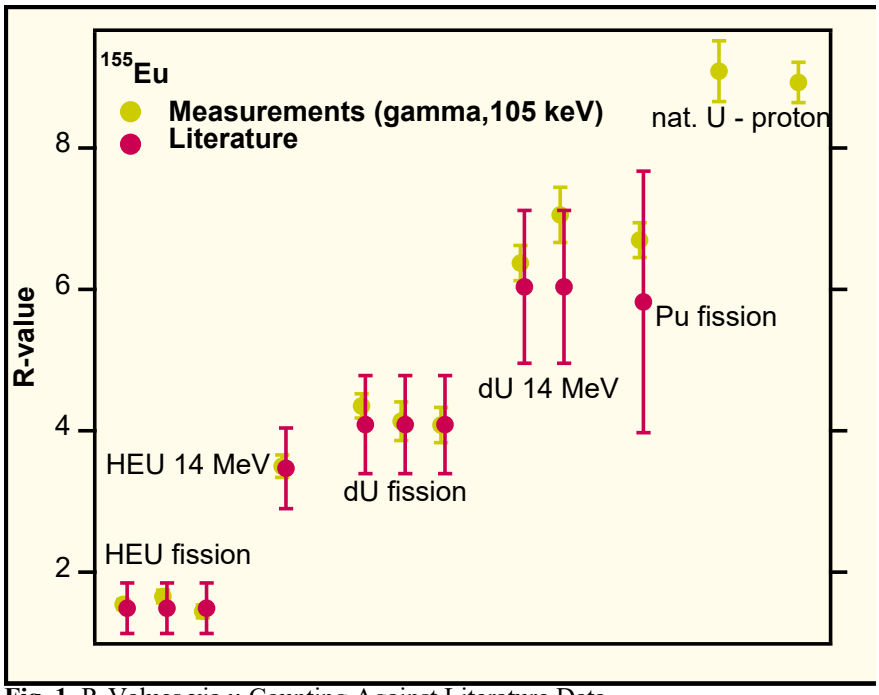

Fig. 1. R-Values via γ-Counting Against Literature Data.

Fig. 2 shows that the method produces values between those of ^{156}Eu and ^{153}Sm. Increasing fuel mass or neutron energy tends to systematically change R-values in correlation to the mass number of the fission product; this would indicate that R-values for ^{155}Eu should be found between ^{153}Sm and ^{156}Eu, and

Nuclide	Analysis Method
^{156}Eu	Beta Counting
^{155}Eu	Gamma
^{153}Sm	Beta Counting

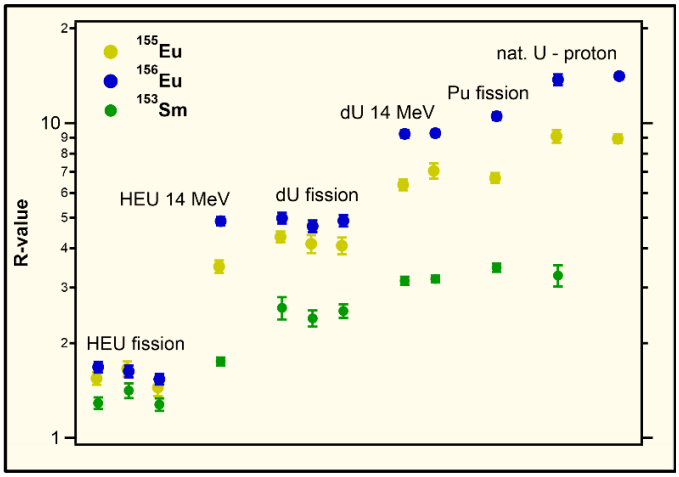

Fig. 2. Results of ^{155}Eu Analyses on Non-Standard Irradiations.

Fig. 2 shows that this relationship holds across several unique fission fuels and neutron energies. ^{153}Sm and ^{156}Eu are short-lived nuclides previously analyzed for these irradiations.

This study has been cleared for release by LANL (LA-UR-23-28541). As a result of this work, ^{155}Eu measured by γ-spectrometry can be utilized in future irradiation campaigns.

[1] M.J. Jackson *et al.*, J. Radioanal. Nucl. Chem. **318**, 107 (2018). doi:10.1007/s10967-018-6048-1
[2] The JEFF-3.1/-3.1.1 radioactive decay data and fission yields sub-libraries, JEFF report 20.

High energy neutron production and high momentum tail in intermediate heavy ion collisions

R. Wada, Q. Hu, and G. Tian

Short range correlation (SRC) between two nucleons in a nucleus, especially np pair, has been intensively studied in the knockout reactions of (e,e'p), (e,e'np) and (p,pnp) on various targets at GeV incident energies [1-3]. In heavy ion collisions, the same SRC process may enhance the high energy nucleon emissions and as the result the production cross section show K-4 power dependence in the high momentum tail (HMT), where K=p/PF and PF is Fermi momentum [4].

In our previous report in 2021, the simulated results of AMD/D-FM [5] and AMD/D-3NC [6] for ^{12}C+^{12}C, ^{12}C+^{16}O at 290 MeV/nucleon are presented where the high energy neutron productions are rather well reproduced by AMD/D-3NC. This study is extended to the higher incident energy. For ^{12}C+^{12}C at 400 MeV/nucleon, the simulated results are compared with the experimental data [7] in Fig.1. On the left, the neutron energy spectra are compared at different measured angles. AMD/D-3NC results (red histograms) start to underpredict the experimental high energy neutron tails. On the right, the weighted cross section $K^4 d\sigma^2/dKd\Omega$ is plotted as a function of the relative momentum $\boldsymbol{K}$. The experimental data indeed show K^{-4} power dependence as a more or less constant distribution at the high momentum side.

An attempt is made to reproduce the experimental high momentum tail distribution with K^{-4}

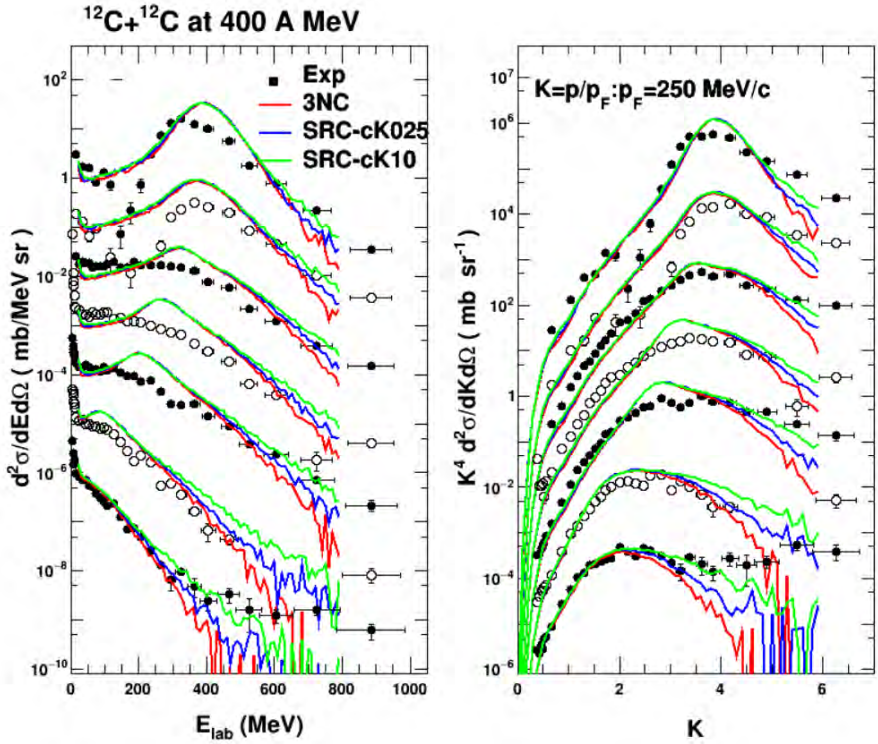

Fig. 1. AMD simulated results are compared with the experimental data from Ref.[7] at angles from 5o, 10o, 20o, 30o, 40o, 60o, 80o, from top to bottom. The red histograms are with AMD/D-3NC. Blue and green histograms are those with HMT in the Fermi distributions shown in Fig.2 with same color lines, respectively.

dependence with AMD/D-3NC. When Fermi boost is applied to the three nucleons in the 3NC process, HMT component is added to the original Gaussian distribution as shown below.

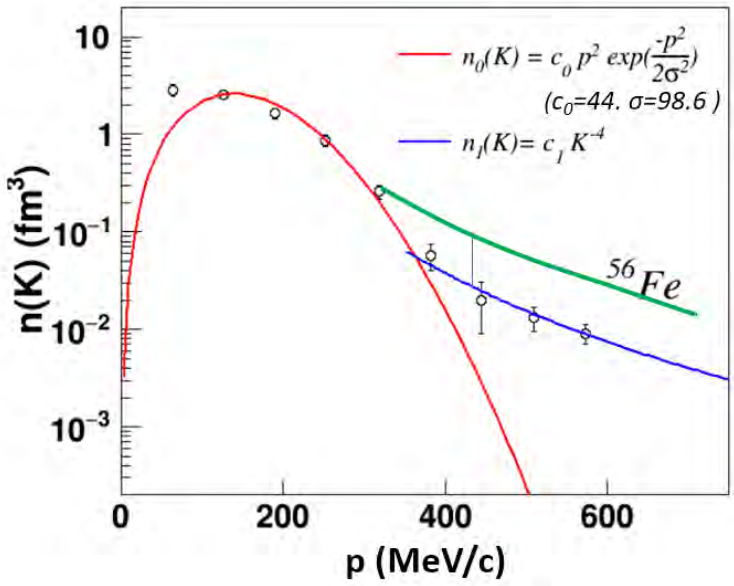

Fig. 2. Fermi momentum distribution incorporated with the Fermi boost. Circles are the experimental data from Ref.[9] and red curve corresponds to the Gaussian distribution, blue and green to the added HMTs with c1/c0=0.0057 and 0.023, respectively.

In the Fermi boost, the new momentum ***P'*** with a momentum fluctuation is given as

$$\boldsymbol{P}' = \boldsymbol{P} + \Delta\boldsymbol{P}',$$

$$\Delta\boldsymbol{P} = (h/2\pi)\sqrt{\nu(\rho/\rho 0)^{1/3}}G(1) \quad for \ \boldsymbol{p} < \boldsymbol{P}_K$$

$$= c_1 (\boldsymbol{p}/\boldsymbol{P}_F)4 \quad for \ \boldsymbol{p} \geq \boldsymbol{P}_K$$

$$\Delta\boldsymbol{P}' = \Delta\boldsymbol{P} - c_R \boldsymbol{P}_F$$

G(1) is a random number generator along the Gaussian distribution with σ=1 and c_R is a reduction factor (c_R=0.3) as described earlier. c_0, c_1 are relative strength between the Gaussian and K^{-4} term shown in the figure. $\boldsymbol{P}_K$ is the crossing momentum between the two curves. When c1/c0=0.023 is used, the experimental HMTs are reasonably well reproduced.

At present the relation between SRC and HMT in heavy ion collisions is not clear. In Refs. [4,8], HMT in heavy ion reactions is attributed to SRC based on the resemblance of K^{-4} power dependence of the cross sections. However in the knockout reaction of np pairs by the GeV electron and proton beams, these pairs are at T~ 0 before they are knocked out and the HMT is reasonably attributed to SRC. On the other hand in the heavy ion collisions studied here, the high energy neutrons are dominantly produced from 3NC process at hot-high density nuclear matter at an early stage of the reactions. If the high temperature for the Fermi-liquid governs the Fermi distribution, HMT originates from the Pauli-blocking. If the high density governs the behavior, it may reflect SRC. Further studies are underway.

[1] R. Weiss et al., Phys. Lett. B **791**, 242 (2019).

[2] M. Duer et al. (CLAS collaboration), Phys. Rev. Lett. 122, 172502 (2019).
[3] S. Stevens et al., Phys. Lett. B 777, 374 (2018).
[4] W.-M. Guo et al., Phys. Rev. C 104, 034603 (2021).
[5] W. Lin, X. Liu, R. Wada, M. Huang, P. Ren et al., Phys. Rev. C 94, 064609 (2016).
[6] R. Wada, Phy. Rev. C 96, 031601(R) (2017).
[7] Y. Iwata et al., Phys. Rev. C 64, 054609 (2001).
[8] G.-C. Yong et al., PRC 96, 064614 (2017).
[9] C. Ciofi degli Atti and S. Simula, Phys. Rev. C 53, 1689 (1996).

Toward understanding relativistic heavy-ion collisions with the STAR detector at RHIC

D.M. Anderson, Y. Liu, S. Mioduszewski, J. Pan, J. Tyler, and the STAR Collaboration

The hard production of a direct photon back-to-back with a jet (γ-jet) is a probe of the parton energy loss in heavy-ion collisions [1]. In the "γ-jet" coincidence measurement, the measured energy of the trigger particle (the photon) serves as a calibrated baseline for the total energy of the jet particles on the recoil side (i.e. opposite in azimuth) of the trigger. The mean-free path of the γ in the medium is large enough so that its momentum is preserved, regardless of the position of the initial scattering vertex. Thus it does not suffer from the geometric biases, i.e. the non-uniform spatial sampling of hadron triggers due to energy loss in the medium, of *e.g.* π^0 triggers.

As the dominant background to direct photons are π^0 (decaying to two photons), the Barrel Shower Maximum Detector (BSMD) has provided the capability of distinguishing direct photons from neutral pions via the transverse shower shape. Our group has used this method in the measurement of direct photon+hadron correlations [2]. The γ-hadron correlation studies can be extended to studies of γ-triggered jet reconstruction measurements (as has been done at the LHC [3, 4]). The away-side jet will then be reconstructed in coincidence with triggers selected as direct photon candidates or (for p_T<20 GeV using the shower shape with the BSMD) identified π^0 triggers. The advantage of this is the ability to reach lower energy fragments in the jet to study jet-shape modification and possible redistribution of energy.

Two papers on charged recoil jets relative to γ/π^0 triggers are in the final stages of collaboration review and should be submitted to PRL and PRC for publication within this fiscal year. Charged-jet reconstruction is performed using the anti-k_T algorithm from the Fastjet package [5]. In this analysis, charged particles with transverse momentum $0.2 < p_T < 30$ GeV/c are included as constituents. A fiducial cut is made on the pseudorapidity of the jet axis, $|\eta_{jet}| < 1-R$, where R is the jet resolution parameter associated with the radial size of the jet.

A key finding of the measurements in medium (Au+Au collisions) vs. vacuum (p+p collisions) is that the suppression of R=0.2 jets on the recoil side of both γ and π^0 triggers is largely restored when reconstructing larger jets of R=0.5. One selective figure from the upcoming papers is shown in Fig. 1.

Fig. 1 shows the ratio of charged recoil-jet yields for R-0.2 to R=0.5, $\Re^{0.2/0.5}$ for π^0 triggers measured with transverse energy E_T=9-11 GeV and 11-15 GeV, and γ triggers with 15-20 GeV. The Au+Au results are in blue and red. Also shown in these figures are the corresponding measurements in p+p collisions, in green. The comparison of the measurements in Au+Au to p+p collisions is a demonstration of in-medium jet broadening.

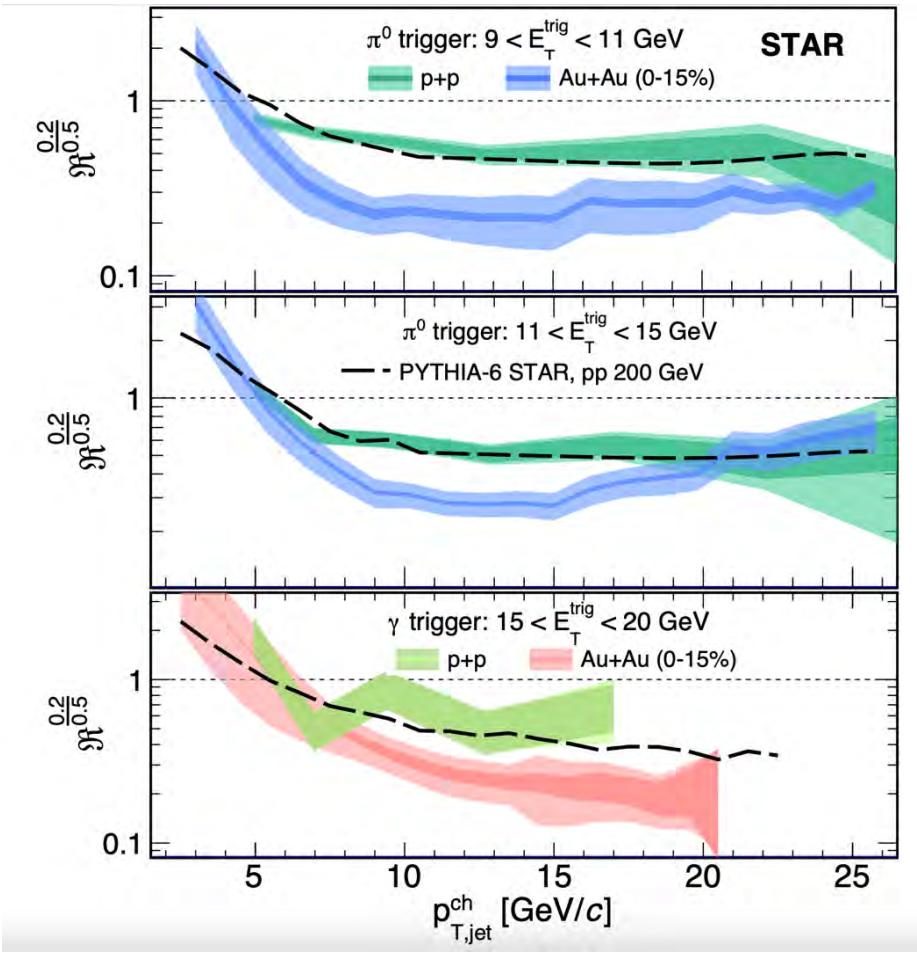

Fig. 1. Yield ratio $\Re^{0.2/0.5}$ for R = 0.2 and 0.5 measured in p+p and Au+Au collisions. Top panel: π^0 trigger, $9 < E_T^{trig} < 11$ GeV; middle panel: π^0 trigger, $11 < E_T^{trig} < 15$ GeV; bottom panel: γ_{dir} trigger, $15 < E_T^{trig} < 20$ GeV. Dark bands are statistical errors; light bands are systematic uncertainty. Also shown are the same distributions calculated using PYTHIA-6 STAR tune for p + p collisions.

[1] X.N. Wang, Z. Huang and I. Sarcevic, Phys. Rev. Lett. **77**, 231 (1996).

[2] L. Adamczyk *et al.* (STAR Collaboration), Phys. Lett. B **760**, 689 (2016); B.I. Abelev *et al.* (STAR Collaboration), Phys. Rev. C **82**, 34909 (2010).

[3] S. Chatrchyan *et al.* (CMS Collaboration), Phys. Lett. B **718**, 773 (2013).

[4] (ATLAS Collaboration), ATLAS-CONF-2012-121.

[5] M. Cacciari and G. Salam, Phys. Lett. B **641**, 57 (2006); M. Cacciari, G. Salam and G. Soyez, JHEP **0804** 005 (2008), http://fastjet.fr.

SECTION III

NUCLEAR THEORY

Calculation of nuclear level density within a micro-macroscopic approach

A.G. Magner,[1] A.I. Sanzhur,[1] S.N. Fedotkin,[1] A.I. Levon,[1] and S. Shlomo
[1]*Institute for Nuclear Research, 03028 Kyiv, Ukraine*

Many properties of heavy nuclei can be described in terms of the statistical level density. The level density $\rho(E,A)$, where E and A are the nuclear energy and particle number of an isotopically symmetric nucleus, can be calculated by the inverse Laplace transformation of the partition function $\mathcal{Z}(\beta,\alpha)$, where β and α are the Lagrange multipliers, respectively. Within the grand canonical ensemble, the standard Darwin-Fowler saddle point method (SPM) can be applied for the inverse Laplace integration over all variables, including β, which is related to the total energy E, but for large excitation energy U. As usually assumed, the temperature T is related to the well-determined saddle point in the integration over β for a finite Fermi system of a large particle number A. However, many experimental data also exist for low-lying excitation energies U, where such a saddle point does not exist. Therefore, the integral over the Lagrange multiplier β should be carried out [1] more accurately beyond the standard SPM. For another variable, related to the number of nucleons, one can apply the SPM assuming that particle number A is relatively large. In this work, we remove divergence at the critical catastrophe point for zero excitation energy limit of $\rho(E,A)$ and study the shell effects in the level density parameter versus the experimental data by using the periodic orbit theory (POT).

Taking more accurately the inverse Laplace integral over Lagrange multiplier β we have derived analytically the level density$\rho(E,A)$ in terms of the modified Bessel function $I_\nu(S)$ of the entropy S, $\rho \propto S^{-\nu} I_\nu(S)$. Here, $S = 2(aU)^{1/2}$, where U is the excitation energy, $U = E - E_0$, E_0 is the background energy, $E_0 \approx E_{\rm ETF} + \delta E$, $E_{\rm ETF}$ is the smooth extended Thomas-Fermi (ETF) part of the background energy E_0 [2], and δE is the shell correction energy. The level density parameter a is proportional to the semiclassical POT level density, $g(\lambda)$, with the decomposition in terms of the ETF $g_{\rm ETF}(\varepsilon)$ [2] and shell corrections $\delta g(\varepsilon)$ components, where both are taken at the chemical potential λ, $\varepsilon = \lambda$, $g(\lambda) \approx g_{ETF}(\lambda) + \delta g(\lambda)$, for which one has the well-known analytical expressions. The modified Bessel function $I_\nu(S)$ of the order ν is determined by the number of integrals of motion κ, except the energy (for the one particle number integral of motion A, we have $\kappa = 1$). We obtained values of $\nu = 3/2$ for the case of relatively small shell-correction effects ($\nu = \kappa/2 + 1$) and $\nu = 5/2$ for the case of large shell correction effects ($\nu = \kappa/2 + 2$).

Fig. 1 shows the inverse level density parameter $K = A/a$ as function of the particle number A of symmetric nuclear system in the semiclassical POT approximation. The results of these calculations [1] are in a qualitative agreement with the recent experimental data [3], which included in the analysis the excited states in much more nuclei than those known earlier for neutron resonances. For the oscillating shell correction $\delta g(\varepsilon)$, for simplicity, we used the well-known explicitly given POT result for the infinitely deep square well potential because the only single-particle states near the Fermi surface essentially contribute to $\delta g(\varepsilon)$. Its Gaussian averaging with the width $\gamma = 0.3$ has been calculated analytically, which almost identically coincides with the corresponding quantum results of the Strutinsky shell correction method, and it is well describes the major shell structure. The smooth part $g_{\rm ETF}(\varepsilon)$ is calculated on the basis of the

realistic Skyrme forces SKM* and KDE0v1 with the effective mass [2]. The positions of maxima of the level density parameter a (or oscillating level density $\delta g(\varepsilon)$) cannot be accurately reproduced because of neglecting the spin-orbit interaction. However, according to the POT results for the isomeric state in ^{240}Pu, we took into account the effect of the spin-orbit forces effectively by shifting the curve $K(A)$ in about the period of the major shell structure, $\Delta A = 20$, along the A axis. In spite of very simple explicitly analytical calculations of the inverse level density parameter K, the magnitudes of the periods for the oscillations of $K(A)$ are basically in good agreement with data for particle numbers of the order of 45-150. However, there is a discrepancy for particle numbers in the range of 150-240 for several reasons. Experimental data for K were obtained [3] in good agreement with those for neutron resonances because they are dominating in the specific least mean-square fit using relatively large widths. For this nuclear range the low excitation energies spectra are dramatically different than those of neutron resonances. Another reason might be that the pairing effects should be taken into account along with the shell structure, e.g., in magic nucleus ^{208}Pb. Especially for nuclei in this low excitation energy range, we need the model-independent results of experimental data for level density; see Ref. [1].

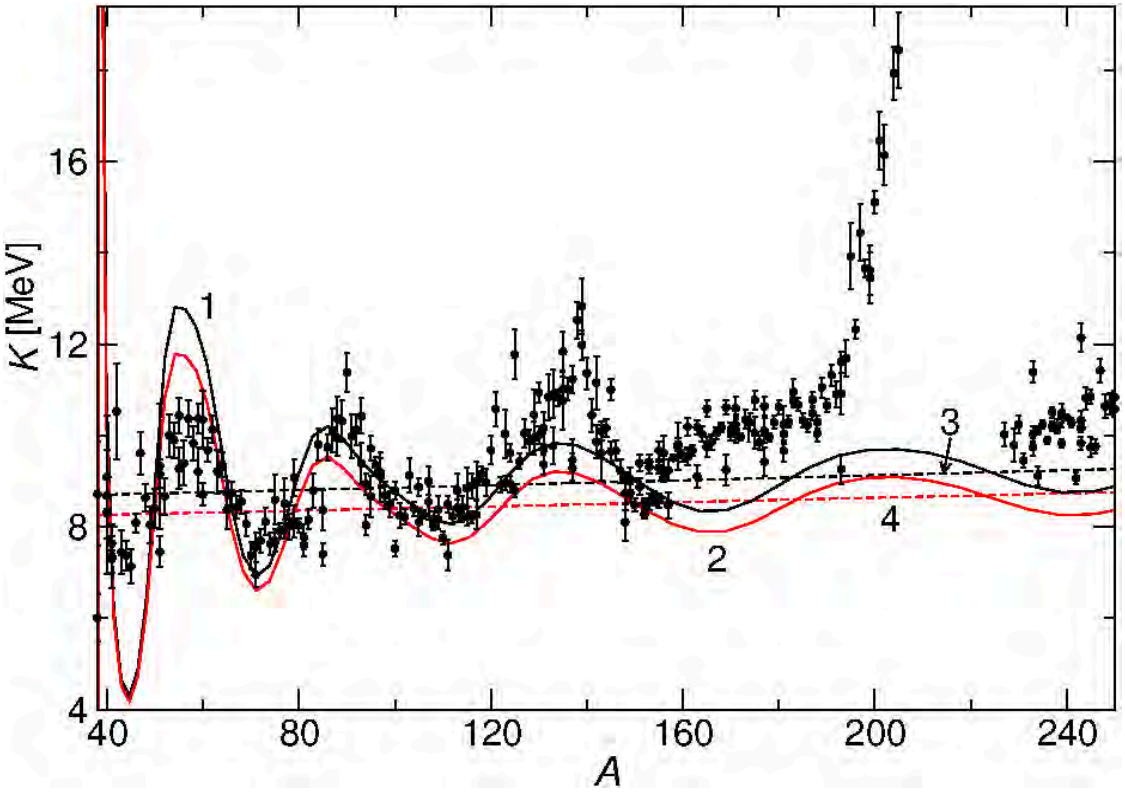

Fig. 1. The inverse level-density parameter $\boldsymbol{K = A/a}$ (solids "1" for SKM* and "2" for KDE0v1 forces) is shown as function of the particle number $\boldsymbol{A}$. The smooth part in the ETF approach is taken from Ref. [2] for these two versions of the Skyrme forces SKM* ("3" dashed) and KDE0v1 ("4" dashed). The solid oscillating curves are obtained by using the semiclassical POT approximation for the shell corrections $\boldsymbol{\delta g(\varepsilon)}$ of the single-particle density $\boldsymbol{g(\varepsilon)}$ with the Gauss width averaging parameter $\boldsymbol{\gamma = 0.3}$ in dimensionless energy units $\boldsymbol{kR}$ where $\boldsymbol{k = (2m\varepsilon/\hbar^2)^{1/2}}$, $\boldsymbol{R}$ is the radius of a spherical system, $\boldsymbol{m}$ is the particle mass (see Ref. [1]). The dashed curves "3" and "4" present smooth parts, both include the important effective mass contribution. The chemical potential is $\boldsymbol{\lambda = 40}$ MeV. Experimental values, shown by solid points, are taken from Ref. [3].

[1] A.G. Magner, A.I. Sanzhur, S.N. Fedotkin, A.I. Levon, and S. Shlomo, Nucl. Phys. **A1021**, 122423 (2022).
[2] V.M. Kolomietz, A.I. Sanzhur, and S. Shlomo, Phys. Rev. C **97**, 064302 (2018).
[3] T. von Egidy and D. Bucurescu, Phys. Rev. C **80**, 054301 (2009).

Microscopic-macroscopic nuclear level densities for low excitation energies

A.G. Magner,[1] A.I. Sanzhur,[1] S.N. Fedotkin,[1] A.I. Levon,[1] U.V. Grygoriev,[1] and S. Shlomo
[1]*Institute for Nuclear Research, 03028 Kyiv, Ukraine*

The statistical level density is a fundamental tool for the description of many properties of atomic nuclei. The level density $\rho(E,N,Z,M)$ of a nucleus is defined as function of the energy E, neutron N and proton Z numbers, and the projection of the angular momentum M on a laboratory-fixed coordinate system. The level density $\rho(E,N,Z,M)$ can be presented as the inverse Laplace transformation of the partition function $Z(\beta,\alpha)$, where β and $\alpha=\{\alpha_N,\alpha_Z,\alpha_M\}$ are the Lagrange multipliers. These multipliers are determined by the neutron N and proton Z numbers, and the spin projection M, respectively. Within the grand canonical ensemble, one can apply the standard Darwin-Fowler saddle point method (SPM) for the inverse Laplace integration over all variables, including β, which is related to the total energy E, but for large excitation energy U. As it can be assumed, the temperature T is related to the well-determined saddle point in the integration over β for a finite Fermi system of large particle numbers N and Z, and the spin projection M. However, many experimental data also exist for low-lying excitation energies U where such a saddle point does not exist. Therefore, the integral over the Lagrange multiplier β should be carried out [1] more accurately beyond the standard SPM. For other variables, related to the neutron N and proton Z numbers, and the spin projection M, one can apply the SPM assuming that particle numbers N and Z, and spin I are relatively large. In this work we have removed divergence at the critical catastrophe point at zero excitation energy limit, where all high-order derivatives of the entropy are zeros, using the semiclassical periodic-orbit theory (POT) for calculations of $\rho(E,N,Z,M)$, and have derived analytical expressions for the spin-dependent level density $\rho(E,N,Z,I)$ for the nuclear collective rotations.

Taking the inverse Laplace transformation of the partition function $Z(\beta,\alpha)$ over β more accurately, beyond the standard SPM, we have derived [1] an approximate expression for the level density, $\rho(E,N,Z,M)\propto S^{-\nu}I_\nu(S)$, where $I_\nu(S)$ is the modified Bessel function of the entropy S at $\nu=5/2$ for the MMA1 case (i) of negligibly small shell corrections, and $\nu=7/2$ for the MMA2 case (ii) of the dominating shell effects. For the spin-dependent level density $\rho(E,N,Z,I)$, one obtains $\rho(E,N,Z,I)\propto a\hbar^2(2I+1)S^{-(\nu+1)}I_{\nu+1}(S)/\Theta$. The shell and isotopic asymmetry effects are taken into account through the level density parameter a and nuclear moment of inertia Θ. For collective rotations one obtains $\rho_{\rm coll}(E,I)\approx(1/2)\int_{-I}^{I}d\,\Lambda\,\rho_{\rm intr}(U_0-E^{\perp}_{\rm rot},\Lambda)$, where $\rho_{\rm intr}(U_{\rm coll},\Lambda)\equiv\rho(E,M=\Lambda)$ is the intrinsic level density, Λ is the nuclear spin projection to the intrinsic axis of the coordinate system rotating together with a nucleus, $U_0=E-E_0$, E_0 is the background energy, $U_{\rm coll}=U_0-E^{\perp}_{\rm rot}$, $E^{\perp}_{\rm rot}=[I(I+1)-\Lambda^2]/2\Theta_\perp$ is the rotation energy and $\Theta_\perp$ is the moment of inertia with respect to the axis perpendicular to the symmetry axis. As the "parallel" moment of inertia $\Theta_\parallel$ is much smaller than $\Theta_\perp$ of the total effective moment of inertia $\Theta_{\rm eff}$, $\Theta^{-1}_{\rm eff}=\Theta^{-1}_\perp+\Theta^{-1}_\parallel$, we have proved analytically the well-known enhancement of the level density due to the collective rotations of axially deformed symmetric nuclei. For the total MMA level density $\rho(E,N,Z)=\int dM\,\rho(E,N,Z,M)$ we arrived at a similar expression, $\rho(E,N,Z)\propto S^{-\nu}I_\nu(S)$, but with $\nu=2$ for the MMA1 case (i) and $\nu=3$ for the MMA2 case (ii).

Fig. 1 shows the inverse level density parameter $K = A/a$ in the long Nd isotope chain with the particle number $A = 131 - 156$. The values of K are obtained by the least mean squares (LMS) fitting of our theoretical results to the experimental data on the known excitation spectra found by the sample method from the database, http://www.nndc.bnl.gov/ensdf. A reasonable agreement with these experimental data are obtained accounting for the shell and isotopic asymmetry effects with the help of the semiclassical POT by using the only one inverse level density parameter K, having a clear physical meaning, in the LMS fitting. As seen from Fig. 1, the results for K for isotopes of Nd as functions of the particle number A are characterized by a very pronounced saw-toothed behavior with alternating low (for odd nucleus) and high K values (for even nucleus). We obtained values of K for low excitation energy range which are essentially different from those for neutron resonances $K \approx 10$ MeV. We have found significant shell effects in the MMA level densities mainly because of dominating contributions from MMA2b (ii) approach, which is the MMA2 (ii) but for small shell corrections and for their large derivatives over the chemical potential, in the nuclear low-energy states range. The interparticle interaction beyond the mean field approach is taken into account approximately in average through the extended Thomas-Fermi component of the level density parameter a, proportional to the semiclassical POT level density. Accounting for the strong pairing effect (two magenta points for ^{140,142}Nd in Fig. 1) we showed that pairing correlations lead to a smoothing of the inverse level density $K(A)$ behavior as function of the particle number A.

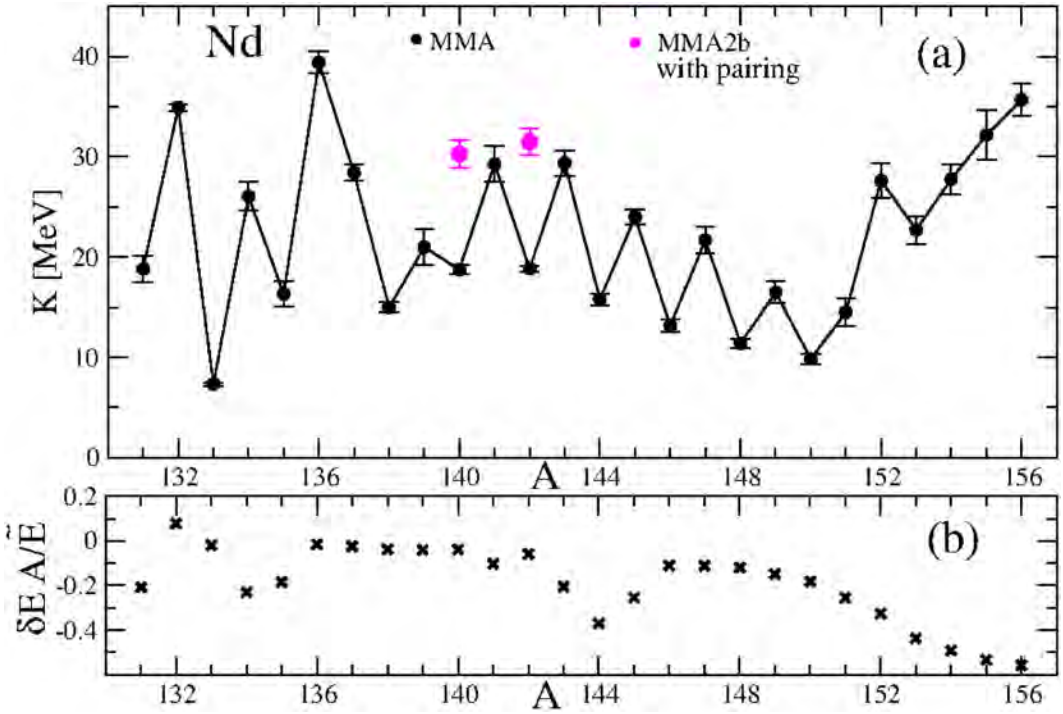

Fig. 1. (a) Inverse level-density parameter $\boldsymbol{K}$(with errors bars) for Nd isotopes is shown as function of the particle number $\boldsymbol{A}$ within a long chain $\boldsymbol{A = 131 - 156}$. The close black dotted points are the results of the MMA approach taken with the smallest relative error parameter, $\boldsymbol{\sigma^2 \propto \chi^2}$, normalized to the number of points, in the LMS fitting among all MMAs (MMA1, MMA2a, and MMA2b), including MMA2a which is MMA2(ii) but with the numerical shell corrections taken from Ref. [2]. (b) The relative shell correction energies , $\boldsymbol{\delta E\, A/\tilde{E}}$ [2], in units of the background energy $\boldsymbol{\tilde{E} \approx E_{ETF}}$ per one particle, $\boldsymbol{E_{ETF}}$ is the smooth energy POT component of the extended Thomas-Fermi model. The chemical potential is $\boldsymbol{\lambda = 40}$ MeV.

[1] A.G. Magner, A.I. Sanzhur, S.N. Fedotkin, A.I. Levon, U.V. Grygoriev, and S. Shlomo, Low Temp. Phys. **48**, 920 (2022).
[2] P. Moeller, A.J. Sierk, T. Ichikawa, and H. Sagawa, Atom. Data Nucl. Data Tables **109-110**, 1 (2016).

Semi classical nuclear level density in the micro-macroscopic approach

A.G. Magner,[1] A.I. Sanzhur,[1] S.N. Fedotkin,[1] A.I. Levon,[1] U.V. Grygoriev,[1,2] and S. Shlomo
[1]*Institute for Nuclear Research, National Academy of Sciences of Ukraine, Kyiv, Ukraine*
[2]*Faculty of Science and Engineering, University of Groningen, Groningen, Netherlands*

Many properties of atomic nuclei were described in terms of the statistical level density, ρ, for large excitation energies U at a thermal equilibrium with temperature T [1]. The nuclear level density ρ(E,**Q**) was derived within the micro-macroscopic approximation (MMA) for a system of strongly interacting nucleons with the energy E and additional integrals of motion **Q** [2,3]. Within the extended Thomas-Fermi (ETF) approach and semiclassical periodic-orbit theory (POT), beyond the Fermi-gas saddle-point method we obtain $\rho_A \approx \bar{\rho} I_\nu(S)/S^\nu$,where I_ν is the modified Bessel function of the entropy S of order ν, and $\bar{\rho}$ is a constant independent of S. For small shell-structure contribution, one finds $\nu = \kappa/2 + 1$, where κ is the number of additional integrals of motion. This integer number is of a dimension of **Q**, **Q** = (N,Z,…) for the case of atomic nuclei. Here, N and Z are the numbers of neutrons and protons, respectively. For much larger shell structure contributions, one obtains ν=κ/2+2. The MMA level density ρ reaches the well-known Fermi gas asymptote [1] for large entropy S (large excitation energy U), and the finite micro-canonical combinatoric limit for low entropy S (low excitation energies U→0), see Fig. 1.

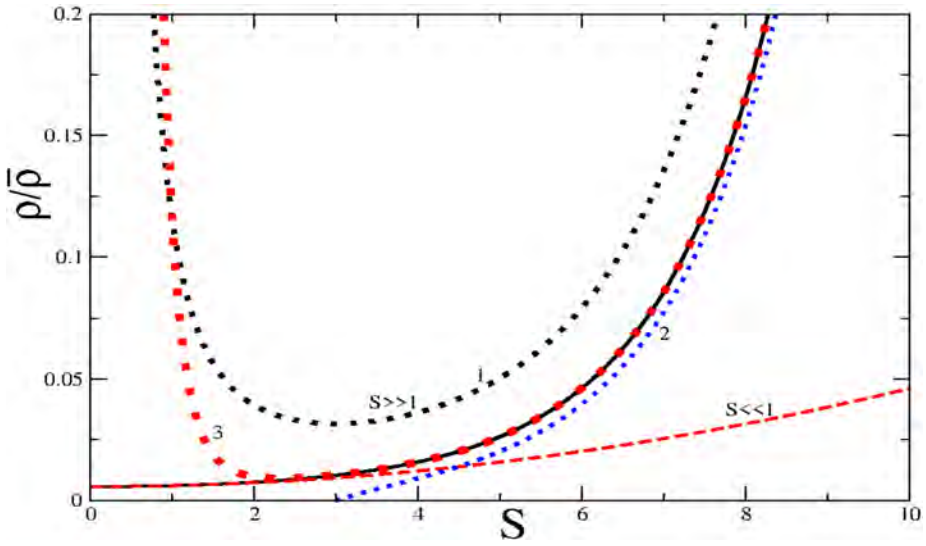

Fig. 1. The MMA level density $\boldsymbol{\rho}$ (solid line in units of $\bar{\boldsymbol{\rho}}$) is shown as function of the entropy $\boldsymbol{S}$ for different approximations: 1) $\boldsymbol{S} \ll \mathbf{1}$ (red dashed line) at quadratic order $\boldsymbol{\rho} \propto \mathbf{1} + \boldsymbol{S}^2/\mathbf{14} + \cdots$; 2) $\boldsymbol{S} \gg \mathbf{1}$ «1», «2», and «3» for expansions, up to zeroth, first, and second-order terms, respectively, in the square brackets of: $\boldsymbol{\rho} \propto \mathbf{exp}(\boldsymbol{S})\left[\mathbf{1} - \frac{\mathbf{3}}{\boldsymbol{S}} + \frac{\mathbf{3}}{\boldsymbol{S}^2} \ldots\right]$.

Additional integrals of motion can also be the projection of angular momentum M of a nuclear system for rotational of deformed nuclei [2,3]. Fitting the MMA total level density, ρ, for a set of the integrals of motion, $\mathbf{Q} = (N, Z, M)$, to the experimental data for low excitation energy states in a nucleus, one obtains the results for the inverse level-density parameter $K = A/a$, where a, is the level density

parameter a, and $A = N + Z$. For the entropy S, one obtains $S = 2(aU)^{1/2}$ where $U = E - E_0 - J\omega^2/2$, $E_0 = E_{\rm ETF} + \delta E$, $E_{\rm ETF}$ is the smooth ETF energy part, and δE is the energy shell correction to the background energy E_0. Similarly, one has $J = J_{\rm ETF} + \delta J$ as the corresponding decomposition for the moment of inertia J. The shell corrections δE and δJ determine the oscillating part δS of the entropy S through the shell corrections $\delta\Omega$ to the generalized grand-canonical potential Ω with a similar decomposition $\Omega = \Omega_{\rm ETF} + \delta\Omega$. Within the semiclassical periodic-orbit theory at thermal equilibrium with temperature T and zero spin, one finds

$$\delta\Omega = \sum\nolimits_{\rm PO} \left(\hbar^2/t_{\rm PO}^2\right)(\tau_{\rm PO}/\sinh\tau_{\rm PO})\, g_{\rm PO} \cos(S_{\rm PO}/\hbar - \mu_{\rm PO}\pi/2 + {\rm const})\,,$$

where $\tau_{\rm PO} = \pi T t_{\rm PO}/\hbar$; $t_{\rm PO} = \partial S_{\rm PO}/\partial e$ is the period, $S_{\rm PO}(e)$ is the classical action, $\mu_{\rm PO}$ is the Maslov index, and $g_{\rm PO}$ is the single-particle level-density amplitude for the periodic orbit (PO) at the Fermi energy $e = e_F$. For small temperatures T, one obtains $\delta\Omega \to \delta E$. For large temperatures, $T \gtrsim T_{\rm SH} \approx D_{\rm SH}/\pi = (2-3)$ MeV, at large particle numbers $A = 100 - 200$, one finds an exponential decrease of shell effects. Here, the distance between major shells was evaluated semiclassically as $D_{\rm SH} \approx 2\pi\hbar/t_{\rm PO} \approx e_F/A^{1/3} = (7-10)$ MeV. Fig. 2 shows nice agreement of the MMA results [2] for the level density with experimental data for several deformed nuclei at low excitation energies. The MMA at low excitation energies clearly manifests an advantage over the standard Fermi gas asymptote (FG) [1] because of no divergences of the MMA in the limit of small excitation energies U. Another advantage takes place for ^{166}Ho, which has a lot of states in the very low-energy range (cf. Fig. 2(b), and Fig. 2(a)). Shell effects of the MMA approach are important for nuclei ^{166}Ho and ^{240}Pu, in contrast to the nucleus ^{150}Sm.

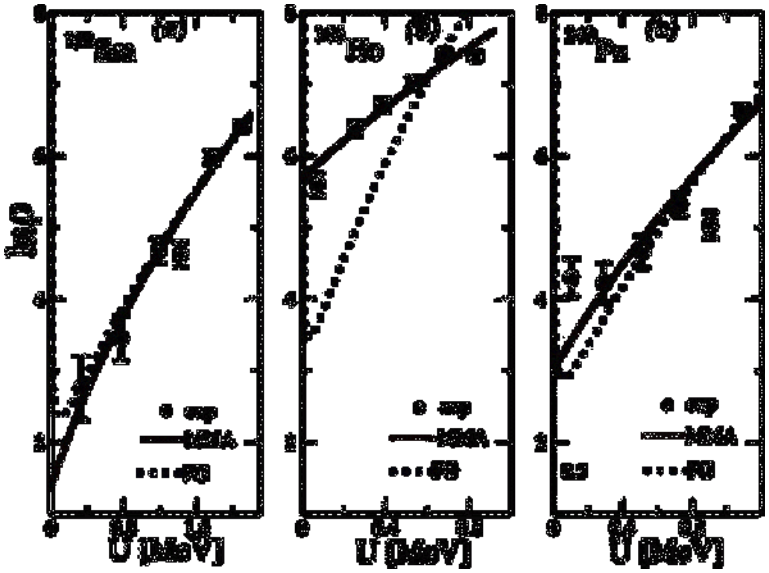

Fig. 2. Level density, $\ln\rho$, as function of the excitation energy U in shown nuclei, obtained in the MMA approach (red solids) for the smallest critical error parameter of the least mean-square fit σ [2]. Blue dots present the results of the Fermi gas (FG) approach [1]. Experimental dots are obtained by the sample method from quantum spectra of the ENSDF database http://www.nndc.bnl.gov/ensdf, accounting for spin degeneracies of nuclear states.

The inverse level density parameter, K, was obtained by one-parametric fit of the MMA level densities ρ, taking into account the shell and neutron-proton asymmetry effects, with the experimental results for several chains of isotopes. We have found a significant shell effect in the parameter K as function of the particle number A for the nuclear low-energy states range within the POT. We emphasize the importance of the shell, neutron-proton asymmetry, and rotational effects in these calculations. Taking long Pt and Nd isotope chains as typical examples, one finds a saw-toothed behavior of $K(A)$ as function of the particle numbers A, and its remarkable shell oscillation. We obtained values of K, that are significantly larger than those obtained for neutron resonances, due mainly to accounting for the shell effects. We show that the semiclassical POT is helpful in the low-energy states range for obtaining analytical shell-structure descriptions of the level density. The main part of the interparticle interaction is described in terms of the ETF counterparts of the statistically averaged nuclear potential, and of the level density parameter. Our MMA approach accounting for the spin dependence of the level density was extended to the collective rotations of deformed nuclei within the unified rotation model [2,3]. The well-known effects of the enhancement due to the nuclear collective rotations were found with accounting for the shell structure and neutron-proton asymmetry [3]. This approach might be interesting in the study of isomeric quasistationary states in strongly deformed nuclei at high spins. For perspectives, we suggest also to use our results for collective quantum spectra in deformed rotating nuclei obtained in the two-neutron transfer reactions (p,t), and for calculations of the fission widths. We may apply the MMA approach for metallic clusters and quantum dots, as well as for several problems in nuclear astrophysics.

[1] T. Ericson, Adv. In Phys. **9**, 425 (1960).

[2] A.G. Magner, A.I. Sanzhur, S.N. Fedotkin, A.I. Levon, and S. Shlomo, Phys. Rev. C **104**, 044319 (2021); Int. J. Mod. Phys. E **30**, 2150092 (2021); Nucl. Phys. **A1021**, 122423 (2022).

[3] A.G. Magner, A.I. Sanzhur, S.N. Fedotkin, A.I. Levon, U.V. Grygoriev, and S. Shlomo, Low Temp. Phys. **48**, 920 (2022).

Particle-number fluctuations near the critical point of nuclear matter

A.G. Magner,[1,2] S.N. Fedotkin,[1] and U.V. Grygoriev[1,3]
[1]*Institute for Nuclear Research, 03028 Kyiv, Ukraine*
[2]*Cyclotron Institute, Texas A&M University, College Station, Texas 77843, 120 Spence St., USA*
[3]*University of Groningen, Van Swinderen Institute for Particle Physics and Gravity, 9747 AG, Groningen, Netherlands*

Many works have been devoted to studying the properties of nuclear systems with strongly interacting particles. Thermodynamical behavior of the nuclear matter leads to liquid-gas first-order phase transition, which ends at the critical point, with special theoretical and experimental emphasis on finiteness of nuclear systems in multifragmentation reactions. The role and size of the effects of quantum statistics were studied [1] for van der Waals (vdW) and Skyrme (SLD) local density interparticle interactions for relatively low temperatures T, which is assumed to be smaller or of the order of 30 MeV and not too large particle number density ρ. In the present work [2] we apply the same analytical method for the equation of state [1] to analyze the particle number fluctuations ω near the critical point of nuclear matter with a focus on the finiteness of a sufficiently large average particle number $\langle N\rangle$ within the grand canonical ensemble.

Using the ideas of Smoluchowski and Einstein we use the expansion of the free energy $F(\rho)$ in powers of small deflections $\rho - n$, where $n = \langle\rho\rangle$ is a statistical average of the particle density ρ for symmetrical nuclear matter. The standard results for particle number fluctuations $\omega = T/K$, where K is the isothermal incompressibility, diverge at the critical point T_c, ρ_c of the nuclear matter because of $K \to 0$ for $T \to T_c$ and $\rho \to \rho_c$. They can be obtained for such a quadratic expansion of the free energy $F(\rho)$ on a finite distance from the critical point, defined by equations $(\partial P/\partial \rho)_T = 0$ and $(\partial^2 P/\partial \rho^2)_T = 0$, in the T, ρ plane for dominating second order terms with finite $K = (\partial P/\partial \rho)_T$. Here, $P = P(T, \rho)$ is the pressure of the equation of state. Taking into account the quantum statistical corrections at first order we derived the analytical expressions for such a fluctuation, $\omega = T/K$, near the critical point for the vdW and SLD effective interparticle interactions. This fluctuation is obtained as an explicit analytical functions of the temperature T, particle density ρ, particle's mass and their degeneracy in good agreement with more accurate numerical results; see, e.g., Ref. [3] for the SLD interaction case.

Within the same Smoluchowski and Einstein method, expanding $F(\rho)$ over powers of small differences $\rho - n$ up to fourth order terms and including the second order ones, for a finite second order derivative of the incompressibility, $K_2 = \partial^2 K/\partial \rho^2$ near the critical point $\rho = n_c$, we have derived analytically a simple expression for the generalized particle number fluctuations ω, in terms of the modified Bessel functions. We found the fluctuation ω as function of the parameter $\alpha \propto K^2\langle N\rangle(n^2 T K_2)^{-1}$ depending on the particle number average $\langle N\rangle$. From this expression we obtained the two asymptotic limits. One of them is the Landau classical limit $\omega \to T/K$ for $\alpha \gg 1$, working well for infinite nuclear matter everywhere, except for a small range near the critical point. Another one is the Rowlinson and Tolpygo finite limit, approximately $\omega \to (6\langle N\rangle T(n^2 K_2)^{-1})^{(1/2)}$ to the critical point for $\alpha \ll 1$ at a finite particle-number average $\langle N\rangle$.

Fig. 1 shows the particle number fluctuations $\omega/\langle N\rangle$ as functions of the averaged density n at the critical temperature $T = T_c$ for different finite large values of $\langle N\rangle$. We clearly present divergence of the asymptote $\alpha \gg 1$ by dashed lines, and convergence to our generalized result (solid lines). The solid curves of a generalized approach have finite pronounced maxima near the critical density value $n \approx n_c$, in contrast to the Landau asymptotic formula. The SLD (with different set of parameters for $\gamma = 1/6$ and $\gamma = 1$) and vdW results for fluctuations are rather similar. The difference between the fluctuations $\omega/\langle N\rangle$ for the SLD and vdW forces are a slightly greater asymmetry of the curves for the vdW case with respect to the critical value of the particle number density, n_c, and a little larger values at the corresponding vdW maxima. Notice also that with increasing values of $\langle N\rangle$ the fluctuations $\omega/\langle N\rangle$ are decreasing to zero when $\langle N\rangle \to \infty$.

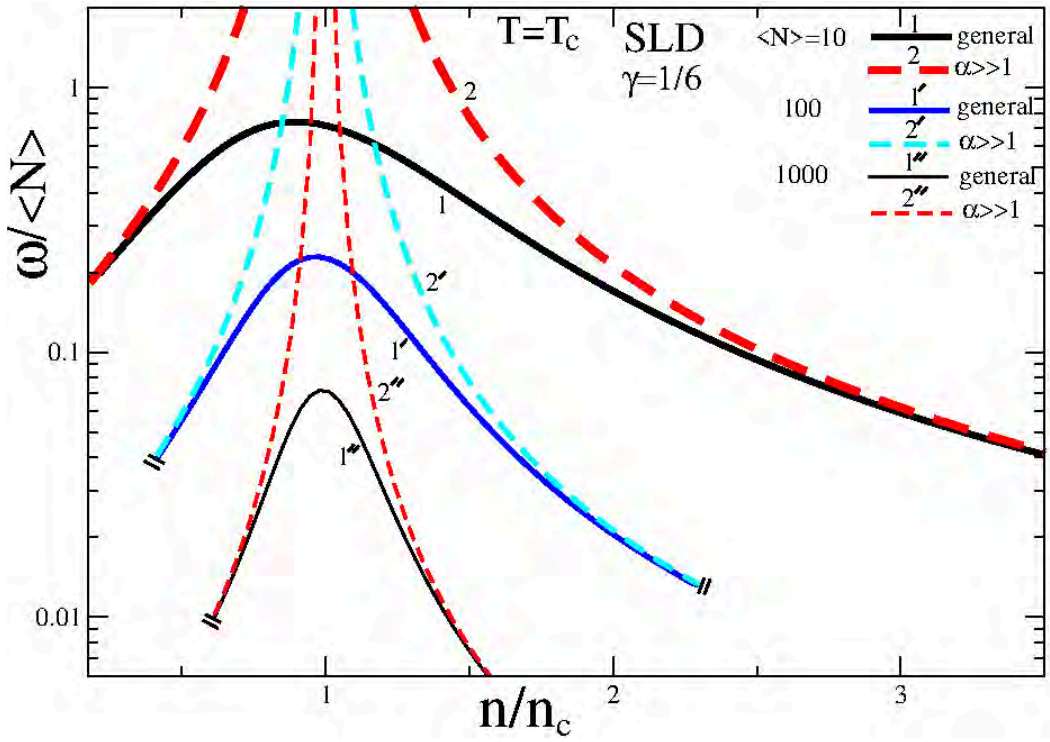

Fig. 1. Particle number fluctuations $\boldsymbol{\omega}$, divided by mean particle numbers $\langle \boldsymbol{N}\rangle$, at different typical values of $\langle \boldsymbol{N}\rangle$, are shown by solid lines as functions of the mean particle-number density $\boldsymbol{n}$ (in units of its critical value $\boldsymbol{n_c}$) at the critical temperature $\boldsymbol{T = T_c}$ for symmetric nucleon system with the Skyrme local-density effective interparticle interaction with some parameters $\boldsymbol{a = 1.167 GeV \cdot fm^3}$, $\boldsymbol{b = 1.475 GeV \cdot fm^{3+3\gamma}}$, and $\boldsymbol{\gamma = 1/6}$, for which one has [1,2] good agreement for the critical point with more accurate numerical calculations [3]. Dashed lines present the corresponding Landau asymptotes for $\boldsymbol{\alpha \gg 1}$.

[1] S.N. Fedotkin, A.G. Magner, and U.V. Grygoriev, Phys. Rev. C **105**, 024621 (2022).

[2] A.G. Magner, S.N. Fedotkin, and U.V. Grygoriev, Phys. Rev. C **107**, 02610 (2023).

[3] L.M. Satarov, I.N. Mishustin, A. Motornenko, V. Vovchenko, M.I. Gorenstein, and H. Stocker, Phys.Rev. C **99**, 024909 (2019).

Resonances in low-energy nuclear processes and nuclear astrophysics and asymptotic normalization coefficients. A review

A. M. Mukhamedzhanov

This paper is continuation of the previous review [Mukhamedzhanov and Blokhintsev, Eur. Phys. J. A **58**, 29 (2022)] in which the asymptotic normalization coefficient (ANC) of a bound state was addressed. However, the ANC is important characteristics not only of bound states but also resonances. In this paper, the role of the ANCs in resonance processes is addressed. Among various topics considered here are Gamow-Siegert resonance wave functions for charged particles and their normalization, relationship between ANCs and resonance widths. Significant part is devoted to the R-matrix approach for resonance processes. The resonance wave functions, internal and external and their projections on the two-body channel are given. Important ingredients of the R-matrix method for resonance states are also discussed. Elastic resonance scatterings are analyzed and extended for subthreshold resonances. It is shown how the notion of the subthreshold resonance works in practical analysis. To this end, the ^{13}C(alpha, n)^{16}O reaction, which is considered to be the main neutron supply to build up heavy elements from iron-peak seed nuclei in AGB stars, is analyzed. Important part of the review is analysis of the relationship between resonance width and ANC of mirror resonance and bound states using the Pinkston-Satchler equation and the Wronskian method. Practical examples are given. Among important parts of the theoretical research is the theory of transfer reactions populating resonance states. Comparative analysis of prior and post-form DWBA amplitudes shows that the prior form is preferable over the post form due to faster convergence of the matrix element over the radius rnA between the transferred neutron and target . Calculations of the stripping to resonance reaction ^{16}O(d; p)^{17}O(d3/2) performed using the prior form of the CDCC method. A special attention is given to resonance astrophysical processes. Useful equations for internal and external radiative widths are given. Radiative capture through subthreshold resonance is considered. In particular, radiative capture reactions ^{11}C(p,gamma)^{12}N and ^{15}N(p,gamma)^{16}O and the role of the ANC is addressed in detail.

The paper was published in Eur. Phys. J. A **59**, 43 (2023).

Status of deep subbarrier $^{12}C + ^{12}C$ fusion and advancing the Trojan horse method

A.M. Mukhamedzanov

In this work, I updated the current status of thecarbon–carbon fusion research taking into account that after the latest analysis (Beck et al. in Eur Phys J A 56:97, 2020) new important experimental and theoretical results had been published and discussed how to advance new THM measurements to extract the low-energy astrophysical S-factors. The kinematical conditions of two different suggested experiments are analyzed. The preparation for one of them, 13C(12C, n)24Mg*, where 24Mg* is the resonance decaying into alpha+20Ne and p+23Na channels, is underway by the group
of Prof. G. Rogachev (Cyclotron Institute).

This work was published in Eur. Phys. J. A **58**, 71 (2022).

Carbon burning towards the zero energy limit: An α-cluster study in imaginary time

T. Depastas and A. Bonasera

The carbon burning process is a fundamental step of stellar evolution and governs the synthesis of chemical elements important for the formation of life. It has already been investigated from the late 1960's [1]. Since then, its description is the central theme of several studies, both theoretical [2-4] and experimental [5-8]. In this work, we utilize the microscopic hybrid α-cluster (HαC) model and an analytical approach, both in the framework of the Imaginary Time Method (ITM), to study the carbon fusion reaction towards zero energy. The HαC model [9] is a semi-classical dynamical approach to the nuclear N-Body problem, that considers the dynamical evolution of the α-degrees of freedom within A=4n nuclei. The ITM [2] on the other hand, is a procedure based on the Feynman Path Integral method, that simulates the quantum tunneling below the Coulomb barrier (Fig. 1), in a microscopical dynamic model, such as HαC.

We obtain the values of the cross sections, astrophysical factors (Fig. 2) and correlate our results to collective motion. We also include a calculation for the 2^+ carbon fusion and discuss a possible experimental investigation. The results confirm direct experimental and theoretical results close to the barrier, while suggest possible 2^+ mixtures in the indirect experimental data. Our study offers an accurate view of the burning process in the somewhat unexplored low energy region.

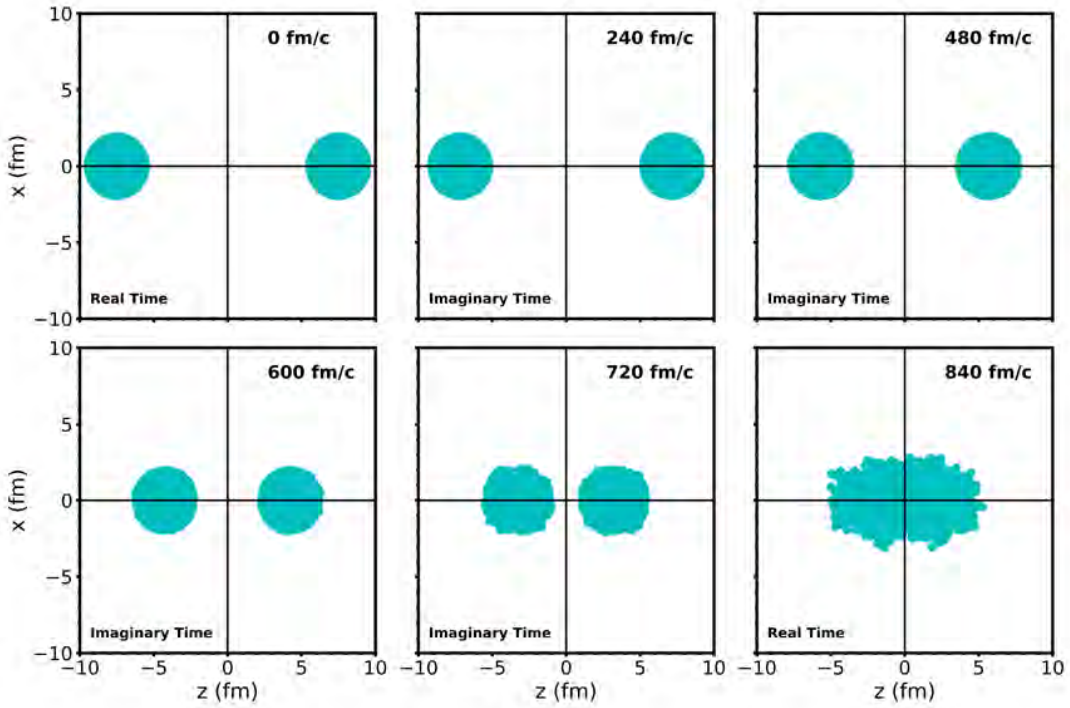

Fig. 1. (Color online) Evolution of the 12C+12C fusion in the xz plane with EC.M. = 3.5 MeV. The cyan points are the densities of the alpha particles from 300 event calculations with the HαC model, while the reaction axis is defined to be the z-axis.

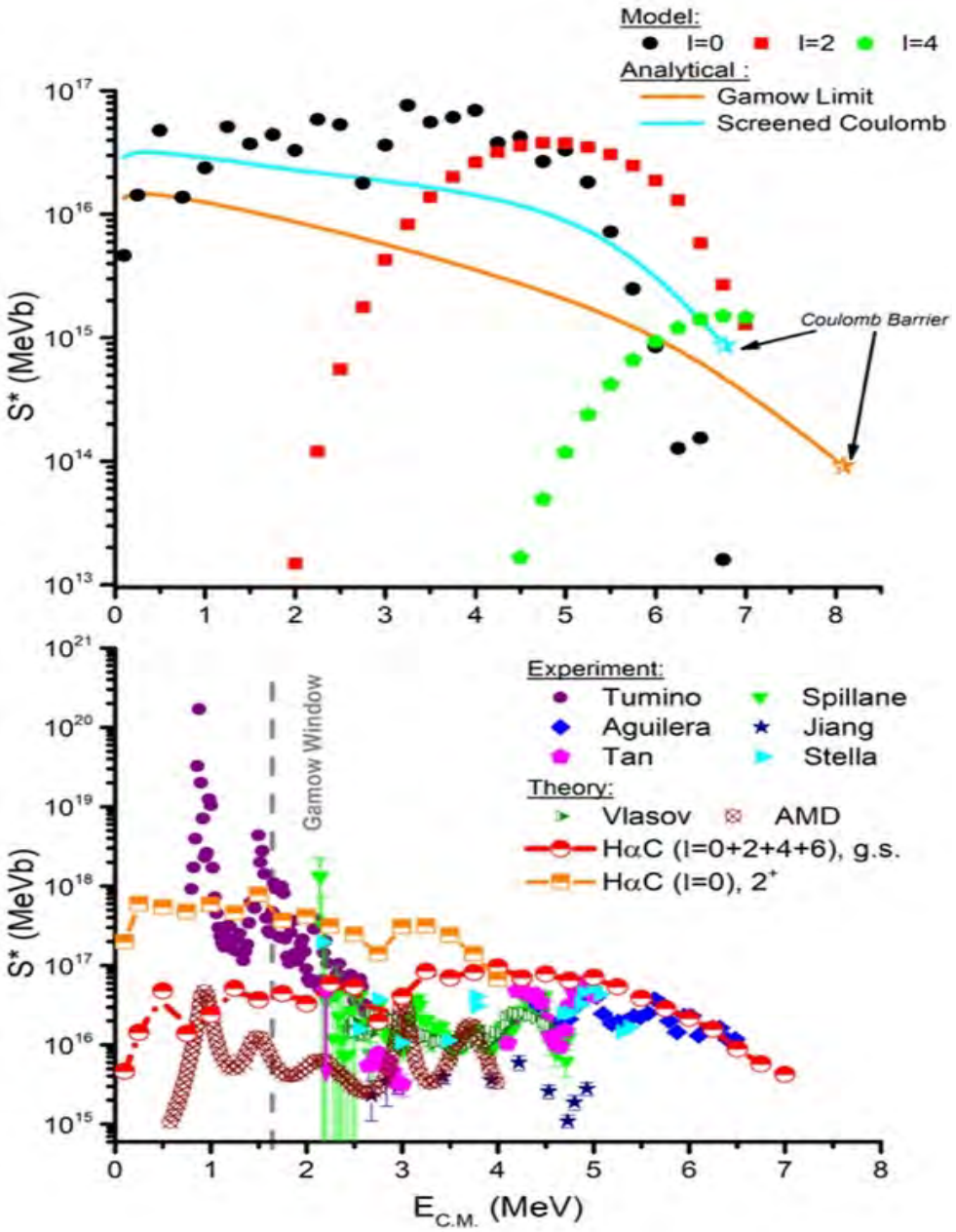

Fig. 2. (Color online) Top Panel: The S∗ factors as a func:on of energy for different l-values (points) obtained via the HαC model and via the analytical approach with free and screened Coulomb (lines), according to the key. BoIom Panel: The S∗ factors as a func:on of energy from several experimental [5-8] and theoretical [2,4] data sets. This work corresponds to the red curve for all l-values (g.s.) and orange curve (4.44 MeV, 2+), as obtained with the HαC model. The pink arrow corresponds to the lowest energy direct measurement and represents an upper limit.

[1] J. Patterson, H. Winkler, and C. Zaidins, Astrophys. J. **157**, 367 (1969).
[2] A. Bonasera and V. Kondratyev, Phys. Lett. B **339**, 207 (1994).
[3] A. Bonasera and J.B. Natowitz, Phys. Rev. C **102**, 061602 (2020).
[4] Y. Taniguchi and M. Kimura, Phys. Lett. B **823**, 136790 (2021).
[5] E.F. Aguilera *et al*., Phys. Rev. C **73**, 064601 (2006).
[6] C. Beck, A. Mukhamedzhanov, and X. Tang, Eur. Phys. J. A **56** (2020).
[7] C. Jiang *et al.*, Phys. Rev. C **97**, 012801 (2018).
[8] A. Tumino *et al.*, Nature **557**, 687 (2018).
[9] H. Zheng and A. Bonasera, Symmetry **13**, 1777 (2021).

Dynamical pair production at sub-barrier energies for light nuclei

T. Settlemyre, H. Zheng,[1] and A. Bonasera
[1]School of Physics and Information Technology, Shaanxi Normal University, Xi'an 710119, China

In the collision of two heavy ions, the strong repulsion coming from the Coulomb field is enough to produce e^+e^- pair(s) from vacuum fluctuations [1]. The energy is provided by the kinetic energy of the ions and the Coulomb interaction at the production point. If, for instance, the electron is located at the center of mass (C.M.) of the two ions moving along the z-axis, and the positron is at a distance x from the electron, the ions can be accelerated towards each other since the Coulomb barrier is lowered by the presence of the electron. This screening results in an increase in the kinetic energy of the colliding ions and may result in an increase in the fusion probability of light ions above the adiabatic limit.

In Fig. 1, we plot the effective potential (bottom panel) and the potential ($\pm m_T$−top panel) vs. the relative distance between the pair. The only acceptable solution is the lowest one given by the red line. A simple inspection of the top panel shows that the positron for this case is initially in the negative energy region and tunnels to the positive one. The other solution gives the positron already in the positive energy region (green line); thus, is not allowed by our proposed mechanism. Other possible solutions can be found

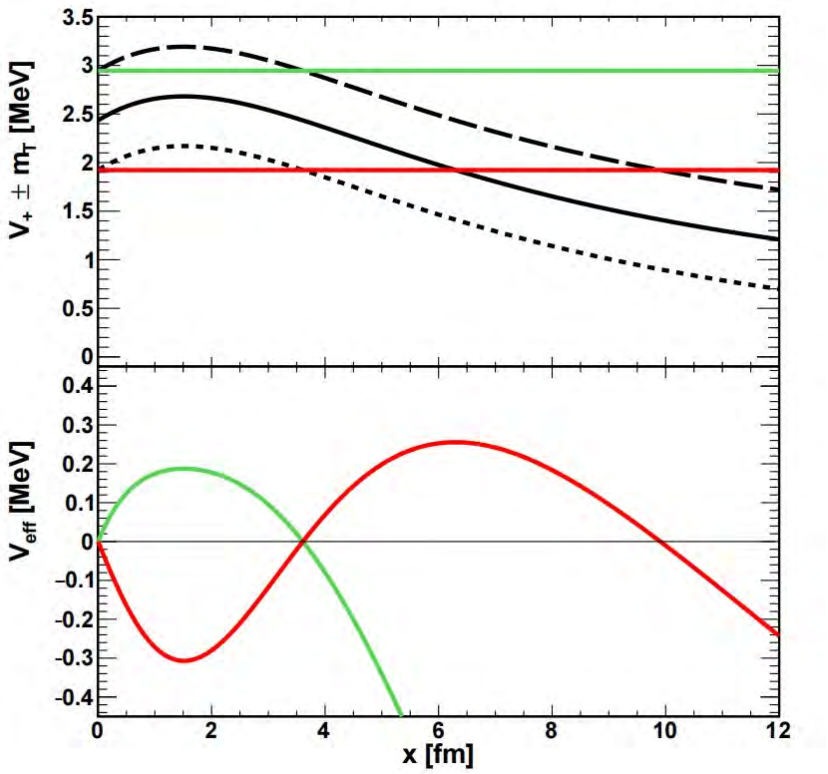

Fig. 1. (Color online) An illustrative example when $V_{eff}(R, 0) = 0$. In the bottom panel we plot V_{eff} vs. x and the corresponding potential with full line ($\pm m_T = m_e$−top panel, dashed and dotted lines) seen by the positron. The calculations are performed for $^{12}C+^{12}C$ collisions.

if $V_{eff}(R, x = 0) < 0$. From this discussion, we learned that the two ions can gain kinetic energy because of the location of the electron (in the middle) and the positron (away from the ions) (Fig. 1), and may enhance the sub-barrier fusion probability

For $^{12}C+^{12}C$, we find the maximum number of pairs produced in the collisions by summing over the trajectory without taking into account the energy loss after a pair is produced. The maximum is attained near $E_{c.m.}= 4$ MeV ($\Delta E_k = 2m_e$) in Fig. 2. Clearly, the maximum number of pairs produced in the collisions, and the relative cross-section of Fig. 2, critically depends on the ultraviolet cutoff x_s and it must be confirmed or modified by future experimental data. Furthermore, microscopic calculations following the heavy ion trajectory and the dynamics of one or more pairs created during the time evolution must be implemented in order to make predictions for heavier colliding nuclei and collisions of different mass number nuclei.

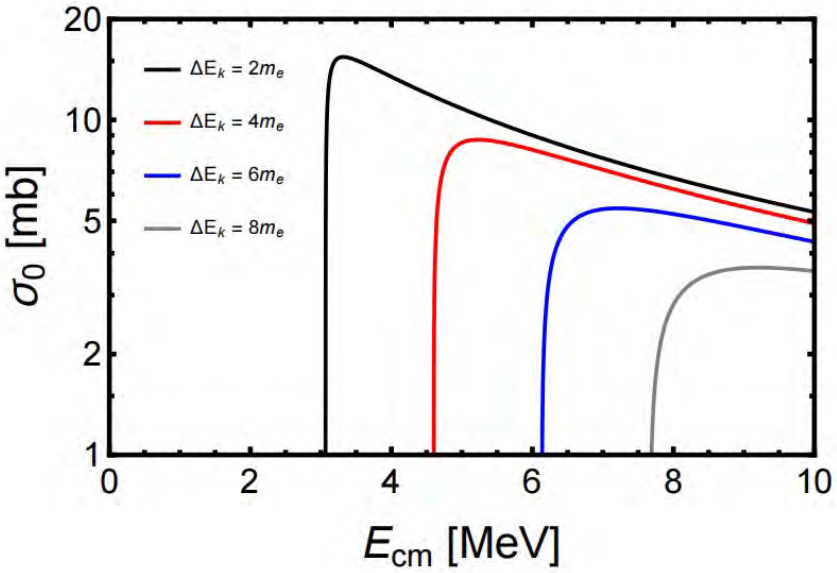

Fig. 2. (Color online) Upper limit for the integrated cross-section for e^+e^- production in $^{12}C+^{12}C$ scattering below the Coulomb barrier for different values of ΔE_k. We stress that $\Delta E_k \geq 0$.

We have discussed pair production from a vacuum within the Schwinger formalism. We have shown the conditions for tunneling and the possibility that, if the electron is situated at the c.m. of the colliding nuclei, extra screening may occur. This screening may enhance sub-barrier fusion of light nuclei above the adiabatic limit. For $^{12}C+^{12}C$ collisions, we predict $E_{c.m.}\geq 1$ MeV for this effect to occur. The cross-sections are of the order of mb or less. These predictions call for detailed experimental investigation of pair production for this system, and also their energies, in coincidence with fusion fragments to be able to extract correlation functions. An enhancement may be shown by performing a correlation between fusion events with and without pair production.

[1] T. Settlemyre, H. Zheng and A. Bonasera, Particles **5**, 580 (2022).

Pair production as a probe for the dynamics of nuclear fission and alpha decay

T. Settlemyre, H. Zheng,[1] and A. Bonasera
[1]*School of Physics and Information Technology, Shaanxi Normal University, Xi'an 710119, China*

Electron-positron pairs can be produced via the Schwinger mechanism in the presence of strong electric fields [1]. In particular, the fields involved in alpha decay and nuclear fission are strong enough to produce them. The energy of the e^+e^- pair is related to the relative distance and velocity of the daughter nuclei. Thus, the energy distribution of the produced pairs can give information about the dynamics of the fission and alpha-decay processes. A neck model of nuclear fission is used to illustrate how the pairs can be used as a probe of the dynamics.

The positron spectra for symmetric fission of several heavy nuclei are shown in Fig. 1. Previous experimental investigations have looked for a coincidence between e^+ and e^- [2]. In our approach the coincidence is lost because the electron gets trapped by the nuclei. We suggest an experiment to look for e^+ in coincidence with a fission fragment and not with e^-.

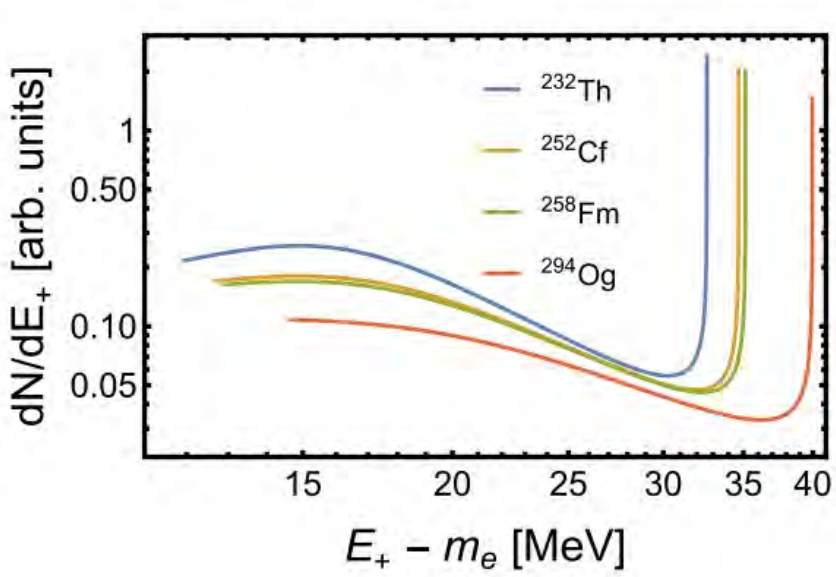

Fig. 1. (Color online) dN/dE_+ for fission of a selection of nuclei. The fission dynamics are based on the neck model. Here, $m_T = m_e$, $\beta = 0$, and $E_k = 2m_e$.

Our model predicts that electron-positron pairs can be created during alpha decay or fission. The energy of the created positron is related through the conservation of energy to the distance between the progeny nuclei. Careful observation of the energy spectrum of pairs produced during fission could reveal the dynamics of the fission process, properties of the vacuum polarization, and the tunneling "dynamics."

[1] T. Settlemyre, H. Zheng and A. Bonasera, Phys. Rev. C **107**, L031301 (2023).
[2] T. Tsunoda *et al.*, Workshop on Dynamical Symmetry Breaking (Nagoya University, Nagoya, Japan pp. 175 (1989).

2023 progress in research

C. Parker, R.J. Fries and JETSCAPE collaborators

Bayesian Tuning of JETSCAPE

The JETSCAPE framework exists to model relativistic heavy ion collisions by combining several separate codes, such as MATTER, Pythia, and custom modules, in order to provide a universal framework for generating events [1]. Our work has been on evaluating its potential in $p + p$ and $e^+ + e^-$ systems. We do so by running the framework for a variety of parameter combinations and then using Bayesian analysis to determine which combination yields the best results compared to experimental data. Of principal interest are the MATTER and hybrid hadronization modules in JETSCAPE.

We run JETSCAPE for 3 systems, $e^+ + e^-$ at 91.2 GeV, $p + p$ at 200 GeV, and $p + p$ at 2760 GeV. $p + p$ events must be generated in sections, where we divide up the events by momentum transfer $\hat{p}_T$ in the hard scattering. The combination of both low and high momentum events is unusual for JETSCAPE runs but is critical for being able to describe the data accurately.

Results

The Bayesian tuning itself involves comparing the generated events to data for a spread of event generation parameters. They are given scores based on how well they match, and then we use a Gaussian Process Emulator to creat new simulated data for a new spread of event generation parameters. This process is repeated until the spread converges onto the values that best recreate the data. For this, the simulated data must be close enough to the actual data so that a good value can be found. The Transformation of the generated runs is shown below in Figs 1 and 2 for p+p only.

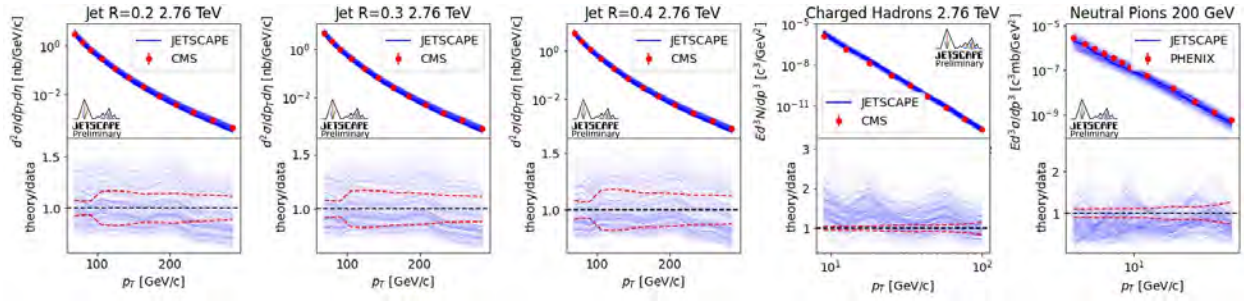

Fig. 1. Observables for the generated JETSCAPE runs before the parameter distribution is transformed. We use data from the CMS collaboration [2-4] and the PHENIX Collaboration [5]. Each blue line corresponds to a single set of parameters.

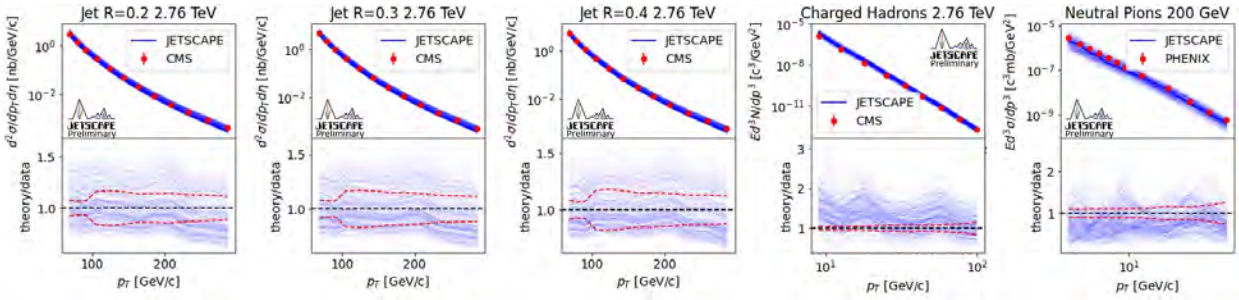

Fig. 2. Observables for the generated JETSCAPE runs after the parameter distribution is transformed. The spread narrowing corresponds to the new distribution finding a good set of values that describe the data.

Future Work

We are currently updating our spectra to use a new form of event combining. Rather than attempt to blend low and high momentum events, we are instead separating them into distinct regions and comparing them to observables specific to them. This allows us to tune over all regions. We are also using our tune to provide predictions to the ALICE collaboration for some of their heavy flavor studies.

[1] J.H. Putschke *et al.* The JETSCAPE framework (2019).
[2] ALICE Collaboration. HEPData (collection) (2014). https://doi.org/10.17182/hepdata.62520.
[3] CMS Collaboration. HEPData (collection) (2012). https://doi.org/10.17182/hepdata.58980.
[4] CMS Collaboration. HEPData (collection) (2018). https://doi.org/10.17182/hepdata.77601.
[5] PHENIX Collaboration, Phys. Rev. D **76**, 051106(R) (2007).

Excited states in hadronization

R.J. Fries, C.M. Ko, J. Purcell and M. Kordell

In the previous report we have discussed the computation of probabilities for coalescence of two distinguishable, non-relativistic particles into bound state with well-defined angular momentum, described by a isotropic 3-D harmonic oscillator potential [1]. The initial particles are represented by generic Gaussian wave packets of given average positions and momenta. Using a phase-space formulation we had arrived at final probabilities $P_{kl}(\boldsymbol{r},\boldsymbol{p})$ for forming bound state with quantum numbers k,l and summed over all possible m (k = radial, l = angular momentum, m = magnetic quantum numbers). They are expressed in terms of the relative center coordinates of the wave packets in phase space, $\boldsymbol{r}$ and $\boldsymbol{p}$. For example, in the simplest case[1]

$$P_{10} = \frac{1}{2} e^{-v} \left(\frac{1}{3} v^2 - \frac{1}{3} t \right)$$

for $k = 1$, $l = 0$. Here $v = (\nu^2 r^2 + p^2/\nu^2\hbar^2)/2$ and $t = (r^2 p^2 - (\boldsymbol{r}\cdot\boldsymbol{p})^2)/\hbar^2$. Since $t = L^2/\hbar^2$, where L is the classical angular momentum of the wave packet centroids, one can clearly correlate the initial angular momentum of the 2-quark system with the probabilities to form states with a particular orbital angular momentum l.

In the current reporting period we have used these probabilities to implement the recombination of quarks and antiquarks into mesons up $N = 2k + l = 4$ into Hybrid Hadronization. Taking into account the correct spectrum of hadrons is important in many applications, and we expect this to hold for hadronization as well. Hybrid Hadronization is a hadronization model which combines quark recombination and Lund string fragmentation [2]. By sampling recombination probabilities, quarks close enough in phase space will directly recombine into hadrons while partons further apart in phase space are forming color singlet string systems which then fragment into hadrons. The total probability for recombination of a given quark-antiquark pair contains the probability for overlap in phase space as well as factors from the overlap of spin and color states, $P_{tot} = P_{kl} \times P_{spin} \times P_{color}$.

We use PYTHIA 8 to prepare final parton systems in 91 GeV e^++e^- collisions and feed these, including their color tag information, into a standalone version of Hybrid Hadronization.

Fig. 1 shows the yields per event (recombination only) for mesons with different quantum numbers, radial $n_r = k$, orbital angular momentum l, and total angular momentum j. The most important outcome of this study is that p- and d-wave mesons are important channels for recombination even in the most dilute collision system represented by e^++e^-. Note that many mesons up to $N = 4$ are not available in the Particle Data Book and have been assumed in this study, with their masses extrapolated from empirical scaling laws. More detailed studies of the impact of excited mesons are under way.

[1] This refers to the fact that results are simplest if the widths of the particle wave packets and the harmonic oscillator potential are in a certain relation [1].

This work was support by the U.S. National Science Foundation under awards 1812431 and 2111568, the U.S. Department of Energy under Award No. DE-SC0015266, and the Welch Foundation under Grant No. A-1358.

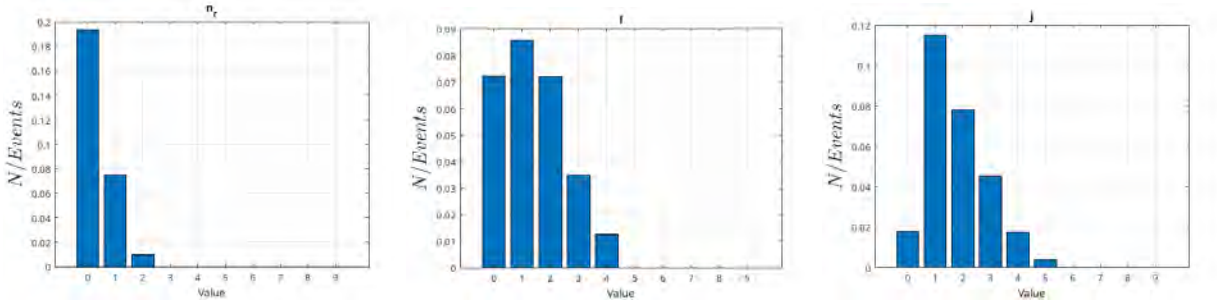

Fig. 1. Yields per events for recombined mesons states with particular quantum numbers n_r, l and j. $n_r = k$ here is the radial quantum number and j denotes total angular momentum from the operator $\boldsymbol{J} = \boldsymbol{L} + \boldsymbol{S}$**.** One can see that p-wave and d-wave mesons ($l = 1, 2$, resp.) play an important role in recombination, even in a dilute systems.

[1] M. Kordell II, R.J. Fries and C.M. Ko, Annals Phys. **443**, 168960 (2022).
[2] K. Han, R.J. Fries and C.M. Ko, Phys. Rev. C **93**, 045207 (2016).

The JETSCAPE collaboration: First X-SCAPE release and major hybrid hadronization updates

R.J. Fries with JETSCAPE collaborators

In previous versions of this report we have discussed the continuing work of the JETSCAPE collaboration. The original product, the JETSCAPE framework, has the main task of providing a framework for comprehensive simulations of A+A collisions. It is now available in version 3.5x [1]. In addition, in 2020 the NSF has approved the X-SCAPE project as the follow-up to JETSCAPE. The new framework will allow users to simulate lower energy nuclear collisions as well as proton-nucleus and electron-nucleus collisions. Thus X-SCAPE will offer much needed capabilities to support experiments at the Electron-Ion Collider. The EIC is the next-generation nuclear physics experiment planned by the Department of Energy at Brookhaven National Laboratory for 2030 and beyond. Fig. 1 shows a schematic flow diagram for the X-SCAPE framework. In the current reporting period version 1.0 of the X-SCAPE framework has been published.

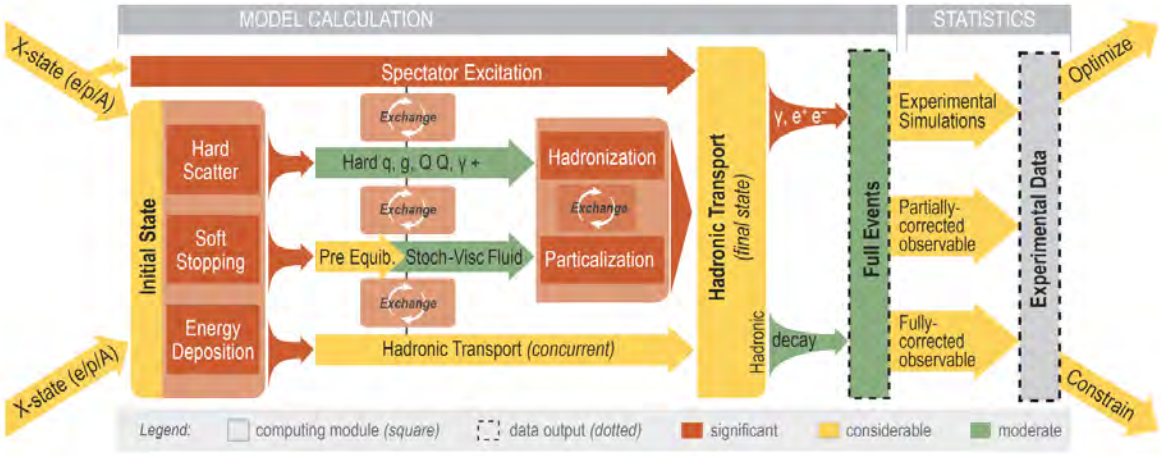

Fig. 1. Schematic Flow Diagram of the X-SCAPE event generator that will be able to simulate p+p, p+A, A+A, e+p and e+A collisions at high energies.

The JETSCAPE group at Texas A&M University maintains the Hybrid Hadronization module which will undergo a major update in the next versions of the JETSCAPE/X-SCAPE frameworks. Many of these updates were developed in collaboration with the JETSCAPE group of Hannah Elfner at the University in Frankfurt. These updates are briefly discussed below.

(i) There are several bug fixes to the handling of string junctions. String systems can get quite complex in Hybrid Hadronization, with multiple connected junctions carrying baryon number. Proper treatment of such string systems, taking into account the odds for PYTHIA 8 sucessfully fragmenting them, is important to accurately account for baryon number. Previous versions could lead to instances of PYTHIA 8 crashing or to violations of baryon number conservation. In the new version all junctions are given to PYTHIA separately to achieve excellent stability. (ii) There is now the option to force final hadrons onto the mass shell while preserving energy and momentum of the event. This is necessary for feeding hadrons in the

hadronic afterburner SMASH, but it is optional if final state hadrons are instead given to PYTHIA 8 for decay. (iii) Energy and momentum conservation at the start of the module, when the initial parton list is prepared for recombination, e.g. by decaying gluons non-perturbatively, are more strictly enforced in the new version. (iv) The process of adding beam partons to events, which is necessary if the full underlying event is not read into the framework, e.g. in p+p, has also been improved to avoid adding too much energy to the event. (v) There are tantalizing hints, e.g. from Λ_c production, that making full use of the hadron spectrum and the pertinent feeddown are important for a correct description of hadronization (see also a companion report in this volume). The recombination into excited and highly excited meson states has been implemented in the new version following [2]. However, currently these states can only be decayed by PYTHIA 8 with additional particle information data, as they are not implemented in SMASH. For the future, it is planned to restructure the handling of cross-sections in SMASH, such that the addition of new particles and channels is easier. (vi) There is also a more precise determination of the position of hadrons from string fragmentation. Hadrons that can be identified as coming from a particular string segment are now distributed evenly along the string segment, hadrons connected to a junction are placed along the junction legs.

With these improvements, new physics capabilities have been unlocked, e.g. the study of hadronic final state interactions of hadrons from hard processes using SMASH.

This work was support by the U.S. National Science Foundation under awards 2004571, and by the ExtreMe Matter Institute EMMI at the GSI Helmholtzzentrum für Schwerionenforschung, Darmstadt, Germany.

[1] The JETSCAPE 3.5x and X-SCAPE 1.0 packages, https://github.com/JETSCAPE
[2] M. Kordell II, R.J. Fries and C.M. Ko, Annals Phys. **443**, 168960 (2022).

Nuclear Theory – Nuclear astrophysics

J.W. Holt

Introduction:

The structure, phases, and dynamics of nuclear matter are crucial to understand stellar explosions, the origin of the elements, patterns in observed gravitational waves, and the composition of the densest observable matter in the universe. The appropriate tool to study strongly interacting matter at the typical scales relevant in nuclear astrophysics (well below the scale of chiral symmetry breaking $\Lambda_\chi \approx 1$ GeV) is chiral effective field theory [1-3]. In recent years, chiral effective field theory has become a cornerstone of the modern approach to nuclear many-body dynamics that provides a systematic framework for describing realistic microphysics, such as multi-pion exchange processes and three-body forces, within a well-defined organizational hierarchy. The long and intermediate-range parts of the nuclear potential result from one- and two-pion exchange processes, while short-distance dynamics, not resolved at the wavelengths corresponding to typical nuclear Fermi momenta, are introduced as contact interactions between nucleons. Chiral effective field theory is unique in its multichannel methods for quantifying uncertainties and especially in its ability to estimate the importance of missing physics.

Optical potential comparison project

Large-scale astrophysical simulations are essential for identifying the site of the r-process, the primary candidates being the wind-driven ejecta from accretion disks surrounding binary neutron-star mergers or collapsars as well as the neutrino-driven winds of core-collapse supernovae. Neutron-capture rates on exotic neutron-rich isotopes are particularly important during the non-equilibrium freeze-out phase of r-process nucleosynthesis, but direct experimental studies at rare-isotope facilities remain unfeasible. The large uncertainties in these capture rates, due in part to difficulties in extrapolating phenomenological optical model potentials far from the valley of stability, limit the precision of predicted heavy-element abundances. Previously, we have constructed [4-6] from chiral effective field theory two- and three-body forces a microscopic global nucleon-nucleus optical potential with quantified uncertainties.

More recently, we have participated in a comparison project of optical potentials [7] to motivate future research directions in the field. In particular, we have clarified the important role of uncertainty quantification in both phenomenological and microscopic reaction theory calculations. In Fig. 1 we show the asymmetry in the total cross section for neutron scattering on ^{40}Ca and ^{48}Ca computed from several microscopic and phenomenological optical potentials. This quantity is a sensitive probe of the isospin dependence of the cross section away from stability, and we find that the microscopic calculation from chiral EFT (shown as the blue band) compares favorably to data as well as the phenomenological Koning-Delaroche optical potential with error analysis

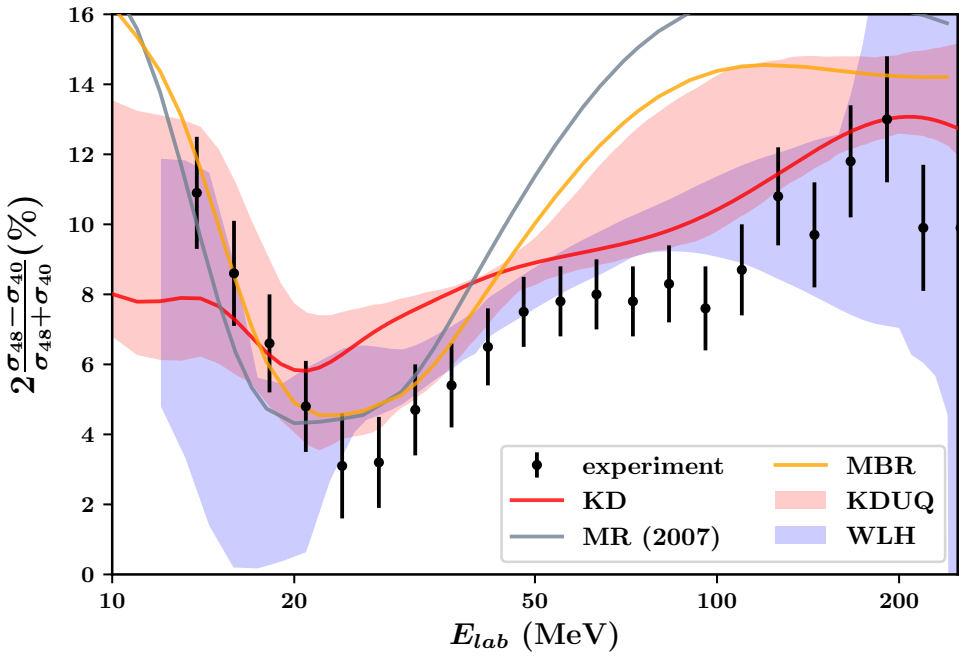

Fig. 1. Asymmetry of the total cross section between 40Ca and 48Ca. The shaded areas associated with the Koning-Delaroche (KDUQ) and Whitehead-Lim-Holt (WLH) global optical potentials correspond to 95% confidence intervals.

Neutron star properties from experimental and ab initio theory constraints of the ^{208}Pb Neutron Skin Thickness

Recent experimental and ab initio theory investigations of the ^{208}Pb neutron skin thickness are sufficiently precise to inform the neutron star equation of state. In particular, the strong correlation between the ^{208}Pb neutron skin thickness and the pressure of neutron matter at normal nuclear densities leads to modified predictions for the radii, tidal deformabilities, and moments of inertia of typical 1.4 solar-mass neutron stars. In recent work [8], we have studied the relative impact of these recent analyses of the ^{208}Pb neutron skin thickness on bulk properties of neutron stars within a Bayesian statistical analysis. Two models for the equation of state prior were employed in order to study the role of the highly uncertain high-density equation of state. From our combined Bayesian analysis of nuclear theory, nuclear experiment, and observational constraints on the dense matter equation of state, we found at the 90% credibility level $R_{1.4} = 12.36^{+0.38}_{-0.73}$ km for the radius of a 1.4 solar-mass neutron star, $R_{2.0} = 12.36^{+0.38}_{-0.73}$ km for the radius of a 2.0 solar-mass neutron star, $\Lambda_{1.4} = 440^{+103}_{-144}$ for the dimensionless tidal deformability of a 1.4 solar-mass neutron star, and $I_{1.338} = 1.425^{+0.074}_{-0.146} \times 10^{45}$g-cm^2 for the moment of inertia of PSR J0737-3039A whose mass is 1.338 solar masses. In Fig. 2 we show the probability distribution for a 1.4 $M_\odot$ neutron star starting, including only constraints from chiral effective field theory and nuclear masses, which is labeled by the blue "Prior" band. Individual posterior probability distributions that include constraints from gravitational wave data (GW170817), NICER radius measurements (NICER I and II), the experimental extraction of the

208Pb neutron skin thickness (PREX II), and the ab initio calculation of the ^{208}Pb neutron skin thickness (R_{np}^{th}) are shown as individual lines. Finally, the combined effect of all likelihood functions is shown as the red shaded band labeled "All".

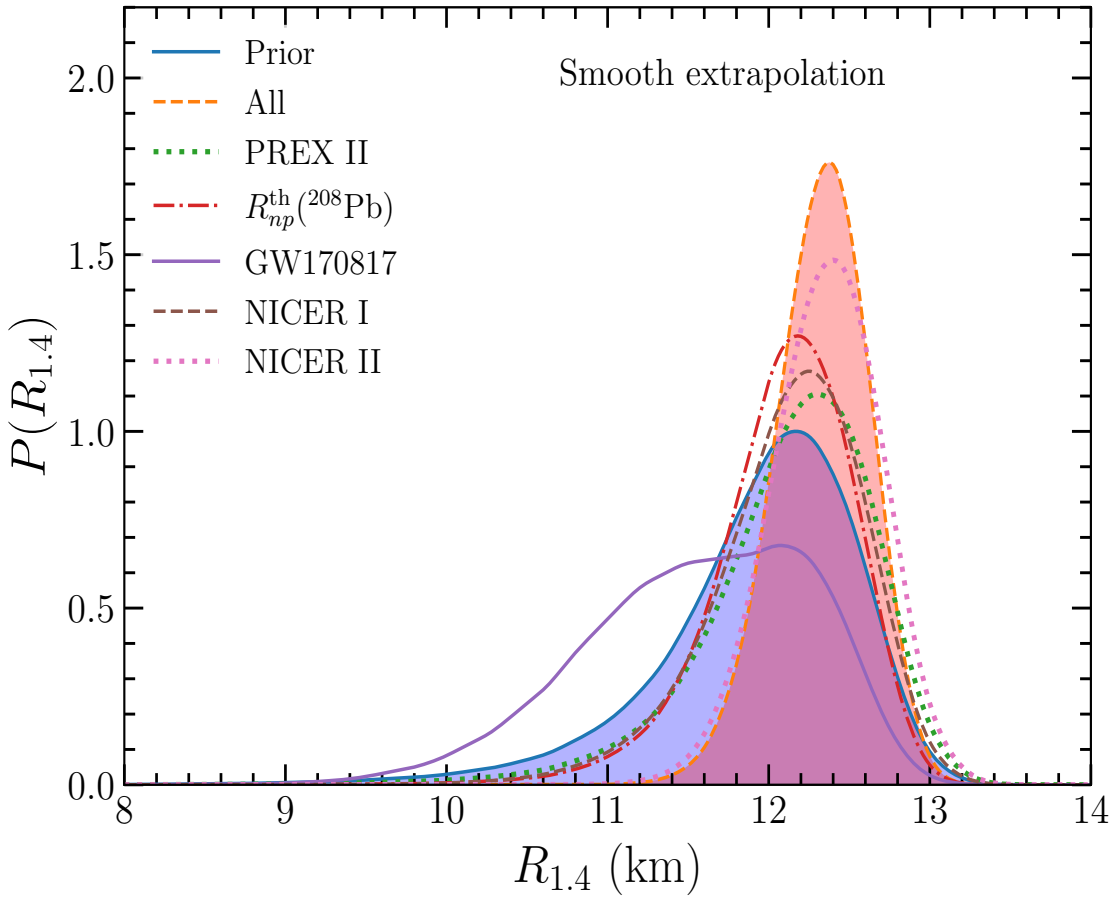

Fig. 2. Probability distribution for the radius of a $\mathbf{1.4}\,\boldsymbol{M_\odot}$ neutron star. The prior distribution is shown as the blue band, while the individual effect of various likelihood functions from gravitational wave (GW170817), electromagnetic (NICER I and II), and 208Pb neutron skin thickness predictions (PREX II and $\boldsymbol{R_{np}^{\rm th}}$) are shown as lines. The complete posterior including all likelihood functions is shown as the red band.

[1] S. Weinberg, Physica A **96**, 327 (1979).

[2] E. Epelbaum, H.-W. Hammer and U.-G. Meissner, Rev. Mod. Phys. **81**, 1773 (2009).

[3] R. Machleidt and D.R. Entem, Phys. Rept. **503**, 1 (2011).

[4] T.R. Whitehead, Y. Lim and J.W. Holt, Phys. Rev. C **100**, 014601 (2019).

[5] T.R. Whitehead, Y. Lim and J.W. Holt, Phys. Rev. C **101**, 064613 (2020).

[6] T.R. Whitehead, Y. Lim and J.W. Holt, Phys. Rev. Lett. **127**, 182502 (2021).

[7] C. Hebborn, F.M. Nunes, G. Potel, W.H. Dickhoff, J.W. Holt *et al.*, J. Phys. G. **50**, 060501 (2023).

[8] Y. Lim and J.W. Holt, Galaxies **10**, 99 (2022).

Angular momentum eigenstates of the isotropic 3-D harmonic oscillator: Phase-space distributions and coalescence probabilities

M. Kordell, R.J. Fries, and Che Ming Ko

The isotropic 3-dimensional harmonic oscillator potential can serve as an approximate description of many systems in atomic, solid state, nuclear, and particle physics. In particular, the question of 2 particles binding (or coalescing) into angular momentum eigenstates in such a potential has interesting applications. We have computed the probabilities for coalescence of two distinguishable, non-relativistic particles into such a bound state, where the initial particles are represented by generic wave packets of given average positions and momenta [1]. We have used a phase-space formulation and hence need the Wigner distribution functions of angular momentum eigenstates in isotropic 3-dimensional harmonic oscillators. These distribution functions have been previously discussed in the literature [2], but we utilized an alternative approach to obtain these functions. Along the way, we have derived a general formula that expands angular momentum eigenstates in terms of products of 1-dimensional harmonic oscillator eigenstates. As an example, Fig. 1 shows the coalescence probabilities P_{kl} for two Gaussian wave packets interacting through an isotropic 3-D harmonic oscillator potential as functions of relative coordinate r and momentum q, with probabilities that depend on the scalar product $\boldsymbol{r}\cdot\boldsymbol{q}$ are plotted for several values of the angle θ given by $\cos\theta = \boldsymbol{r}\cdot\boldsymbol{q}/rq$. The general wave-packet weighted Wigner functions derived in our

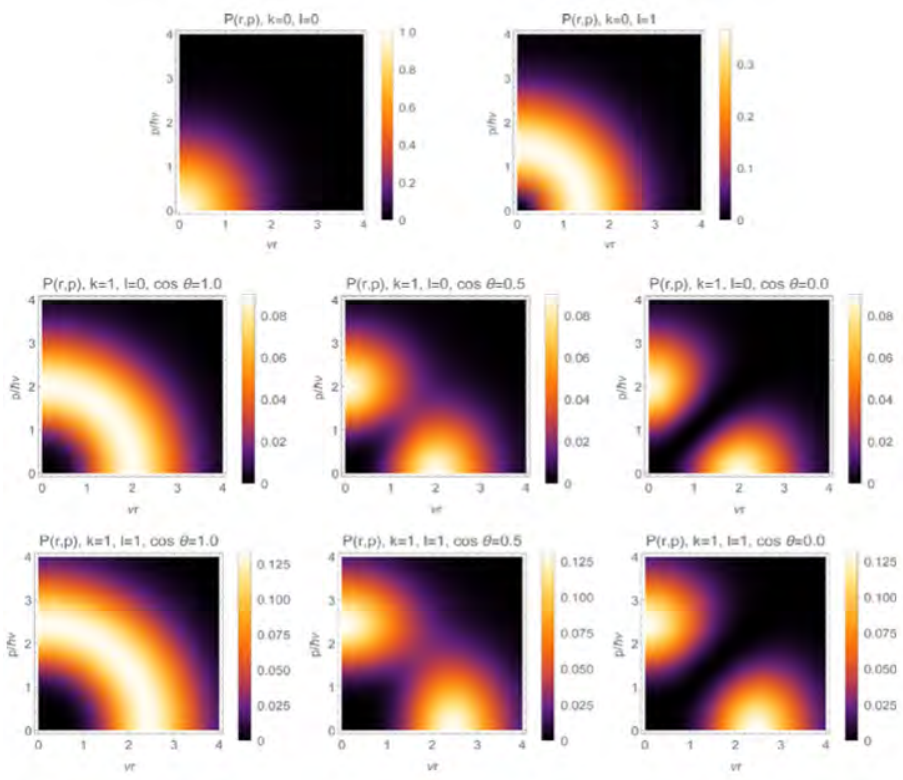

Fig. 1. Coalescence probabilities $\boldsymbol{P_{kl}}$, summed over m, for two Gaussian wave packets interacting through an isotropic 3-D harmonic oscillator potential as functions of relative coordinate r and momentum q, with probabilities that depend on the scalar product $\boldsymbol{r}\cdot\boldsymbol{q}$ are plotted for several values of the angle $\boldsymbol{\theta}$ given by $\boldsymbol{\cos\theta = r\cdot q/rq}$.

study allows us to extend the work in Ref. [3] to include the effect of radial excitations of hadrons on their production in relativistic heavy ion collisions.

[1] M. Kordell, R.J. Fries, and C.M. Ko, Ann. Phys. **443**, 168960 (2022).
[2] S. Shlomo and M. Prakash, Nucl. Phys. **A357**, 157 (1981).

Charged pion production from Au + Au collisions at $\sqrt{s_{NN}}$ = 2.4 GeV in the relativistic Vlasov-Uehling-Uhlenbeck model

Kyle Godbey, Zhen Zhang,[1] Jeremy Holt, and Che Ming Ko
[1]*Sino-French Institute of Nuclear Engineering and Technology, Sun Yat-sen University, Zhuhai 519082, China*

We have used the isospin-dependent Vlasov-Uehling-Uhlenbeck (RVUU) model [1,2], extended from Refs. [3,4], to study the production of charged pions from Au+Au collisions at $\sqrt{s_{NN}}$ = 2.4 GeV [5]. With the medium dependence of the Delta resonance production cross section from the nucleon-nucleon inelastic scattering determined by fitting the total multiplicities of π^- and π^+ measured in the HADES experiment [6], we have obtained a good description of the rapidity distributions of both π^- and π^+ for various centrality bins (Fig.1). For the transverse momentum spectra, the RVUU underpredicts π^- at low transverse momentum p_t, while overpredicts both π^- and π^+ at high p_t region (Fig. 2). We have attributed

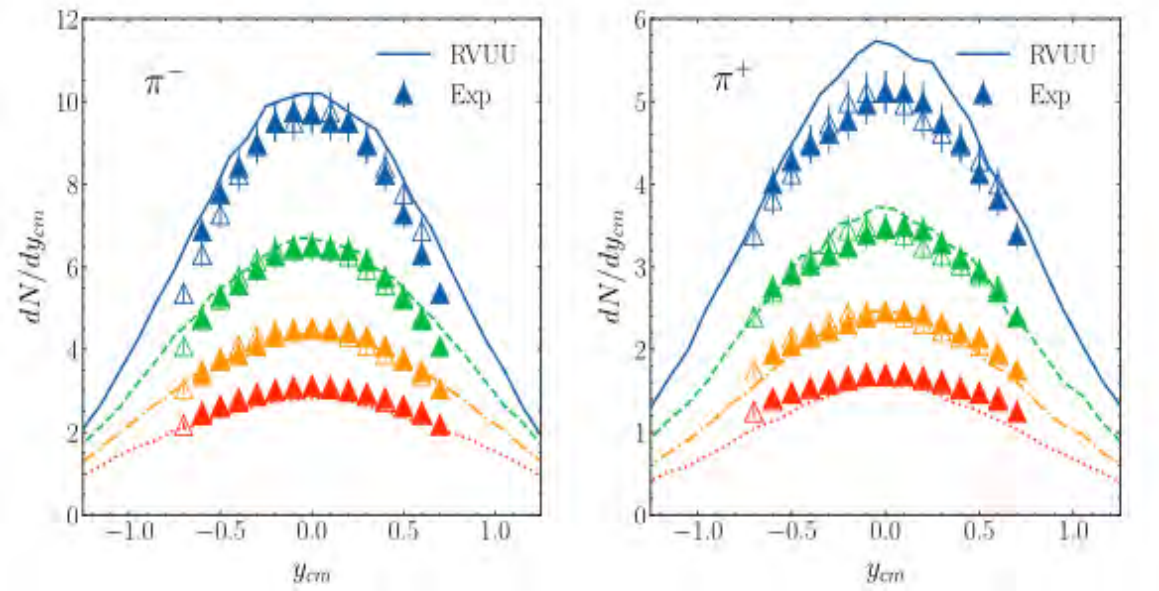

Fig. 1. Rapidity distributions of π^- (left window) and π^+ (right window) from RVUU (lines) and experimental data (triangles) from Ref. [6]. Results are shown across 4 centrality bins: 0% − 10% (blue, solid line), 10% − 20% (green, dashed line), 20% − 30% (orange, dot-dashed line), 30% − 40% (red, dotted line).

this discrepancy to the absence of the pion mean-field potential in the RVUU model. The reasonable success of the RVUU model in describing the HADES pion data is in contrasts to the results from other transport models used by the HADES Collaboration to compare with its data, which all overestimate the π^- and π^+ multiplicities by about a factor of two. The reason for the difference between our results and those from other transport models are mainly due to our introduction of a density-dependent reduction factor to the nucleon-nucleon inelastic cross section, which is absent in other models. To understand the origin of this reduction factor requires further theoretical studies. We have also calculated the proton rapidity distribution

in the most central collisions and found it a factor of 1.23 larger than the coalescence invariant proton rapidity distribution extracted from preliminary HADES data on protons, deuterons tritons, and helium-3 [7], which also requires more theoretical and experimental studies.

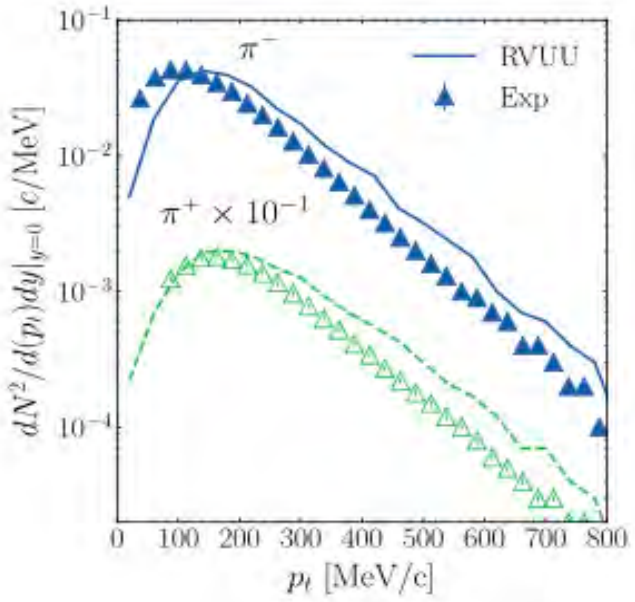

Fig. 2. Charged pion transverse momentum spectrum from RVUU (lines) and experimental data (triangles) from Ref. [35]. Negative pions are represented by filled blue symbols and solid blue line, while positive pions are scaled down by 10^{-1} and are drawn with hollow green symbols and green dashed line. Results are shown for mid-rapidity events for the most central (0% − 10%) class of collisions.

[1] T. Song, C.M. Ko, Phys. Rev. C **91**, 014901 (2015).

[2] Z. Zhang, C.M. Ko, Phys. Rev. C **95**, 064604 (2017).

[3] C.M. Ko, Q. Li, R. Wang, Phys. Rev. Lett. **59**, 1084 (1987).

[4] C.M. Ko, Q. Li, Phys. Rev. C **37**, 2270 (1988),

[5] K. Dogbey, Z. Zhang, J. W. Holt, and C. M. Ko, Phys. Lett. B **829**, 137134 (2022).

[6] J. Adamczewski-Musch, O. Arnold, C. Behnke, A. Belounnas, A. Belyaev, J.C. Berger-Chen, A. Blanco, C. Blume, M. Böhmer, P. Bordalo, et al., Eur. Phys. J. A **56**, 259 (2020).

[7] M. Szala (HADES), Light nuclei formation in heavy ion collisions measured with HADES, in: Proceedings of the ECT* Workshop: Light Clusters in Nuclei and Nuclear Matter: Nuclear Structure and Decay, Heavy Ion Collisions, and Astrophysics, 2019 (unpublished).

Event-by-event antideuteron multiplicity fluctuation in Pb+Pb collisions at $\sqrt{s_{NN}} = 5.02$ TeV

Kai-Jia Sun[1, 2] and Che Ming Ko

[1]*Key Laboratory of Nuclear Physics and Ion-beam Application (MOE), Institute of Modern Phys, Fudan University, Shanghai 200433, China*

[2]*Shanghai Research Center for Theoretical Nuclear Physics, NSFC and Fudan University, Shanghai 200438, China*

Event-by-event multiplicity fluctuations and correlations have been suggested as a sensitive probe to the production mechanism of fragile antinuclei in high-energy nuclear collisions [1]. Using the nucleon coalescence model based on kinetic freeze-out nucleons from the hybrid model of MUSIC hydrodynamics [2] for the quark-gluon stage and UrQMD transport model [3] for the hadronic stage of ultrarelativistic heavy ion collisions, as in Ref. [4], we have studied the production of antideuteron and its event-by-event fluctuation in Pb+Pb collisions at $\sqrt{s_{NN}} = 5.02$ TeV [5]. The adopted MUSIC+UrQMD+COAL model is found to give a good description of the proton and deuteron yields in Pb+Pb collisions at $\sqrt{s_{NN}} = 5.02$ TeV, especially the suppressed *d*/*p* ratio in peripheral collisions. However, this model overestimates the net-proton number fluctuation due to the lack of exact baryon number conservation at particlization when the QGP is converted to the hadronic matter as shown in the left window of Fig. 1. To mimic the effect of baryon number conservation, we have selected a subset of events so that the net-proton number fluctuation is reduced to the level shown in the ALICE data. As shown in panel (a) of right window of Fig. 1, we have

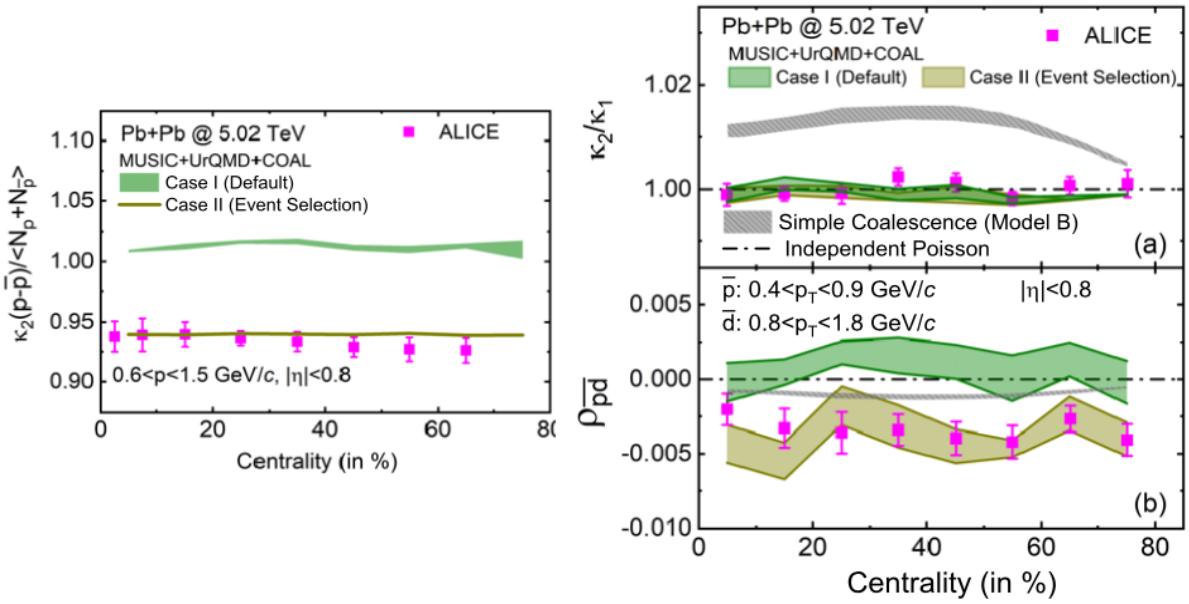

Fig. 1. Centrality dependence of the normalized second-order cumulants of net-proton distribution (left window) and antideuteron distribution (panel (a) of right window) as well as the correlation between antiproton and antideuteron multiplicities (panel (b) of right window)) in Pb+Pb collisions at $\sqrt{s_{NN}} = 5.02$ TeV. The ALICE data are shown by solid squares with combined statistical and systematic uncertainties [6,7].

found that the resulting scaled moment κ_2/κ_1 of the antideuteron multiplicity distribution agrees with the

Poisson limit for a grand canonical ensemble but is smaller than that obtained from the simple coalescence model that assumes the same probabilities for all antiproton and antineutron pairs to form a deuteron. As for the antiproton and antideuteron number correlation $\rho_{\bar{p}\bar{d}}$, which is shown in panel (b) of right window, its value from our model calculations based on the event-selection method is seen to agree with the ALICE data within uncertainties, although calculations including all events in our model fails. Our study has thus shown that the event-by-event fluctuation of net-proton number and also the negative correlation between the antiproton and antideuteron multiplicities measured in relativistic heavy ion collisions can be understood only if the baryon number conservation is preserved in theoretical models. Implementation of baryon number conservation at particlization in the (3+1)-dimensional viscous hydrodynamic model MUSIC is therefore urgently needed.

[1] Z. Fecková, J. Steinheimer, B. Tomášik, and M. Bleicher, Phys. Rev. C **93**, 054906 (2016).
[2] C. Shen and B. Schenke, Phys. Rev. C **97**, 024907 (2018).
[3] M. Bleicher, E. Zabrodin, C. Spieles, S.A. Bass, C. Ernst, S. Soff, L. Bravina, M. Belkacem, H. Weber, H. Stöcker, and W. Greiner, J. Phys. G: Nucl. Part. Phys. **25**, 1859 (1999).
[4] W. Zhao, K. J. Sun, C.M. Ko, and X. Luo, Phys. Lett. B **820**, 136571 (2021).
[5] K. J. Sun and C. M. Ko, Phys. Lett. B **840**, 137864 (2023)
[6] ALICE Collaboration, arXiv:2206.03343, 2022.
[7] ALICE Collaboration, arXiv:2204.10166, 2022.

Transport model comparison studies of intermediate-energy heavy-ion collisions

Hermann Wolter,[1], Maria Colonna,[2] Dan Cozma,[3] Pawel Danielewicz,[4] Che Ming Ko *et al.*
(TEMP Collaboration)
[1]*Faculty of Physics, University of Munich, D-85748, Garching, Germany*
[2]*INFN-LNS, Laboratori Nazionali del Sud, 95123 Catania, Italy*
[3]*IFIN-HH, 077125 Magurele-Bucharest, Romania*
[4]*FRIB and Department of Physics and Astronomy,*
Michigan State University, East Lansing, Michigan 48824, USA

We have participated in the transport evaluation project (TMEP) of simulations for heavy-ion collisions to obtain physics information on the nuclear equation of state and in-medium properties of particles from low to relativistic-energy heavy-ion collisions. The Transport Model Evaluation Project (TMEP) has been pursued to test the robustness of transport model predictions in reaching consistent conclusions from the same type of physical model. To this end, calculations under controlled conditions of physical input and set-up were performed with various participating codes. These included both calculations of nuclear matter in a box with periodic boundary conditions, which test separately selected ingredients of a transport code, and more realistic calculations of heavy-ion collisions. Over the years, six studies have been performed within this project. In this intermediate review [1], we have summarized and discussed the present status of the project. We have also provided condensed descriptions of the 26 participating codes, which contributed to some part of the project. These include the major codes in use today. After a compact description of the underlying transport approaches, we have further reviewed the main results of the studies completed so far. They show that in box calculations [2,3,4], the differences between the codes can be well understood and a convergence of the results can be reached. These studies also highlight the systematic differences between the two families of transport codes, known under the names of Boltzmann–Uehling–Uhlenbeck (BUU) [5] and Quantum Molecular Dynamics (QMD) [6] type codes. However, when the codes were compared in full heavy-ion collisions using different physical models [7], as recently for pion production [8], they still yielded substantially different results. This calls for further comparisons of heavy-ion collisions with controlled models and of box comparisons of important ingredients, like momentum-dependent fields, which are currently underway. Our evaluation studies often indicate improved strategies in performing transport simulations and thus can provide guidance to code developers. Results of transport simulations of heavy-ion collisions from a given code will have more significance if the code can be validated against benchmark calculations such as the ones summarized in this review.

[1] H. Wolter, M. Colonna, D. Cosma, P. Danielewicz, C.M. Ko, *et al.* (TEMP Collaboration), Prog. Part. and Nucl. Phys **125**, 103962 (2022),
[2] Y.X. Zhang *et al.* (TEMP Collaboration), Phys. Rev. C **97**, 034625 (2018).
[3] A. Ono *et al.* (TEMP Collaboration), Phys. Rev. C **100**, 044617 (2019).
[4] M. Colonna, Y.X. Zhang, Y.J. Wang, D, Cozma, P. Danielewicz, C.M. Ko *et al.* (TEMP Collaboration), Phys. Rev. C **104**, 024603 (2021).
[5] G.F. Bertsch and S. Das Gupta, Phys. Rep. **160**, 189 (1988).

[6] J. Aichelin, Phys. Rep. **202**, 233 (1991).
[7] J. Xu *et al.* (TEMP Collaboration), Phys. Rev. C **93**, 044609 (2018).
[8] J. Jhang *et al.* (TEMP Collaboration), Phys. Lett. B **813**, 136016 (2021).

Bottom hadro-chemistry in high-energy hadronic collisions

Min He and Ralf Rapp

Heavy-flavor (HF) hadrons, containing either charm or bottom quarks (or both), are among the most promising probes of the strongly-coupled quark-gluon plasma (sQGP) and its hadronization as being investigated in high-energy collisions of heavy nuclei [1]. Low-momentum diffusion of heavy quarks through the QGP gives unique access to a fundamental transport parameter, the HF diffusion coefficient (scaled by the thermal wavelength), $\mathcal{D}_s(2\pi T)$. In addition, the abundances and transverse-momentum (p_T) distributions of different HF hadron species, emerging from the same underlying distribution of heavy quarks after transport through the QGP, open a direct window on the hadronization process in QCD. The theoretical implementation of these ideas *heavily* relies on the large scale provided by the charm- and bottom-quark masses, compared to other basic scales in the problem, such as the nonperturbative QCD scale, Λ_{QCD}, and the temperature, T, of the ambient medium. This allows the use of static-potential and Fokker-Planck transport approximations, which in turn facilitates the implementation of nonperturbative physics of the sQGP [1], such as string-like interactions, resummations and large-width (i.e., quantum) effects in the HQ coupling to the thermal medium [2,3].

In the present work [4] we extend our previously developed strongly-coupled approach to heavy-quark production in nuclear collisions [5], consisting of a macroscopic medium background simulated by relativistic hydrodynamics and the microscopic T-matrix approach [3] for HQ diffusion and hadronization (as well as diffusion in the hadronic phase), by systematically applying it to the open-bottom sector. We first consider the bottom hadro-chemistry in elementary proton-proton (*pp*) collisions, where the central ingredient is a statistical hadronization model (SHM) with excited bottom mesons and baryons predicted by relativistic quark models (RQMs). This spectrum goes much beyond the currently known states listed by the particle data group (PDG), which, based on observed states in the light- and strange-quark sector, are incomplete. Especially the rich spectrum of excited baryons plays a key role through their decay feeddown into ground-state baryons, such as the Λ_b, resulting in a much improved description of the

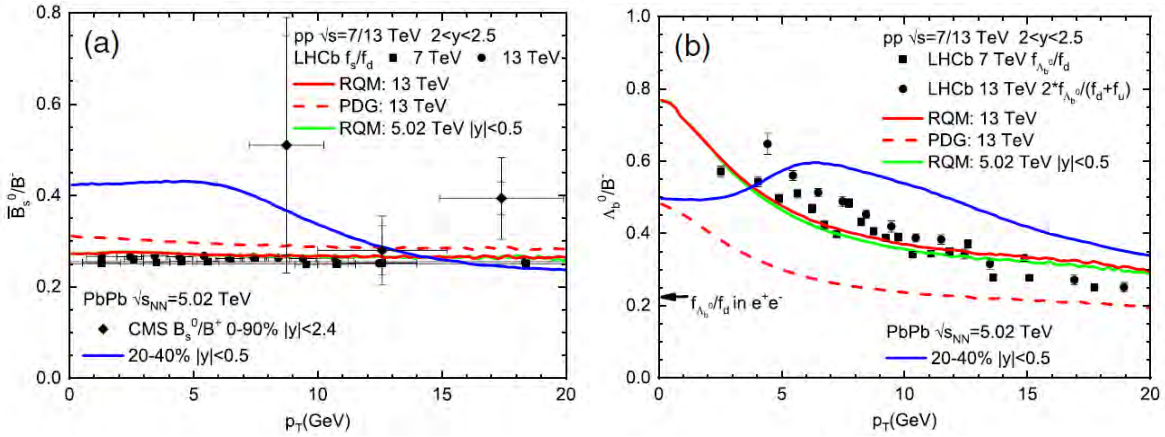

Fig. 1. Ratios of the ground-state strange-bottom meson, B_s (left), and bottom-baryon, Λ_b (right), to the B^- hadron in *pp* collisions within a combined SHM/fragmentation approach using either the states listed by the PDG (dashed lines) or from a relativistic quark model (solid lines), compared to LHCb data. The blue solid lines are the pertinent predictions for semicentral Pb-Pb(5TeV) collisions.

observed Λ_b/B ratio compared to using PDG states only, compare solid vs. dashed lines in the right panel of Fig. 1. Also, the B_s/B ratio slightly improves when using the RQM spectrum (left panel of Fig. 1), while predictions for the Ξ_b/B ratio are also provided (not shown).

The applications to heavy-ion collisions highlight the importance of the diffusion properties of the b-quark as well as its hadronization through recombination with thermal light and strange quarks in the flowing medium: for different b-hadrons we predict markedly different nuclear modification factors (i.e., the ratio between the p_T spectra in *pp* and AA collisions), featuring characteristic "flow bumps" at low p_T which are more pronounced for baryons than mesons, and a yield enhancement for b-hadrons containing strange quarks (B_s and Ξ_b), due to the enhanced concentration of (equilibrated) strange quarks in heavy-ion collisions, see left panel of Fig. 2. In the right panel, we compare our calculations to available LHC data, in terms of so-called "non-prompt" D and D_s mesons originating from decays of B mesons, showing fair agreement with ALICE data. With a much extended set of b-hadron data from future LHC and RHIC runs (with the new sPHENX detector), we believe that our comprehensive predictions will contribute to detailed interpretations and insights of hadronization mechanisms and refined, more accurate determinations of the HF transport coefficients in QCD matter.

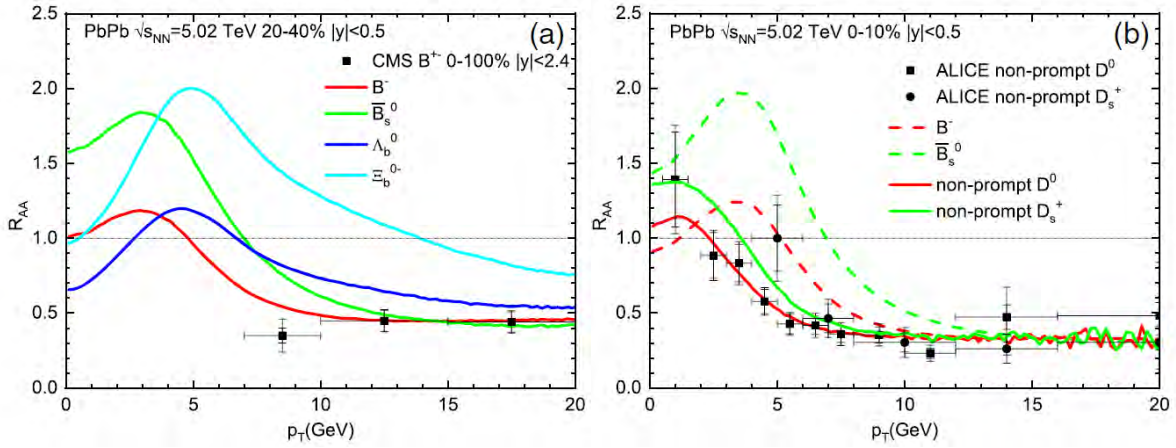

Fig. 2. Our predictions [4] for nuclear modification factors of various bottom hadrons in semicentral Pb-Pb collisions at the LHC (left), and the results of non-prompt D and D_s mesons (arising from pertinent b-hadron decays) compared to ALICE data in central Pb-Pb collisions (right).

[1] M. He, H. van Hees and R. Rapp, Prog. Part. Nucl. Phys. **130**, 104020 (2023).

[2] F. Riek and R. Rapp, Phys. Rev. C **82**, 035201 (2010).

[3] S.Y.F. Liu and R. Rapp, Phys. Rev. C **97**, 034918 (2018).

[4] M. He and R. Rapp, Phys. Rev. Lett. **131**, 012301 (2023).

[5] M. He, R.J. Fries and R. Rapp, Phys. Rev. C **86**, 014903 (2012).

Electric conductivity in hot pion matter

Joseph Atchison and Ralf Rapp

Transport parameters are pivotal to the understanding of strong-interaction matter and its investigations through high-energy heavy-ion collisions. Prime examples of high current interest are the ratio of viscosity over entropy density, η/s, which is a key input to hydrodynamic simulations [1], and the heavy-flavor diffusion coefficient (relative to the thermal wavelength), $\mathcal{D}_s$ $(2\pi T)$, which can be probed through charm and bottom-hadron observables [2].

In this work we focus on the electric conductivity, which is more difficult to extract from experiment and has received less attention thus far. On the theoretical, there are significant discrepancies between various calculations for its value in hot hadronic matter [1]. In the present work we calculate the electric conductivity from the zero-energy limit of the in-medium electromagnetic spectral function at vanishing 3-momentum,

$$\sigma_{el} = e^2/2\ \rho_{EM}(q_0 \to 0, q=0)/q_0 \quad .$$

This is particularly promising as the EM spectral function has been directly probed in heavy-ion collisions through photon and dilepton spectra [4], albeit the very low-mass and momentum region has not been accessible yet. Along the lines of our previous work [5] we employ hadronic many-body theory in connection with the Vector Dominance Model (VDM) to compute the photon coupling to the hadronic EM current via the in-medium ρ-meson spectral function, $\rho_{EM} \sim \mathrm{Im}\, D_\rho$, and focus on the simplified system of hot pion matter. We compute the ρ-meson selfenergy through a dressing of its pion cloud with thermal π-$\rho(770)$ and π-$\sigma(500)$ loops; this, in particular, mandates the inclusion of in-medium corrections to the 3- and 4-point vertices of the ρ-π couplings, to maintain gauge invariance of the current correlator. A further challenge is that all in-medium propagators have to be dressed (i.e., acquire a finite width) to avoid

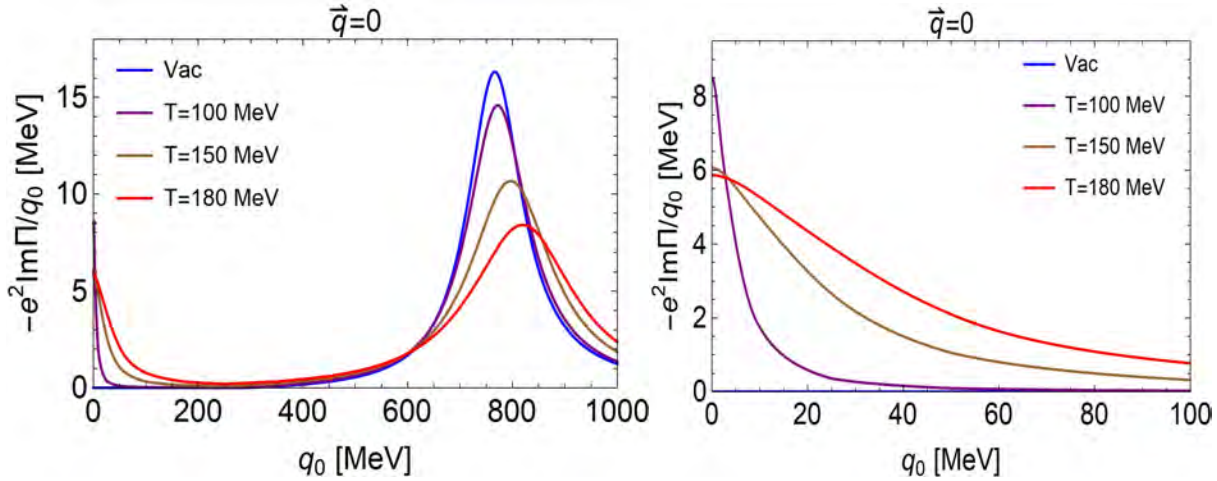

Fig. 1. EM spectral function in the isospin-1 r-meson channel in pion matter for three temperatures. Left: mass range covering the r resonance; right: low-energy region exhibiting the conductivity peak.

singularities in the zero-energy limit. Our results for the in-medium EM spectral function are shown in Fig.1. The ρ-meson peak broadens moderately with temperature (much less pronounced than what was found for baryon-induced medium effects [5]), cf. left panel, while a conductivity peak develops in the low energy limit which also broadens with temperature, see right panel.

The different contributions to the conductivity are displayed in Fig. 2 left. At low temperatures the σ(500) resonance is most effective in reducing σ_{el} via ππ scattering, while for T>100 MeV the scattering through a ρ(770) resonance is more important. Vertex corrections tend to increase the conductivity, as they provide additional channels for charge propagation. In comparison to other model calculations for hot pion matter, we find good agreement with the thermal-field theory calculations by Ghosh *et al.* [6].

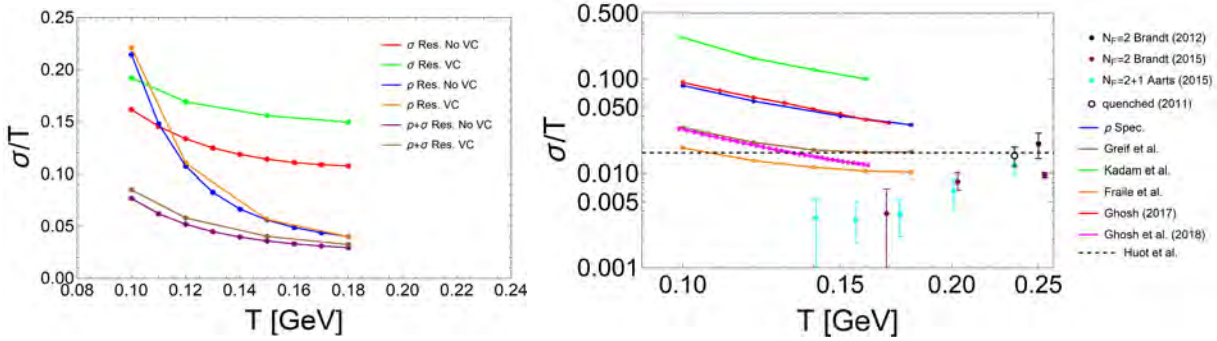

Fig. 2. Electric conductivity, scaled dimensionless by temperature, in hot pion matter as a function of temperature. Left: our results using hadronic many-body theory upon inclusion of only s(500) or only r(770) resonance scattering, and the total (lower lines), with and without vertex corrections (VC). Right: comparison of our result (blue) to results from the literature including lattice QCD (which include more than pions) and other model calculations (see Ref. [3] for more details).

In summary, we have conducted new calculations of the electric conductivity in hot pion matter through the EM spectral function in pion matter, utilizing hadronic many-body theory that has previously been applied to dilepton spectra in heavy-ion collisions. This provides a direct link between dilepton phenomenology and a fundamental transport parameter of QCD matter. Extensions to include the important effects of baryons are in progress, and experimental efforts are underway to measure dileptons at very low mass and momentum in Au-Au(1.23GeV) collisions at SIS with HADES and the future Pb-Pb(5TeV) run-5 at the LHC with the ALICE-3 detector.

[1] J.E. Bernard *et al.*, Nature Phys. **15**, 1113 (2019).
[2] M. He, H. van Hees and R. Rapp, Prog. Part. Nucl. Phys. **130**, 104020 (2023).
[3] J. Atchison and R. Rapp, Nucl. Phys. **A1037**, 122704 (2023).
[4] R. Rapp and H. van Hees, Eur. Phys. J. A **52**, 257 (2016).
[5] R. Rapp and J. Wambach, Eur. Phys. J. A **6**, 415 (1999).
[6] S. Ghosh, Phys. Rev. D **95**, 036018 (2017).

Nucleon-nucleon Bremsstrahlung in heavy-ion collisions at Fermi energies

T. Onyango and R. Rapp

In this work we continue our investigation of nuclear matter formed in heavy-ion collisions (HICs) at low beam energies, specifically E_{lab} = 35 MeV/A. In our previous work we employed a coarse-graining procedure to extract the time evolution of the thermodynamic properties of ^{40}Ca +^{40}Ca collisions in local cells of $(2fm)^3$ [1]. In particular, we found that while the transverse-momentum spectra are amenable to a description with thermal Fermi distribution functions, the energy related to the initial centroid motion of the incoming nuclei (z-direction) undergoes a gradual dissipation on a timescale of about 100 fm/c. In the present work we employ these results to convolute thermal photon rates over the space-time evolution and compare the pertinent spectra to experiment.

Under the present conditions, the local emission of photons is dominated by nucleon-nucleon (NN) Bremsstrahlung. We calculate the photon emission rate per unit 3-momentum and 4-volume in a quantum field theoretical framework by folding the NN Bremsstrahlung's cross section [2,3] over the nucleon distribution functions obtained from the coarse graining, including non-thermal longitudinal motion. Specifically, we employ an energy-dependent NN cross-section (assumed to be S-wave) fitted to experimental data and relax the soft photon approximation by considering the energy of the emitted photon in the final state. A comparison between our calculated photon energy spectra from ^{40}Ca +^{40}Ca at 35 MeV/A and a relevant experiment [4] is shown in Fig. 1. To match the centrality selection in the Ar+Mo system, we apply a NN collision scaling to our calculated spectra. We also account for exeperimental detector accpetance, thereby including the boost from the transverse and longitudinal center-of-mass motion of the local cells into the laboratory frame.

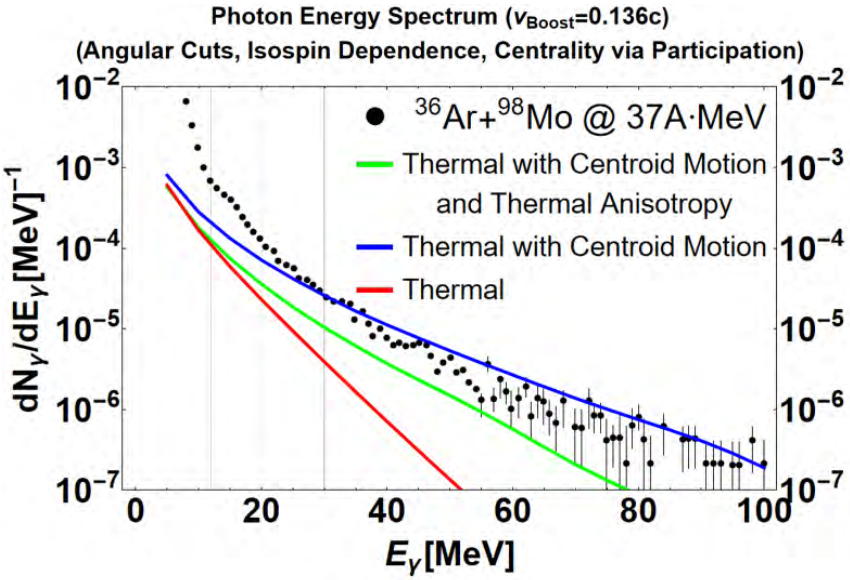

Fig. 1. Photon spectra calculated from a rate convoluted over coarse-grained thermodynamics of 35 A·MeV ^{40}Ca +^{40}Ca collisions, compared to experimental data [4] of a comparable collision system (^{36}Ar + ^{98}Mo at 37 A·MeV), using purely thermalized nucleon distributions (red line), including centroid motion (blue line) and temperature anisotropy (green line).

In a purely thermal approximation, where the centrod motion of the incoming nuclei within the cells is neglected, the data are underestimated. The inclusion of the centroid motion much enhances the yield which now lies slightly above the data for photon energies above ~40 MeV. This demonstrates the importance of the longitudinal motion in the early NN collisions upon nuclear impact (and justifies the collision scaling assumed above). However, when additionally implementing a temperature anisotropy (implying a slightly smaller temperature in the longitudinal direction), the yield reduces again and falls somewhat below the data. We also see that the low-energy data, below ~20 MeV, are beyond the reach of our local emission sources, indicating the presence of a giant-dipole contribution as well as late-stage fragment decays.

In future studies we plan improve our paramterization of the NN cross section by including higher partial waves, additional high-energy sources (e.g., D(1232)-resonance contributions) and in-medium effects through a microscopic model calculation.

[1] T. Onyango, A. Bonasera, and R. Rapp, Nucl. Phys. **A1022**, 122426 (2022).
[2] J.H. Chang, R. Essig, and S. McDermott, JHEP **01,** 107 (2017).
[3] E. Rrapaj and S. Reddy, Phys. Rev. C **94**, 4 (2016).
[4] P. Piattelli *et al.,* Nucl. Phys. **A649**, 181c (1996).

Photon radiation from thermally anisotropic nuclear matter produced from Fermi-energy

T.J. Onyango and R. Rapp

I am a fifth-year graduate student. I started at Texas A&M University and the cyclotron in August 2018. I did my preliminary exam in January 2023 and am anticipating defending in October 2023. I work with Dr. Rapp to study nuclear collisions at Fermi energies. The goal of my project is to create a systematic method to correlate temperature and collective-flow extractions with photon production in these collisions. This will be done by first devising a method to accurately extract the time evolution of temperature and chemical potential from a collision in order to properly identify if and when the fireball has thermalized. This thermalization time is important because it signifies the transition between primordial photon production and thermal photon production. Primordial photons are produced from the initial contact between the nuclei. Once the nuclei start to overlap and form a fireball, then thermal photons, which are related to the fireball's temperature distribution in space, are expected to be produced. The impact of this work will be the quantification of the contributions of the different photon production mechanisms present during nuclear collisions at Fermi energy as well as the opportunity to give experimental colleagues an effective tool to interpret data from nuclear collisions. I have been analyzing central collisions of ^{40}Ca nuclei at 35A•MeV lab energy, but this process should be applicable to other collision energies and nuclei of any size.

Since beginning this project, I have learned and modified the Constrained Molecular Dynamics (CoMD) simulation code [1] created by Dr. Bonasera in order to extract the positions and momenta of the individual nucleons involved in the collision. The transport code creates a nucleus by calculating the positions and momenta of nucleons based on prescribed input parameters for the intranuclear interactions. The transport code also collides the nuclei in the center-of-mass reference frame based on a range of specified impact parameters. The transport code then yields the positions and momenta of the center of the gaussian wave packets of the nucleons.

Using the positions and momenta produced by the transport code, I produce density evolutions and localized momentum distributions. From the momentum distributions, I create fit functions using Fermi-Dirac statistics based on the momentum distributions in order to extract time evolutions of chemical potential and temperature. The extracted density is compared to the raw transport density obtained from the transport data of positions and momenta as a constraint when calculating the thermodynamic properties. The momentum distributions along the beam axis require fit functions with more parameters to account for the residual motion of the two independent nuclei entering the cells at different times. The chemical potentials and temperatures extracted from the transverse direction are imported into the longitudinal fit functions. Evolutions of centroidal motion and thermal anisotropy along the longitudinal are produced.

We then calculate the photon production rate from nucleon-nucleon bremsstrahlung [2]. We have replicated a photon emissivity from established literature [3] to establish consistency with the literature. Our current estimates are based on the dipole contribution and therefore assume that every collision is between a proton and a neutron. We find that the photon rate for thermalized nuclear matter is more sensitive to temperature as compared to density. We then started to investigate the roles off-equilibrium

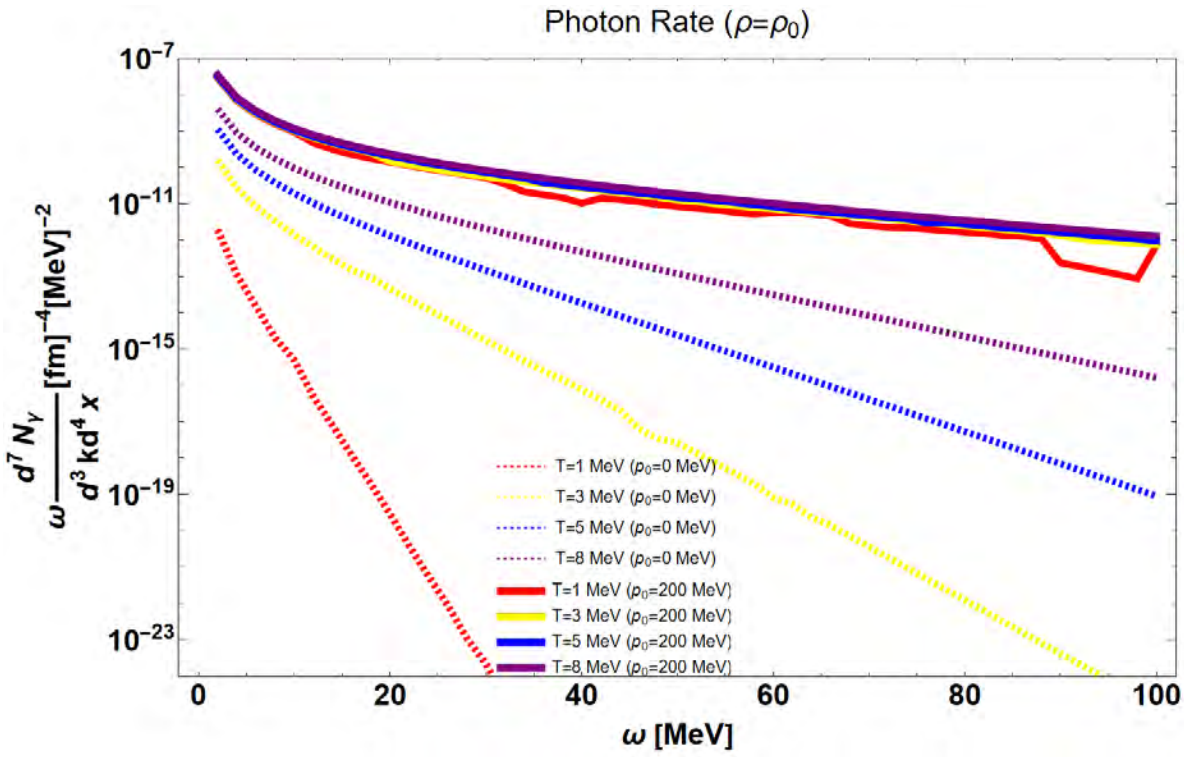

Fig. 1.

effects play in the shape of the photon rate. We incorporate the initial collective nuclear motion by including the centroid momenta in the nucleon distribution functions in the photon rate. We observe a significant increase in the overall yield. We also observe that the photon rate depends more strongly on the centroid momenta than on the temperature. The sensitivity of the photon rate to temperature is very weak in the presence of large centroid momenta.

From the photon rate we have calculated photon energy spectra with and without centroid motion and compared them to what has been experimentally produced. We see a significant increase in the production of high energy ($E_\gamma > 30$ MeV) photons when accounting for the energy of the initial longitudinal motion.

The plan for the near future is to finish implementing the off-equilibrium parameters, specifically the thermal anisotropy parameter. After that we will comment on the significance of isospin dependence by comparing the dipole and quadrupole contributions to the photon rate. Then we will implement realistic characteristics (such as angular cuts representative of the placement of experimental detectors) so that our calculations more accurately reflect experimental conditions.

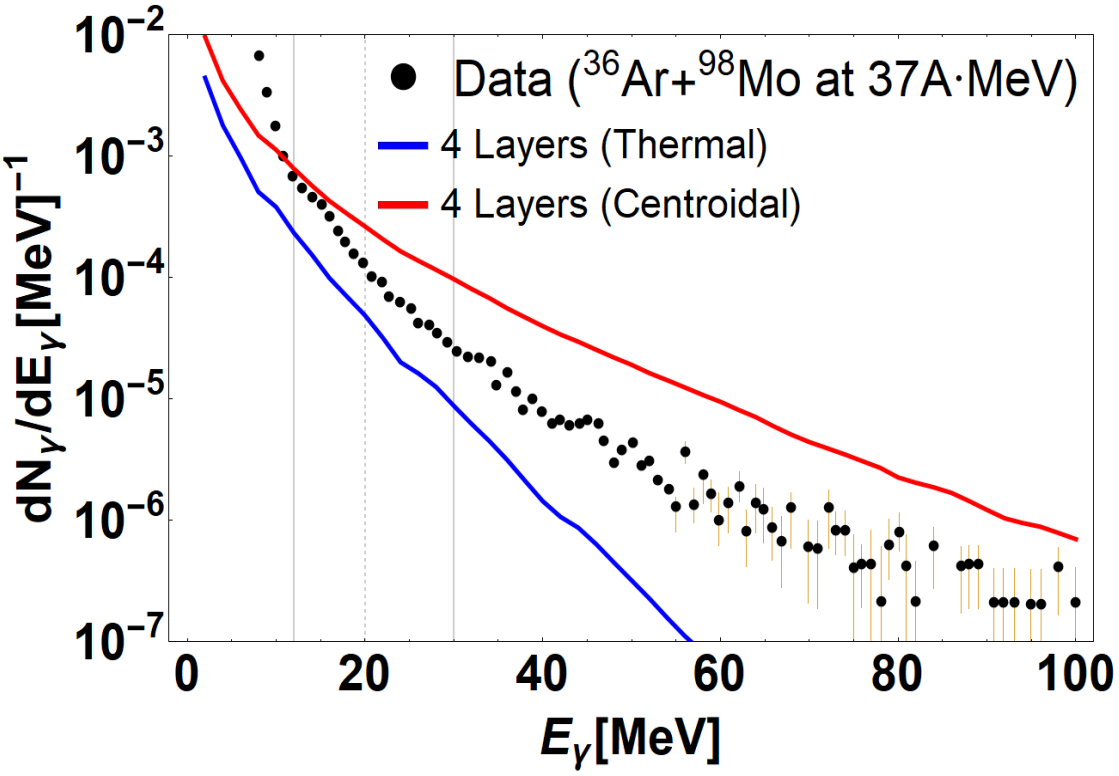

Fig. 2.

[1] H. Zheng, G. Bonasera, J. Mabiala, P. Marini, and A. Bonasera, Eur. Phys. J. A **50,** 167 (2014).

[2] J. H. Chang, R. Essig, and S. McDermott, JHEP **01,** 107 (2017).

[3] E. Rrapaj, S. Reddy, Phys. Rev. C **94**, 4 (2016).

Spin-induced interactions and heavy-quark transport in the QGP

Zhanduo Tang and Ralf Rapp

Heavy quarks play an important role in the spectroscopy of hadrons in vacuum and in the study of the quark-gluon plasma (QGP) in ultra-relativistic heavy-ion collisions (URHICs). The former has enabled critical tests of the fundamental potential between a heavy quark and its antiquark. In the latter, open heavy-flavor (HF) particles are a powerful probe of the transport properties of the QGP [1,2], which can be further utilized to investigate the microscopic in-medium force on heavy quarks [3]. In this work, we continue to combine these two areas.

Toward this end we have extended the thermodynamic T-matrix approach [4] to incorporate spin-dependent interactions between heavy quarks, representing $1/M_Q$ corrections (M_Q: heavy-quark mass) [6] which generate hyper/-fine splittings in the vacuum quarkonium spectra. In addition, an admixture of a Lorentz-vector component in the confining potential [5,6] (previously assumed to be scalar), further improved the description of the experimental mass splittings of in S- and P-wave states, especially for the charmonium, see Fig. 1.

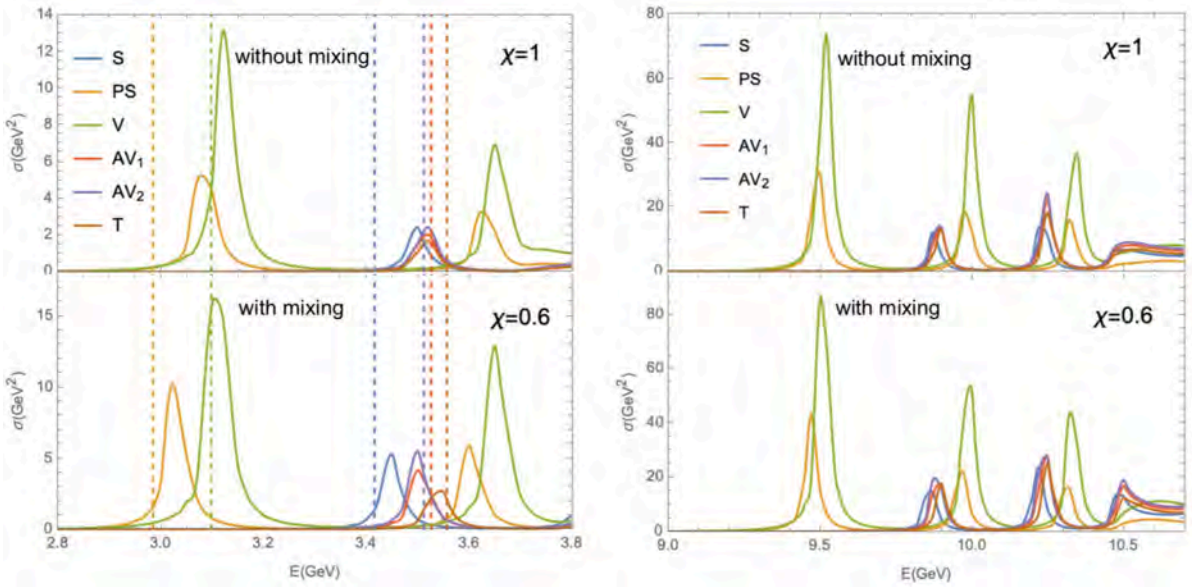

Fig. 1. Left panels: Vacuum charmonium spectral functions in scalar (S), pseudoscalar (PS), vector (V), axial-vector (AV) and tensor (T) channels computed with scalar confining potential ($\chi = 1$) and with mixed confining potential ($\chi = 0.6$). Right panels: Same as in the left panels but for bottomonium. Dashed lines indicate the observed masses.

We then employed the modified interaction to compute the thermal relaxation rate of charm quarks in the QGP. Comparing to the results with a purely scalar confining potential, we find a slightly higher rate at low momenta (which generates a smaller spatial diffusion coefficient, $\mathcal{D}_s$). At larger momenta the relativistic corrections generated by the vector-component of the string interaction produce a substantially larger increase, by a factor of 2-3 or even more, see Fig. 2.

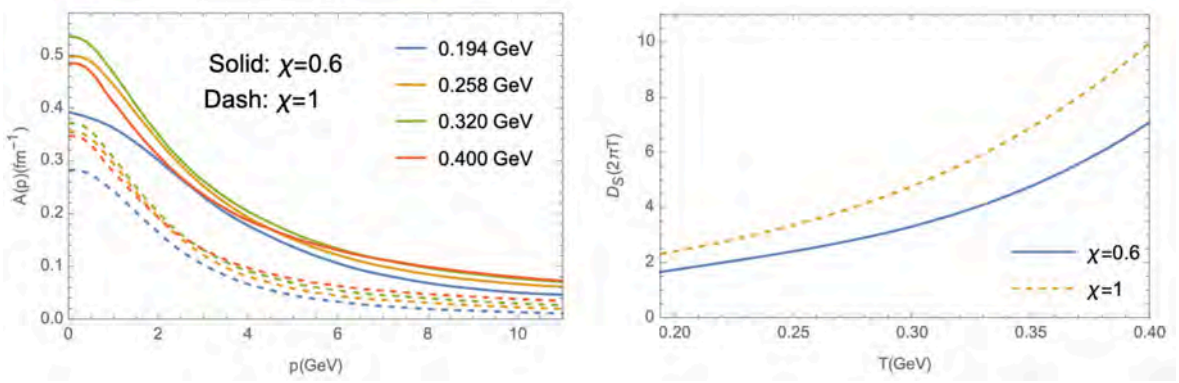

Fig. 2. Thermal relaxation rate of charm quarks vs. 3-momentum at different temperatures (left panel) and spatial diffusion coefficient vs. temperature (right panel); the parameter χ controls the vector admixture in the HQ potential which vanishes for χ=1 (dashed lines) and amounts to 40% for our new results with χ=0.6 (solid lines).

In the future, we plan to deploy our results in relativistic Langevin simulations of HF particles in URHICs. Combining our findings with radiative HQ scattering processes [7] yields transport coefficients that are quite comparable to the ones employed in Ref. [8] where a good description of D, D_s and Λ_c observables at the Relativistic Heavy-Ion Collider (RHIC) and the Large Hadron Collider (LHC) has been achieved. Our results could therefore play an important role in achieving a quantitative description of HF data in URHICs based on microscopically and non-perturbatively calculated transport coefficients.

[1] F. Prino and R. Rapp, J. Phys. G **43**, 093002 (2016).
[2] R. Rapp et al., Nucl. Phys. **A979**, 21 (2018).
[3] M. He, H. van Hees and R. Rapp, Prog. Part. Nucl. Phys. **130**, 104020 (2013).
[4] S. Y. F. Liu and R. Rapp, Phys. Rev. C **97**, 034918 (2018).
[5] A. P. Szczepaniak and E. S. Swanson, Phys. Rev. D **55**, 3987 (1997).
[6] D. Ebert, R. N. Faustov, and V. O. Galkin, Phys. Rev. D **67**, 014027 (2003).
[7] S. Y. F. Liu and R. Rapp, JHEP **08**, 168 (2020).
[8] M. He and R. Rapp, Phys. Rev. Lett. **124**, 042301 (2020).

Event-by-event antideuteron multiplicity fluctuation in Pb+Pb collisions at $\sqrt{s_{NN}} = 5.02$ TeV

Kai-Jia Sun[1, 2] and Che Ming Ko

[1]*Key Laboratory of Nuclear Physics and Ion-beam Application (MOE), Institute of Modern Phys, Fudan University, Shanghai 200433, China*

[2]*Shanghai Research Center for Theoretical Nuclear Physics, NSFC and Fudan University, Shanghai 200438, China*

Event-by-event multiplicity fluctuations and correlations have been suggested as a sensitive probe to the production mechanism of fragile antinuclei in high-energy nuclear collisions [1]. Using the nucleon coalescence model based on kinetic freeze-out nucleons from the hybrid model of MUSIC hydrodynamics [2] for the quark-gluon stage and UrQMD transport model [3] for the hadronic stage of ultrarelativistic heavy ion collisions, as in Ref. [4], we have studied the production of antideuteron and its event-by-event fluctuation in Pb+Pb collisions at $\sqrt{s_{NN}} = 5.02$ TeV [5]. The adopted MUSIC+UrQMD+COAL model is found to give a good description of the proton and deuteron yields in Pb+Pb collisions at $\sqrt{s_{NN}} = 5.02$ TeV, especially the suppressed *d*/*p* ratio in peripheral collisions. However, this model overestimates the net-proton number fluctuation due to the lack of exact baryon number conservation at particlization when the QGP is converted to the hadronic matter as shown in the left window of Fig. 1. To mimic the effect of baryon number conservation, we have selected a subset of events so that the net-proton number fluctuation is reduced to the level shown in the ALICE data. As shown in panel (a) of right window of Fig. 1, we have

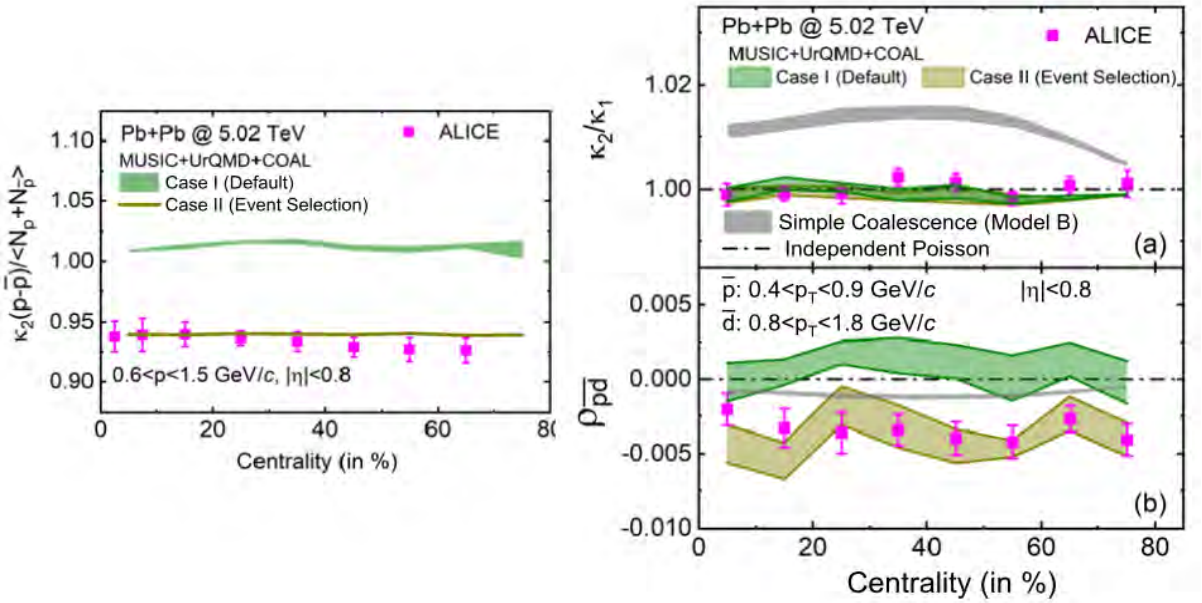

Fig. 1. Centrality dependence of the normalized second-order cumulants of net-proton distribution (left window) and antideuteron distribution (panel (a) of right window) as well as the correlation between antiproton and antideuteron multiplicities (panel (b) of right window)) in Pb+Pb collisions at $\sqrt{s_{NN}} = 5.02$ TeV. The ALICE data are shown by solid squares with combined statistical and systematic uncertainties [6,7].

found that the resulting scaled moment κ_2/κ_1 of the antideuteron multiplicity distribution agrees with the

Poisson limit for a grand canonical ensemble but is smaller than that obtained from the simple coalescence model that assumes the same probabilities for all antiproton and antineutron pairs to form a deuteron. As for the antiproton and antideuteron number correlation $\rho_{\bar{p}\bar{d}}$, which is shown in panel (b) of right window, its value from our model calculations based on the event-selection method is seen to agree with the ALICE data within uncertainties, although calculations including all events in our model fails. Our study has thus shown that the event-by-event fluctuation of net-proton number and also the negative correlation between the antiproton and antideuteron multiplicities measured in relativistic heavy ion collisions can be understood only if the baryon number conservation is preserved in theoretical models. Implementation of baryon number conservation at particlization in the (3+1)-dimensional viscous hydrodynamic model MUSIC is therefore urgently needed.

[1] Z. Fecková, J. Steinheimer, B. Tomášik, and M. Bleicher, Phys. Rev. C **93**, 054906 (2016).
[2] C. Shen and B. Schenke, Phys. Rev. C **97**, 024907 (2018).
[3] M. Bleicher, E. Zabrodin, C. Spieles, S.A. Bass, C. Ernst, S. Soff, L. Bravina, M. Belkacem, H. Weber, H. Stöcker, and W. Greiner, J. Phys. G: Nucl. Part. Phys. **25**, 1859 (1999).
[4] W. Zhao, K. J. Sun, C.M. Ko, and X. Luo, Phys. Lett. B **820**, 136571 (2021).
[5] K. J. Sun and C. M. Ko, Phys. Lett. B **840**, 137864 (2023)
[6] ALICE Collaboration, arXiv:2206.03343, 2022.
[7] ALICE Collaboration, arXiv:2204.10166, 2022.

SECTION IV

SUPERCONDUCTING CYCLOTRON, INSTRUMENTATION AND RIB UPGRADE

K500 operations and development

D.P. May, G.J. Kim, B.T. Roeder, H.L. Clark, G. Tabacaru, and F.P. Abegglen

Introduction

During the 2022-2023 reporting period a total of 13 different beams, including one newly developed beam, were used for experiments, and there were a total of 17 beam tunings for these experiments. The SEE program and the radioactive-beam effort are treated separately in this progress report.

Ion Sources

During this reporting period the newly repaired ECR1 ion source was recommissioned and again used for injection into the K500.

Cyclotron Beams

One new beam of ^{24}Mg at 35 AMeV was developed for experiments.

Operations

For the period April 1, 2022 through March 31, 2023, the operational time is summarized in Table I. Unscheduled maintenance hours reflects the repair of a water leak in a dee-stem as well as the difficult releveling of the pole-cap on its jack-screw support after it failed to lower properly during the January shut-down.

Table I. 2022-2023 Operational Time

Time	Hrs	%Time
Science	1544	18
SEE Line	3748	43
Beam Development	444	5
Unscheduled Maintenance	1072	12
Scheduled Maintenance	1928	22
Total	8736	100

K150 operations and development

G.J. Kim, B.T. Roeder, F. Abegglen, H. Clark, L. Gathings, D.P. May, H.I. Park, and H. Peeler

We had a busy year operating the K150 cyclotron. For the reporting period 4/22-3/23 we logged over 3912 hours of beam-on-target and 2296 hours for beam developments as shown in Table I. Included in the beam-on-target time was 3360 hours for in-house science experiments, and 552 hours for the SEE tests.

Table I. 2022-2023 operational time for K150 cyclotron.

Time	Hours	% Time
Beam on target	3912	45
Beam development	2296	26
Scheduled maintenance	1960	22
Unscheduled maintenance	568	7
Total	8736	100

The active users of the K150 beams were: LIG, Yennello, Rogachev and Folden groups, and the SEE testers, who used proton beams as well as heavy ion beams.

The LIG ran more than a dozen times using from 9.0 to 27 MeV proton beams, using intensities from 2 to 10 μA for their radioactive ion production and then charge breeding with CBECR for injection into K500. Getting the proton beam intensity up to 10 μA is relatively easy with the H^- source and the strip extraction. The source output is regulated with the H^- arc current, and with a few amps on the arc current there is enough to get to 10 μA on FC02. The injection efficiency into cyclotron is good and the extraction efficiency is very high, around 80%. But not all the extracted beam can be transported to the experimental cave as the beam spot at the object slit is a little wide. As for the beam transmission to the LIG gas cell, we averaged about 80 to 90%, (from FC02 to FC23) as the beam current was optimized onto the faraday cup (FC23) just downstream of the gas cell.

The astatine 211 production program continues to run regularly, once a month usually, and uses 8 to 12 μA of the 7.2 MeV/u $^{4}He^{1+}$ beam for 12 to 16 hour irradiation on a water-cooled bismuth target. We have extracted up to 18 μA on FC02 thus far, but the RF and the deflector run more stably near the 10 μA level. The deflector extraction efficiency has improved to about 50%, and the throughput from ILC02 to FC02 is about 10%. Typical beam intensity numbers are: starting with about 200 μA on ILC02, with 50% $^{4}He^{1+}$ and the rest $^{16}O^{4+}$, 10 μA of $^{4}He^{1+}$ is extracted on FC02.

We tuned out 6.6 and 6.9 MeV/u $^{48}Ti^{13+}$ beams for the Folden group, and we used a high temp oven and also a Ti-MIVOC method to feed the ion source. To run the high temp oven, it required 157 W (109 A at 1.44 V) to produce metal vapor into the source, and this gave us more than 800 nA out of the cyclotron. Unfortunately this much beam current ate up the source material too fast and just after one day of running it needed to be loaded again. Running at a lower oven power at about 130 W and hence a lower beam current of about 200 nA to stretch the run without reloading the Ti metal into the source did

work, but running the high temp oven was not entirely trouble free for the run. In the Fall of 2022, we tried a MIVOC method, whereby Ti-MIVOC (Titanocene) powder in a bottle was leaked into the ion source. This method is much easier to run than setting up the high temp oven, however for this first go around the beam current was insufficient, as less than 100nA was extracted from the cyclotron and deemed inadequate for the experiment. For the next time, because the larger conductance is important, a larger diameter tube between the MIVOC bottle to the source will be used. Since our usual gas inlet tube is ¼" diameter, a larger inlet will need be connected to the side port on the source, where the sputter fixture or the low temp oven gets installed.

The SEE testing continues to run regularly and both proton and heavy ion beams are used for the testing. Since last year beams heavier than ^{78}Kr have been used in testing, such as ^{90}Zr and ^{107}Ag at 13 and 11 MeV/u, respectively. This year 9.4 MeV/u $^{124}Xe^{34+}$ beam has been added. However, our established 15 MeV/u beams are requested more often, and in order to save time tuning one beam to another, we have tried switching the beams by changing the RF frequency while keeping the magnetic field the same. For example, after tuning out the $^{40}Ar^{14+}$ (z/A=0.3504) beam at 8.6988 MHz for 15.3 MeV/u, to change to similar charge-to-mass (z/A) beam near 0.35, the RF frequency is scaled with the charge-to-mass. So to switch to $^{78}Kr^{27+}$ (z/A=0.3466), the new RF frequency of 8.6037 MHz would be used. However the energy of the new beam goes as the square of the frequency, thus the energy would be 15.0 MeV/u for the $^{78}Kr^{27+}$ beam.

The effectiveness of the internal cryopanel on the cyclotron vacuum and beam vacuum attenuation were studied during the summer and fall of 2022. The cyopanel has two cooling plates and each is separately cooled by flowing LN2 or LHe. The refrigerant consumption rate and cyclotron vacuum values are evaluated. The typical cyclotron vacuum, without the cooled cryopanel, is around $1x10^{-6}$ torr and is referred to as the base vacuum. With LN2 on flowing on the larger of the cooling plates and the other cooled by the LHe the vacuum improved to $7x10^{-7}$ torr. A better vacuum was obtained with LHe cooling both the plates, and it got to $1x10^{-7}$ torr. The vacuum improvement should help especially with heavy ion beams and we tested that with 6.3 MeV/u $^{129}Xe^{31+}$ and 3.0 MeV/u ^{197}Au 37+ and 38+ beams. For the Xe beam the extracted current improved from ~1 nA at the base vacuum to ~2 nA at $1x10^{-7}$ torr. However, for the gold beams the improvements were much more dramatic. Tuning up 3.0 MeV/u $^{197}Au^{37+}$ beam, we saw tiny 4 pA on FC02 with the base vacuum, and as the cryopanel cooled and the vacuum dropped to $1.1x10^{-7}$ torr the beam current increased to 170 pA. We even saw 50 pA of 3.0 MeV/u $^{197}Au^{38+}$ at $1.1x10^{-7}$ torr, and then as cryopanel warmed up only 1.5 pA remained as the cyclotron vacuum return to the base value.

Texas A&M Cyclotron Radiation Effects Facility
April 1, 2022 – March 31, 2023

H.L. Clark, G. Avila, V. Horvat, B. Hyman, M. Kennas, G. Kim, H. Park, C. Parker,
R. Rinderknecht, B. Roeder, G. Tabacaru and E. Wilkinson

The activity of the Radiation Effects Facility (REF) decreased slightly from last year but was still the third highest reported year ever. In this reporting period, the facility was used for 3,684 hours, which is a 4% decrease over the hours of 2021-2022. The decrease was mainly due to issues with the K500 cyclotron RF system in December 2022 which lead to an early annual shut down. Users of the facility

Table 1. Radiation Effects Facility usage by commercial and government customers for this and previous reporting years.

Reporting Year	Total Hours	Commercial Hours (%)	Government Hours (%)
2022-2023	3,684	2,991 (81%)	693 (19%)
2021-2022	3,852	3,122 (81%)	730 (19%)
2020-2021	3,300	2,435 (74%)	865 (26%)
2019-2020	3,982	2,862 (72%)	1120 (28%)
2018-2019	3,678	2,939 (80%)	739 (20%)
2017-2018	3,681	2,622 (71%)	1,059 (29%)
2016-2017	3,355	2,501 (75%)	854 (25%)
2015-2016	3,042	2,326 (76%)	716 (24%)
2014-2015	3,024	1,975 (65%)	1,049 (35%)
2013-2014	2,399	1,517 (63%)	882 (37%)
2012-2013	2,626	1,856 (71%)	770 (29%)
2011-2012	2,673	1,630 (61%)	1,043 (39%)
2010-2011	3,042	1,922 (63%)	1,121 (37%)
2009-2010	2,551	1,692 (66%)	859 (34%)
2008-2009	2,600	1,828 (70%)	772 (30%)
2007-2008	2,373	1,482 (62%)	891 (38%)
2006-2007	2,498	1,608 (64%)	890 (36%)
2005-2006	2,314	1,314 (57%)	1,000 (43%)
2004-2005	2,012	1,421 (71%)	591 (29%)
2003-2004	1,474	785 (53%)	689 (47%)
2002-2003	1,851	1,242 (67%)	609 (33%)
2001-2002	1,327	757 (57%)	570 (43%)
2000-2001	1,500	941 (63%)	559 (37%)
1999-2000	548	418 (76%)	131 (24%)
1998-1999	389	171 (44%)	218 (56%)
1997-1998	434	210 (48%)	224 (52%)
1996-1997	560	276 (49%)	284 (51%)
1995-1996	141	58 (41%)	83 (59%)

(and hours used) over the past year were: Northrop Grumman (447), Texas Instruments (270), Renesas (245.5), RTS (186), Sandia Nat Lab (181.75), AFRL (168), Amazon (142), Infineon (135.5), Lockheed Martin (122), Milanowski (115), NAVSEA (111), Cobham (96), Raytheon (96), Draper (82), Boeing Satellite Systems (80), Johns Hopkins (66), SEAKR (64), Space X (62), EPC Space LLC (61), NASA GSFC (56), VPT Inc (56), Axiom Space (48), L3Harris (48), Boeing R&T (40), Millennium (39), Troxel Engineering (37), AirBus-France (32), Aria Labs (32), Microchip (32), Scientic (32), Signal Analysis (32), Teledyne (32), Honeywell (31), NASA JPL (28), Vanderbilt (28), TAMU EE/Physics (28), Utah State University (26), Apogee (24), Blue Origin (24), MOOG (24), Thales Alenia-Spain (24), Space Micro (19), Astranis (16), CFDR (16), CoolCad (16), Innoflight (16), Viasat (16), JD Instruments (16), Avalanche (14), Firefly (14), General Dynamics (13), TruVentic (12), Analog Devices (8), and VPT RAD (8). Firefly was the only new user.

Table I compares the facility usage by commercial and government customers. While commercial hours still dominate, the ratio from this reporting year (81% to 19%) is similar to usage from previous reporting periods (see Fig 1). Commercial usage decreased by 4% and was the second highest commercial usage ever. Government usage decreased by 5% and was the lowest usage since the 2004 – 2005 reporting period. The 15 MeV/u ions were the most utilized and especially 15 MeV/u Au. No new

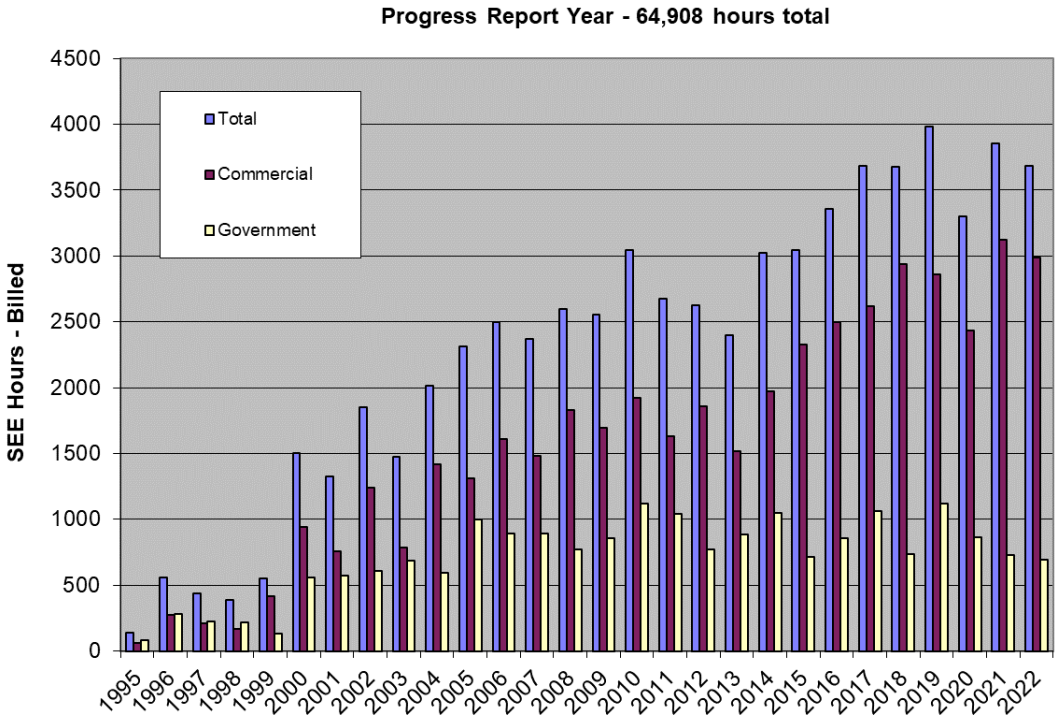

Fig. 1. Radiation Effects Facility usage by commercial and government customers for this and previous reporting years. While commercial hours still dominate, the ratio from this reporting year (81% to 19%) is similar compared to usage from prior reporting period. Usage hours decreased slightly from last year's reporting period but was the third highest amount in history. 64,908 hours have been billed since the start of the project in 1995.

beams were added to the K500 cyclotron SEELine users list. Much of the testing conducted at the facility continues to be for defense systems by both government and commercial agencies. We had three foreign

users at the facility: AirBus-France (32 hours), Teledyne-Canada (32 hours) and Thales Alenia-Spain (24 hours).

Development of an electron cyclotron emission imaging system

L.E. Henderson, H.L. Clark, C.A. Gagliardi, and D.P. May

The electron cyclotron emission imaging system for the Cyclotron Institute's electron cyclotron resonance ion sources (ECRIS) is actively being assembled. The current state of the receiver tower, which houses the electronics for the system, and the receiver cage, which houses the antennas and many of the optical elements, is shown in Fig. 1. The mechanical design and construction is largely complete, and the optical elements and custom electronics will be finalized and fabricated in the coming weeks.

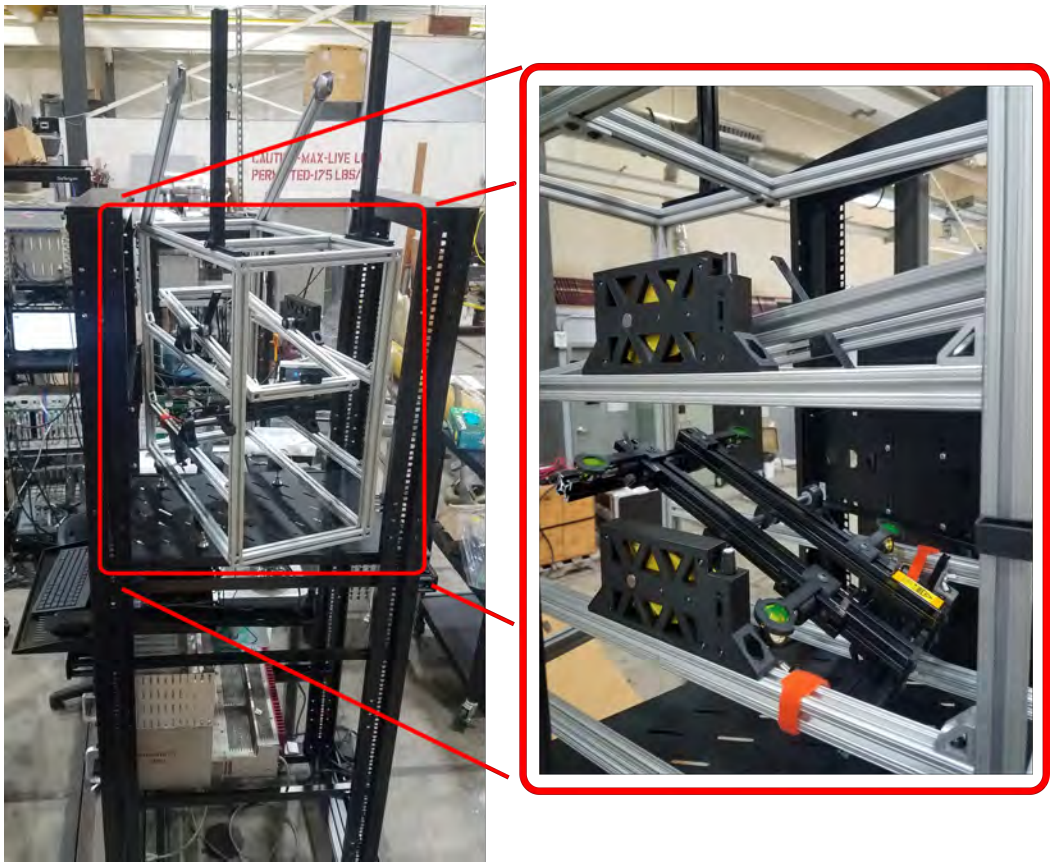

Fig. 1. The receiver cage sitting on its platform in the receiver tower, which houses the support electronics. The inset shows the 3D-printed gearboxes supporting the frames which will mount the beamsplitters and receiver antennas

It was found necessary to revisit the design of the primary optic, which was originally designed by a fastest descent algorithm that iteratively ran 2D full-wave electromagnetic simulations using the MEEP package. Those simulations did not adequately predict the interaction of the optics with the waveguides, and it recently became possible to specify aspheric lens surfaces as a custom geometry within MEEP. Combined with an improved design pipeline, with a new paraxial calculation Python code and ray-tracing in BEAM4, the new 3D MEEP simulations give a much more accurate prediction of diffraction and interference effects.

The new optical design pipeline made it possible to find a single aspherical alumina lens (Fig. 2a) that can replace the five-layer alumina and teflon spherical lens stack of the previous primary optic design. This is not without trade-offs, as the new design has a lower numerical aperture, but fabrication and assembly will be much easier with the new design. The transmitivity of the single lens also varies relatively smoothly with frequency, unlike the old design.

(a) (b)

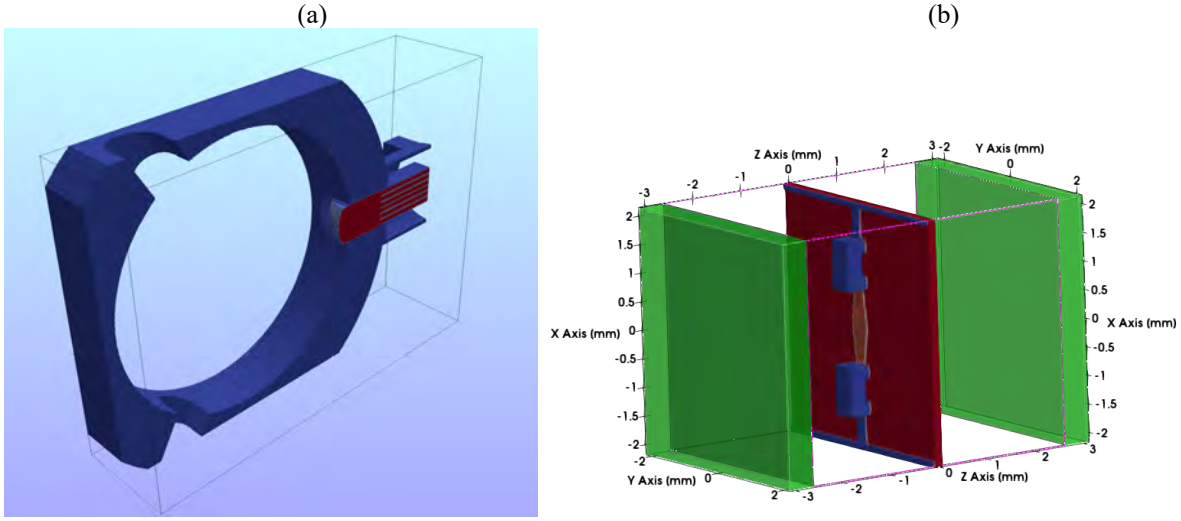

Fig. 2. Paraview renderings of the MEEP simulation geometries for (a) a cutaway of the plasma chamber with the primary optics and (b) the EVRS unit cell. Electromagnetic absorbers along the simulation domain boundaries are omitted from (a) since they line all sides of that simualtion, but the absorbers for (b) are shown in green.

The design of the electronically variable reflective surfaces (EVRS) has also been improved over the past year. Numerous unwanted resonances and couplings were found and explained, leading to a revised unit cell that is much simpler than before. Our anechoic test chamber will be used to verify if the frequency response of prototypes of the new design match simulations, and if they do match the prototypes can be used as the beamsplitter elements in the receiver cage.

The overall electronics scheme and timing sequence for camera operation has been worked out and most of the off-the-shelf components (such as the spectrum analyzers) have been acquired. Once the remaining custom electronics (like the EVRS control boards) have been fabricated, all of the electronics will be integrated in the receiver tower with the data acquisition computer.

Progress on the light ion guide project

G. Tabacaru, V. Kolhinen, J. Ärje, D.P. May, A. Saastamoinen, F.P. Abegglen, L.N. Gathings, G.J. Kim, S. Molitor, and B.T. Roeder

The Light Ion Guide (LIG) group continued to work on improving the LIG's overall efficiency. For the 2.4 m long sextupole consisting of 5 sections a short, about 10 cm long movable section/Si-detector has been installed before the fifth sextupole section which finally guides the ions into the ECR charge breeder. The position of the mobile detector can be adjusted remotely (photo in Fig.1.).

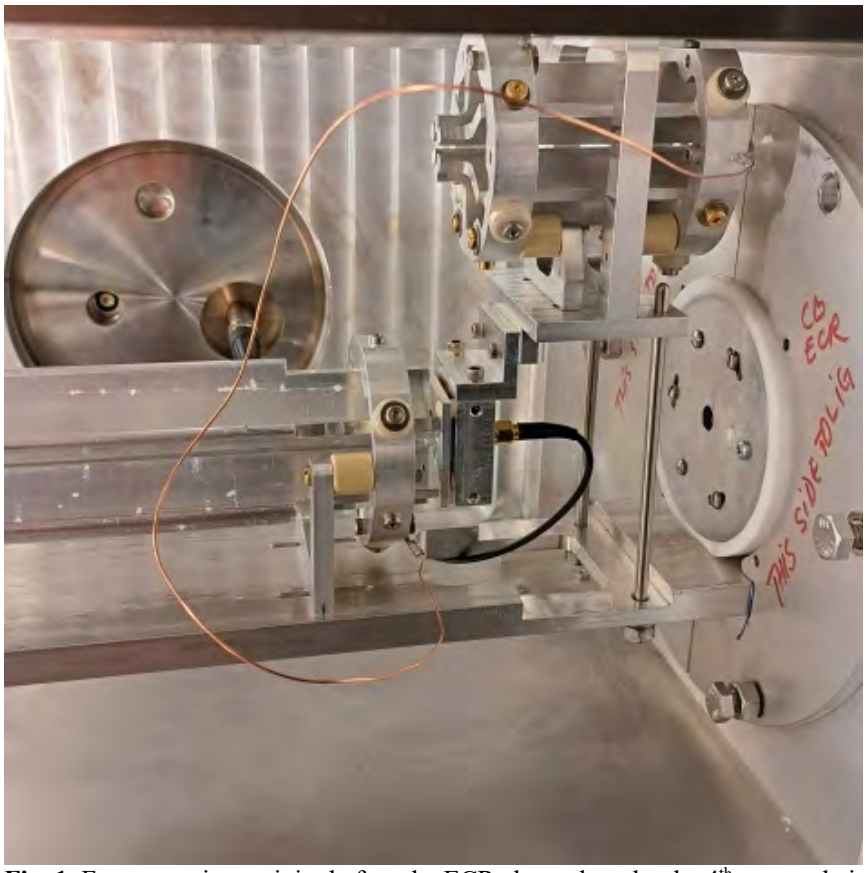

Fig. 1. For measuring activity before the ECR charge breeder the 4th sextupole is raised up and the detector is in collecting position.

This movable detector made transport of radioactive species more consistent. We focused especially to improve our ability to create desired highly charged ions, the main goal being presently a good production of 89Nb for the reacceleration.

The latest result with the charge breeding of $^{89}Nb^{17+}$ is shown in Fig. 2.

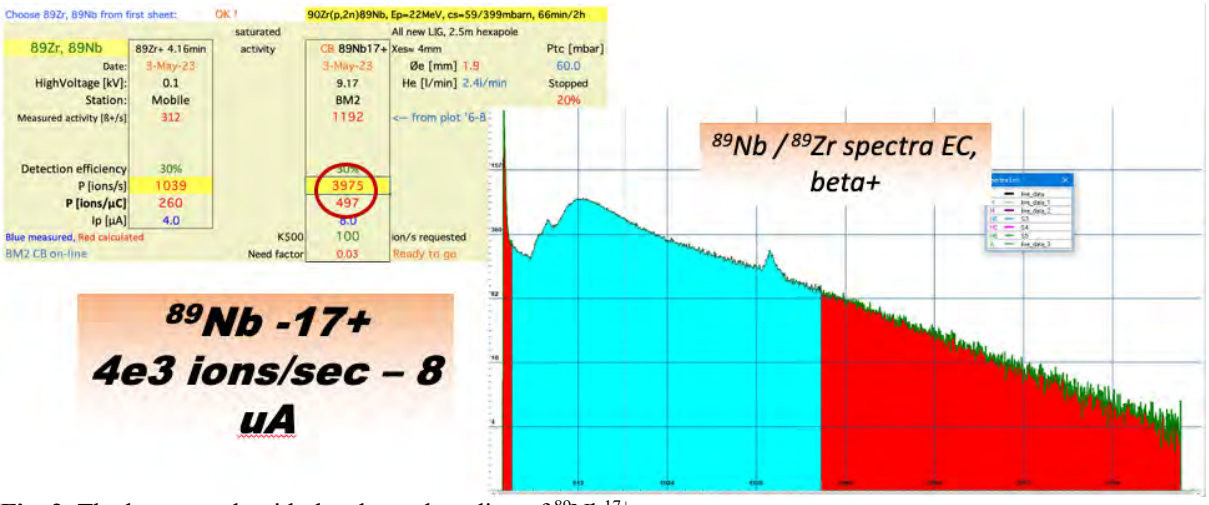

Fig. 2. The latest result with the charge breeding of $^{89}Nb^{17+}$

With the proton beam intensity of 8 μA the charge bred yield of $^{89}Nb^{17+}$, over 4000 ions/s is 40 times more than the minimum yield requested for the K500.

Electronic check in and check out for SEE-line customers

V. Horvat

Program CheckW was written and implemented to allow customers of the TAMU Radiation Effects Facility (SEE-line customers) to electronically check in each time they come in and check out each time they leave the Cyclotron building. The corresponding dates and times are logged automatically. On their first check-in per visit the program prompts the customers to update their contact information, which includes their first name (and nickname), last name, company name, email address, and cell-phone number. The information already existing in our database is shown, if available, in order to minimize typing. The updated or just confirmed information is saved in a file, but the database must be updated manually, because the computer on which CheckW is running is intentionally not connected to the internet and because, to ensure its integrity, the entered information should be verified by a live person before updating the database.

As a customer checks out, file TimeSheet.txt is created and displayed. This file contains a complete list of the customer's check-in and check-out records. It can be saved under a different name in order to preserve this information or it can be closed in order to be overwritten by the records from the next customer who checks out. This feature was made available on customers' request.

CheckW graphic user interface for the customers is made as simple as possible. Interface for the administrator is somewhat less intuitive, but very efficient. The dialog box of CheckW, as illustrated in FIG. 1, consists of two sections. One contains displays and controls available to the customers, while the other contains displays and controls available exclusively to the administrator. The administrator is

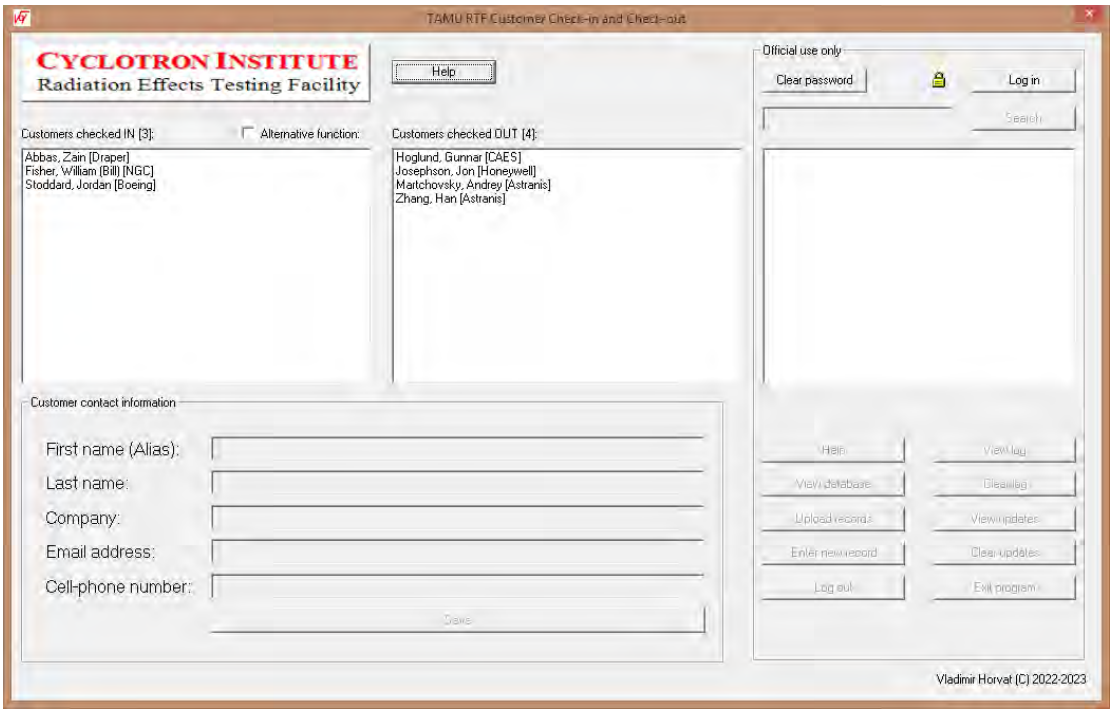

Fig. 1. Example of the default CheckW graphic user interface.

expected to prepare a list of all the customers who are expected to use the software in the near future by placing their names in the "Customers checked OUT" window. In the process the corresponding records are set for a first-time check-in per visit. The customer then checks in by clicking on his or her name and following the prompts, until the customer's name gets moved to the "Customers checked IN" window. To check out, the customer clicks on his or her name in the "Customers checked IN" window and decides what to do with the time sheet information that pops up. The customer's name is then automatically moved to the "Customers checked OUT" window.

The administrator must log in to unlock the privileged functions that let him or her exit the program, add a new record to the database or edit an existing one, remove a record from the list or from the database, as well as view and/or search the database, the ledger and the record updates. The ledger and the record updates also can be erased in order to start fresh.

Normally, a customer is allowed only to check in and check out by clicking on his or her name listed in one of the two windows labeled "Customers checked OUT" and "Customers checked IN". The only exception is a possibility to reset a customer's status, so that his or her next check-in is treated as the first one per visit. This is set so that customer's contact information, if erroneously entered, can be re-entered correctly. The most common mistakes are related to spelling or entering information for a wrong individual. To use this feature the customer's name must be listed in the "Customers checked IN" window and the "Alternative function" box must be checked. Then the customer's name should be clicked. The "Alternative function" box should be unchecked as son the alternative functions are no longer needed in order to avoid unwanted results in the future. Otherwise, it will be unchecked automatically after 60 seconds of inactivity.

When the administrator logs in, all the buttons and windows in the dialog box became enabled and the image of a closed padlock disappears. However, for security reasons, the administrator will be logged out automatically after 60 seconds of inactivity. After the log-in, the administrator can

- View a copy of the ledger file by clicking the "View log" button,
- Clear the ledger by clicking the "Clear log" button
  (a backup copy of the ledger will be made before its contents are erased.),
- View the contact information updates or confirmations by clicking the "View updates" button,
- Clear the contact information updates or confirmations by clicking the "Clear updates" button
  (a backup copy will be made before the file contents are erased),
- Exit the program by clicking the "Exit program" button, or
- Log out and fall back to the customer mode by clicking the "Log out" button.

No database information is lost upon exit from the program. A log-out will be performed before exit and the program will restart with the same lists presented in the "Customers checked IN" and "Customers checked OUT" windows.

Customer records that are listed in the "Customers checked OUT" window can be hidden, i.e., removed from display, but still kept in the database. To hide a record, make sure that you are logged in and that the "Alternative function" box is unchecked. Then click on the record in the "Customers checked OUT" window and confirm the prompt that pops up.

To add an existing record from the database to the "Customers checked OUT" list (and set it for a first-time check-in per visit), fist find it by entering a suitable string pattern in the Search window and then click the "Search" button. The record, if found, will be listed in the window below (possibly along with some additional matching records). Make sure that the "Alternative function" box is unchecked. Then click on the record you want to add. Be aware that the search function will ignore the records that are already displayed, either in the "Customers checked OUT" window or in the "Customers checked IN" window. This is set that way in order to avoid displaying duplicate records. Also be aware that the search function is case sensitive.

To edit an existing record or to remove it from the database, fist find the record by entering a suitable string pattern in the Search window and then click the "Search" button. The record, if found, will be listed in the window below (possibly along with some additional matching records). Make sure that the "Alternative function" box is checked. Then click on the record you want to work on. Select between edit or delete in the prompt that pops up. Unless the delete option was chosen. edit the record components displayed in the corresponding edit windows, and click the "Save" button. To verify that the operation was successful, search for the updated record.

To add a new record to the database, start by filling out the appropriate edit windows with First Name (Nickname), Last Name, Company Name, Email address, and cell-phone number, and then click the "Save" button. To verify that the operation was successful, search for the newly entered record.

The search capability can be used not only to search the database (with "Alternative function" box unchecked), but also to search the ledger (when the "Alternative function" box is checked). In the latter case the results are listed in file TimeSheet.txt, a copy of which opens following the search. This way the actual time sheets can be re-created at any time. Also, any other information listed in the ledger can be compiled, such as the number of customers present at the Facility as a function of time.

The database file is compatible with the Microsoft Excel file shared within the SEE-line group on Microsoft Teams, from which the CheckW database can be (re)created at any time in its default mode, *i.e.*, with no records displayed in the "Customers checked IN" window or in the "Customers checked OUT" window. It should be noted that the customer records are created by the program using the information stored in the database. It is those records that are searched, not the actual database or spreadsheet entries. Their format is "Last Names, First Names (Nick Names) [Company Name]". Email addresses and cell-phone numbers are not displayed except that a customer can see his or her own data when checking in for the first time per visit.

CheckW administration should parallel handling of customer dosimeters. When a customer's dosimeter is put on the rack, his or her record should be put in the "Customers checked OUT" window, set for the first-time check-in per-visit. After the customer's final check-out per visit, his or her record should be hidden and his or her dosimeter should be stored in the designated dosimeter organizer.

Improvements in the radiation-testing hardware and software

V. Horvat and B. Hyman

In 2020 our software package (SEUSS) [1], used for control of the hardware and characterization of the beams at the Radiation Effects (SEE-line) Facility, has undergone a major upgrade from its 2019 version [2], in which SEUSS results for ion energy loss and range were set to match those obtained using the latest version of the Stopping and Range of Ions in Matter (SRIM) code [3], while keeping an option to do the calculations using the pre-upgrade method. Meanwhile, development of the software continued in response to hardware updates and users' requests.

In 2021 the selection of K500 beams imbedded in SEUSS was updated and made consistent with the list of K500 beams available for radiation testing. Furthermore, a separate selection of K150 beams, consistent with the list of K150 heavy-ion beams available for radiation testing, was created and made available for runs involving the K150 cyclotron. In the new beam lists atomic mass number of the ion is now a part of the beam name.

Since the 2022 version of SEUSS the users may define the background flux level used by the software to determine whether the beam is present or not present. This has an effect on the live-time fraction of the run time. The background flux level may be significant in a series of runs involving high beam intensity. Under these conditions the detectors and the surrounding structures may be activated, so that the ion detectors count even in the absence of the ion beam.

The data from the most-recently finished run are now available in the JSON format, which is easily read and parsed using java scripts. This is convenient for the users who want to analyze the data in real time, as soon as each run is finished.

A pdf tutorial for new users of SEUSS is now available online [4]. This tutorial is also a good reference for more experienced users and it provides answers to frequently asked questions. In contrast to the existing SEUSS Manual, which addresses the features of the software available in each dialog box or window, the tutorial explains the use of available features as needed during a run in a typical chronological order.

Further progress has been made regarding the migration toward a complete hardware and software solution supported by the Windows 10 operating system. To reach this goal, a new hardware has to be acquired and set to be controlled by the software in order to perform the following tasks: (*i*) generate suitable output voltages for inputs to nine detector power supplies, as well as provide an indicator that the beam path is clear all the way to the target; (*ii*) count the signals originating from the ion detectors; and (*iii*) physically move the target and the beam-energy degraders. The hardware for items (*i*) and (*ii*) already has been obtained from National Instruments [5], while the hardware for item (*iii*) is expected to become available soon. Development of the software for items (*i*) and (*ii*), illustrated in Fig. 1, is now completed and ready to be tested.

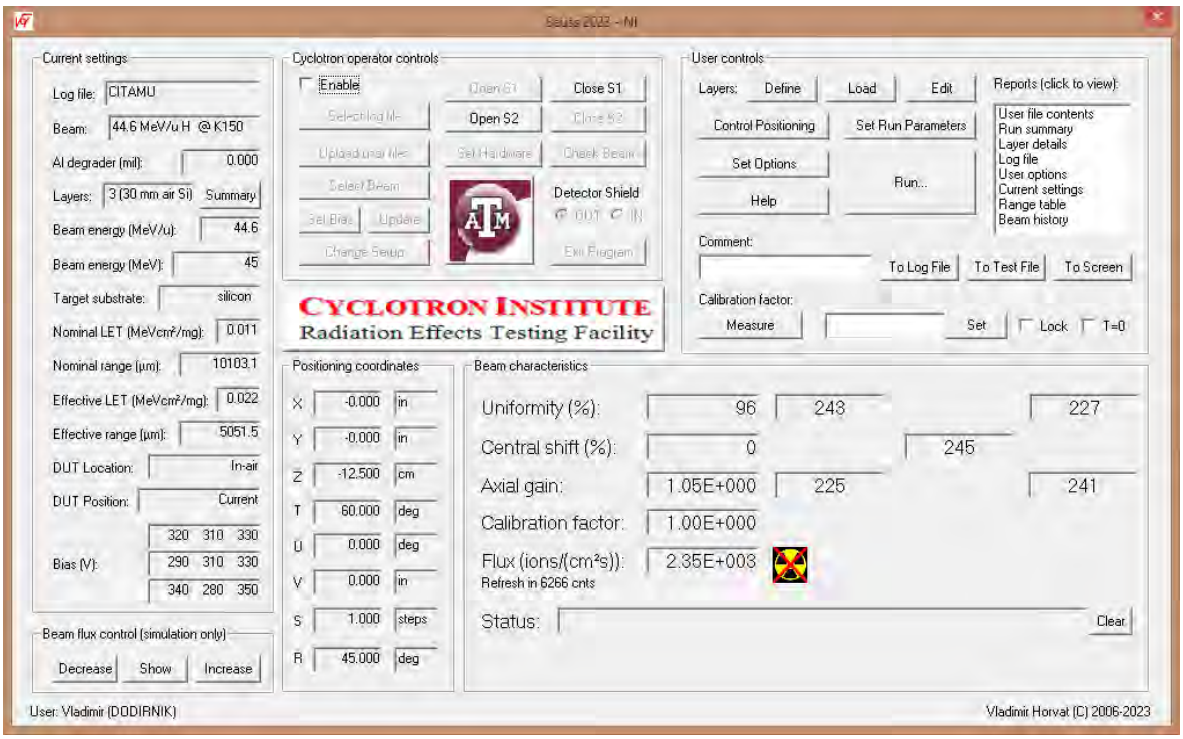

Fig. 1. A fully functional version of SEUSS software that supports hardware from National Instruments [5] is now available. Two NI modules are to replace the obsolete CAMAC system. One of the modules sets the required voltage levels, while the other module counts signals generated by the ion detectors.

[1] https://cyclotron.tamu.edu/vladimir/SeussW-Download.htm .

[2] V. Horvat, B. Hyman, M. Kennas and H.L. Clark, *Progress in Research*, Cyclotron Institute, Texas A&M University (2019-2020), p. IV-26.

[3] http://www.srim.org/ .

[4] https://mare.cyclotron.tamu.edu/vladimir/SEUSS-Tutorial.pdf .

[5] https://www.ni.com .

Liquid He cyropanel test for the K150 cyclotron

B.T. Roede, F. Abegglan, R.S. Olsen, and G.J. Kim,

This year, the K150 cyropanel was tested with liquid nitrogen and liquid helium for the first time since its installation in 2013. The cyropanel is shown in Fig. 1, while it was under construction. The cyropanel is made of copper and consists of an inner chamber intended for liquid helium surrounded by an outer chamber intended for liquid nitrogen. The cyropanel has a large surface area and is placed in the cyclotron in such a manner as to allow the removal of residual gases throughout the cyclotron chamber. At temperatures less than 20 K, achievable with such a device, the cyropanel can pump and remove any residual oxygen, nitrogen and argon present in the cyclotron chamber and thus improve the transmission for heavy ion beams.

Fig. 1. The K150 cyropanel during its construction.

The K150 cyropanel was tested in September through November of 2022 with two different configurations and two different heavy ion beams of interest. A summary of the tests is shown in Table I and II. The first configuration for the cryopanel was the originally intended one: cooling the inner chamber with liquid He and the outer chamber with liquid nitrogen. In this mode, the cyropanel improved the measured cyclotron chamber vacuum from $9.0*10^{-7}$ torr to $6.0*10^{-7}$ torr and consumed about 2-3 L/hr of liquid He. This setup was tested with two beams: $^{129}Xe^{31+}$ at 6.3 MeV/u and $^{197}Au^{37+}$ at 3.0 MeV/u. For ^{129}Xe, the beam transmission improved by nearly a factor 2 vs. when the cryopanel was not cold. For ^{197}Au, the beam transmission improved by a factor of 3.

Table I. Results of cyropanel tests with 129Xe31+ at 6.3 MeV/u.

Date	Cryopanel Configuration	K150 Vacuum	FC02 Reading
9/27/22	Warm	$9.0*10^{-7}$	1.4 nA
9/27/22	Liquid N_2 outer chamber, Liquid He, inner chamber	$6.0*10^{-7}$	2.2 nA
10/22/22	Warm	$9.0*10^{-7}$	0.7 nA
10/22/22	Liquid He, both chambers	$1.1*10^{-7}$	2.0 nA

Table II. Results of Cyropanel Tests with 197Au37+ at 3.0 MeV/u.

Date	Cryopanel Configuration	K150 Vacuum	FC02 Reading
11/3/22	Warm	$9.0*10^{-7}$	7 pA
11/3/22	Liquid N_2 outer chamber, Liquid He, inner chamber	$6.0*10^{-7}$	20.5 pA
11/3/22	Liquid He, both chambers	$1.1*10^{-7}$	170 pA

The second configuration tested was with both chambers of the cyropanel cooled with liquid He. In this configuration, the entire surface area of the cyropanel was cooled to less than 20K. In this mode, the measured cyclotron chamber vacuum improved from $9.0*10^{-7}$ torr (cyropanel warm) to $1.1*10^{-7}$ torr and consumed about 18-20 L/hr of liquid He. This setup was tested with the same two heavy ion beams as in the previous test. For ^{129}Xe, the beam transmission improved by a factor 3. For ^{197}Au, the beam transmission improvement was more dramatic; it improved by more than a factor of 20! This test demonstrated what was possible with the increased pumping capacity provided by the cyropanel, at the cost of higher liquid He consumption.

In conclusion, the liquid He cyropanel for the K150 cyclotron was tested and shown to improve both the cyclotron vacuum and heavy ion beam transmission for the K150. However, the available intensity for the heavy ion beams also depended on the production of high charge states by the ECR2 ion source. The combination of a higher frequency, higher power ECR ion source and the improved vacuum of the K150 cyclotron will allow the production of new heavy ion beams at higher intensity for future experiments and SEE line testing.

MARS status report for 2022-2023

B.T. Roeder and A. Saastamoinen

This year, we continued the program of providing rare isotope beams (RIBs) for the physics program at the Cyclotron Institute at Texas A&M University with the Momentum Achromat Recoil Separator (MARS) [1]. The MARS beam line was utilized in 6 separate experimental runs for various experiments involving rare isotope beams.

Several experiments with rare isotope beams were conducted with ions that had been developed in previous years. A summary of these RIBs is given in Table I. ^{12}N was produced for an experiment of Professor Rogachev's group in collaboration with experimenters from Brazil. There was a ^{6}He beam made for an experiment with Professor Lee Sobotka's group from Washington University in St. Louis (WUSTL). A ^{11}Be beam was produced for Greg Christian's group and Dr. Shuya Ota for a transfer reaction measurement. The ^{14}O for Professor Rogachev's group was used in an experiment in collaboration with a group from the Institute of Basic Science (IBS) in South Korea. A higher energy ^{14}O beam was also developed for the WUSTL group. It will be used in an upcoming experiment later in 2023. Finally, a ^{13}B beam was produced for Professor Rogachev's group for a transfer reaction measurement with TexAT.

Table I. Summary of MARS RIBs for 2022-2023.

RIB beam	**Reaction**	**Production Rate (eV/nC)**	**Purity**	**Intensity on Target (est.)**
^{12}N	^{10}B+^{3}He at 10.2 MeV/u(Transfer)	7.3 eV/nC	~44%	~2*10^{3} p/s
^{6}He	^{2}H(^{7}Li,^{6}He)^{3}He (Transfer)	126 eV/nC	~69%)	5*10^{4} p/s (~10^{5} possible)
^{11}Be	^{13}C+^{9}Be at 30 MeV/u (Frag.)	78 eV/nC	~70%	~10^{4} p/s
^{14}O	p(^{14}N,^{14}O)n at 17 MeV/u (Transfer)	322 eV/nC	~75%	~2*105 p/s
^{14}O	p(^{14}N,^{14}O)n at 9.1 MeV/u (Transfer)	207 eV/nC	100%	1.8*10^{5} p/s
^{13}B	^{15}N+^{9}Be at 30 MeV/u (Frag.)	54 eV/nC	82%	~10^{4} p/s

During the ^{12}N experiment with the Rogachev group / Brazil collaboration, the MARS liquid nitrogen cooled gas production target had several sudden failures of the HAVAR windows. This was due to the interaction of the primary beam (^{10}B) with the epoxy used to seal the windows. The damage to the epoxy seal was evident from discoloration of the seal in the region where the beam had heated it. The failure of the epoxy seal had been an ongoing problem and occurred most often when low energy, high intensity primary beam from the K150 cyclotron was used for the production of RIBs. In the 2021-2022 year, an aluminum collimator with a 0.6 inch diameter hole, designed by A. Saastamoinen, was added to the front of the gas target to attempt to address this problem by blocking any beam tails from entering the

target. However, gas window failures continued to occur. The only way to prevent the gas window failure was to use lower beam intensity, which severely limited the RIB intensities that could be available.

Following the ^{12}N experiment, A. Saastamoinen painted the 0.6 inch diameter collimator with a mixture of ZnS and glue, such that any beam tails impinging on the gas target could be observed via camera during beam tuning and during the course of the experiment. The resulting painted collimator is shown in Fig. 1. During the subsequent experiments with ^{6}He and ^{14}O RIB production, it was observed that, while it was possible to have the primary beam centered on the MARS quadrupole magnet by adjusting only the upstream dipole magnet MARSBLD1, that adjustment forced the path of the primary beam to hit the right hand side of the gas target, as seen with the new painted collimator. It is now believed that this was the cause of the repeated gas target window failures.

With the help of the painted collimator, a new optics beam tune was developed where both the upstream dipole magnets, the "Indiana" magnet and the MARSBLD1, are adjusted in tandem to obtain a primary beam tune where 1) the primary beam is centered on the gas target and 2) the primary beam is centered with respect to the first quadrupole doublet of MARS. For the K150 cyclotron beam, the adjustment is typically 1-2 A lower on "Indiana" magnet (Spectrograph power supply) and up to 30 A lower on MARSBLD1. A similar adjustment for the beam from the K500 beam is also needed, but the parameters of that adjustment are still being determined.

The adjustments to the primary beam optics have resulted in less failures of the gas cell windows and improved primary beam intensities on target. Transmission of up to 50% from the cyclotron FC02 to target has been obtained, whereas typical transmissions were less than 25% previously. Record measured intensities of 700 pnA for ^{7}Li and 220 pnA for ^{14}N were observed on the MARS coffin faraday cup without corresponding window failures.

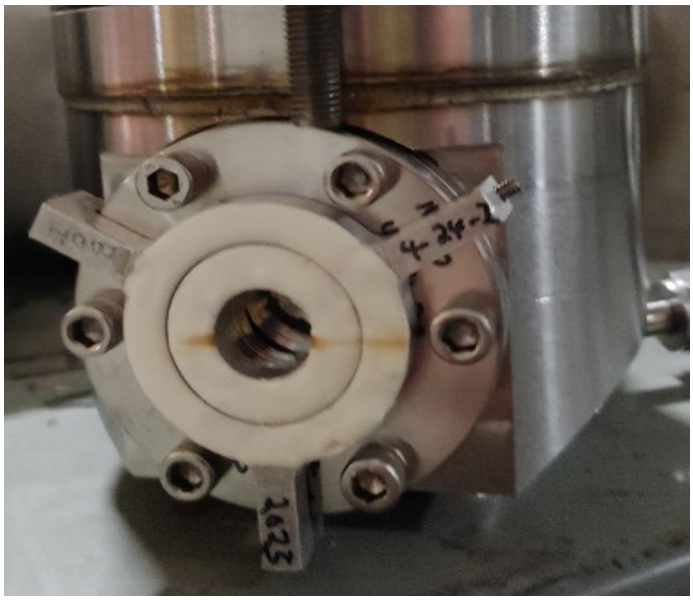

Fig. 1. The new collimator for the MARS gas target painted with ZnS / glue mixture. A brown line from the beam hitting the collimator during tuning is visible across the face of the collimator.

[1] R.E. Tribble, R.H. Burch and C.A. Gagliardi, Nucl. Instrum. Methods Phys. Res. **A285**, 441 (1989).

Computing at the Cyclotron Institute for 2022-2023

R. Burch, J. Gauthier, K. Hagel, and Y.-W. Lui

General

The computational support team has made significant advancements in three key areas this year: automation, compute, and security. In terms of automation, the team successfully implemented an Infrastructure as Code (IaC) philosophy to enhance computer installation, deployment, upgrade, and patching processes. This involved utilizing a centralized repository and creating configuration tooling to facilitate collaborative development, improve editing, distribution, and revision processes, and maintain code integrity.

Regarding compute, the team deployed 8 compute blades using Zero-Touch Provisioning, specifically the Preboot Execution Environment (PXE) Boot and Infrastructure as Code (IaC) installation process. This deployment significantly increased the available job slots by 320. The servers were configured to meet the Institute's specifications and were equipped with the required software and applications to support the Institute's mission.

In the realm of security, the team prioritized the installation of security software and the update of the firewall infrastructure. Leveraging their configuration management and deployment capabilities, they adopted a proactive approach to strengthen security measures and safeguard sensitive data. Additionally, they collaborate with TAMU Security, and implement additional measures to maintain a robust security framework.

Collectively, these efforts in automation, compute, and security have yielded positive results by enhancing the efficiency, reliability, and security of the infrastructure. The team remains committed to further optimizing systems, adapting to evolving needs, and aligning with best practices to ensure a secure and efficient computing environment for the Institute.

New backup server

In 2022, we implemented a backup solution for the Cyclotron Institute's Windows and Mac computers. A Synology Diskstation DS418 has been bought and configured with 36 TB of disk space in RAID 5. A single shared drive is used to back up data in individual folders owned by each user. The backups with file history are accessible through a web browser interface and Cyclotron Institute users who have an account on the computer can recover files without the assistance of an administrator. The Diskstation is behind the Cyclotron firewall, so it's only accessible from inside the Cyclotron network and the shared drive is fully encrypted. We also wrote scripts for Windows and Mac operating systems to allow the backups to be done when connected to the TAMU WIFI. Those scripts use a SSH tunnel to pass through the Cyclotron firewall.

Astatine-211 extraction and fundamental chemistry in nitric acid media

S.J. Schultz,[1,2] J.D. Burns,[3] B. Green,[2] T. Hankins,[1,2] L.A. McCann,[1,2] L.A. McIntosh,[1] G. C. Tabacaru,[1] A. Tabacaru,[1] E.E. Tereshatov,[1] J. Tobar,[1,3] Z. Tobin,[1,2] and S.J. Yennello[1,2]
[1]*Cyclotron Institute, Texas A&M University, College Station, TX 77840*
[2]*Department of Chemistry, Texas A&M University, College Station, TX 77840*
[3]*Department of Chemistry, University of Alabama at Birmingham, Birmingham, AL 35294*

Instruction

Astatine-211 has a half-life of 7.2 hours, a high linear energy transfer (97 keV·μm^{-1} maximum), a quantitative decay by α-emission (41.80% immediate, 58.20% ec), and no serial decay. As such, it is one of a small number of α-emitting radionuclides whose decay characteristics are ideal for use in Targeted Alpha Therapy (TAT). Moreover, what little is known of astatine chemistry indicates that the element possesses diverse avenues of interaction and bonding, with both metallic and halogenic properties having been observed [1]. Its chemistry, however, is perhaps the most poorly understood of all naturally occurring elements due to its extreme unavailability. Since production parameters limit recovered astatine to ultra-trace amounts, characterization of the element and its behaviors is chiefly limited to separation and mobility experiments measured by gamma or alpha spectrometry. Studies at Texas A&M are ongoing to explore promising solvent systems that preferentially extract ^{211}At out of nitric acid, with an eye also towards understanding astatine speciation and interactions.

2022-2023 progress in research

From August 2022 to April 2023, the Isotope Production team at Texas A&M University produced over 500 mCi of astatine-211 across 7 distinct production runs. Following each successful ^{211}At production the irradiated Bi target is dissolved and extracted with the assistance of an automated dissolution apparatus (hereafter, ADA), and the ^{211}At collected by extraction chemistry or chromatography. Established procedures are used for shipment [2], and these have been further developed this year to increase loading efficiency across multiple columns. This has permitted regular

Table I. Extraction constants, K_{ext}, of ^{211}At with select ketones.

Ketone		***n***	K_{ext}	R^2
4-butoxyacetophenone*		1.07 ± 0.11	120 ± 13	0.934
2,4,6-trimethylacetophenone*		1.01 ± 0.10	68 ± 7	0.984
1,3-dibenzoylpropane‡		1.06 ± 0.10	50.4 ± 3.3	0.958
Acetophenone*		1.11 ± 0.13	8.3 ± 0.7	0.885
dibenzoylmethane‡		1.19 ± 0.08	5.4 ± 0.26	0.977
3-octanone‡		0.91 ± 0.04	5.2 ± 0.11	0.992
2,2,2-trifluoroacetophenone*		0.48 ± 0.05		

*Contributed, †Previously published

shipment of ^{211}At to both MD Anderson UAB. Progress has also been made in advancing fundamental chemistry of astatine through research into new extraction systems. Work on ketone extraction systems has expanded to include functionally tuned ketone interactions with astatine (Table I).

From the systems tested, several extraction constants have been calculated according to equations and derivations given elsewhere [3].

It is apparent that the electron donating groups have the anticipated effect of increasing the D-values of ^{211}At extraction in nitric acid systems, likely due to increased n-pair donation from the ketone moiety. Studies have also been done with *ortho*-, *meta*-, and *para*- substituted benzophenones, which demonstrate the expected trends, albeit with much lower distribution ratios. It is likely that the out-of-plane strain of these benzophenones limit donation of electron density, and the proximity of the aryl groups provides some steric hindrance to the AtO^+ interaction. The 2,2,2-trfluoroacetophenone extracted so poorly that a K_{ext} could not be calculated by the same method, further corroborating the effect of donating and withdrawing substituents on the AtO^+–ketone interaction.

Earlier work demonstrated very high distribution ratios of ^{211}At using methyl anthranilate to extract out of dilute HNO_3 [4]. Several aniline derivatives have been tested (figure 2) to elucidate the mechanism by which the responsible interaction occurs. For these experiments ^{211}At is isolated by 1-octanol impregnated TK400 resin [5], which attends the subsequent liquid-liquid extraction as a surfactant preventing third-phase formation. Of the derivatives tested, 2,6-diethylaniline possessed the highest D-values (>1000), by a factor of 2. It is possible that the occupied *ortho* positions are assisting in directing a *para* position interaction with astatine.

First steps in the qualification and quantification of astatine's redox species in nitric acid media have been taken by the development of the following: (I) a radio-thin-layer chromatography analysis method (radio-TLC) for tracking astatine polarity and speciation in a reaction, (II) the isolation of astatine from bismuth by ion exchange chromatographic resins selected according to our batch studies (Fig.7) [6],[6] and (III) the control of astatine speciation through redox agents. Utilized together, the control of astatine oxidation states may be established, and a subsequent exploration of AtO^+/At^+ equilibrium will be

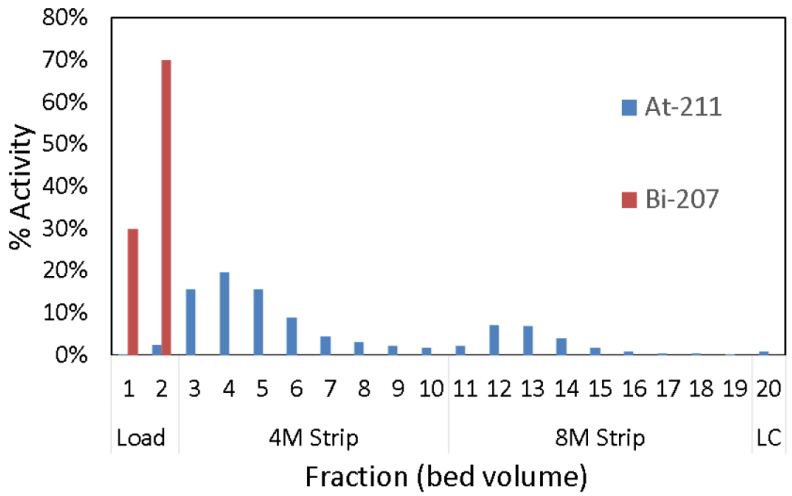

Fig. 1. Separation of 211At and 207Bi on Dowex 50x4 cation exchange resin. Column 4mm ID x 80mm length.

undertaken. Furthermore, of the ion exchange resins tested, Dowex 50x4 seemed most promising for the removal of bismuth from astatine. This resin was tested by column extraction, demonstrating quantitative elution of Bi in the load fractions, immediately followed by At in the 4M HNO_3 strip (Fig. 1). It is believed this separation can be improved with 2 M loading, followed by a water wash/flush, and then a high acidity (>6M) strip.

Experimental studies performed this year have also begun to explore several classes of extractant not yet adequately addressed in literature, including ionic liquids, deep eutectic liquids,[7] phosphines, phosphine-oxides, and crown ethers. Results acquired thus far are both chemically and pragmatically interesting, with the latter two classes expanding further on AtO^+ molecular cation interactions with oxygen functional groups in the extractants used.

[1] G.-J. Meyer, J. Label. Compd. Radiopharm. **61(3)**, 154 (2018); https://doi.org/10.1002/jlcr.3573.

[2] J.D. Burns, E.E. Tereshatov, G. Avila, K.J. Glennon, A. Hannaman, K.N. Lofton, L.A. McCann, M.A. McCarthy, L.A. McIntosh, S.J. Schultz, G.C. Tabacaru, A.L. Vonder Haar, and S.J. Yennello, Rapid Recovery of At-211 by Extraction Chromatography. Sep. Purif. Technol. 256, 117794 (**2021**); https://doi.org/10.1016/j.seppur.2020.117794.

[3] J.D. Burns, E.E. Tereshatov, B. Zhang, G.C. Tabacaru, L.A. McIntosh, S.J. Schultz, L.A. McCann, B.M. Harvey, A. Hannaman, K.N. Lofton, M.Q. Sorensen, A.L.Vonder Haar, M.B. Hall, S.J. Yennello, Inorg. Chem. 61(31) 12087 (2022); https://doi.org/10.1021/acs.inorgchem.2c00085.

[4] E.E.Tereshatov, J.D. Burns, A.L. Vonder Haar, S.J. Schultz, L.A. McIntosh, G.C. Tabacaru, L.A. McCann, G. Avila, A. Hannaman, K.N. Lofton, M.A. McCarthy, B. Zhang, M.B. Hall, and S.J. Yennello, Sep. Purif. Technol. 282, 120088 (2022); https://doi.org/10.1016/j.seppur.2021.120088.

[5] E.E. Tereshatov, J.D. Burns, S.J. Schultz, B.D. Green, G.A. Picayo, L.A. McCann, L.A. McIntosh,G.C. Tabacaru, A. Abbott, M. Berko, E. Engelthaler, K. Hagel, T. Hankins, B. Harvey, L. Hoekstra, K. Lofton, S. Regener, R. Rider, M. Sorensen, A. Tabacaru, D. Thomas, J. Tobar, Z. Tobin, S.J. Yennello, Chem. Eng. J. **464**, 142742 (2023); https://doi.org/10.1016/j.cej.2023.142742.

[6] E. Tereshatov, J. Burns, S. Schultz, Media. Rev. 2023.

[7] E. Tereshatov, J. Burns, A.Vonder Haar, and S. Schultz, Acid Media. Prog. 2023.

Production, isolation, and shipment of clinically relevant quantities of Astatine-211: A simple and efficient approach to increasing supply

L.A. McIntosh,[1] J.D. Burns,[2] E.E. Tereshatov,[1] R. Muzzioli,[3] K. Hagel,[1] L.A. McCann,[1,4] G. Picayo,[1,4] F. Pisaneschi,[3] D. Piwnica-Worms,[3] S.J. Schultz,[1,4] G.C. Tabacaru,[1] A. Abbott,[1,4] B. Green,[1,4] T. Hankins,[1,4] A. Hannaman,[1,4] B. Harvey,[1,5] K. Lofton,[1,4] R. Rider,[1,4] M. Sorensen,[1,4] A. Tabacaru,[1] Z. Tobin,[1,4] and S.J. Yennello[1,4]

[1]*Cyclotron Institute, Texas A&M University, College Station, TX 77843, USA*

[2]*Chemistry Department, The University of Alabama at Birmingham, Birmingham, AL 35924, USA*

[3]*Department of Cancer System Imaging, University of Texas MD Anderson Cancer Center, Houston, TX 77030, USA*

[4]*Chemistry Department, Texas A&M University, College Station, TX 77843, USA*

[5]*Physics Department, Texas A&M University, College Station, TX 77843, USA*

Astatine-211 (^{211}At) is a promising and elusive candidate of considerable interest for novel cancer treatment as a modality of targeted alpha therapy (TAT). In the United States, a small number of facilities are capable of accelerating α beams to produce ^{211}At [1], and it has a modestly short half-life (7.2 h). It is desirable to develop strategic methods for shipping ^{211}At in a form adaptable to advanced radiochemical reactions, or other desirable uses, so to advance biomedical applications. For this study, a 3-octanone impregnated Amberchrom® CG300M resin bed in a column cartridge was used to separate ^{211}At from the bismuth matrix at the production accelerator (Texas A&M). Aliquots of 6 M HNO_3 containing up to ~2.22 GBq of ^{211}At from the dissolved target were successfully loaded and retained on columns. Air-dried column hold times of 6.4 h and 34 h did not inhibit simple and efficient recovery of ^{211}At. Seven shipments of exempted packages (less than 370 MBq) arrived at a destination radiochemistry facility (University of Texas MD Anderson Cancer Center) in the form of an air-dried column. The eluted solution from the column was used to successfully radiolabel a model compound, 4-(4,4,5,5-tetramethyl-1,3,2-dioxaborolan-2-yl)aniline, with ^{211}At. An HPGe gamma-ray detector was utilized to confirm the identity of ^{211}At. This method to prepare and ship ^{211}At paves the way for the distribution of ^{211}At to research institutions and clinical oncology centers in Texas and elsewhere.

Astatine-211 shows promise using alpha-emitting radionuclides connected to a targeting agent such as a monoclonal antibody or other small molecule [2]. The half-life of 7.2 h requires a cyclotron near the site of use with sufficient power to produce an alpha beam of 28.8 MeV total energy to produce the reaction ^{207}Bi(α,2n)^{211}At. There are only about thirty cyclotrons in the world that have the capacity to accelerate alpha particles sufficiently to produce ^{211}At thereby limiting the number of laboratories where studies of fundamental astatine chemistry and subsequent development of radiotherapies can be performed.

Some institutions are developing the capability to produce enough ^{211}At for clinical trials. Currently in the United States, ^{211}At is only available through the National Isotope Development Center (NIDC) from the University of Washington in Seattle [1,3]. It is shipped in liquid form as sodium astatide in 4 N NaCl solution for radiochemistry research and clinical trials. Other sites around the country (Duke University, University of California-Davis, and University of Pennsylvania) are currently producing or

developing the capability to produce ^{211}At in useful quantities. The Texas A&M University Cyclotron Institute (TAMU CI) is in the process of increasing its ^{211}At production capability, having made up to 3700 MBq, with the goal of becoming part of the University Isotope Network (UIN) of the NIDC. This will allow more clinical trials with ^{211}At -radiolabeled drugs to be performed in the United States and expand the regions in which such trials can be performed.

A vital part of the effort to increase the availability of ^{211}At includes developing processing chemistry for the target and resulting solution. Previously, we have developed a unique chemical procedure that begins by dissolving the target in HNO_3 and allows for At and Bi separation by utilizing a nitric acid dissolution solution without chemical manipulations [4-6]. In order to expand the availability of ^{211}At across the country and minimize the amount of chemical processing at the destination facility, it is advantageous to have a method that allows ^{211}At to be directly added to various desired radiochemistry reaction configurations. We have since developed and use an automated approach of dissolving the target with minimal dose to personnel [7].

By shipping the ^{211}At on an air-dried column cartridge, the ^{211}At can be washed off the column using pure ethanol (EtOH) which could expedite the use of ^{211}At for labeling and radiochemistry studies. This work describes the process of loading and stripping the column, the effects of leaving the ^{211}At on a dry column with the freestanding liquid removed for long periods of time (>24 h), as well as progress made in shipping an exempt package (less than 370 MBq at the time of shipment) from TAMU CI, College Station, TX to The University of Texas MD Anderson Cancer Center, (UTMDACC) in Houston, TX via a commercial courier service. The distance of the shipment traversed is 103 miles, door-to-door, which takes approximately two hours with normal traffic. After the shipment arrived the ^{211}At was eluted and used to label a model compound 4-(4,4,5,5-tetramethyl-1,3,2-dioxaborolan-2-yl)aniline, demonstrating the success of our column cartridge shipping procedure and proving the reactivity of the resultant ^{211}At.

We developed a simple method to load ^{211}At on a dried column cartridge, ship it from the production site, TAMU CI, to an external research institution, UTMDACC, and recover the ^{211}At activity from the cartridge by eluting with ethanol. Focused tests were performed before shipping ^{211}At outside our production center. The cartridge was loaded with ^{211}At solution in ~6 M HNO_3, washed, flushed, air-dried, and set aside for 6.4 h and 34 h, to mimic shipment to facilities within a day's journey and overnight shipments. Both tests resulted in a simple and efficient recovery of ^{211}At. The ^{207}Bi produced from the decay of ^{211}At accumulates on the column during shipment and can be eluted from the cartridge prior to ^{211}At stripping. The remaining sample's radiopurity and the contaminants' removal are discussed in further detail in Refs. [5,7].

Once this column cartridge was received by UTMDACC, it was stripped using EtOH. Fig. 1 shows the stripping profile of ~215 MBq of ^{211}At from the column cartridge on September 21, 2021, October 20, 2021, and November 15, 2021. For all three shipments shown, the column cartridge left the TAMU CI between 10:30–11:10AM and arrived at UTMDACC between 1:45–3:00PM. The stripping profile for the shipments was very similar, which demonstrated the reproducibility of these processing methods.

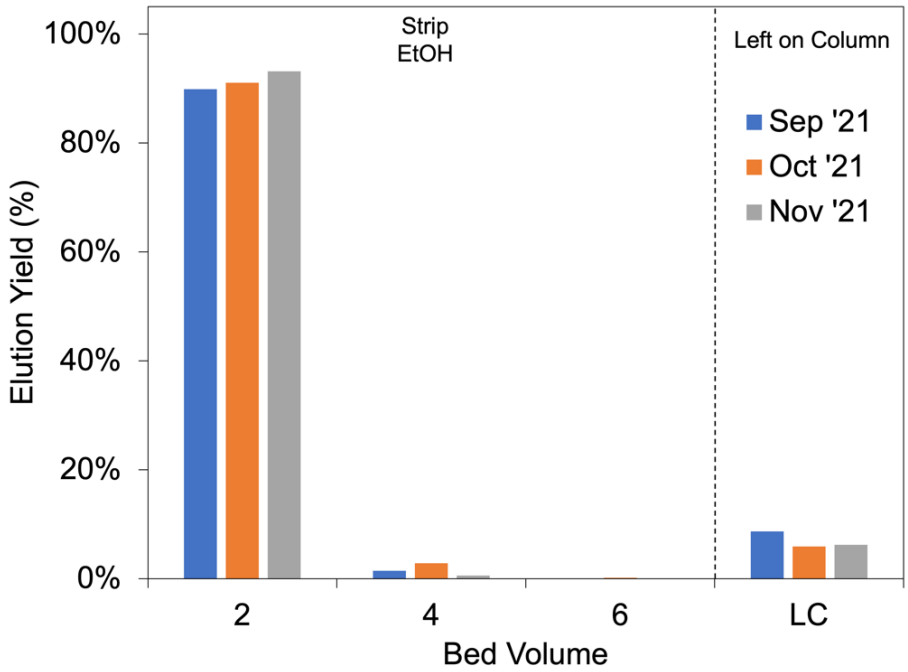

Fig. 1. Stripping profile of ~215 MBq of ^{211}At of a 3-octanone impregnated Amberchrom® CG300M resin bed housed in a column cartridge (0.5 mL BV, 8 mm ID x 10 mm height). Cartridge had been shipped from the TAMU CI at 11:00 AM and stripped by UTMDACC at 2:55 PM on September 21, 2021 (blue), and at 11:10 AM and stripped by UTMDACC at 2:32 PM on October 20, 2021 (orange) and at 10:30 AM and stripped by UTMDACC at 2:14 PM on November 15, 2021 (grey).

Shipments:

Table I details the activity and eluted activity on each column that was shipped from TAMU CI to UTMDACC in June, July, September, October, and November 2021. The percent ^{211}At eluted has been 87-94%, which demonstrates that the majority of the ^{211}At could be eluted from a shipped column.

Drying the column and leaving the ^{211}At to sit on the column for 34 h, to mimic an overnight shipment from College Station, TX did not impede the stripping of the column with EtOH. A small amount of ^{211}At remained on the column, presumably due to resin imperfections. This amount is negligible when the loading is above 37 MBq.

The amount of ^{211}At loaded onto the cartridge was also scaled up to 2.2 GBq, which has the potential to be enough radioactivity to support the synthesis of a radiopharmaceutical for a robust set of experimental animal studies. This column performed similarly to the other, smaller amounts of ^{211}At, and demonstrates the applicability of this method to larger shipment sizes.

Table I. This table details the activity and eluted activity on each column that has been shipped from TAMU CI to UTMDACC. An error of 10% was assigned to address sources of error. *In July, the lur lock cap leaked, which resulted in the loss of some activity, not due to the column or the stripping process.

Date	Activity of Column at Delivery (MBq)	Eluted Activity (MBq)	Activity left on Column (MBq)	Elution Yield	Column Residues
June 9, 2021	135±14	118±12	15.0±1.5	86.9±8.7%	11.2±1.1%
July 28, 2021*	204±20	137±14	37.7±3.8	67.5±6.8%	18.5±1.9%
September 21, 2021	218±22	192±19	18.4±1.8	88.0±8.8%	8.4±0.8%
October 20, 2021	222±22	202±20	12.8±1.3	91.0±9.1%	5.8±0.6%
November 15, 2021	126±13	114±11	7.6±0.8	93.8±9.4%	6.2±0.6%
April 6, 2022	226±23	196±20	20±2	96.7±9.7%	8.8±0.9%
April 26, 2022	233±23	176±11	44±4	75.5±7.6%	18.9±1.9%
August 2,2022	188±19	179±18	15.9±16	95±9.6%	8.5±1.2%
September 8,2022	222±22.2	209±20.9	6.8±0.7	94±13%	3.1±0.4%
October 11,2022	148±15	132±13	8.5±0.9	89±13%	5.7±0.8%
October 12,2022 ∗ ∗	22.6±2.3	20.7±2.1	1.0±0.1	92±13%	4.4±0.6%
December 14,2022	161±16	151±15	6.8±0.7	94±13%	4.2±0.6%
December 15,2022 ∗ ∗	61.6±6.2	58.4±5.8	1.4±0.1	95±13%	2.2±0.3%

[1] Y. Feng and M.R. Zalutsky, J. Nucl. Med. Bio. **100-101**, 12 (2021).

[2] J. Elgqvist *et al.*, Front. Oncol., **3**, 1 (2014), https://doi.org/10.3389/fonc.2013.00324.

[3] V. Radchenko *et al.*, J. Nucl. Med. Bio. **62**, 1495 (2021).

[4] J.D. Burns *et al.*, Chem. Commun. **56**, 9004 (2020); 10.1039/d0cc03804k.

[5] J.D. Burns *et al.*, Sep. Purif. Tech. **256**, 117794 (2021); 10.1016/j.seppur.2020.117794.

[6] E.E. Tereshatov *et al.*, Sep. Purif. Tech. **282**, 120088 (2022); 10.1016/j.seppur.2021.120088.

[7] E.E. Tereshatov *et al.*, Chem. Eng. J. **442,** 136176 (2022); 10.1016/j.cej.2022.136176.

Development of compact MWPC detectors for TRINAT experiment (MWPC demonstrator)

J. Klimo, D. Melconian, G. Chubaryan, V. Iacob, D. McClain, M. Nasser,
B. Diaz, and B.M. Vargas-Calderon

As the analysis to measure the Fierz interference parameter from the last TRINAT (Neutral Atom Trap for β Decay) wraps up, we are preparing for the next correlation measurement of polarized ^{37}K at TRIUMF. One of our limiting systematics is the performance of our current β detectors, which are made up of 300 um-thick double-sided Si-strip (DSSSD) ΔE-detector backed by a BC408 plastic scintillator E-detector. We are upgrading these telescopes to reduce the large (~100 keV) energy loss in the DSSSD and the (back-) scattering by replacing the DSSSD with a multiwire proportional counter (MWPC), see Fig 1. We will also replace the magnetic-field-sensitive PMT readout of the scintillator with Si photomultipliers (SiPMs). In order to avoid completely changing our overall system, we will use the same detection chamber and in particular the existing re-entrant flanges for the β telescopes. This set the limits for the new telescope dimensions. In the present work, we describe development of two compact, small area, position sensitive MWPC detectors for the detection of β particles in spin-polarized β^+ decay experiment. The detectors will help to reconstruct momentum vector of β particles on event-by-event basis, with higher precision than DSSSD detectors.

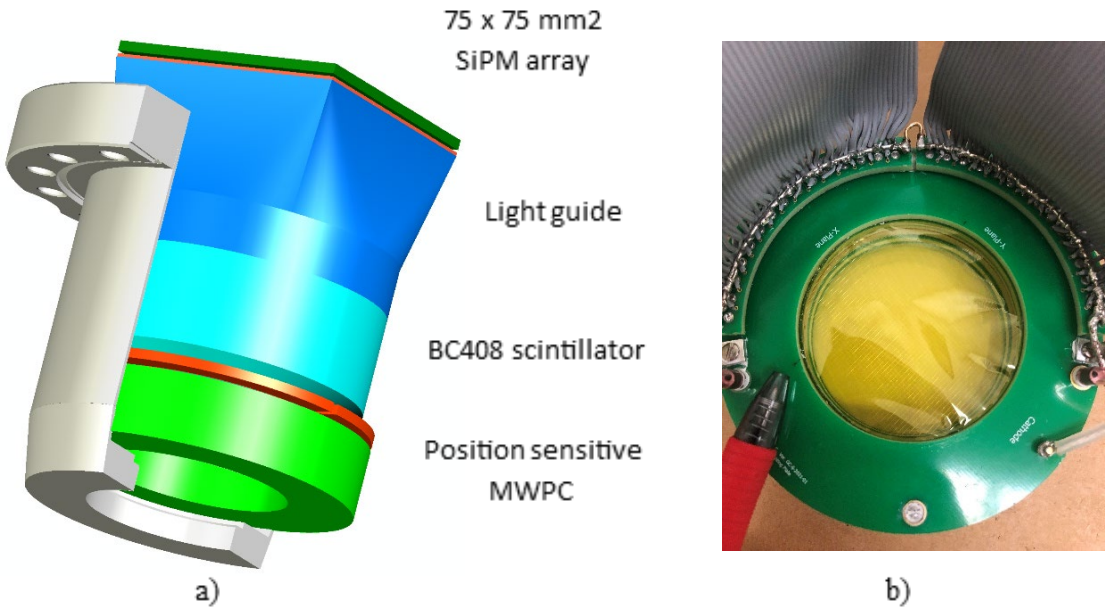

Fig. 1. a) New design. for TRINAT's β telescope b) The design of MWPC detector.

MWPC detector design

All wire frames are made from PCB material, where gold plated tungsten wires of 16 um in diameter are stretched and soldered on PCB frame of three electrodes. The thickness of each PCB frame is 3 mm and two electrodes are always span by a spacer of the same thickness, thus resulting in 6 mm distance

in between electrodes. One can find in a comparable design in [1]. The spacing in between wires is 3.75 mm and 1.0 mm, for anode and cathodes, respectively. The central electrode, the anode, is supposed to be biased to high voltage of 2.5-3.0 kV relative to the cathodes floated at 0 V.

Signal readout and XY – position reconstruction

Anode signal serves as trigger (start) signal for cathode (stop) signals, two signals for one cathode, and this trigger can be used as a master trigger in TRINAT DAQ system. All signals from anode wires are sum up to one signal, typically with higher amplitude than signal from single cathode wire. For processing of anode signal a standard ORTEC 9306 fast pre-amplifier can be utilized after decoupling stage of the detector, managing by high voltage decoupling box. The fast pre-amplifier is then followed by TRINAT digital electronics.

Besides the resistive charge division method, the delay-line (DL) technique represents another centroid finding method. DL technique is a simple and relative accurate technique for MWPC. The position of a particle traversing the MWPC sensitive volume is reconstructed from X_1 and X_2 signals readout for the top (X-plane), and from Y_1 and Y_2 signals from the bottom (Y-plane) cathode, only two signals per cathode. Coincidence of two signals from DL board also helps to suppress spurious events and electronical noise. In the order to reach high position resolution a custom-made DL boards have been made, one for every cathode, and are currently in testing phase. Every DL board gathers a passive DL chip of inductors and multi-layer capacitors (series SP10), taking care of stable transmission of signal and reliable performance. Two cathode wires are electronically always bunched together and the delay time between two consecutive pairs of wires is 2 ns, corresponding to 2 mm spacing. After a delay stage, a signal from cathode wire is then gained by a custom-made fast pre-amplifier. A characteristic for this pre-amplifier is its high dynamic range with gain ranging as 10 up to 10^2. Such high gain is demanded as the most of β particles deposit only small fraction of its total energy in sensitive volume of MWPC, typically not more than ~ 5 keV. This must be compromised with electronic noise to be able to read cathode signal with amplitude of about ~10 μV/wire. Then DL signals from a cathode are feed to Constant Fraction Discriminator (CFD) resulting two fast discriminator signals with sub-ns rise time. The delay time is then measured using time-to-digital converter (TDC) as $(T_{x1} - T_{x2})$ and the sum of DL total time is always constant for one DL board, determined by the sum of all delay stages, i.e.

$$T_{sum} = T_{x1} + T_{x2} = 29 \text{ wire pairs} \times 2 \text{ ns} = 58\text{ns},$$

and the centroid in X and Y direction is reconstructed as [2],

$$X = K_x . \frac{(T_{x1} - T_{x2})}{2} + X_{\text{off}},$$

where X_{off} (mm) is the offset correction, K_x (mm/ns) is the position coefficient.

Gas system

A high purity quenching mixture of Ar+Co2 (90%-10%) is considered as an optimal detection medium for both MWPC detectors. The pressure stability of MWPC is critical for the whole operation and thus the gas pressure and flow must be under control. For this purpose, we use a manual gas system consists of 2 stage pressure regulators with a needle valve. The outlet of MWPC can be monitored by pressure and

flow meter at the outlet stage. A critical situation, like high overpressure scenario of the MWPC is prevented by 1 mm inlet port of much smaller diameter than diameter of injection line, and by the fact that the detector is leak tight up to ~ 6 mbar.

Efficiency test with ^{90}Sr

The β counting curve was measured for both detectors (Fig 2) to select an appropriate operating voltage to stabilize variation in counting rate, caused by high voltage instability leading to gain variation, and considering an acceptable background condition. The counting rate was recorded under constant

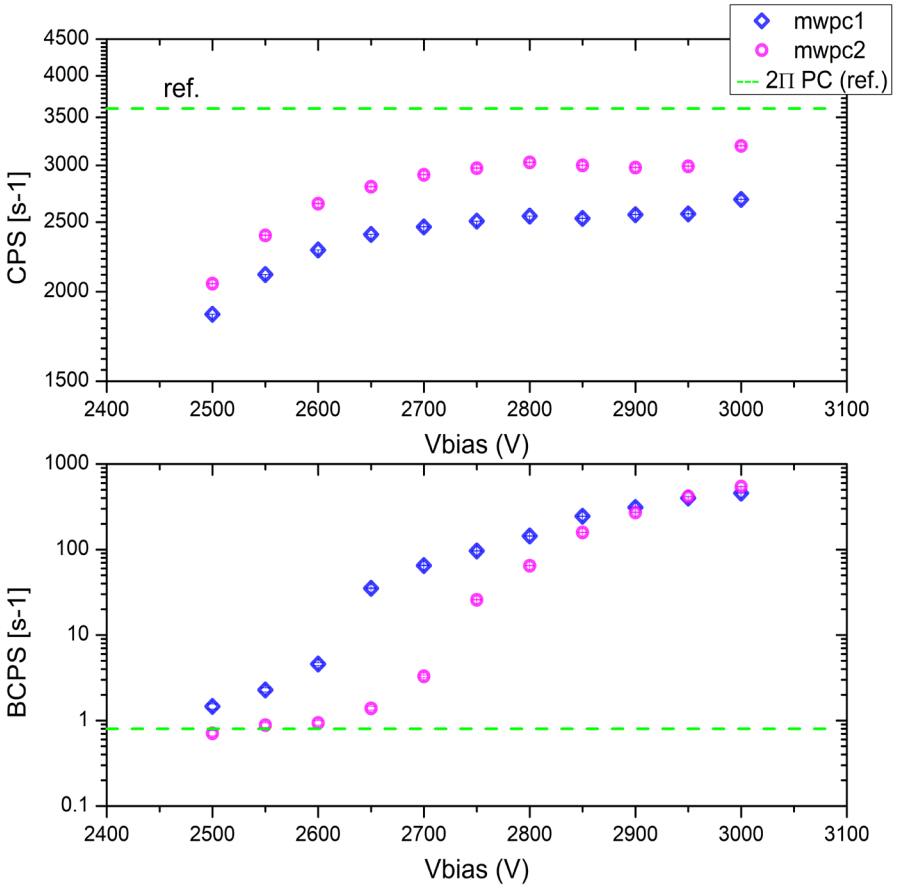

Fig. 2. The counting curve measurement for both MWPC detectors and compared with a reference measurement by 4π detector used in 2π configuration. CPS represents background subtracted count rate of the β source ^{90}Sr. BCPS is for background measurement.

source conditions as the detector voltage is varied. An operating point is then selected, normally, corresponding to a flat region or "plateau" on the resulting rate versus voltage curve. The efficiency test for MWPC is compared with 4π single wire proportional detector measurement [3], which is well characterized with detection efficiency exceeding 99%. That detector is also characteristic by very low background. The geometry of 4π detector is slightly different but provide a good reference point to ongoing simulations. The difference in efficiency curve in between two detectors can be canceled by the next optimization of the

detectors so they will match each other, and approach 100% limit. Efficiency for cathodes is usually not as high as for anode.

[1] Ran Hong, Ph.D. Thesis, University of Washington, 2016.
[2] H. Kumagai *et al.*, Nucl. Instrum. Methods Phys. Res. **B317**, 717 (2013).
[3] V.E. Iacob *et al.*, Phys. Rev. **C 77**, 045501 (2008).

He6CRES experiment and ion trap addition update

D. McClain, V. Iacob, J. Klimo, D. Melconian, and M. Nasser

Through the use of the cyclotron radiation emission spectroscopy (CRES) technique developed by the Project-8 collaboration [1] to measure the β spectrum of ^{6}He, ^{14}O, and ^{19}Ne, the He6-CRES collaboration seeks to test the standard model (SM) by searching for scalar and tensor currents. The CRES technique gives a uniquely precise window to view the β energy E_e through the cyclotron frequency, f of the electron according to

$$f = \frac{1}{2\pi}\frac{eB}{m_e + E_e},$$

where e is the electron charge, B is the magnetic field, and m_e is the rest mass of the β. This non-destructive technique allows incredible sensitivity the energy of the β [2]. The goal is to apply the CRES technique to search for distortions to the β spectrum caused by an interference of SM and beyond-the-SM scalar and/or tensor currents, described by the Fierz parameter, b_{Fierz}. This parameter, which is zero in the SM, is linearly sensitive to new physics and has discovery potential if measured to $\leq 1 \times 10^{-3}$ [3].

The experiment originally consisted of a rectangular waveguide with a U-shape turn to read frequencies from either end to cancel Doppler effects from the betas confined in the magnetic bottle (see Fig. 1). However, due to frequency-dependent abberations within the data we have terminated the I-side of the waveguide, *i.e.* the side that does not include the U-bend.

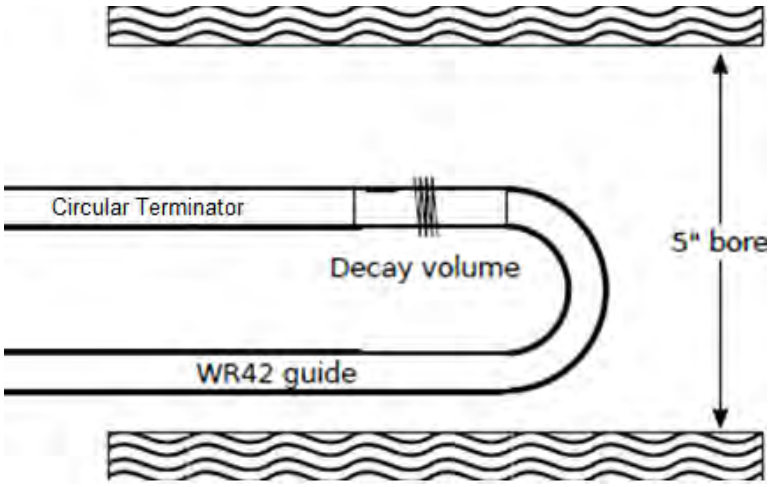

Fig. 1. Drawing of the U-shaped waveguide in the magnet.

A current limitation of the experiment is caused by a lack of radial confinement of the isotope of interest. As gaseous atoms are pumped into the system we expect an energy dependence on countable events within a region of our decay volume. In this case, the emitted betas of the ^{6}He nuclei that are near the walls are lost, and because of an increasing cyclotron radius with higher energy, higher energy betas

would be more likely to hit the wall as show in Fig. 2, resulting a bias toward lower energies in our energy spectrum. With this issue it is still expected to get the uncertainty of b_{Fierz} [6] < 10^{-3} [4].

To negate the issues of the wall effects, we have opted for measurements on the ratio between the

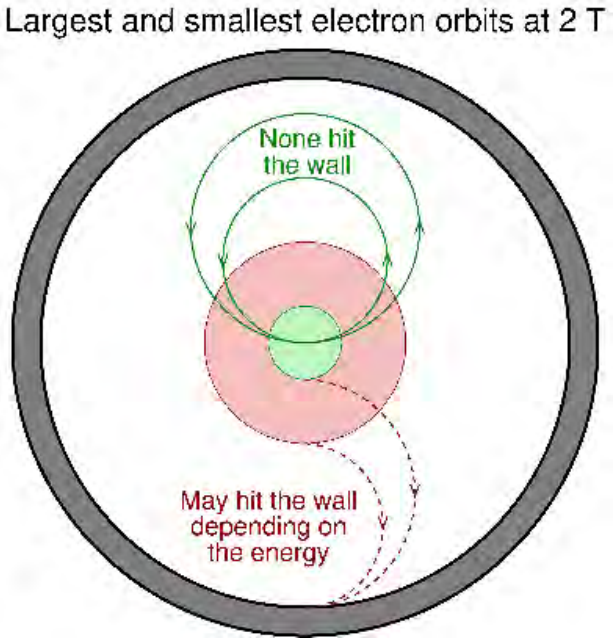

Fig. 2. The geometric effect of wall collisions in the case where there is no radial confinement of the isotopes.

beta spectra of two nuclei, ^{6}He and ^{19}Ne, where the ratio will wash out the energy-based efficiency effects. Also, given that effect of a non-zero $b_{\mathbf{Fierz}}$ on β^{+} to β^{-} energies is opposite, we double our sensitivity on the measurement. Over the last year two measurements were performed, one with the original waveguide and another with the updated, terminated waveguide.

However, to reach the desired precisions we must greatly increase our statistics, and eliminate the wall effects as well. To this end, two ion traps have been in development. The first, a radiofrequency quadrupole trap, will be used to cool and bunch a beam of ions before passing it to the second, a Penning trap, which will axially confine the ions while the magnetic field holds radially confines them. The Penning trap is designed with the same dimensions as the current decay volume being ~10 cm in length and 1.156 cm in diameter. This radius propagates frequencies between 18-24 GHz well. The magnetic field can be varied from 0.5-6 T to shift our 18 - 24 GHz window to different energies and scan the whole β spectrum.

SimION simulations have shown that the radiofrequency quadrupole trap (RFQ) is able to cool $^{6}He^{+}$ ions to allow for efficient injection and radial confinement within the small Penning trap. For this experiment we have rescaled a version of the TAMUTRAP RFQ [5] from $r_0 = 6$ mm to $r_0 = 12$ mm, which allows us to operate with $V_{RF} = 200$ V, and frequencies between 0.5-1.5 MHz. These parameters in the simulation gives us a time spread of 0.84 μs and an energy spread of 2.9 eV which is used to plan the rest of the beamline after the RFQ.

The limiting factor then became the maximum bunch size, as the CRES technique already has an extremely low efficiency due to the fact the magnetic bottle only confines one in 10^3 betas long enough to observe a CRES signal And in order to reach the desired precision, we expect to require 10^9 counts. Rate limitations of RFQs have not been studied in great detail since mass-measurements require low (single-ion) counting rates, with most RFQs presumed to be limited to 10^4/bunch. This rate would, however, result in months of counting for the shortest lived isotope of interest, and years to reach 10^9 for longer-lived isotopes. Along with other studies, such as for the General Purpose Ion Buncher [6], SIMION simulations have been performed which indicate it should be possible for the RFQ we designed for He6-CRES to reach $10^5 - 10^6$ ions per bunch without space-charge effects overloading the RFQ. This hypothesis, if true would greatly increase our count rate and lower our counting time to the point of making experiments with ^{19}Ne and even ^{14}O accessible, as shown in Fig. 3.

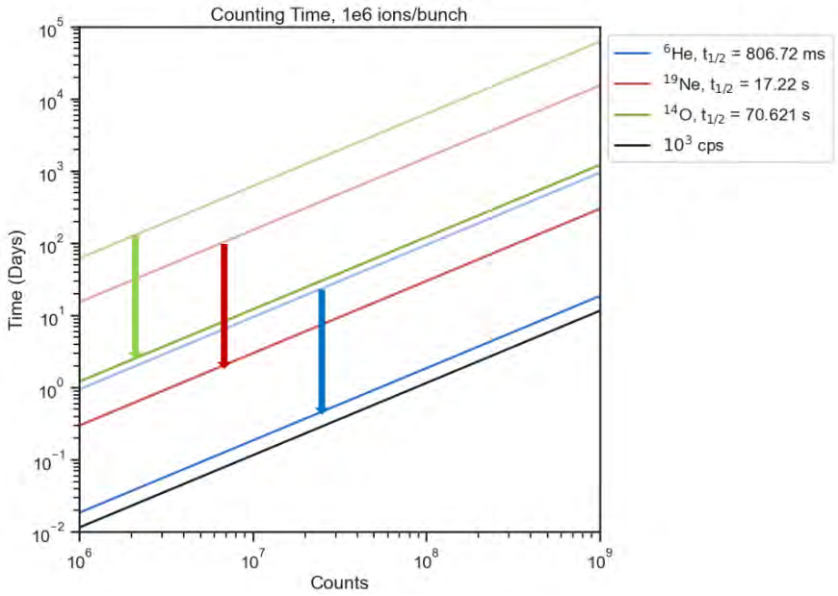

Fig. 3. The expected time to count in days to reach a given number of counts. The more transparent lines are for 10^4 particles per bunch, where the opaque lines represent 10^6 particles per bunch.

Testing the RFQ limits on bunch size will be occurring over the next year. First with the TAMUTRAP RFQ while the new RFQ is ordered, then with the new RFQ. Once the RFQ has shown that it is able to successfully transport large bunches with time and energy spreads allowing for efficient trapping within the Penning trap, it will be transported to the University of Washington where we will begin the Penning-trap upgrade to the He6-CRES experiment.

[1] D.M. Asner *et al.*, Phys. Rev. Lett. **114**, 162501 (2015).
[2] A.A. Esfahani *et al.*, J. Phys. G **44**, 054004 (2017).
[3] J. D. Jackson, S.B. Treiman, and H.W. Wyld, Phys. Rev. **106**, 517 (1957).
[4] A. García, private communication.

[5] M.S. Mehlman, Ph.D. Thesis, Texas A & M University, 2015.
[6] M.Gerbaux *et al.*, Nucl. Instrum. Methods Phys. Res. **A1046**, 167631 (2023).

Pepperpot development for TAMUTRAP and He6CRES

D. McClain, M. Parnell, V. Iacob, J. Klimo, D. Melconian, and M. Nasser

Using the cyclotron radiation emission spectroscopy (CRES) technique developed by the Project-8 collaboration [1], the ^{6}HeCRES experiment plans to measure the β-spectrum of ^{6}He, ^{14}O, and ^{19}Ne. This is done by allowing the atoms to decay within a small waveguide that will propagate the cyclotron radiation emitted from the beta. Future iterations of the experiment plan to use an ion beam and trap the ions of interest within a Penning trap that is also a waveguide. Due to the constraint of radial confinement within the waveguide, precise control of the position and divergence of the beam as it enters the trap is required. The position-momentum phase space of the beam is called the emittance, and can be measured using a pepper-pot. Following Liouville's theorem, the emittance remains constant in time barring non-conservative forces [2]. Employing a radiofrequency quadrupole Paul trap (RFQ) we are able to cool and bunch the beam lowering the emittance, the extent of which can be tested with a pepper-pot.

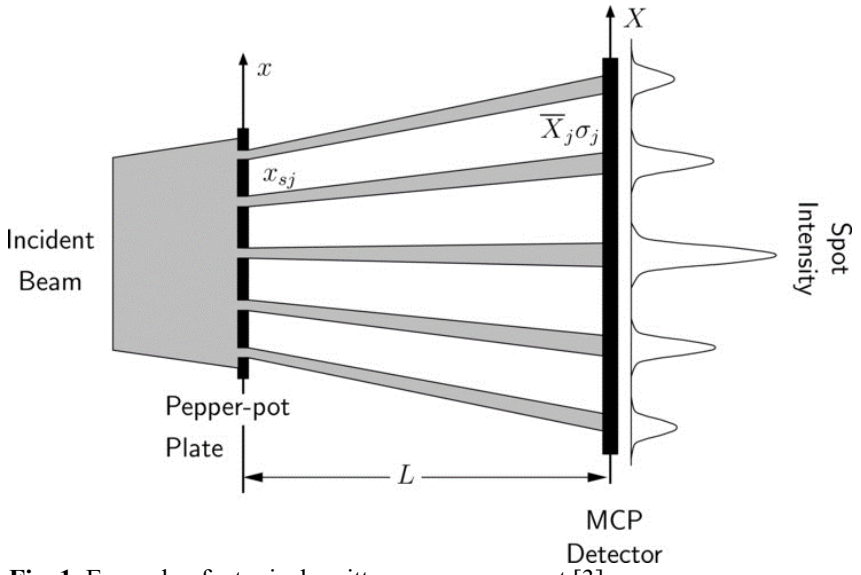

Fig. 1. Example of a typical emittance measurement [3].

The analysis of the pepper-pot is non-trivial and requires precise knowledge of the pepper-pot mask applied before the detector and the distance to the detector. With knowledge of the holes on the mask, as well as their image on the detector one can compute the rms emittance in one direction from the observables shown in Fig. 1, according to:

$$\varepsilon_x = \sqrt{\langle x^2\rangle\langle x'^2\rangle - \langle xx'\rangle^2}$$

$$\varepsilon_x = \frac{1}{N}\sqrt{\left[\sum_{j=1}^{p} n_j\left(x_{sj}-\bar{x}\right)^2\right]\left[\sum_{j=1}^{p}\left[\frac{n_j\sigma_j^2}{L^2}+n_j\left(\overline{x_j'}-\overline{x'}\right)^2\right]\right]-\left[-N\bar{x}\overline{x'}\sum_{j=1}^{p} n_j x_{sj}\,\overline{x_j'}\right]^2}\,.$$

where N is the total intensity of the beam on the detector, n_j is the intensity of beamlet j, x_{sj} is the position of the j^{th} hole in the mask, $\bar{x}$ is the mean position of the beam on the detector, σ_j is the standard deviation of the j^{th} beamspot, and L is the distance between mask and detector. The divergence of the beam $\overline{x_j'}$ is given by the following:

$$\overline{x_j'} = \frac{\overline{X_j} - x_{sj}}{L},$$

where $\overline{X_j}$ is the mean position of the j^{th} spot on the screen. This process can be completed in both transverse directions and the reported emittance is then the average of the two.

An analysis software named Pypperpot has been written in the python programming language [4] to read images of a pepperpot emittance measurement and return the emittance of the beam as well as the phase space profile. The software has been tested with simulated pepperpot experiments of various beam and mask conditions to maximize understanding before upcoming measurements on the TAMUTRAP beamline. After successful testing, the constructed pepperpot, and Pypperpot will be a useful tool for understanding beam profiles wherever applied, not only for TAMUTRAP and CRES, but also the He-LIG and LSTAR upgrades and throughout the Cyclotron Institute.

[1] D.M. Asner *et al.*, Phys. Rev. Lett. **114**, 162501 (2015).
[2] J.W. Gibbs, Proceedings of the American Association for the Advancement of Science (1848).
[3] M. Zhang, No. FNAL-TM-1988. Fermi National Accelerator Lab.(FNAL), Batavia, IL (United States),(1996).
[4] G. van Rossum, *Python tutorial*, Technical Report CS-R9526, Centrum voor Wiskunde en Informatica (CWI), Amsterdam, (1995).

Update on the He-LIG and LSTAR projects to produce RIB for TAMUTRAP

D. Melconian, J. Klimo, D. McClain, G.P.A. Berg,[1], M. Couder,[1] and M. Brodeur[1]
[1]*University of Notre Dame, Notre Dame, IN, USA*

As described in last year's report [1], we are developing a ^{3}**He**-based **l**ight-**i**on **g**uide (He-LIG) system, complementing the existing (proton-driven) *p*-LIG system, to increase RIB production at the CI using the high intensity of the K150 cyclotron. The **l**ight-ion guide **s**eparator for **T**exas **A**&M's K150 **r**are isotope beams (LSTAR) will transport and purify the RIBs produced by the He-LIG.

We have been concentrating on the design of LSTAR recently, optimizing the new purely horizontal 2x62.5-degree layout (see Fig. 1). This was again accomplished with COSY [2] calculation

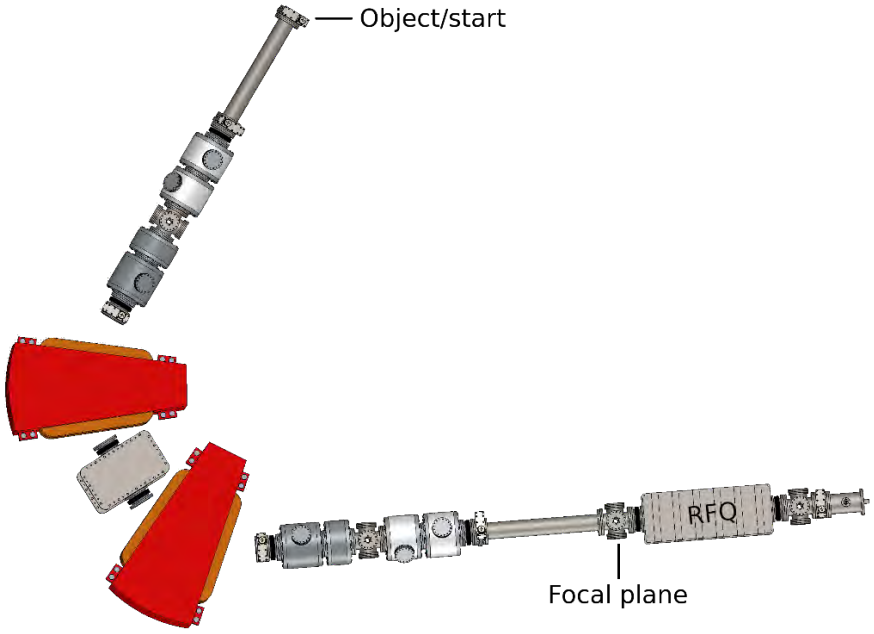

Fig. 1. CAD drawing of the design for LSTAR, including the TAMUTRAP RFQ placed at the focal plane of LSTAR.

using realistic rays from Simion [3] simulations of the He-LIG production. Figure 2 shows some results from these studies. Simion calculations indicate the RIB out of the He-LIG and transported with a SPIG will enter LSTAR with an emittance of 0.65π mm mrad and an energy spread of 3.3 eV; we expect, with precise laser-interferometric alignment techniques, to limit misalignments to ±100 μm. The left plot in Fig. 2 shows the resulting ion distributions at the focal plane of LSTAR. The filled curves are transmitted while unfilled are vetoed. The green curves show the "good" ions, while red are "contaminant" ions with a relative mass difference of 3.3×10^{-4}. In this case, 95% of "good" ions are transmitted with only 0.1% "contaminants" passing through the separator. The middle plot is similar, however in this case the misalignments, energy spread and emittance were all doubled (±200μm, 6.6 eV and 1.30π mm mrad); in this case the transmission of "good" ions is down to 80% and the fraction of contaminant ions rises to 3.3% which is higher than the design specifications. The plot on the right of Fig. 2 shows the trend of the

transmission and contaminant fractions as a function of the average misalignment (with nominal energy spread and emittance values). Similar studies were done to find the sensitivity of LSTAR's performance to other parameters.

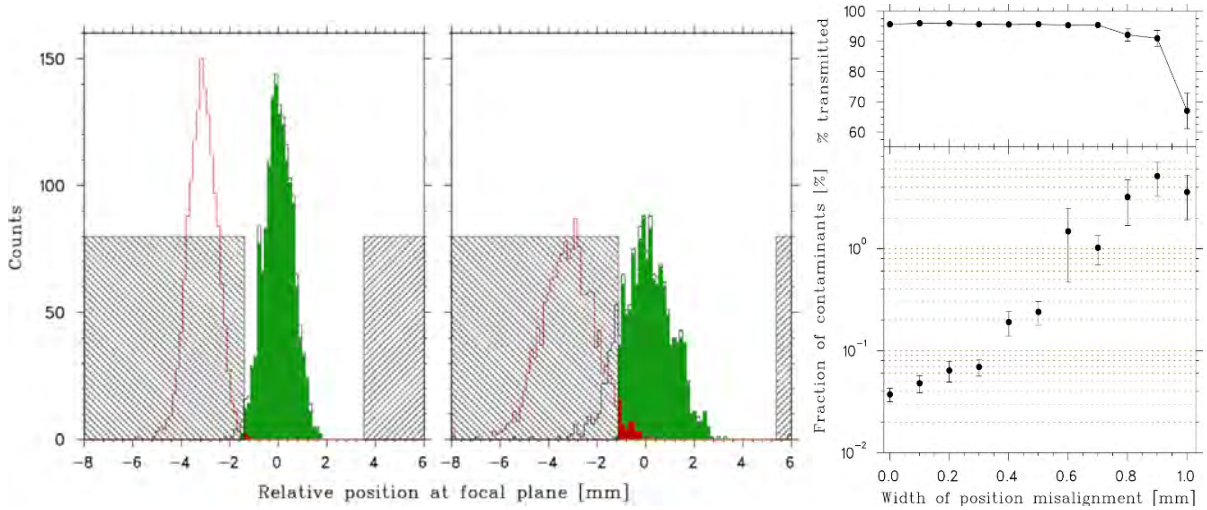

Fig. 2. Sample of the studies done to characterize the performance of LSTAR. Shown are the ion distributions at the focal plane for "good" ions (green) and "contaminant" ions with $M/\Delta M = 3000$ (red) with the expected (left) and 50% larger emittance, energy spread and misalignments (middle). In these plots, the filled histograms are transported through the slits at the focal plane (hatched region), while unfilled are vetoed either in the separator or by the final slits. On the right is a plot of the efficiency for transporting good ions (top) and the fraction of contaminant ions that also passed through LSTAR.

In the spring, we completed a technical specification document and requested bids to construct the separator. As we wait for LSTAR to be constructed, we will now concentrate on installing the *p*/He-LIG chamber, He-LIG gas cell and beam transport to LSTAR. In parallel we will work with the *p*-LIG group to prepare Cave 5 for installation of LSTAR, which will hopefully be ready by summer 2025.

[1] D. Melconian *et al*., Progress in Research 2021-2022, IV-61.

[2] K. Makino and M. Berz, COSY INFINITY Version 9, Nucl. Instrum. Methods Phys. Res. A558, 346 (2006)., Proceedings of the 8th International Computational Accelerator Physics Conference. doi:https://doi.org/10.1016/j.nima.2005.11.109.

Characterization of the TexNAAM detector

M. Barbui,[1] R. Bartsch,[1] A. Ascione,[1] E. Koshchiy,[1] A.J. Saasatamoinen,[1] and G.V. Rogachev[1,2]
[1]*Cyclotron Institute, Texas A&M University, MS3366 College Station, Texas, 77843*
[2]*Department of Physics & Astronomy, Texas A&M University, College Station, Texas 77843*

The TexNAAM array is a detector to perform gamma spectroscopy in experiments studying nuclear reactions of astrophysical interest. The array is made of 16 NaI(Tl) detectors of size 11x5.5x40 cm^3. Each detector is coupled to a photomultiplier. A drawing of the TexNAAM array is shown in Fig. 1. The signal output from each NaI(Tl) detector is read directly by SIS3316 digitizers from STUCK. The array was assembled and tested in the laboratory with different gamma sources ^{137}Cs, ^{60}Co, and ^{22}Na. Count rates up to 15kHz were measured during the tests. The dead time of the system was evaluated by counting the events from an 11 Hz pulser fed to one of the channels. With the present configuration, the measured dead time is zero up to count rates of 5kHz and raise to 5% at 15 kHz. The energy resolution of each scintillator was measured as a function of the PMT bias. After a rough gain matching obtained by tuning the PMT bias, we performed an energy calibration using the three gamma sources mentioned above.

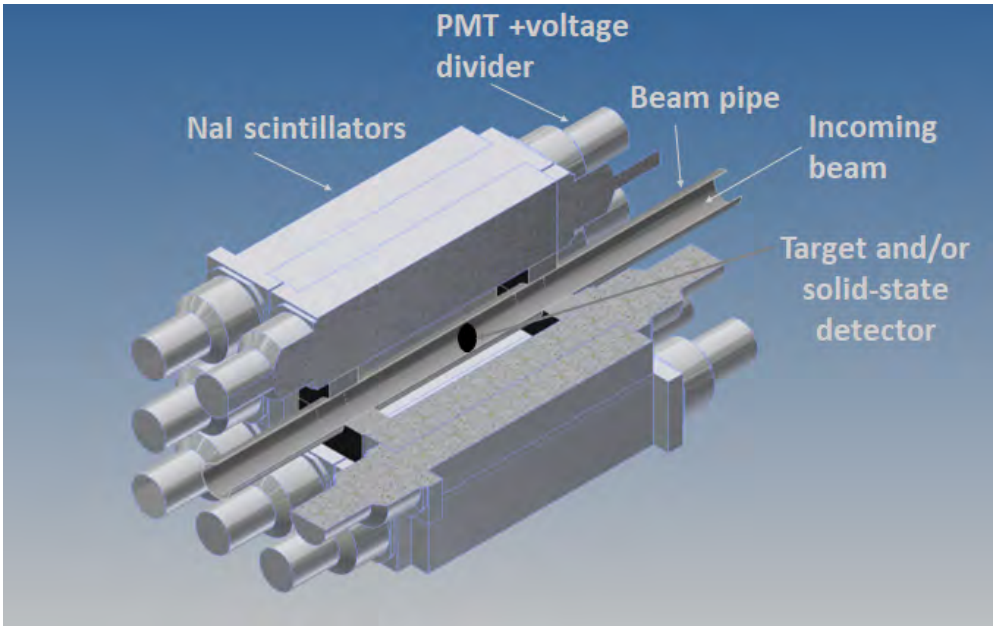

Fig. 1. Drawing of TexNAAM. The array top-right quarter is removed to allow the view of the interior of the assembly. Each scintillator is sealed in a 1mm-thick Aluminum case and coupled to the PMT through a glass window. The PMTs are surrounded by mu-metal.

We measured the photopeak efficiency of the system at 511 keV, 1173 keV, 1274 keV, and 1332 keV, using ^{60}Co and ^{22}Na sources of known activity. We compared the measured photopeak efficiencies with a Geant4 evaluation of the array's efficiencies for the ^{60}Co and ^{22}Na gamma sources. The efficiency from Geant4 is systematically 10-12% higher than the experimental value. Fig. 2 shows the experimental

photopeak efficiency determined from the sum spectra and the corresponding Geant4 calculation. The causes of this discrepancy are under investigation. Using different physical models available in Geant4 did not produce significant differences in the calculated efficiency. The current simulation is based on the simulated gamma-ray energy deposit in the scintillators.

The loss of scintillation light due to the absorption in the crystal and the photocathode efficiency were not explicitly treated in the simulation. The loss of energy resolution due to these effects is accounted for, crystal by crystal, by folding the simulated energy deposit with the measured energy resolution as a function of the energy. For each scintillator, the experimental energy thresholds are also included in the simulation.

We did not consider the possible presence of an inactive layer on the crystal surface due to oxidation of the NaI(Tl) scintillator.

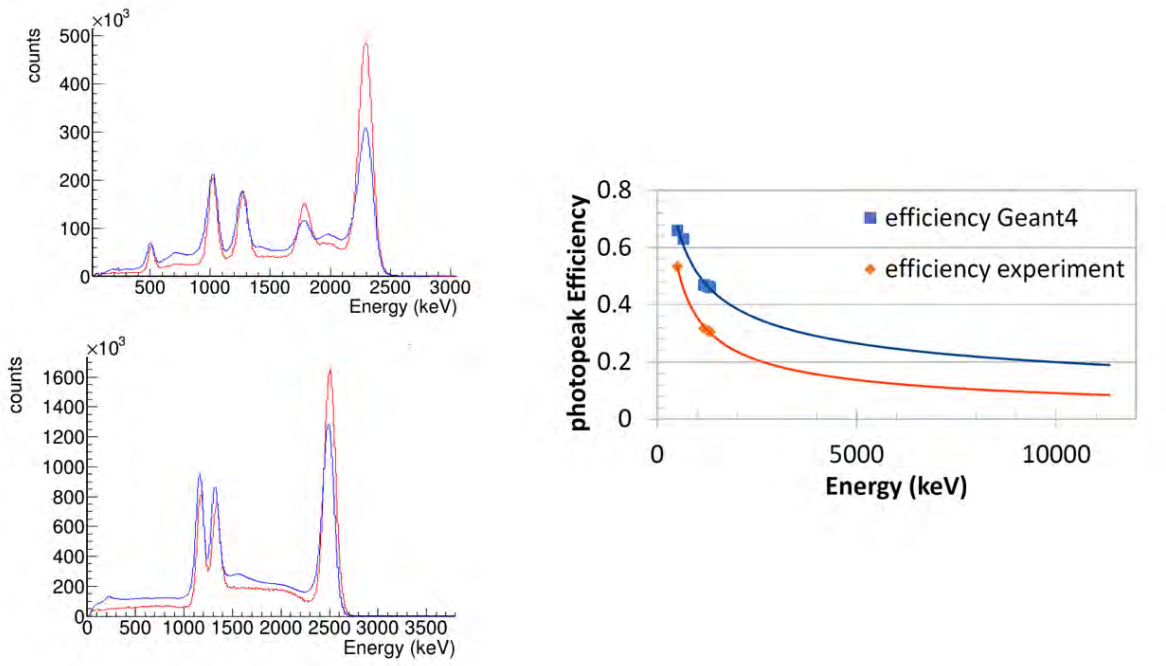

Fig. 2. The two spectra on the left show the sum of the gamma-ray energies measured by the 16 detectors with the gamma sources ^{22}Na (top) and ^{60}Co (bottom). The blue line is from the experimental data; the red line is from the Geant4 simulation. The figure on the right shows the photopeak efficiency obtained with these sources in the experiment and in the Geant4 simulation.

Further tests will be performed with a beta-decaying ^{11}Be beam to measure the photopeak efficiency at higher energies.

Development of a YAP-CsI phoswich for use with TexAT-TPC

M. Roosa, G. Christian, G. Rogachev, J. Bishop, C.E. Parker, M. Barbui, and A. Saastamoinen

Transfer reaction measurements performed in inverse kinematics are a key tool for exploring the nuclear landscape. Several such measurements - to be performed using the Texas Active Target (TexAT) Time Projection Chamber (TPC) [KOS20] have been proposed at the Texas A&M University Cyclotron Institute. The reactions of interest for these measurements are ^{12}B(d,^{3}He)^{11}Be, ^{13}B(d,^{3}He)^{12}Be, and ^{14}B(d,3He)^{13}Be. The latter will be coupled to the TexNeut neutron detector array.

One of the foremost challenges to the success of transfer measurements in active target TPCs is that of reliable reaction ID. Due to the various energy scales and stopping powers of the involved particles, it is difficult to identify both the beam-like and target-like reaction products using the TPC alone. However this can be remedied by coupling the TPC system to a solid-state detector array as is done in the TexAT system. This work aims to develop a heavy recoil identification detector capable of separating unreacted beam and beam contaminants from the reacted beam of interest. This detector would need to, at minimum, separate Z=3,4 and 5, have a radiation hardness sufficient to survive the dose from multiple experiments and fit into the TexAT footprint.

The TexAT set-up would typically use a Silicon-Cesium-Iodide (Si-CsI) telescope, but due to the desired radiation hardness constraints, this is suboptimal. Because scintillators are simple to source and can be designed with exceptional radiation hardness, a phosphor sandwich or phoswich could satisfy the above requirements. A phoswich is a scintillator detector composed of two different crystals with different timing properties. A pulse shape analysis can then be used to extract the energy deposited in each layer of the sandwich; this then can be used as PID through the standard dE-E method.

A phoswich composed of 100-μm-thick cerium doped yttrium aluminium perovskite (YAP:Ce) and a 2-cm-thick CsI was designed and tested at the TAMU-CI. A schematic of the design and a model of the relative pulse shape is shown in Fig. 1. As care had to be taken to ensure the timing resolution and

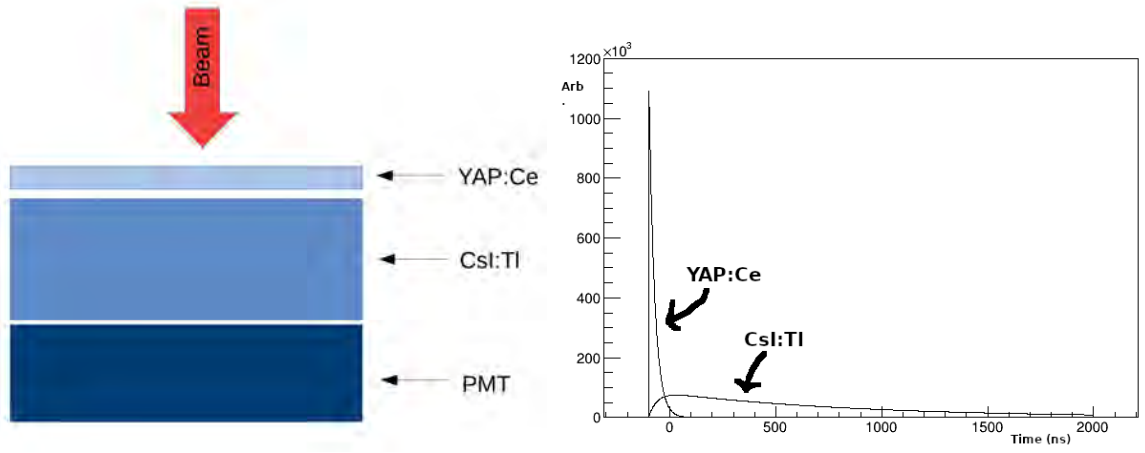

Fig. 1. (Left) A cartoon demonstrating the design of the detector. (Right) modeled pulse shape from the reported brightness, rise and decay times of each scintillator.

light collection efficiency would not destroy the pulse shape information; a Hamamatsu R12699-406-M4 PMT was determined to be a good candidate.

A ^{14}N beam at 15MeV/u was impinged on 100 μg/ cm^2 gold and 1 mg/cm^2 carbon during a beam test in April 2022. Plots of the short integration against the total integration gate from that test are shown in Fig. 2. This gate pairing corresponds to energy loss in the YAP(Ce) vs Total energy and is analogous to a typical dE-E plot used for charged particle identification. When using the gold target, we can see a distinct grouping of events that correspond to elastically scattered ^{14}N and a characteristic energy dependence of the short component (ΔE) on energy. Analysis of the data on the carbon target was complicated by the experimental noise issues and it may be necessary to repeat this test run to demonstrate efficacy of the phoswich detector system for recoil ID.

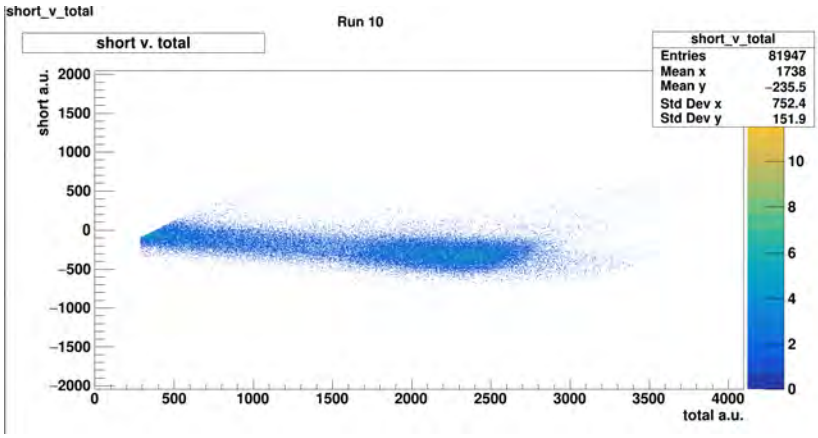

Fig. 2. Short Gate v. Total Integration is plotted for 15Mev/u 14N on Gold (Left) and 15Mev/u 14N on Carbon (Right). See text for discussion.

[1] E. Koshchiy *et al.*, Nucl. Instrum. Methods Phys. Res. **A957**, 163398 (2020).

He-3 gas system for experiments with TPC

E. Koshchiy, G.V. Rogachev, J.E. Bishop, M. Barbui, C.E. Parker, and A. Saastamoinen

In the last decade, considerable progress has been achieved in implementing the Active Target TPC technique for experiments with rare isotope beams at low energies relevant to nuclear structure and nuclear astrophysics. The versatile TexAT detector has been in operation since 2017. Several successful experiments on resonance elastic and inelastic scattering of protons and □-particles, (□,p) and (p,□)-reactions, nucleon-transfer reactions, such as (d,p), (d,3He), (p,d), (p,t), (□,t) and β- delayed charged particle decay spectroscopy were carried out [1]. The discovery of β- delayed emission of 3□ particle and a proton by 13O [2] has been made with TexAT recently. We are now implementing TexAT upgrade which will allow us to use He-3 gas as an active target volume.

There are several good reasons to use TexAT advantages in experiments with He-3 as an active gas target and rare isotope beams available at CI or other RIB facilities. For instance, a proton transfer reaction (3He,d) is one of the best indirect tools for the evaluation of the reaction rates, which are important for astrophysics [3]. Another important reason for using interactions between He-3 and proton-rich exotic nuclei is a possibility to explore properties of even more proton-rich nuclei through the two-proton stripping reaction of (3He,n), using a capability of recently created neutron TexNeut detector [4].

The challenge of experiments with He-3 target gas is related to the shortage and high price of the rare isotope of 3He and the high demand for the applications in homeland security, science, medicine, and industry [5]. At the moment production, sales and distribution of helium-3 in the United States are managed by the US Department of Energy [6]. The required quantity of He-3 gas for experiments with TexAT is about 40L NTP.

To reduce a loss of expensive He-3 gas in the gas handling system the following requirements were taken into consideration:

- the system must be closed;
- A mixture of several gasses needs to be produced online;
- He-3 needs to be recovered with high efficiency and as little loss as possible.

The He-3 gas is quenched by adding a small amount of carbon dioxide gas (at the level of 2 - 10%, depending on the experiment) to prevent scintillations that substantially suppress electron ionization.

Due to the limited usage of He-3 gas, there are no specific compressors available on the market. Commercial compressors for He-4 are mostly designed to run a large volume of He gas and the compression rate is as high as ~100 bar, which makes it difficult to use them for our applications. Instead of designing a custom compressor, it has been decided to use a possibility of modern dry pumps not only to pump working gas but to compress it in an exhaust line up to ~2 bar [7].

The simplified He-3 vacuum/gas handling system has been designed (shown at Fig.1) and tested with regular He-4 gas. The vacuum part consists of fore-vacuum (Agilent NDP-15) and turbo (Agilent

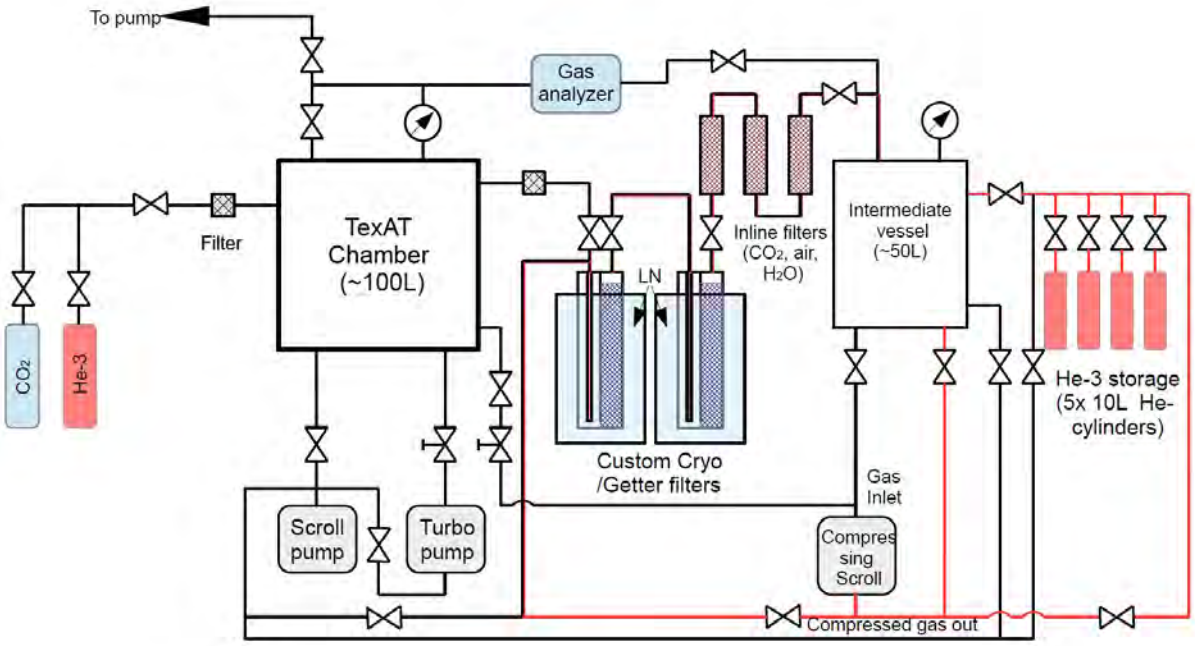

Fig. 1. He-3 Vacuum/He-3 Gas handling system. The compressed gas lines are shown in red.

Twistorr 304FS) pumps providing high vacuum (better than 1E-6 Torr) before experiments. Then the TexAT chamber fills up with a calculated mixture of 3He/CO2 gases. The gas composition is maintained and controlled automatically. To prevent the effect of "layering" in the gas system, the fan is installed inside the TexAT chamber. The working gas purity and composition can be checked periodically. According to the tests, the quality of the gas stays satisfactory for up to hours, and then it requires some purification. The main impurities are air (mostly, N2) because of some leaking and Hydrocarbons because of the cables/plastic outgassing.

During purification, the working gas is cleaned from CO2/H2O by two connected in series Cryo/Getter filters, and from other impurities - by a set of specific gases inline filters. The purified gas is stored in the intermediate vessel and then returns back to the experimental chamber after the additional purity check by BGA244HP gas analyzer. The purification procedure takes about 2 hours.

After the experiment gas goes through another purification and compression stage and is stored in the set of He-cylinders at the pressure of ~ 2 bar.

To minimize the gas losses most of vacuum adapters and nipples are SS "Conflat"- type, the high quality VCR-type compression fittings and all metal tubing were used. It was shown that irreversible losses of He gas during a single experiment were at the level of 1 to 1.5%.

[1] J.E. Bishop *et al*., TexAT & TeBAT – a multitude of experiments. International Workshop TPC2023, Cyclotron Institute, TAMU (2023).
[2] J. Bishop, G.V.Rogachev *et al*., Phys.Rev.Lett. **130** 22501 (2023).
[3] Y. Fujii *et al*., Cyclotron Rad. Center, Tohoku Univ., Ann. Rept. 1994, 1 (1995).

[4] D. Scriven *et al*. Nucl. Instrum. Methods Phys. Res. **A1010**, 165492 (2021).
[5] Dana A. Shea and Daniel Morgan, CRS Report for Congress, R41419 (2010).
[6] Isotope Development & Production for Research and Applications (IDPRA). US Department of Energy Office of Science. 18 October 2018.
[7] Inverted Dry Scroll Pump IDP-10 Hermetic, 10.2 m3/hr, 6.0 CFM | Agilent

Status of TeBAT (Texas-Birmingham Active Target) detector development

G.V. Rogachev,[1,2] J. Bishop,[1] E. Koshchiy,[1] S. Ahn,[1] M. Barbui,[1] A. Hollands,[3] T. Kokalova,[3]
C.E. Parker,[1] S. Pirrie,[3] E. Pollacco,[4] A. Saastamoinen,[1] C. Wheldon,[3] and J.C. Zamora[5]
[1]*Cyclotron Institute, Texas A&M University, College Station, TX 77843, USA*
[2]*Department of Physics&Astronomy, Texas A&M University, College Station, TX 77843, USA*
[3]*School of Physics and Astronomy, University of Birmingham, Birmingham, United Kingdom*
[4]*IRFU, CEA, Saclay, Gif-Sur-Ivette, France*
[5]*Instituto de Fisica, Universidade de Sao Paulo, SP 05508-090, Brazil*

A new state-of-the-art active target TPC (Time Projection Chamber) detector system, TeBAT, has been under development at the Cyclotron Institute since 2019. The TeBAT detector utilizes a new technology based on Micromegas with a DLC (Diamond-like **c**arbon) resistive readout layer, which allows for position resolution as good as 200 μm. We expect this will result in unprecedented angular resolution on the order of 0.1 degrees, which is critical for many nuclear reaction studies.

The design of TeBAT is similar to the existing TexAT detector [1] in terms of geometry. TeBAT consists of a micromegas-based gas detector, surrounded by an array of Si/CsI(Tl) detector telescopes to measure the total energy of light fragments escaping the active TPC volume. Both TexAT and TeBAT setups will share solid-state detector parts. The details of the conceptual design of TeBAT are presented in [2].

Here we report on the status of the TeBAT project.

Detectors:

- The first (out of five total) resistive (DLC) layer micromegas detector has been manufactured by CERN, delivered, and is under testing in the lab (shown in Fig.1). Two more DLC- layer micromegas detectors are in production now and are expected to be delivered by the end of 2023. Another standard micromegas (no DLC) is expected by the Fall of 2023.
- Five GEM (**G**as **E**lectron **M**ultipliers) produced by CERN are delivered and ready to be tested. They consist of a thin (50 mm) double-copper-clad kapton foil, chemically perforated by a high density (50 holes/mm^2) holes of □=50 mm. The geometry of the active area is custom designed to fully match the TeBAT Micromegas detector. The GEM foil is segmented into 6 zones allowing us to create avalanche areas with different gas gain by varying the applied bias by region.
- A set of 10 custom-designed silicon detectors to match the current TexAT/TeBAT detectors from Micron Semiconductor Co. (UK) have been purchased and were delivered in 2022. The thickness of the Si- detectors is 500 μm (8 total) and 1000 μm (2 total). They will be shared between both the TexAT and TeBAT setups. With the 10 existing 50 mm x 50 mm Si-detectors for TexAT, the total Si-detector coverage is about 30%. We are planning to order ten more Si detectors in 2023 to make all but the bottom sides of TexAT/TeBAT covered.
- CsI(Tl) scintillation detectors are available to totally cover TexAT/TeBAT.

- Beam monitoring detectors - 3 different detectors are designed for TexAT and will be shared for operation with TeBAT. They are a) a gas ionization counter; b) an auxiliary small Micromegas-based gas detector ([3]); c) a thin scintillation detector with SiPM readout following the design used for TexAT_v2 ([4]).

a b

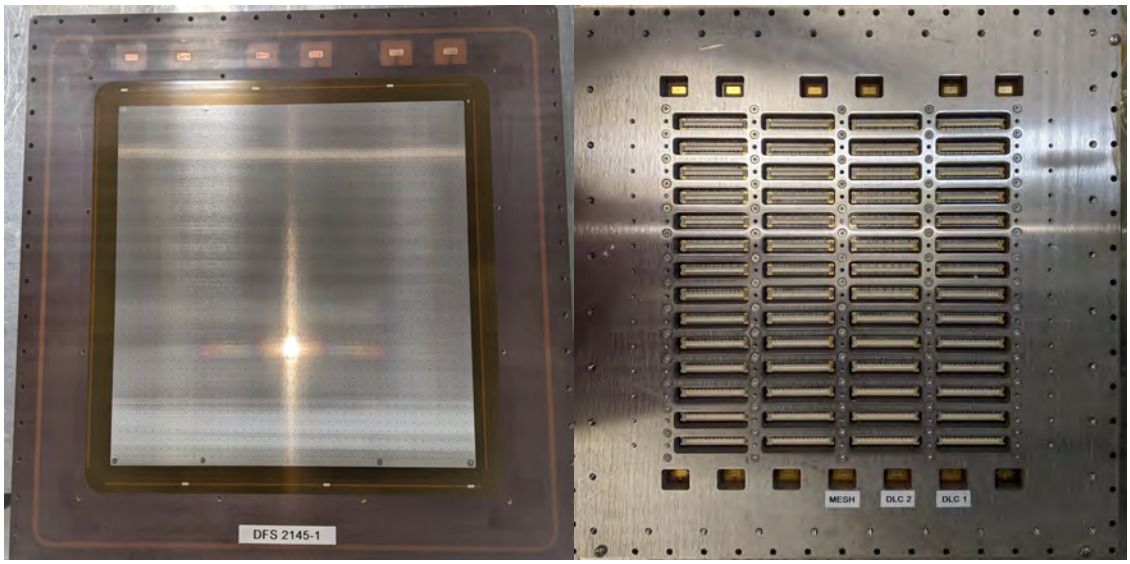

Fig. 1. TeBAT DLC Micromegas detector. a) Front side view; b) Rear (readout) side view.

Hardware:

- The flexible printed circuits (FPC) "flex" cables to carry signals from 7,000 channels without any cross-talk among channels were designed and tested. Four out of 28 cables have been produced by CERN, the rest are expected by the end of 2023. Each cable carries 256 signals.
- The Scattering chamber has been designed and now is in production at local workshops (split between the Cyclotron Institute and the Department of Physics TAMU). We expect it to be ready for tests by early Fall 2023.
- The support structure for the front-end electronics (ASAD- boards) and ZAP (protection) boards have been designed and developed in-house.
- The vacuum/gas handling system, similar to TexAT's has been designed. The parts of the system have been purchased. The system is expected to be completed by the Fall of 2023.
- Additional LV and HV supplies have been ordered. The LV modules to power all the ASAD boards have been delivered and tested.

Parts to be made:

- Transparent field cage for TeBAT – designed and expected at the end of 2023.
- Gating grid to solve the "space charge" problem of the incoming beam area.

Electronics:

As described previously [2], the readout of signals from TeBAT is performed by the General Electronics for TPC (GET) [5]. The GET electronics for TeBAT consist of 1 μTCA crate, 1 Mutant trigger module, 9 CoBo (Concentrator Board) modules, and 28 AsAd motherboards. Two of these AsAd boards will have the new STAGE chips to replace the older AGET chips. These new chips have been tested recently and allow for better low-multiplicity triggering and a long peaking time (8 μs) to facilitate the readout of the CsI(Tl) detectors directly without the need for external shaping. A detailed description of the GET electronics is explained in Ref. [5]. Most of the electronic modules are present and are to be shared with TexAT. The new AsAd (24 total) and CoBo modules (6 total) are tested and operational.

Software:

A new streamlined conversion tool to allow for quicker analysis of the data (Catalytic [6]) has been developed and tested. Additionally, a base analysis framework (Himalaya [7]) to analyze the new TeBAT data has also been written and tested with previous TexAT data. Both of these software tools will undergo further development as the first test data become available from TeBAT to optimize the track reconstruction techniques.

[1] E. Koshchiy *et al*. Nucl. Instrum. Methods Phys. Res. **A957**, 163398 (2020).
[2] S. Ahn *et al*. *Progress in Research*, Cyclotron Institute, Texas A&M University (2020-2021) p. IV-118
[3] J. Holmes, E. Galyaev, R. Alarcon, R. Acuna, D. Blyth, B. Fox, N. Mullins, and K. Scheuer, J. Instrum. **15**, T05001 (2020).
[4] C. Park *et al*.,Nucl. Instrum. Methods Phys. Res. **B541**, 221 (2023).
[5] E.C. Pollacco *et al.*, Nucl. Instrum. Methods Phys. Res. **A887**, 81 (2017).
[6] https://github.com/tamu-edu/gr-Catalytic
[7] https://github.com/tamu-edu/gr-Himalaya

Advantages and requirements of an active target TPC for DAPPER

A.B. McIntosh

The Detector Array for Photons, Protons, and Exotic Residues has been developed and commissioned. DAPPER was commissioned with a stable beam and used to measure 57Fe(d,pg) reactions. The calibration is well in hand, and analysis is underway. This experiment will result in a determination of the photon strength function via the Forward Method, and a determination of the photon strength function via the Oslo Method. Nonetheless, improvements can be made to DAPPER to improve its capabilities. In particular, an active target time projection chamber (TPC) could offer several advantages to DAPPER.

A TPC filled with pure deuterium gas provides a target largely free from impurities, so background reactions on target contaminants would no longer be a significant concern; currently, fusion evaporation on the carbon in the CD2 target is a background which can't be removed event by event.

An active target provides a significantly higher areal density of deuterium than even the relatively thick (~500ug/cm2, which is ~125ug/cm2 deuterium) deuterated plastic targets used previously. Assuming a pressure of 500 Torr, we obtain 1100ug/cm2 of deuterium, a ten-fold increase.

Currently, the uncertainty in the measurement of the excitation energy is dominated by two things: the energy loss of the ejectile proton, and the angle of the ejectile proton. These contribute roughly equally to the uncertainty. Currently, we can only assume the reaction takes place at halfway through the solid target, and correct on average for the proton's energy loss. With an active target, we can accurately correct event by event for the energy loss. The finite size of the beam spot and the granularity of the S3 silicon detector used to measure the proton limit the accuracy of the deduced angle of the proton. With a time projection chamber, the endpoint of the track can still be measured with the S3 inside the gas, and angle of the track can be additionally be measured with TPC.

The TPC needs to be as small as possible to accommodate the gamma ray detectors; the current gamma detectors fit around an ISO-160 Tee. The larger the TPC, the farther the gamma detectors will be and thus the lower the efficiency will be. The TPC needs to use low-Z material and as little material as possible to minimize photon scattering.

The TPC needs to be able to handle a reaction rate of 500 protons per second, which is easily achievable. However, to attain that rate, we anticipate a rate of at least 3e5 iron nuclei per second. There may well need to be a central region of the TPC blind to the ionization. The ionization in this region needs to not distort the electric field.

To maintain current ejectile angle knowledge, the angle should be measured with an accuracy of 1.5 degrees. Angular accuracy in the TPC will depend on the angle of the track, and resolution of the reaction vertex in all dimensions. Vertex accuracy on the order of 1.5mm should be achievable and in much of phase space is sufficient. Even if the vertex is not known to this accuracy, the track angle relative to the beam axis should be measured with 1.5 degree accuracy of better.

The gas gain should be high enough, and the preamp gain appropriate, that the tracks from protons between 200 keV and 10 MeV can be measured. These tracks deposit 13.1 keV/mm and 0.57 keV/mm respectively.

For the protons that stop in the gas, the track length should be used to deduce the proton energy; this should be possible to benchmark at a variety of energies (from a variety of initial positions) at which they punch through the gas and into the silicon detector.

A cylindrical TPC with axis parallel (or perhaps nearly parallel) to the beam axis, and with electric field along the cylinder's axis, seems more attractive than other geometries. For example, a rectangular TPC with field perpendicular to the beam results in the high ionization of the beam tracks creating a large background over a larger region in which protons should be measured. With cylindrical design, the S3 silicon for residual proton energy would cover backward angles in the lab, and the electron multipliers and pad plane would be on the downstream end of the TPC.

Exploring novel direct reactions for the production of terbium-149 using Hyperion

L.A. McCann,[1,2] A.B. McIntosh,[1] L.A. McIntosh,[1] P. Adsley,[1,3] J.G. Duarte,[4] M. Gott,[5] J.T. Harke,[4] Y. Mishnayot,[4] J.T. Morrell,[6] A.S. Tamashiro,[4] C.E. Vermeulen,[6] and S.J. Yennello[1,2]

[1] *Cyclotron Institute, Texas A&M University, College Station, TX 77843, USA*
[2] *Department of Chemistry, Texas A&M University, College Station, TX 77843, USA*
[3] *Department of Physics, Texas A&M University, College Station, TX 77843, USA*
[4] *Lawrence Livermore National Laboratory, Livermore, CA, 94550, USA*
[5] *Physics Division, Argonne National Laboratory, Lemont, IL 60439, USA*
[6] *Los Alamos National Laboratory, Los Alamos, NM 87545, USA*

Targeted alpha therapy (TAT) is an emerging field in cancer research that links an alpha-emitting radionuclide to a targeting agent that can travel to the tumor location, allowing most of the damage due to the radioactive decay to occur within the tumor, reducing damage to healthy cells. There are several factors that need to be considered when selecting a TAT isotope such as its half-life and toxicity of nuclide and its decay products. While there are a number of isotopes that meet biologically relevant criteria, there is only one that has been identified to decay via both alpha and positron emission, allowing it to be used in TAT, but also to be imaged via positron emission tomography (PET) without the use of another imaging isotope [1-3]. This unique isotope is terbium-149. Its dual functionality of both therapy and diagnostic properties is termed "theranostic" and is very valuable as it eliminates the need for a chemically similar homolog to be used for imaging purposes [4]. Despite the potential value of ^{149}Tb as a TAT isotope, there are a number of challenges facing its production including its biologically-relevant half-life of 4.1 hours, its low neutron-to-mass ratio, and the favorable production of the metastable state which does not decay via alpha emission.

Although ^{149}Tb has been made via a variety of pathways over the years, none of these currently produce the yields that are necessary for isotope production with worldwide availability [5,6]. Many experiments, particularly heavy-ion direct reactions, have attributed these low production rates to the competing production of the 4 minute half-life metastable isomer, but none have been designed to quantify this contribution [7-9]. In an effort to explore new pathways for the production of ^{149}Tb, it is valuable to know this ratio of population of the ground state to the excited state based on projectile energy and mass. With this in mind, the Hyperion high-purity germanium (HPGe) detector array was chosen [10], to allow measurement of the decay of all of the isotopes produced in the reaction immediately after beam, including the short-lived ^{149m}Tb. The reaction chosen for this experiment was a ^{6}Li beam impinging on a variety of enriched samarium targets (Z = 147-149), due to its high predicted cross-sections found using PACE4 [11,12]. While PACE4 is known to overpredict cross-sections, it is also unable to distinguish between production of the ground state or other excited states of a given nucleus, likely a large source of error particularly in the case where the excited state population is high

and does not decay to produce the ground state. It is, however, accurate for choosing beam energies, allowing us to choose our maximum yield energies for this experiment.

A series of reactions were then measured at TAMU using Hyperion. The reactions that were measured include $^{147}Sm(^{6}Li,4n)^{149}Tb$ at 45 MeV, $^{148}Sm(^{6}Li,5n)^{149}Tb$ at 55 MeV, and $^{149}Sm(^{6}Li,6n)^{149}Tb$ at 55, 60, and 65 MeV. These systems were chosen to experimentally measure for the first time the cross-sections of these reactions, and determine the contribution to the total predicted cross section of ^{149}Tb by the metastable isomer. From the resulting measurements, the effect of the differing target mass could be measured, and to determine how close to the actual peak cross section our single-energy measurements were based on PACE4 predictions. A week of beam was necessary for these experiments with overnight irradiations, while the decay measurements, beam tuning, and target changing occurred during the day. Given the 4.1 h half-life of the isotope of interest, this amount of time allowed for maximum production of ^{149g}Tb, and the subsequent immediate decay measurement of the products, followed by delayed target extraction and movement to an offline HPGe detector for further measurement of isotopes with longer half-lives.

In order to prepare for these experiments, a series of samarium targets needed to be prepared. An aluminum backing was chosen for the foils so that it would result in a limited number of known activation lines interfering with the measured production gamma rays. Additionally, the short-lived ^{28}Al peak ($t_{1/2}$ = 2.25 m) should allow for better characterization of the beam current during the overnight irradiations. Since enriched samarium comes only in the oxide form, it was necessary to reduce it in order to create the desired metallic targets. Samarium is also considered to be a low melting point lanthanide, meaning that these targets were able to be produced via physical vapor deposition (PVD) at Argonne National Laboratory. The enriched

Fig. 1. Tantalum pinhole boat containing a pressed pellet of Sm2O3 and Zr.

samarium oxide was measured and pressed into a pellet with an excess of zirconium metal, and placed into a tantalum pinhole boat (Fig. 1). From there, a current is passed through the boat,

heating up the pellet, allowing the zirconium to reduce the samarium oxide powder to samarium metal, and then selectively evaporate it onto the overhead aluminum frames. Targets of thickness 1 mg/cm2 were prepared using this method, shown in Fig. 2.

Fig. 2. PVD Sm target with Al backing mounted on a Hyperion frame.

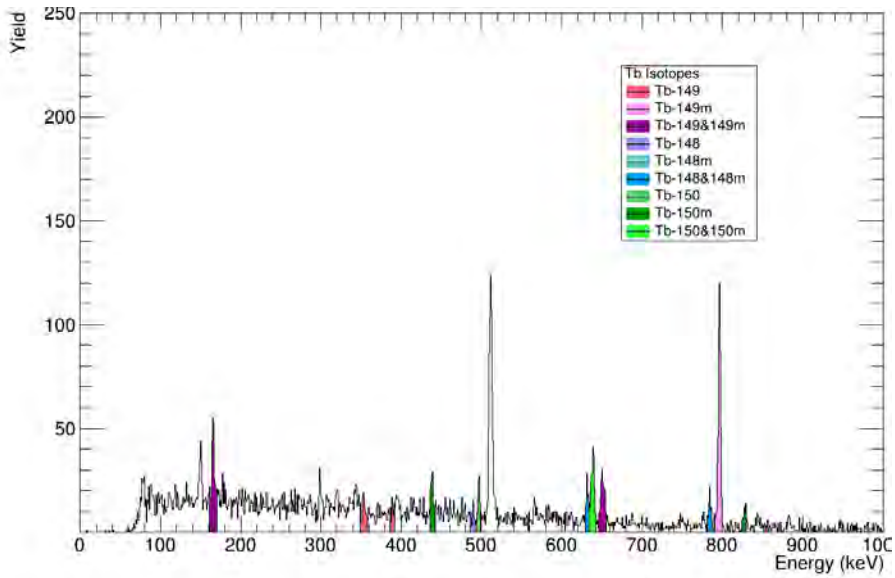

Fig. 3. HPGe clover spectrum taken 8 min after the end of beam for the ^{6}Li on ^{147}Sm system. The highlighted peaks indicate the gamma emissions associated with the ^{149}Tb isomers (pinks), ^{148}Tb isomers (blues), and ^{150}Tb isomers (greens).

From analyzing the resulting HPGe spectra in Fig. 3, it can be seen that both ^{149g}Tb and ^{149m}Tb were produced in the reactions. Terbium-148 and ^{150}Tb were also able to be confirmed through peak

analysis. Cross sections for every isotope measured in the experiment are currently being calculated, to get a comprehensive picture of the isotopes produced in the reaction to better inform nuclear codes in this region, and determine if these reactions pose a viable pathway for the large-scale production of ^{149}Tb for medical applications.

Acknowledgements

This work is indebted to the operations staff at the Texas A&M Cyclotron Institute and Radiological Safety program for their contributions to this work. This work was supported by the U.S. DOE Isotope Program, Award No. DE-SC0020958, DE-SC0022539 and DE-SC0022550 (HIPPO program); U.S. DOE under Award No. DE-NA0003841 and DE-FG02-93ER4077; the NSF GRFP; TAMU through the Bright Chair in Nuclear Science, the Nuclear Solutions Institute and a T3 grant: TAMU NLO and LANL through the joint collaborative research program. Work at ANL was supported by the U.S. DOE, Office of Science, Office of Nuclear Physics, under Award No. DE-SC-0017208. Argonne's ATLAS facility, which is a DOE Office of Science User Facility. Hyperion Array made possible by DE-AC52-07NA27344.

[1] M.R. McDevitt *et al.*, Eur. J. Nucl. Med. Mol. Imaging **25**, 1341 (1998); DOI: 10.1007/s002590050306

[2] D.S. Wilbur, Curr. Radiopharm **4**, 214 (2011); DOI: 10.2174/1874471011104030214

[3] M.R. Zalutsky and M. Pruszynski; Curr. Radiopharm. **4**, 177 (2011); DOI:10.2174/1874471011104030177

[4] C. Kratochwil *et al.*, J. Nucl. Med. **57**, 1941 (2016); DOI: 10.2967/jnumed.116.178673

[5] C. Ducheminet *et al.*, Front. Med. **8**, 625561 (2021); DOI: 10.3389/fmed.2021.625561

[6] H. Verhoeven, MSc Thesis, KU Leuven (Belgium), 2018; CERN-THESIS-2018-157.

[7] R.D. Macfarlane, Phys. Rev. **126**, 274 (1962); DOI: 10.1103/PhysRev.126.274

[8] M. Maiti *et al.*, Radiochim. Acta. **99**, 527 **(**2011); DOI: 10.1524/ract.2011.1839

[9] J.T. Wilkinson *et al.*, Appl. Rad. Isot. **178**, 109935 (2021); DOI: 10.1016/j.apradiso.2021.109935

[10] R.O. Hughes *et al*., Nucl. Instrum. Methods Phys. Res. **A856**, 47 (2017); DOI: 10.1016/j.nima.2017.03.012

[11] O.B. Tarasov and D. Bazin, Nucl. Instrum. Methods Phys. Res. **B266**, 4657 (2008).

[12] A.Gavron, Phys.Rev. C **21**, 230 (1980).

Yttrium Aluminum Perovskite (YAP) scintillator array as a heavy ion detector for DAPPER

A.B. McIntosh

The detector array for photons, protons, and exotic residues is designed for use with secondary beams to allow measurement of (*d, p*) reactions on unstable nuclei. Such secondary beams typically contain contaminants. The ability to distinguish the contaminants event by event is highly desirable to allow a clean measurement of the photon strength function of a single nuclide. When the secondary beams are already prepared with a selection on rigidity and on velocity, as is the case with MARS, the contaminants can't be distinguished by energy or time-of flight.

To identify heavy ions by Z, the ions can be passed through a degrader and be distinguished by their residual energy. Iron, which is both the beam species of interest, and the reactant of interest in (*d, p*) reactions, will have the highest residual energy after degradation. The cobalt contaminant, and its (*d, p*) residues, will have less residual energy after degradation. Residues arising from fusion evaporation on carbon in the plastic target will have even less energy after degredation.

An array of Yttrium Aluminum Perovskite (YAP) scintillator array has been developed to serve this purpose. It needs to discriminate between iron and cobalt at a rate of at least 3e5 particles per second. Active bases were used for the photomultiplier tubes. Various resistors were used for the active bases. Smaller resistances allow faster recharging of dynodes, which allow higher rate. However, resistors that are much too small draw too much current and are prone to failure of the transistors. Resistors that are somewhat too small do not afford as good energy resolution as larger resistors. A balance must be struck between rate and resolution.

YAP detectors were tested in beam with various bases and at various voltages. The signals from the phototube were sent directly to the input of the SIS3316 flash ADC. Waveforms were recorded, and the timing MAW was used with peak=2 and gap=2 (previously shown to be optimal for measuring 5-9 MeV alpha particles). High and mid resistance bases performed similarly. Adequate resolution can be obtained at high rate. The 7.5 MeV/u copper beam contained chlorine impurity; use of single and double hits of copper and chlorine allowed us to establish that the light output was linear with energy in this energy range. Very high intensity beam was applied to the YAP to simulate 9 days-worth of beam time; the resolution held up sufficiently well.

A secondary beam of ^{57}Fe and ^{57}Co @ 7.5 MeV/u was produced in MARS with roughly equal components of each. This was impinged directly on a YAP and a resolution better than 2% FWHM was obtained. A degrader of aluminum foil of approximately 25μm (heavy duty commercial aluminum foil) was inserted to degrade the beam energy immediately before the YAP. The resolution worsened to around 6%. Rotation of the degrader (to precision of 1 degree) up to 61 degrees allowed increasing the thickness of the degrader to just beyond double the initial thickness. Within this range, the iron and cobalt should have begun to be discernible. However, the peak became broader faster than the two constituents would be expected to separate, and no distinction between iron and cobalt was achieved.

Use of 2 layers of the heavy duty foil performed identically to a rotation of the foil to 60 degrees. Translation of the degrader 14" farther upstream (to a total distance of about 18") to reduce the relative amount of multiple scattering did nothing to improve the situation. The thickness of the foil was measured

with a micrometer in multiple places with an accuracy of 0.00005”; 5 measurements reported identical values, one higher by 0.00005” and one lower by 0.00005”, indicating the variation of the foil is flat to within the precision of the micrometer, and ruling out gross thickness variations as the primary cause of the lack of Fe/Co resolution; thickness variation might contribute to the problem, but is not the main problem. The energy resolution degrades far faster than a sqrt(E) dependence; photon counting statistics is not the problem. Delta rays are not the problem, as reasonable resolution (6%) was obtained with the degrader at 0 degrees. The iron and cobalt is degraded into the Bragg peak when the degrader is turned to 60 degrees, but the energy is still far above the region where nuclear stopping dominates over electronic stopping. Integrating the waveforms, rather than using the MAW MAX, did not show a significant change in the resolution obtained with the degrader turned near 60 degrees. Changing the degrader from 59 to 60 to 61 degrees produced a very rapidly worsening resolution. At 59 degrees, a poor resolution peak was clearly visible; at 61 degrees the peak was just discernible; at 61 degrees, no peak was observed at all, merely a broad peak at E=0 with a tail extending to higher energy. According to LISE++, energy straggling is too small (<1%) to be the primary cause, though one may question the accuracy of the straggling prediction with this much energy loss.

It is possible that fluctuations in the quenching is the cause of the problem. For highly ionizing particles near the Bragg peak, the excitation and ionization density is very high, and quenching is very large. Since quenching is a stochastic process, some events have more quenching than others. If only the Bragg peak, or just beyond, is in the active volume of the detector, the fluctuations in the quenching must be relatively largest. Perhaps when the signal is nothing but Bragg peak, the fluctuations are so large compared to the amplitude of the signal that the resolution is completely destroyed. It is also possible that there exists a dead layer on the surface of the YAP which is highly non-uniform. It is not clear how either of these possible causes could be dealt with in order to use the YAP to measure very small residual energy.

An experiment could be done with low energy direct beams to verify unambiguously that the thick degrader is playing no role in the destruction of the energy resolution. However, it is not clear what the path forward with YAP for this application would be for any possible result of such a test. An alternate detector technology is likely necessary.

Zero deadtime event readout of the neutron ball for NIMROD experiments at the cyclotron institute

K. Hagel and M.K. Youngs

We reported [1] an upgrade to our data acquisition where we exploited the dual bank nature and multievent capability of the Struck 3316 digitizers [2] to significantly enhance our data taking rate capabilities in experiments performed at the Cyclotron Institute. The software was optimized for large multi-parameter experiments in NIMROD [3], FAUST[4] and DAPPER[5], but has been used to enhance data rate capabilities in smaller scale experiments as well.

While the multievent capability works well for the charged particle array in NIMROD [4], experiments requiring information from the Neutron Ball [6] presented a readout issue with the heretofore method used for the neutron ball. Readout from the neutron ball to date has involved taking the signals from the PMTs, amplifying them, inserting the amplified signals into discriminators, and counting the logic outputs of any signal above threshold in a two 100us gates, the first starting with the trigger from the event and the other following at the end of the first, using VME scalers with the first window used to count neutrons associated with the reaction and the second used to estimate the background. Various configurations of this method involved either simply counting the signals from the discriminators or requiring signals from at least two PMTs in the same neutron ball segment within a short period of time to discriminate against random noise and counting those coincidences.

Such an approach does not lend itself easily to the multievent readout of NIMROD that we now routinely employ in most of our current experiments. In order to address this issue and exploit current technology, we have extended our software to exploit the multievent capability of the Struck Digitizers to acquire multievents from the neutron ball within the multievents being used for the charged particle array. In order to utilize the digitizers, the PMT signals were connected directly to the digitizers and thresholds were set. The clocks of the digitizers were synchronized with the clocks of the other digitizers in the rest of the experiment. In order to acquire neutron ball signals associated the reactions of interest, the NIMROD trigger (min bias in the test run) was used to open a 200us gate that was used as an external gate to the digitizers for the neutron ball. All signals within the 200us gate were thus multievents that contained all of the neutron ball information for the particular event, but were embedded inside each event in the multievents from NIMROD.

In addition to allowing readout of the neutron ball in the multievent mode, the information from the digitizer in the "events" (neutron ball hits) in 200us external gate is significantly enhanced compared to the information available from the previous single event readout of NIMROD with neutron ball scalers. The neutron multiplicity comparable to the previous method is simply the number of "events" in the first 100us and the background is simply the number of "events" in the second 100us. In addition to that information, we now have access to the time of each hit as well as the amplitude of each hit. This gives a measure of the capture time distribution on an event-by-event basis. In addition, the time of each hit allows to easily construct coincidences between the various PMTs in a single sector and since all data is written, different combinations can be tried with different gate widths in order to ascertain the most dependable results. Also, the amplitude of the signals may allow to discriminate noise in the "true" (1st

100us) gate. For example, if a large signal is observed in coincidence with another sector, it is quite possible that such a signal results from a cosmic muon traversing the detector and it would be eliminated from the counting of the neutron ball multiplicity.

As a proof of concept, we present in Fig. 1 the time difference between each PMT hit in the neutron ball from the trigger time of the event given by a minimum bias trigger from NIMROD. We note a strong peak near just after the trigger, near zero in the plot, followed by a more gradually varying

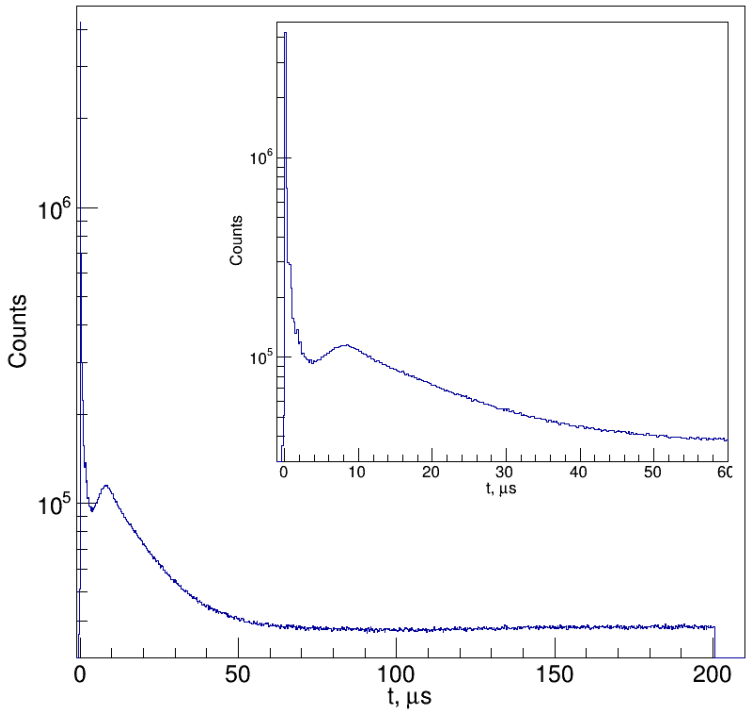

Fig. 1. Neutron Ball Capture time distribution. The inset shows the same, but with a range to 60 μs.

distribution having peak near but below 10μs. The strong peak at small times relative to the trigger time shows the gamma flash that originates from γ-rays from the reaction and recoil protons from the scattering of neutrons in the scintillator [7]. The distribution at later times indicates the capture time distribution of neutrons which are captured on Gd nuclei from the dopant and, hence, the sum of all hits after the gamma flash provides the total number of neutrons detected from the reaction [7]. We note a similar capture time distribution to what was reported in [7] hence indicating that the technique works.

The data are on disk and are currently being analyzed in order to understand how well the extra information provided by the multievent readout of the neutron ball can be utilized to enhance the measure of the neutron multiplicity from the neutron ball. Initial indications are that technique works well.

[1] K. Hagel *et al.*, *Progress in Research*, Cyclotron Institute, Texas A&M University (2020-2021), p. V-58.

[2] Struck Innovative Systems, https://struck.de/sis3316.html.

[3] A. Hannaman *et al.*, *Progress in Research*, Cyclotron Institute, Texas A&M University (2021-2022), p. II-19.
[4] Z. Tobin *et al.*, *Progress in Research*, Cyclotron Institute, Texas A&M University (2021-2022), p. II-6.
[5] M. Sorensen *et al.*, *Progress in Research*, Cyclotron Institute, Texas A&M University (2021-2022), p. IV-43.
[6] R.P. Schmitt *et al.*, Nucl. Instrum. Methods Phys. Res. **A354**, 487 (1995).
[7] U. Jahnke *et al.*, Nucl. Instrum. Methods Phys. Res. **A508**, 295 (2003).

SECTION V

PUBLICATIONS

PAPERS PUBLISHED
April 1, 2022– March 31, 2023

K^{*0} production in Au+Au collisions at √sNN = 7.7, 11.5, 14.5, 19.6, 27 and 39 GeV from the RHIC beam energy scan, M.S. Abdallah, D.M. Anderson, J. Atchison, C.A. Gagliardi, A. Hamed, T. Lin, X. Liu, Y. Liu, S. Mioduszewski, N.R. Sahoo, and R.E. Tribble, Phys. Rev. C **107**, 034907 (2023).

Apparent temperatures of neutron-poor and neutron-rich compound nuclei, A.B. McIntosh, K. Hagel, L. A. McIntosh, R. Wada, J. Gauthier, P.J. Cammarata, A. Keeler, A. Abbott, A. Hannaman, B. Harvey, A. Jedele, Y.W. Lui, L.W. May, M. Sorensen, M. Youngs, A. Zarrella, and S.J. Yennello, Phys. Rev. C **107**, 024612 (2023).

Azimuthal anisotropy measurement of (multi)strange hadrons in Au + Au collisions at √sNN = 54.4 GeV, M.S. Abdallah, D.M. Anderson, J. Atchison, C.A. Gagliardi, A. Hamed, T. Lin, X. Liu, Y. Liu, S. Mioduszewski, N.R. Sahoo, and R.E. Tribble, Phys. Rev. C **107**, 024912 (2023).

Beam energy dependence of fifth- and sixth-order net-proton number fluctuations in Au+Au collisions at RHIC, B.E. Aboona, D.M. Anderson, J. Atchison, C.A. Gagliardi, A. Hamed, T. Lin, X. Liu, Y. Liu, S. Mioduszewski, N.R. Sahoo, and R.E. Tribble, Phys. Rev. Lett. **130**, 082301 (2023).

Determining the nuclear temperature dependence on source neutron-proton asymmetry in heavy-ion reactions at intermediate energy, G. Qu, Y. Huang, H. Zheng, X.Q. Liu, R. Wada, W.P Lin, M. Huang, J. Han, P.P. Ren, Z.Yang, X. Zhang, and Q. Leng, Chinese Phys. C **47**, 054002 (2023).

FITEVT: A FORTRAN program for arrival-time analysis of nuclear-decay events, V. Horvat, Comput. Phys. Communications **284**, 108600 (2023).

High event rate analysis technique for the dual-axis duo-lateral position-sensitive silicon detectors of FAUST, A. Hannaman, A.B. McIntosh, K. Hagel, B. Harvey, S. Regener, A. Abbott, J. Gauthier, T. Hankins, Y.W. Lui, L. McCann, L.A. McIntosh, R. Rider, S. Schultz, M.Q. Sorensen, Z.N. Tobin, R. Wada, and S.J. Yennello, Nucl. Instrum. Methods Phys. Res. **1050**, 168130 (2023).

Higher-order cumulants and correlation functions of proton multiplicity distributions in √sNN = 3 GeV Au+Au collisions at the RHIC STAR experiment, M.S. Abdallah, D.M. Anderson, J. Atchison, C. A. Gagliardi, A. Hamed, T. Lin, X. Liu, Y. Liu, S. Mioduszewski, N.R. Sahoo, and R.E. Tribble, Phys. Rev. C **107**, 024908 (2023).

Investigating the time dependence of neutron-proton equilibration using molecular dynamics simulations, A. Jedele, K. Hagel, M.Q. Sorensen, B. Harvey, A. Abbott, J. Gauthier, A. Hannaman, A.A. Hood, Y.W. Lui, L. McCann, A.B. McIntosh, L.A. McIntosh, S. Schultz, Z. Tobin, R. Wada, M. Youngs and S. Yennello, Phys. Rev. C **107**, 024601 (2023).

Measurement of Sequential YY Suppression in Au+Au Collisions at √sNN = 200 GeV with the STAR Experiment, B.E. Aboona, D.M. Anderson, J. Atchison, C.A. Gagliardi, A. Hamed, T. Lin, X. Liu, Y. Liu, S. Mioduszewski, N.R. Sahoo, and R.E. Tribble, Phys. Rev. Lett. **130**, 112301 (2023).

Nondestructive and destructive assay for forensics characterization of weapons-grade plutonium produced in LEU irradiated in a thermal neutron spectrum, S.P. Martinson, J.R. Garcia, I.W. Haynes, S.P. Saini, E.R. Wagner, G.R. Long, C.M. Folden III, and S.S. Chirayath, Ann. Nucl. Energy **183**, 109645 (2023).

Nuclear Data Sheets for A=141, N. Nica, Nucl. Data Sheets **187**, 1 (2023).

Pair production as a probe for the dynamics of nuclear fission and α decay, T. Settlemyre, H. Zheng and A. Bonasera, Phys. Rev. C **107**, L031301 (2023).

Pattern of global spin alignment of ϕ and K^{*0} mesons in heavy-ion collisions, M.S. Abdallah, D.M. Anderson, C.A. Gagliardi, A. Hamed, T. Lin, X. Liu, Y. Liu, S. Mioduszewski, N.R. Sahoo, and R.E. Tribble, Nature **614**, 244 (2023).

Potential experimental evidence of an Efimov state in ^{12}C and its influence on astrophysical carbon creation, G. Cardella, A. Bonasera, S.M. Nunzia, L. Acosta, E.D. Filippo, E. Geraci, B. Gnoffo, C. Guazzoni, C. Maiolino, A. Pagano, V.P. Emanuele, M. Papa, S. Pirrone, G. Politi, F. Risitano, F. Rizzo, P. Russotto, and M. Trimarchi, Nucl. Phys. in Astrophysics – X (NPA-X 2022), {EPJ} Web of Conferences **279**, pages 03001, {EDP} Sciences, (2023).

Progress on nuclear reaction rates affecting the stellar production of ^{26}Al, A.M. Laird, M. Lugaro, A. Kankainen, P. Adsley, D.W. Bardayan, H.E. Brinkman, B. Côté, C.M. Deibel, R. Diehl, F. Hammache, J.W. den Hartogh, J. José, D. Kurtulgil, C. Lederer-Woods, G. Lotay, G. Meynet, S. Palmerini, M. Pignatari, R. Reifarth, N. Séréville, A. Sieverding, R.J. Stancliffe, T.C.L. Trueman, T. Lawson, J.S. Vink, C. Massimi, and A. Mengoni, J. Phys. G **50**, 033002 (2023).

Resonances in low-energy nuclear processes and nuclear astrophysics and asymptotic normalization coefficients: a review, A.M. Mukhamedzhanov, Eur. Phys. J. A **59**, 56 (2023).

Search for the chiral magnetic effect in Au + Au collisions at √sNN = 27 GeV with the STAR forward event plane detectors, B.E. Aboona, D.M. Anderson, J. Atchison, C.A. Gagliardi, A. Hamed, T. Lin, X. Liu, Y. Liu, S. Mioduszewski, N.R. Sahoo, and R.E. Tribble, Phys. Lett. B **839**, 137779 (2023).

Tomography of ultrarelativistic nuclei with polarized photon-gluon collisions, M.S. Abdallah and C. A. Gagliardi, Sci. Adv. **9**, eabq3903 (2023).

Transfer Reactions in Nuclear Astrophysics, P. Adsley, in: European Summer school on Nuclear Astrophysics, {EPJ} Web of Conferences **275**, Catania, pages 01001, {EDP} Sciences, (2023).

β-delayed charged-particle decay of ^{22,23}Si, A.A. Ciemny, C. Mazzocchi, W. Dominik, A. Fijałkowska, J. Hooker, C. Hunt, H. Jayatissa, Ł. Janiak, G. Kamiński, E. Koshchiy, M. Pfützner, M. Pomorski, B. Roeder, G.V. Rogachev, A. Saastamoinen, S. Sharma, N. Sokołowska, W. Satuła, and J. Singh, Phys. Rev. C **106**, 014317 (2022).

A new ^{12}C+^{12}C nuclear reaction rate: Impact on stellar evolution, E. Monpribat, S. Martinet, S. Courtin, M. Heine, S. Ekström, D.G. Jenkins, A. Choplin, P. Adsley, D. Curien, M. Moukaddam, J. Nippert, S. Tsiatsiou, and G. Meynet, Astronomy & Astrophys. **660**, A47 (2022).

A new reaction rate of the ^{27}Al(p/α)^{24}Mg reaction based on indirect measurements at astrophysical energies and implications for ^{27}Al yields of intermediate-mass stars, M.L. Cognata, S. Palmerini, P. Adsley, F. Hammache, A.D. Pietro, P. Figuera, F. Dell'Agli, R. Alba, S. Cherubini, G.L. Guardo, M. Gulino, L. Lamia, D. Lattuada, C. Maiolino, A. Oliva, R.G. Pizzone, P.M. Prajapati, G.G. Rapisarda, S. Romano, D. Santonocito, R. Spartá, M.L. Sergi, A. Tumino, and P. Ventura, The Astrophysical J. **941**, 96 (2022).

Alpha-cluster structure of ^{18}Ne, M. Barbui, A. Volya, E. Aboud, S. Ahn, J. Bishop, V.Z. Goldberg, J. Hooker, C.H. Hunt, H. Jayatissa, T.Z. Kokalova, E. Koshchiy, S. Pirrie, E. Pollacco, B.T. Roeder, A. Saastamoinen, S. Upadhyayula, C. Wheldon, and G.V. Rogachev, Phys. Rev. C **106,** 054310 (2022).

Angular correlation between the fission fragment intrinsic spins, A. Bulgac, Phys. Rev. C **106**, 014624 (2022).

Angular momentum eigenstates of the isotropic 3-D harmonic oscillator: Phase-space distributions and coalescence probabilities, M. Kordell, R.J. Fries, and C.M Ko, Annals of Phys. **443**, 168960 (2022).

Azimuthal transverse single-spin asymmetries of inclusive jets and identified hadrons within jets from polarized *pp* collisions at √s =200 GeV, M.S. Abdallah, D.M. Anderson, J. Atchison, C.A. Gagliardi, A. Hamed, T. Lin, X. Liu, Y. Liu, S. Mioduszewski, N.R. Sahoo, and R.E. Tribble, Phys. Rev. D **106**, 072010 (2022).

Centrality and transverse-momentum dependence of higher-order flow harmonics of identified hadrons in Au + Au collisions at √sNN = 200 GeV, M.S. Abdallah, D.M. Anderson, C.A. Gagliardi, A. Hamed, T. Lin, X. Liu, Y. Liu, S. Mioduszewski, N.R. Sahoo, and R.E. Tribble, Phys. Rev. C **105**, 064911 (2022).

Characterization and description of a spectrum unfolding method for the CATRiNA neutron detector array, A.B. Morelock, J.F. Perello, S.A. Calderon, B.W. Asher, K. Brandenburg, J. Derkin, G. Hamad, Y.J.

Alberty, E.L. Saavedra, T. Massey, Z. Meisel, N. Singh, D. Soltesz, S.K. Subedi, A. Voinov, and J. Warren, Nucl. Instrum. Methods Phys. Res. **A1034**, 166759 (2022).

Charged pion production from Au + Au collisions at √sNN = 2.4~GeV in the relativistic Vlasov-Uehling-Uhlenbeck model, K. Godbey, Z. Zhang, J.W. Holt, and C.M. Ko, Phys. Lett. B **829,** 137134 (2022).

Collectivity of J/ψ Mesons in Heavy-Ion Collisions, M. He, B. Wu, and R. Rapp, Phys. Rev. Lett. **128**, 162301 (2022).

Compact automated apparatus for rapid astatine recovery from nitric acid media: Design, application, and impurity characterization, E.E. Tereshatov, J.D. Burns, S.J. Schultz, L.A. McCann, L.A. McIntosh, G.C. Tabacaru, M. Berko, E. Engelthaler, A. Hannaman, B. Harvey, K. Lofton, A. Tabacaru, Z. Tobin, and S.J. Yennello, Chemical Engineering Journal **442**, 136176 (2022).

Comparison of ^{10}B+^{6}Li and ^{10}B+^{7}Li elastic scattering: The role of ground state reorientation and breakup, A.T. Rudchik, A.A. Rudchik, O.O. Chepurnov, K.W. Kemper, N. Keeley, K. Rusek, E.I. Koshchy, S. Kliczewski, S.Y. Mezhevych, V.M. Pirnak, O.A. Ponkratenko, R. Siudak, H.M. Maridi, A. P. Ilyin, B.V. Mishchenko, Y.M. Stepanenko, V.V. Uleshchenko, Y.O. Shyrma, K.A. Chercas, and B. Zalewski, Phys. Rev. C **106**, 014615 (2022).

Complexation of Astatine(III) with Ketones: Roles of NO^-_3 Counterion and Exploration of Possible Binding Modes, J.D. Burns, E.E. Tereshatov, B. Zhang, G.C. Tabacaru, L.A. McIntosh, S.J. Schultz, L.A. McCann, B.M. Harvey, A. Hannaman, K.N. Lofton, M.Q. Sorensen, A. L. Vonder Haar, M.B. Hall, and S.J. Yennello, Inorganic Chemistry **61**, 12087 (2022).

Constraints on key ^{17}O(α, γ)^{21} resonances and impact on the weak *s* process, M. Williams, A.M. Laird, A. Choplin, P. Adsley, B. Davids, U. Greife, K. Hudson, D. Hutcheon, A. Lennarz, and C. Ruiz, Phys. Rev. C **105**, 065805 (2022).

Determination of asymptotic normalization coefficients for the channel ^{16}O→α+^{12}C: excited state ^{16}O(0$^+$;6.05 MeV), L.D. Blokhintsev, A.S. Kadyrov, A.M. Mukhamedzhanov, and D.A. Savin, The European Physical J. A **58**, 1 (2022).

Differential measurements of jet substructure and partonic energy loss in Au + Au collisions at √sNN = 200 GeV, M.S. Abdallah, D.M. Anderson, C.A. Gagliardi, A. Hamed, T. Lin, X. Liu, Y. Liu, S. Mioduszewski, N.R. Sahoo, and R.E. Tribble, Phys. Rev. C **105**, 044906 (2022).

Dilepton signature of a first-order phase transition, F. Seck, T. Galatyuk, A. Mukherjee, R. Rapp, J. Steinheimer, J. Stroth, and M. Wiest, Phys. Rev. C **106**, 014904 (2022).

Disappearance of partonic collectivity in √sNN = 3 GeV Au+Au collisions at RHIC, M.S. Abdallah, D.M. Anderson, C.A. Gagliardi, A. Hamed, T. Lin, X. Liu, Y. Liu, S. Mioduszewski, N.R. Sahoo, and R.E. Tribble, Phys. Lett. B **827,** 137003 (2022).

Evidence for nonlinear gluon effects in QCD and their mass number Dependence at STAR, M.S. Abdallah, D.M. Anderson, C.A. Gagliardi, A. Hamed, T. Lin, X. Liu, Y. Liu, S. Mioduszewski, N.R. Sahoo, and R.E. Tribble, Phys. Rev. Lett. **129**, 092501 (2022).

Evidence of mass ordering of charm and bottom quark energy loss in Au + Au collisions at RHIC, M.S. Abdallah, D.M. Anderson, J. Atchison, C.A. Gagliardi, A. Hamed, T. Lin, X. Liu, Y. Liu, S. Mioduszewski, N.R. Sahoo, and R.E. Tribble, The European Physical J. C **82,** 1150 (2022).

Evolution of the isoscalar giant monopole resonance in the Ca isotope chain, S.D. Olorunfunmi, R. Neveling, J. Carter, P. Neumann-Cosel, I.T. Usman, P. Adsley, A. Bahini, L.P.L. Baloyi, J.W. Brümmer, L.M. Donaldson, H. Jivan, N.Y. Kheswa, K.C.W. Li, D.J. Marín-Lámbarri, P.T. Molema, C.S. Moodley, G.G. O'Neill, P. Papka, L. Pellegri, V. Pesudo, E. Sideras-Haddad, F.D. Smit, G.F. Steyn, A.A. Avaa, F. Diel, F. Dunkel, P. Jones, and V. Karayonchev, Phys. Rev. C **105**, 054319 (2022).

Extending the Hoyle-State Paradigm to $^{12}C+^{12}C$ Fusion, P. Adsley, M. Heine, D.G. Jenkins, S. Courtin, R. Neveling, J.W. Brümmer, L.M. Donaldson, N.Y. Kheswa, K.C.W. Li, D.J. Marín-Lámbarri, P.Z. Mabika, P. Papka, L. Pellegri, V. Pesudo, B. Rebeiro, F.D. Smit, and W. Yahia-Cherif, Phys. Rev. Lett. **129,** 102701 (2022).

High and low energy nucleon productions in intermediate heavy ion collisions, R. Wada, Q. Hu, G. Tian, W. Lin, Z. Chen, R. Han, X. Liu, M. Huang and H. Zheng, in: IWM-EC2021, Il Nuovo Cimento C **45,** Ganil, France, pages Jun, SIF, (2022).

High-energy-density plasma in femtosecond-laser-irradiated nanowire-array targets for nuclear reactions, D. Kong, G. Zhang, Y. Shou, S. Xu, Z. Mei, Z. Cao, Z. Pan, P. Wang, G. Qi, Y. Lou, Z. Ma, H. Lan, W. Wang, Y. Li, P. Rubovic, M. Veselský, A. Bonasera, J. Zhao, Y. Geng, Y. Zhao, C.B. Fu, W. Luo, Y.G. Ma, X. Yan, and W. Ma, Matter and Radiation at Extremes **7,** 064403 (2022).

Horizons: nuclear astrophysics in the 2020s and beyond, H. Schatz, P. Adsley, A. Banu, J. Bishop, H. Jayatissa, A. Kwiatkowski, A. Simon, A. Spiridon, L. Trache, and S. Upadhyayula, Journal of Phys. G: Nuclear and Particle Physics **49,** 110502 (2022).

Investigating the possible existence of hyper-heavy nuclei in a neutron-star environment, M. Veselsky, V. Petousis, Ch. C. Moustakidis, G. A. Souliotis and A. Bonasera, Phys. Rev. C **106,** L012802 (2022).

Investigating the predicted breathing-mode excitation of the Hoyle state, K.C.W. Li, F.D. Smit, P. Adsley, R. Neveling, P. Papka, E. Nikolskii, J.W. Brümmer, L.M. Donaldson, M. Freer, M.N. Harakeh, F.

Nemulodi, L. Pellegri, V. Pesudo, M. Wiedeking, E.Z. Buthelezi, V. Chudoba, S.V. Förtsch, P. Jones, M. Kamil, J.P. Mira, G.G. O'Neill, E. Sideras-Haddad, B. Singh, S. Siem, G.F. Steyn, J.A. Swartz, I.T. Usman, and J.J. Van Zyl, Phys. Lett. B **827**, 136928 (2022).

Investigation of sCVD diamond detectors for low energy heavy-ion reactions, A. Abbott, M. Sorensen, Z. Tobin, A.B. McIntosh, A. Hannaman, J. Gauthier, K. Hagel, B. Harvey, A. Hood, A. Jedele, Y.W. Lui, L. McCann, L.A. McIntosh, S. Schultz, R. Wada, A. Wakhle, M. Youngs, and S.J. Yennello, Nuclear Instruments and Methods in Physics Research Section A: Accelerators, Spectrometers, Detectors and Associated Equipment **1034**, 166796 (2022).

Level density within a micro-macroscopic approach, A.G. Magner, A.I. Sanzhur, S.N. Fedotkin, A.I. Levon, and S. Shlomo, Nucl. Phys. **A1021**, 122423 (2022).

Light nuclei collectivity from √sNN = 3 GeV Au + Au collisions at RHIC, M.S. Abdallah, D.M. Anderson, C.A. Gagliardi, A. Hamed, T. Lin, X. Liu, Y. Liu, S. Mioduszewski, N.R. Sahoo, and R.E. Tribble, Phys. Lett. B **827**, 136941 (2022).

Longitudinal double-spin asymmetry for inclusive jet and dijet production in polarized proton collisions at √sNN = 510 GeV, M.S. Abdallah, D.M. Anderson, C.A. Gagliardi, A. Hamed, T. Lin, X. Liu, Y. Liu, S. Mioduszewski, N.R. Sahoo, and R.E. Tribble, Phys. Rev. D **105,** 092011 (2022).

Measurement of 4ΛH and 4ΛHe binding energy in Au+Au collisions at √sNN = 3 GeV, M.S. Abdallah, D.M. Anderson, J. Atchison, C.A. Gagliardi, A. Hamed, T. Lin, X. Liu, Y. Liu, S. Mioduszewski, N.R. Sahoo, and R.E. Tribble, Phys. Lett. B **834**, 137449 (2022).

Measurement of fusion-evaporation cross sections for reactions of ^{44}Ca with ^{154,156,157,160}Gd targets, T.A. Werke, C.S. Salas, K.J. Glennon, D.A. Mayorov, E.E. Tereshatov, M.F. Volia, D.M. Wright, and C.M. Folden, III, Phys. Rev. C **106,** 054615 (2022).

Measurement of the ^{18}Ne(α,p)^{21}Na reaction with the ANASEN active-target detector system at $E_{c.m.}$ = 2.5 − 4 MeV, M. Anastasiou, I. Wiedenhöver, J.C. Blackmon, L.T. Baby, D.D. Caussyn, A.A. Hood, E. Koshchiy, J.C. Lighthall, K.T. Macon, J.J. Parker, T. Rauscher, and N. Rijal, Phys. Rev. C **105,** 055806 (2022).

Measurements of 3ΛH and 4ΛH Lifetimes and Yields in Au + Au Collisions in the High Baryon Density Region, M.S. Abdallah, D.M. Anderson, C.A. Gagliardi, A. Hamed, T. Lin, X. Liu, Y. Liu, S. Mioduszewski, N.R. Sahoo, and R.E. Tribble, Phys. Rev. Lett. **128,** 202301 (2022).

Measurements of Proton High Order Cumulants in √sNN = 3 GeV Au + Au Collisions and Implications for the QCD Critical Point, M.S. Abdallah, D.M. Anderson, C.A. Gagliardi, A. Hamed, T. Lin, X. Liu, Y. Liu, S. Mioduszewski, N.R. Sahoo, and R.E. Tribble, Phys. Rev. Lett. **128,** 202303 (2022).

Microscopic-macroscopic level densities for low excitation energies, A.G. Magner, A.I. Sanzhur, S.N. Fedotkin, A.I. Levon, U.V. Grygoriev, and S. Shlomo, Low Temperature Phys. **48**, 920 (2022).

Neutron-upscattering enhancement of the triple-alpha process, J. Bishop, C.E. Parker, G.V. Rogachev, S. Ahn, E. Koshchiy, K. Brandenburg, C.R. Brune, R.J. Charity, J. Derkin, N. Dronchi, G. Hamad, Y.J. Alberty, T. Kokalova, T.N. Massey, Z. Meisel, E.V. Ohstrom, S.N. Paneru, E.C. Pollacco, M. Saxena, N. Singh, R. Smith, L.G. Sobotka, D. Soltesz, S.K. Subedi, A.V. Voinov, J. Warren, and C. Wheldon, Nature Communications **13,** 7 (2022).

New narrow resonances observed in the unbound nucleus ^{15}F, V.G. Alcindor, A. Mercenne, I. Stefan, F.D.O. Santos, N. Michel, M. Płoszajczak, M. Assié, A. Lemasson, E. Clément, F. Flavigny, A. Matta, D. Ramos, M. Rejmund, J. Dudouet, D. Ackermann, P. Adsley, M. Assunção, B. Bastin, D. Beaumel, G. Benzoni, R. Borcea, A.J. Boston, D. Brugnara, L. Caceres, B. Cederwall, I. Celikovic, V. Chudoba, M. Ciemala, J. Collado, F.C.L. Crespi, G. D'Agata, G.D France, F. Delaunay, C. Diget, C.D. Pardo, J. Eberth, C. Fougères, S. Franchoo, F. Galtarossa, A. Georgiadou, J. Gibelin, S. Giraud, V. González, N. Goyal, A. Gottardo, J. Goupil, S. Grévy, V. Guimarães, F. Hammache, L.J.H. Brennan, H. Hess, N. Jovančević, D.S.J. Oliver, O. Kamalou, A. Kamenyero, J. Kiener, W. Korten, S. Koyama, M. Labiche, L. Lalanne, V. Lapoux, S. Leblond, A. Lefevre, C. Lenain, S. Leoni, H. Li, A.L. Martens, A. Maj, I. Matea, R. Menegazzo, D. Mengoni, A. Meyer, B. Million, B. Monteagudo, P. Morfouace, J. Mrazek, M. Niikura, J. Piot, Z. Podolyák, C. Portail, A. Pullia, B. Quintana, F. Recchia, P. Reiter, K. Rezynkina, T. Roger, J. S. Rojo, F. Rotaru, M.D. Salsac, A.M.S. Benítez, E. Sanchis, M. Şenyigit, N.D. Séréville, M. Siciliano, J. Simpson, D. Sohler, O. Sorlin, M. Stanoiu, C. Stodel, D. Suzuki, C. Theisen, D. Thisse, J.C. Thomas, P. Ujic, J.J.V. Dobón, and M. Zielińska, Phys. Rev. C **105,** L051301 (2022).

Non-equilibrium charmonium regeneration in strongly coupled quark-gluon plasma, X. Du and R. Rapp, Physics Letters B **834,** 137414 (2022).

Pair invariant mass to isolate background in the search for the chiral magnetic effect in Au+Au collisions at √sNN = 200 GeV, M.S. Abdallah, D.M. Anderson, C.A. Gagliardi, A. Hamed, T. Lin, X. Liu, Y. Liu, S. Mioduszewski, N.R. Sahoo, and R.E. Tribble, Phys. Rev. C **106,** 034908 (2022).

Probing strangeness canonical ensemble with K^-, $\phi(1020)$ and Ξ^- production in Au + Au collisions at √sNN = 3 GeV, M.S. Abdallah, D.M. Anderson, C.A. Gagliardi, A. Hamed, T. Lin, X. Liu, Y. Liu, S. Mioduszewski, N.R. Sahoo, and R.E. Tribble, Physics Letters B **831,** 137152 (2022).

Projections of two-particle correlations onto transverse rapidity in Au+Au collisions at √sNN = 200 GeV at STAR, M.S. Abdallah, D.M. Anderson, C.A. Gagliardi, A. Hamed, T. Lin, X. Liu, Y. Liu, S. Mioduszewski, N.R. Sahoo, and R.E. Tribble, Phys. Rev. C **106,** 044906 (2022).

Proton and neutron exchange as a prelude to fusion at near-barrier energies, J.E. Johnstone, V. Singh, R. Giri, S. Hudan, J. Vadas, R.T.D. Souza, D. Ackermann, A. Chbihi, Q. Hourdille, A. Abbott, C. Balhoff, A. Hannaman, A.B. McIntosh, M. Sorensen, Z. Tobin, A. Wakhle, S.J. Yennello, M.A. Famiano, K.W. Brown, C. Santamaria, J. Lubian, H.O. Soler, and B.V. Carlson, Phys. Rev. C **106,** L011603 (2022).

Search for rare 3-α decays in the region of the Hoyle state of ^{12}C, G. Cardella, A. Bonasera, N.S. Martorana, L. Acosta, E.D. Filippo, E. Geraci, B. Gnoffo, C. Guazzoni, L.L. Monaco, C. Maiolino, A. Pagano, E.V. Pagano, M. Papa, S. Pirrone, G. Politi, F. Risitano, F. Rizzo, P. Russotto, and M. Trimarchi, Nucl. Phys. **A1020**, 122395 (2022).

Sensitivity of time-dependent density functional theory to initial conditions, A. Bulgac, I. Abdurrahman, and G. Wlazłowski, Phys. Rev. C **105,** 044601 (2022).

Status of deep subbarrier ^{12}C+^{12}C fusion and advancing the Trojan horse method, A.M. Mukhamedzhanov, The European Physical J. A **58**, 6 (2022).

Superradiance in alpha clustered mirror nuclei, A. Volya, M. Barbui, V.Z. Goldberg, and G.V. Rogachev, Com. Phys. **5,** 322 (2022).

Temperatures of compound nuclei produced in complete and incomplete fusion and the role of neutron excess, A.B. McIntosh, K. Hagel, L.A. McIntosh, and S.J. Yennello, in: International Workshop on the Multi-facets of the Equation of state and Clustering, Il Nuovo Cimento C **45,** GANIL, Caen, France, pages May, SIF, (2022).

The impact of ^{17}O+α reaction rate uncertainties on the *s*-process in rotating massive stars, J. Frost-Schenk, P. Adsley, A.M. Laird, R. Longland, C. Angus, C. Barton, A. Choplin, C.A. Diget, R. Hirschi, C. Marshall, F.P. Chaves, and K. Setoodehnia, Monthly Notices of the Royal Astronomical Society **514,** 2650--2657 (2022).

The Novel Scaling of Tsallis Parameters from the Transverse Momentum Spectra of Charged Particles in Heavy-Ion Collisions, J.Q. Tao, W. Wu, M. Wang, H. Zheng, W.C. Zhang, L. Zhu, and A. Bonasera, Particles **5**, 146 (2022).

Thermalization of nuclear matter in heavy-ion collisions at Fermi energies, T. Onyango, A. Bonasera, and R. Rapp, Nucl. Phys. **A1022,** 122426 (2022).

Thick target neutron yields from Beryllium, Carbon, Tungsten, and Lead targets irradiated by 26.7 MeV/nucleon ^{4}He ions, X. Zhang, Z. Chen, R. Wada, R. Han, G. Tian, B. Liu, F. Shi, and H. Sun, Nucl. Instrum. Methods Phys. Res. **B516**, 48 (2022).

SECTION VI

APPENDIX

TALKS PRESENTED
April 1, 2022 – March 31, 2023

The development of TexNeut and Spectroscopy of ^{10}Li using Isobaric Analogue States, **D. Scriven**, **Talk**, Lawrence-Livermore National Lab, Livermore, California (March 2023).

Data Needs & Capabilities for TAMU: Capabilities for ^{149}Tb production, **A. McIntosh**, **Talk**, Workshop for Applied Nuclear Data Activities (WANDA), Washington D.C. (March 2023).

Exploring sub-barrier fusion reaction, **A. Bonasera**, **Talk**, Frontiers, http://imp.fudan.edu.cn/1002xshd/list.htm, zoom meeting, Shanghai, China (February 2023).

Photon Production in Fermi-Energy Heavy-Ion Collisions, **T. Onyango**, **Talk**, Stewardships Science Academic Programs Symposium , Santa Fe, New Mexico (February 2023).

Photon Strength Function of ^{58}Fe Using DAPPER and The Oslo Method, **A. Abbott**, **Talk**, 2023 Stewardship Science Academic Programs Symposium, Santa Fe, New Mexico (February 2023).

β decay as a probe of new physics: an overview of the fundamental symmetries research at the CI, **D. Melconian**, **Invited Seminar**, UT Knoxville Physics Seminar, University of Tennessee Knoxville, Knoxville, Tennessee (February 2023).

Astatine and bismuth behavior in the presence of ionic liquids, **E. Tereshatov**, **Talk**, 5th International Conference on Ionic Liquids in Separation and Purification Technology, Scottsdale, Arizona (February 2023).

Neutron-upscattering enhancement of the triple-alpha process, **J. Bishop**, IReNA **Online Seminar Series**, Online (February 2023).

Photon strength function of ^{58}Fe using DAPPER and the Oslo method, **A. Abbott**, **Talk**, 2023 DOE Review Visit, Texas A&M University, College Station, Texas (January 2023).

Neutron-upscattering enhancement of the triple-alpha process, **J. Bishop, Talk**, ECT* Workshop on "Key Reactions in Nuclear Astrophysics", ECT*, Trento, Italy (December 2022).

Precision β decay: nuclei, **D. Melconian**, **Invited Talk**, Fundamental symmetries LRP Town Hall Meeting, University of North Carolina, Chapel Hill, North Carolina (December 2022).

Calculation of light nuclei sub-barrier fusion cross section in an imaginary time-dependent mean field theory, **A. Bonasera**, **Invited Talk**, Key Reactions in Nuclear Astrophysics – KRINA22, ECT*, Trento, Italy (December 2022).

Signatures of short-range correlations in intermediate energy heavy ion collisions, **K. Hagel**, **Invited Talk**, 22nd Zimányi Winter Workshop on Heavy Ion Physics, Wigner Research Center for Physics, Budapest, Hungary (December 2022).

Precision internal conversion coefficients measurements for US nuclear data program, **N. Nica**, **Talk**, NSAC Long Range Plan Town Hall Meeting on Nuclear Structure, Reactions and Astrophysics, Argonne National Laboratory, Lemont, Illinois (November 2022).

Technical developments for fundamental symmetry measurements, **D. Melconian**, **Invited Talk**, Nuclear Structure Town Hall Meeting, Argonne National Laboratory, Argonne, Illinois (November 2022).

Future indirect approaches at Texas A&M, **J. Bishop**, **Talk**, NSAC Long Range Plan Town Hall Meeting on Nuclear Structure, Reactions, and Astrophysics, Virtual (November 2022).

Texas A&M University US nuclear data program Texas A&M evaluation center report 2022, **N. Nica**, **Talk**, National Nuclear Data Center, Brookhaven National Laboratory, Upton, New York (November 2022).

Overview of radiochemistry at Texas A&M University, **E. Tereshatov**, **Talk**, LRC Seminar, Virtual, Paul Scherrer Institute, Villigen, Switzerland (November 2022).

Progress in Research, **J. Mildon**, **Talk**, TAMU, College Station, Texas (November 2022).

Development of a methodology for the radiochronometric analysis of a radium pigment sample for nuclear forensics, **J. Garcia**, **Talk**, Progress in Research, Texas A&M University, College Station, Texas (November 2022).

Graduate Program at Texas A&M University Cyclotron Institute, **L. McIntosh**, **Talk**, CAARI-SNEAP 2022, Denton, Texas (November 2022).

Investigating low energy heavy-ion response of sCVD diamond detectors, **A. Abbott**, **Talk**, 2022 CAARI-SNEAP, Denton, Texas (November 2022).

Undergraduate research at the Cyclotron Institute at Texas A&M, **L. McIntosh**, **Talk**, CAARI-SNEAP 2022, Denton, Texas (October 2022).

Radiation effects facility at the Texas A&M University Cyclotron Institute, **C. Parker**, **Talk**, CAARI-SNEAP 2022, Denton, Texas (October 2022).

Coarse graining of heavy-ion collisions at Fermi energy, **T. Onyango**, **Talk**, Division of Nuclear Physics American Physical Society, New Orleans, Louisiana (October 2022).

Investigating resonant state modification with a Coulomb trajectory model, **T. Hankins**, **Talk**, Division of Nuclear Physics (DNP), New Orleans, Louisiana (October 2022).

Toward the future: Upgrading the 6He-CRES experiment with an ion trap, **D. McClain**, **Talk**, 2022 Fall Meeting of the APS Division of Nuclear Physics, New Orleans, Louisiana (October 2022).

Neutron-upscattering enhancement of the triple-alpha process, **J. Bishop**, **Talk**. Fall 2022 Meeting of the APS Division of Nuclear Physics, New Orleans, Louisiana (October 2022).

Understanding globular cluster pollution through nuclear reactions, **P. Adsley**, **Talk**, APS DNP Meeting, New Orleans, Louisiana (October 2022).

Expanding RIB capabilities at the Cyclotron Institute: 3He-LIG production with an Isobar Separator LSTAR, **D. Melconian**, **Talk**, APS DNP, New Orleans, Louisiana (October 2022).

Apparent temperatures of neutron-poor and neutron-rich compound nuclei, **A. McIntosh**, **Talk**, Annual Meeting of the Division of Nuclear Physics of the American Physical Society, New Orleans, Louisiana (October 2022).

Horizon-broadening isotope production pipeline opportunities (HIPPO) program, **L. McIntosh**, **Talk**, 2022 Fall Meeting of the APS Division of Nuclear Physics, New Orleans, Louisiana (October 2022).

Educational impact of ARUNA labs, **L. McIntosh**, **Talk**, ARUNA Town Hall Meeting, New Orleans, Louisiana (October 2022).

Studying structure of ^{10}Li by ^{9}Li(p,p)^{9}Li of T=2 isobaric analogue states in ^{10}Be, **D. Scriven**, **Talk**, American Physical Society Division of Nuclear Physics, New Orleans, Louisiana (October 2022).

Evaluation issues, **N. Nica, Talk**, Technical Meeting of the Nuclear Structure and Decay Data Network, Australia National University , Canberra, Australia (October 2022).

TAMU NSDD evaluation center report 2021-2022, **N. Nica**, **Talk**, Technical Meeting of the Nuclear Structure and Decay Data Network, Australia National University, Canberra, Australia (October 2022).

Automated purification and study of fundamental properties of medical radioisotope Astatine-211 by solvent extraction from nitric acid media, **E. Tereshatov**, **Talk**, International Solvent Extraction Conference, Chalmers University of Technology, Göteborg, Sweden (September 2022).

Signatures of short-range correlations in collisions of 47 MeV/u projectiles, **K. Hagel**, **Talk**, NuSym22, X International Symposium on Nuclear Symmetry Energy, INFN Catania, Catania, Italy (September 2022).

Chromatography study of fundamental properties of medical radioisotope Astatine-211, **E. Tereshatov**, **Talk**, 33rd International Symposium on Chromatography, Budapest, Hungary (September 2022).

Understanding globular cluster pollution through nuclear reactions, **P. Adsley**, **Talk**, International Nuclear Physics Conference 2022, Cape Town, WC, South Africa (September 2022).

S*teps forward in Astatine-211 production and chemistry at Texas A&M University*, **L. McIntosh**, **Talk**, DOE Isotope Program Astatine-211 Users' Meeting, Knoxville, Tennessee (September 2022).

Dynamics of fusion in laser produced non-equilibrated plasmas, **A. Bonasera**, **Talk**, 2nd International Workshop on Proton-Boron Fusion, Acicastello, Italy (September 2022).

Astatine interaction with ion exchange and extraction chromatography resins in nitric acid media, **E. Tereshatov**, **Talk**, ACS Fall 2022, Chicago (August 2022).

Targetry advancements for Isotope production at Texas A&M, **L. McCann**, **Talk**, WTTC18, Whistler, BC, Canada (August 2022).

Calibrating DAPPER to measure photon strength function of ^{58}Fe using (d,pγ) in inverse kinematics, **A. Abbott**, **Talk**, 2022 CENTAUR SAC Meeting, Lawrence Livermore National Laboratory, Livermore, California, (August 2022).

Metal sorption on functionalized silicon detectors for the future study of meitnerium chemistry, **V. Zakusilova**, **Talk**, CENTAUR Scientific Advisory Committee Meeting, Lawrence Livermore National Laboratory (In-person, poster), Livermore, California (August 2022).

CENTAUR neutron detector update: TexNeut, **D. Scriven**, **Talk**, CENTAUR Scientific Advisory Committee Meeting, Lawrence-Livermore National Lab, Livermore, California (August 2022).

Coarse graining of heavy-ion collisions at Fermi energies, **T. Onyango**, **Talk**, Scientific Advisory Committee meeting for CENTAUR, Lawrence Livermore National Lab, Livermore, California (August 2022).

^{155}Eu fission product analysis, **I. Haynes**, **Talk**, Keepin Nonproliferation Sciences Program, Los Alamos National Laboratory, Los Alamos, New Mexico (August 2022).

ARUNA 2022 update, **P. Adsley**, **Talk**, Low-Energy Community Meeting, Argonne National Laboratory, Chicago, Illinois (August 2022).

Current status and future plans of super heavy element study at Texas A&M University, **E. Tereshatov**, **Talk**, Low Energy Community Meeting 2022, Virtual, Lemont, Illinois (August 2022).

Fission product analysis of ^{155}Eu, **I. Haynes**, **Talk**, Los Alamos National Laboratory C-NR Team Meeting, Los Alamos National Laboratory, Chemistry Division , Los Alamos, New Mexico (July 2022).

Balance function as a unique probe of the quark gluon plasma: experimental overview and outlook, **J. Pan**, **Talk**, WPCF 2022 – 15th Workshop on Particle Correlations and Femtoscopy, Facility for Rare Isotope Beams, East Lansing, Michigan (July 2022).

Alpha-cluster structure of ^{18}Ne, DREB2022, Direct Reactions with Exotic Beams, **M. Barbui**, **Talk**, Santiago de Compostela, Spain (July 2022).

Nuclear astrophysics with Lasers, **A. Bonasera**, **Invited Talk**, The 11th European Summer School on Experimental Nuclear Astrophysics, laboratori nazionali del sud, Catania, Italy (June 2022).

Transfer reactions in nuclear astrophysics, **P. Adsley**, **Invited Talk**, INFN-LNS, Catania, Italy (June 2022).

Automation of astatine recovery from nitric acid media, **E. Tereshatov**, **Talk**, Horizon-broadening Isotope Production Pipeline Opportunities (HIPPO), Texas A&M University, College Station, Texas (June 2022).

Introduction to superheavy elements, **C. Folden III**, **Invited Talk**, Exotic Beam Summer School 2022, Argonne National Laboratory, Argonne, Illinois (June 2022).

Inclusive excellence: You can make a difference, **S. Yennello**, **Invited Talk**, Exotic Beam Summer School, University of Notre Dame, South Bend, Indiana (June 2022).

Developing a methodology for the radiochronometric analysis of radium pigments and paints for nuclear forensics, **J. Garcia**, **Talk**, 2022 University Program Review (UPR), Michigan League, Ann Arbor, Michigan (June 2022).

Alpha-cluster structure of ^{18}Ne, M. Barbui, Cyclotron colloquium, Texas A&M University, College Station, Texas (May 2022).

Fundamental behavior of metals in the presence of non-conventional solvents, **E. Tereshatov**, **Talk**, The 19th Radiochemical Conference - RadChem 2022, Mariánské Lázně, Czech Republic (May 2022).

Metal adsorption on functionalized silicon detectors for the future study of meitnerium chemistry, **V. Zakusilova**, **Talk**, TASCA 22, 19th Workshop on Recoil Separator for Superheavy Element Chemistry & Physics, GSI (Virtual), Darmstadt, Germany (May 2022).

Extracting photon strength function of ^{58}Fe from $^{57}Fe(d,p\gamma)^{58}Fe$ reaction using DAPPER, **A. Abbott**, **Talk**, 8th Workshop on Level Density and Gamma Strength, University of Oslo, Oslo, Norway (May 2022).

Heavy element research at Texas A&M University, **C. Folden III**, **Invited Talk**, 19th Workshop on a Recoil Separator for Superheavy Element Chemistry & Physics, Darmstadt, Germany (May 2022).

RESEARCH PERSONNEL AND ENGINEERING STAFF

April 1, 2022 - March 31, 2023

Faculty and Research Group Leaders

Adsley, Philip – Assist. Prof. of Physics
Bonasera, Aldo - Senior Scientist
Christian, Gregory – Adjunct Professor
Fries, Rainer - Professor of Physics
Folden, III, Charles M. - Assoc.. Prof. of Nuclear Chemistry
Gagliardi, Carl A. - Professor of Physics
Hardy, John C. - Professor Emeritus
Holt, Jeremy - Assist. Professor of Physics
Ko, Che Ming – Professor of Physics
Melconian, Dan - Professor of Physics
Mioduszewski, Saskia - Professor of Physics
Natowitz, J. B. - Professor Emeritus
Rapp, Ralf - Professor of Physics
Rogachev, Grigory - Professor of Physics and Department Head of Physics and Astronomy
Shlomo, Shalom - Senior Scientist
Tribble, Robert E. – Professor Emeritus
Yennello, Sherry J. - Professor of Chemistry, Bright Chair, Director
Youngblood, Dave H. - Professor Emeritus
Zhanov, Akram M. - Senior Scientist

Research Staff

Ärje, Juha – Research Scientist
Barbui, Marina - Assist. Research Scientist
Bishop, Jack - Assistant Research Scientist
Chubaryan, Grigor – Retired on 5/1/2022
Clark, Henry - Accelerator Physicist (50%)
Gauthier, Jerome - Assist. Research Scientist
Goldberg, Vladilen - Research Scientist, Retired
Hagel, John C. - Research Scientist (50%)
Horvat, Vladimir - Research Scientist (50%)
Iacob, Victor - Research Scientist
Kennas, Miltiadis - ???
Koshchiy, Yevgen - Assoc. Research Scientist
Lui, Yiu-Wing - Research Scientist
McIntosh, Alan - Assoc. Res. Scientist
McIntosh, Lauren –Assist. Research Scientist
Nica, Ninel - Associate Research Scientist
Rodrigues, Marcia Dias - Assist. Res. Scientist
Saastamoinen, Antti (50%) – To 10/27/2022
Tereshatov, Evgeny - Assoc. Research Scientist

Accelerator Physics and Radiation Line Staff

Avila, Geoffrey – Research Assistant
Clark, Henry - Accelerator Physicist (50%)
Horvat, Vladimir - Research Scientist (50%)
Hyman, Bruce - Research Associate
Kennas, Miltiadis – Research Associate
Kim, George - Accelerator Physicist
May, Don – Senior Accelerator Physicist
Roeder, Brian - Accelerator Physicist
Park, Hyo-In - Accelerator Physicist
Parker, Cody – Accelerator Physicist - From 7/1/2022
Saastamoinen, Antti (50%) – To 10/27/2022
Tabacaru, Gabriel - Accelerator Physicist

Computer Systems Staff

Burch, Jr. Robert Lead Microcomputer/LAN Administrator
Hagel, John C. Research Scientist (50%)
Gauthier, Jerome
Lui, Yiu-Wing

Engineering Staff

Molitor, Stephen - Senior Mechanical Engineer
Olsen, Robert - Senior Mechanical Engineer

Postdoctoral Research Associates

Kilmo, Jozef – From 10/25/2022
Kolhinen, Veli Sakari – To 7/31/2023
Pan, Jinjin - To 10/9/2022
Parker, Cody – To 6/30/2022
Picayo, Gabriela – To 10/1/2022
Sun KaiJia – To 8/1/2022
Zakusilova, Vera – From 12/1/2022
Zelga, Kamila – To 4/30/2023

STUDENTS

April 1, 2022 - March 31, 2023

Graduate Students and Research Assistants

Abbott, Austin
Aboona, Bassam
Aboud, Eric – To 1/15/2022
Alafa, Alex – From – From 9/1/2022
Amberger, Ryan – From 8/18/2021
Anderson, Derek – To 9/30/2022
Bartsch, Robert – From ???
Dede, Stefania – To 1/2023
Depastas, Theodoros – From 8/2022
Fentress, Andrew – From ???
Friendenberg, David – From 10/2022
Glennon, Kevin
Hankins, Travis
Hannaman, Andy
Harris, Emily
Haynes, Isaac
Henderson, Lawrence
Kirkland, Amelia
Kopec, Natalia – From 9/2022 To 1/2023
Liu, Yanfang
McCain, David
Mildon, Jordan
Nasser, Morgan
Onyango, Thomas
Ozmetin, Asim
Parker, Cameron – From
Rider, Robert – To 12/31/2022
Rinderknecht, Ryan – To 3/1/2023
Robicheaux, Stephen
Roosa, Michael
Santucci, John – From 8/19/2021
Sarver, Issac
Schultz, Steven
Scriven, Dustin
Sengupta, Arjun
Settlemyre, Thomas
Shin, Eunkyoung
Sorensen, Maxwell
Tang, Zhanduo
Tobar, Justin
Tobin, Zachary
Tyler, Jace
Wellons, Benjamin – From 1/16/2023
Wen, Pengshen
Zakusilova, Vera – To 11/30/2022

Undergraduates and Student Technicians

Alafa, Alex – To 8/31/2022
Ascione, Alexander – To 5/9/2023
Diaz, Briana - From 9/14/2020
Gallegos, Rachel – To 5/1/2023
Green, Brooklyn – From 5/2022
Jeffery, Logan – To 7/9/2021
Jeske, Colby – To 5/1/2023
Kovacs, Isabel – From 2/4/2022
Lofton, Kylie
Reuter, Madison
Stewart, Laynie – To 12/1/2022
Tagoe, Eric – To 12/1/2022

ORGANIZATIONAL CHART - CYCLOTRON INSTITUTE

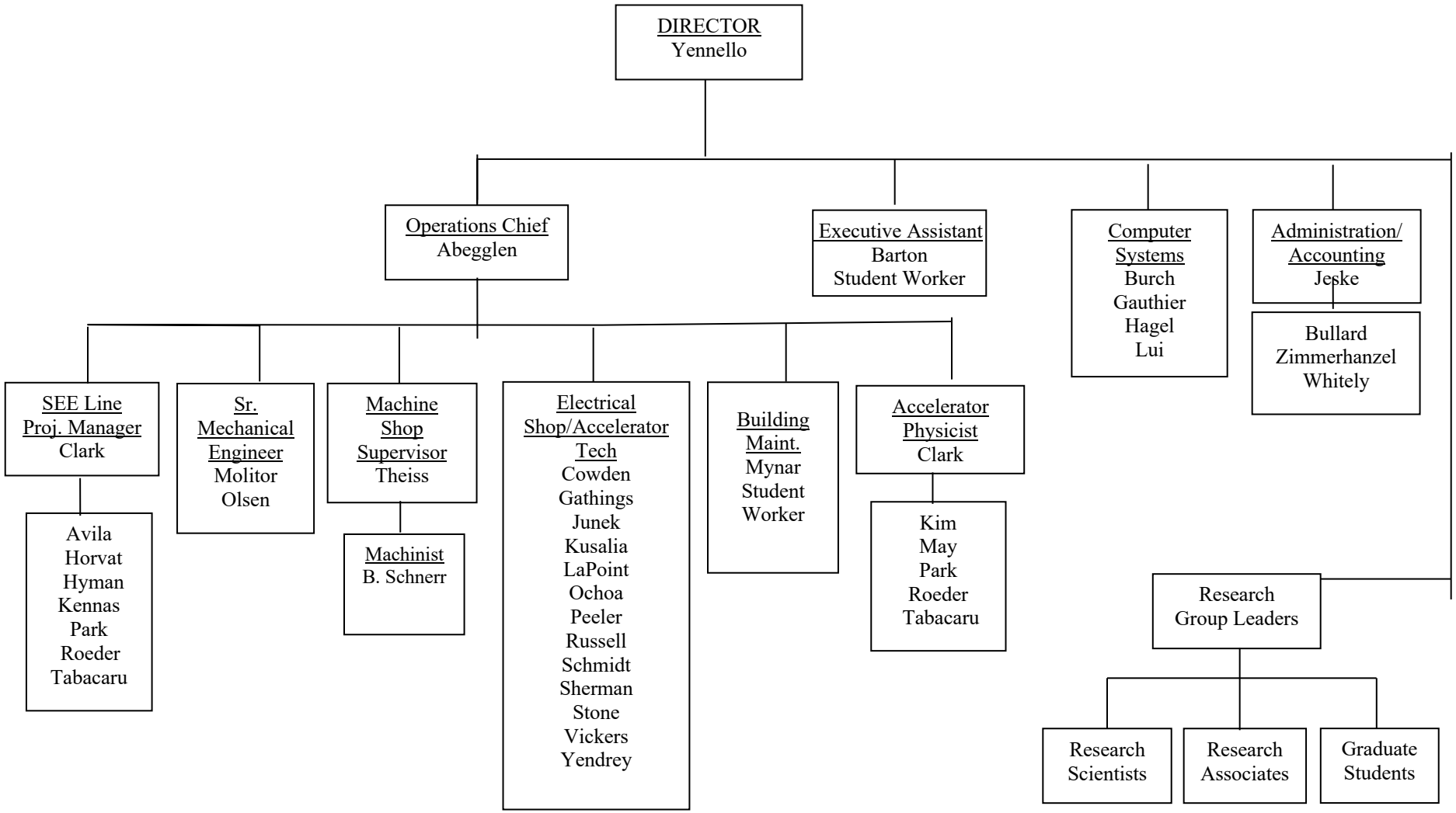

STUDENTS WHO RECEIVED GRADUATE DEGREES
FROM THESIS WORK CONDUCTED
AT
THE CYCLOTRON INSTITUTE

April 1, 2022 – March 31, 2023

Name	Year	Thesis Title	Advisor	Present Position
Derek Anderson	2022	*The electric conducitivity of hot pion matter*	S. Mioduszewski	Postdoctoral research associate at Iowa State University (ACU)

INSTITUTE COLLOQUIA AND SEMINARS

April 1, 2022 - March 31, 2023

2022

April 5	Dr. Ragnar Stroberg, Assistant Physicist, Argonne National Laboratory, Argonne, Illinois 60439	*Thick or thin? Ab initio calculations of the ^{208}Pb neutron skin*
May 3	Asistant Professor Kristina Launey Louidisns State University, Baton Rouge, Louisana	*Nuclear clustering and reactions from first principles*
May 26	Research professor Robert Charity, Department of Chemistry, Washington University in St. Louis, St. Louis, Missouri 63130	*Proton-rich exotica: 4,5,6-body decays in the light nuclei*
August 11	Mr. Theo Depastas, Department of Physics & Astronomy, Texas A&M University, College Station, Texas	*A study of the nuclear equation of state in the context of molecular dynamics: ground state properties and giant resonances*
August 23	Dr. Xiaodong Tang, Institute of modern physics, Chinese academy of sciences, Lanzhou, China	*Deep underground laboratory measurement of $^{12}C(\alpha,n)^{16}O$ in the Gamow windows of the s- and i-process*
September 6	Dr. George A. Souliotis Laboratory of Physical Chemistry, Department of chemistry, National and Kapodistrian, University of Athens, Athens, Greece	*Study of multinucleon transfer channels in heavy-ion-induced peripheral collisions at beam energies of 15-25 Mev/nucleon*
September 13	Professor Alex Magner Kyiv Institute, National Academy of Science of Ukraine, Kyiv, Ukraine	*Nuclear level density in the micro-macroscopic approach*
September 27	Meytal Duer, Technische Universitat Darmstadt, 64289 Darmstadt, Germany	*The quest for the tetra-neutron*

October 20	Dr. Andrea Richard Postdoctoral Research Lawrence Livermore National laboratory, Livermore, California	*Unraveling the mystery of i-process nucleosynthesis one reaction at a time*
December 6	Professor Benoit Gall University of Strasbourg and CNRS-IPHC Strasbourg, France	*Developments of intense metallic beams for spectroscopy and synthesis of superheavy elements*
December 13	Dr. Belen Monteagudo Godoy Facility for Rare Isotope Beams (FRIB) Michigan State University East Lansing, Michigan 48824	*Structure of the Be heavy isotopes ^{16}Be, ^{15}Be and ^{14}Be*

2023

January 24	Dr. Natsumi Ikeno, Tottori University, Japan and Cyclotron Institute, Texas A&M University, College Station, Texas	*Meson-nucleus bound system and exotic hadron*
February 7	Jennifer Smith, Assistant VP &Title IX Coordinator University Risk, Ethics and Compliance, Texas A&M University	*Nine things every faculty and staff should know about title IX (and civil rights!) at Texas A&M University*
February 14	Dr. Matt Williams, Lawrence Livermore national Laboratory, Livermore, California	*Experimental studies on the nuclear fingerprints of massive stars*
March 7	Caleb Benetti John D. Fox Superconducting Accelerator Laboratory Florida State University Tallahassee, Florida 32306	*Two particle transfer reactions for nuclear structure*
March 23	Professor Shelly Lesher, Professor and chair of physics, University of Wisconsin and guest Professor, university of Notre Dame	*What can we learn from history? The impact of nuclear science on society*

STUDENTS WHO RECEIVED GRADUATE DEGREES
FROM THESIS WORK CONDUCTED
AT
THE CYCLOTRON INSTITUTE

April 1, 2022 – March 31, 2023

Name	Year	Thesis Title	Advisor	Present Position
Derek Anderson	2022	*The electric conducitivity of hot pion matter*	S. Mioduszewski	Postdoctoral research associate at Iowa State University (ACU)